Australian National University

LABEL-FREE FUNCTIONAL IMAGING OF PLATELETS AT NANOSCALE

Yujie Zheng

A thesis submitted for the degree of

Doctor of Philosophy of

The Australian National University

November 2022

Declaration

This thesis is an original work conducted by me during the period of April 2017 and December 2021 at the Research School of Engineering and John Curtin School of Medical Research, Australian National University, Canberra, Australia.

This Ph.D. work has been primarily supervised by Dr Woei Ming (Steve) Lee and partial support supervision by Prof. Elizabeth Gardiner throughout.

Parts of the works in the thesis (Chapter 5,7) were conducted as collaboration projects with Dr Samantha Montague in John Curtin School of Medical Research. Works related to sample preparation were done with Dr Yean Jin Lim, Mr Junxiang Zhang, Ms Sarah Hicks, Ms Simone Brysland, Ms Samina Nazir, and Ms Yee Lin Thong. Accordingly, each of their contribution(s) has been mentioned in the relevant chapters.

Yujie Zheng

November 2022

Acknowledgments

I wish to express my most sincere gratitude and appreciation to my supervisor Steve Lee for your guidance, patience, and encouragement for the last four years we worked together. I appreciate everything you have taught me, not just the knowledge on optics, but most importantly, the mindsets for critical thinking and problem-solving. I would also like to thank my co-supervisor Elizabeth Gardiner (Liz), for all the guidance and explanations in platelet biology. Your enthusiasm for platelets always inspired me and made me ask myself how to make better platelet imaging tools.

I would also like to thank all my team members and colleagues, Tahseen Kamal, Yongxiao Li, Xuefei He, Avinash Upadhya, Daniel Lim, Tienan Xu, Tao Xu, Zhiduo Zhang, Junxiang Zhang, Hanqi Lin, Carmen Longbottom, Yi Wang, Samantha (Sam) Montague and Alex Ma. Thanks to all of you for your kindness, support, and companionship throughout the years. To Sam and Daniel, thank you for all the knowledge and discussions on biology and sample preparation. I could never get the results without your help. To Avinash, we have been through a lot together, paper rejections, Covid lockdown, and relocation. We share our feelings and always encourage each other. All of these meant a lot to me, thank you. To Xuefei and Yi, you guys are not just my colleagues but best friends in my life. Thank you for always being on my side, being patient with me, and supporting me whenever needed.

To all my friends and especially my housemates, Zheyu, Shihao, and Siqi, I am glad I am with you guys during the 2020 lockdown. I would never survive without all the fun times cooking, hiking, gaming, and drinking together. To Shihao, thank you for being my driving coach and supervising me drive for a few months. I would not get my license without your help. To Zheyu, we known each other since undergrads and were housemate for the past five

years. Thank you for the companionship, for cooking, driving, finding good hiking spots, and organizing road trips. It is my pleasure to have you during this journey. To Siqi, I missed our times together, watching drama, sharing secrets, gossiping around and other outdoor activities that enriched our weekend and Canberra life.

To my parents, for always supporting me, believing me, no matter what decision I made, for allowing me to grow into an independent, strong human being. Your love, support, and encouragement make me who I am, and I would not have been able to complete this work without your love and support.

Abstract

Platelet is the key cellular machinery of a blood clot/thrombus. Platelet morphodynamics under fluid shear plays an essential role in the quantitative analysis of platelet dysfunction. The mechanical properties of platelets inform the formation of haemostatic plugs that have wide application in bleeding disorders and cardiovascular diseases. During clotting, individual platelets sense physical and biochemical agonists on their surface receptors that trigger the formation of membrane protrusions. Platelets would reorganize their cytoskeletal structure upon sensing agonists to manipulate the extracellular matrix (collagen and fibrin fibres) and form a stable blood thrombus. However, platelet dysfunction would lead to an imbalance between haemostasis and thrombosis that causes life-threatening diseases, including pulmonary embolism and ischemic stroke [1].

In the last few decades, the development of advanced imaging tools (optical [2], electrons [3], conductance [4], and atomic force [5]) have revealed a highly heterogeneous distribution of platelet morphologies at the microscopic scale that spreads across a thrombus. Under platelet spreading assays, the membrane protrusions of platelets have been observed to manipulate fibrin fibres [6] and contribute to the mechanical contraction of a blood clot. Current optical imaging tools in platelet are generally performed with specific fluorescence markers. Since the human platelets sample is unsuitable for genetic manipulation, platelet labelling is often conducted using membrane markers or with fixed samples which could restrict nanoscopic imaging of the platelet dynamics at video rate. Rapid assessment of platelet dysfunction without markers will accelerate many aspects of platelet studies. Therefore, it is imperative to develop a label-free imaging flow assay (video rate and diffraction-limited) that could measure the morphodynamics of single platelet in a thrombus [7]. Existing label-free imaging tools such as differential interference contrast [8], darkfield [9], phase

contrast [10], and reflectance interference contrast [11] are regularly applied to platelets imaging but lack imaging contrast for quantifying platelet motility [2].

Nanoscopic label-free imaging techniques based on light scattering and interferometry have emerged as a rapid high-resolution live-cell imaging technique [12, 13]. Applying nanoscopic label-free imaging permits real-time imaging of platelet membrane protrusion (lamellipodium, filopodia) and morphological profiling. The capability to quantify platelet morphology during thrombus formation and embolization, along with platelets detachment, enables in-depth assessment of functional responses of platelets.

In the first part of the thesis (Chapter 1-3), I shall describe the role of scattering in forming a microscopic image of a cell using numerical models and review current imaging tools tailored for platelet and thrombus studies. The second part of the thesis (Chapter 4) covers the steps to design, calibrate, and characterize a series of label-free tools (COSI) for platelet imaging under flow. Using the COSI system, I demonstrate the detection sensitivity down to 20 nm gold nanoparticles without post-processing. In the third part of the thesis (Chapter 5-6), I shall elaborate on platelet spreading assays and migration studies to quantify single platelet adhesion and characterize platelet membrane protrusions with ECM (collagen, fibrin, fibrinogen, CRP). In the final chapter, I demonstrate label-free imaging on thrombus formation and study the effects of a metalloproteinase inhibitor in embolization with piconewton (pg) and high spatial-temporal resolution (0.4 μm/s).

In summary, this thesis paves the way for label-free nanoscale imaging of quantitative study of platelets and blood thrombus under flow.

References

1. Kaye, A. D.; Jeha, G. M.; Moll, V.; Ward, C. T.; Watson, M. R.; Wynn, J. T., II; Hockstein, M. A.; Hall, K. M.; Viswanath, O.; Urits, I.; Prabhakar, A.; Cornett, E. M., Platelet Dysfunction Diseases and Conditions: Clinical Implications and Considerations. *Advances in Therapy* **2020,** *37* (9), 3707-3722.

2. Montague, S. J.; Lim, Y. J.; Lee, W. M.; Gardiner, E. E., Imaging Platelet Processes and Function—Current and Emerging Approaches for Imaging in vitro and in vivo. *Frontiers in Immunology* **2020,** *11*.

3. Tomaiuolo, M.; Matzko, C. N.; Poventud-Fuentes, I.; Weisel, J. W.; Brass, L. F.; Stalker, T. J., Interrelationships between structure and function during the hemostatic response to injury. *Proceedings of the National Academy of Sciences of the United States of America* **2019,** *116* (6), 2243-2252.

4. Seifert, J.; Rheinlaender, J.; Lang, F.; Gawaz, M.; Schäffer, T. E., Thrombin-induced cytoskeleton dynamics in spread human platelets observed with fast scanning ion conductance microscopy. *Sci. Rep.* **2017,** *7* (1).

5. Nguyen, T. H.; Palankar, R.; Bui, V. C.; Medvedev, N.; Greinacher, A.; Delcea, M., Rupture Forces among Human Blood Platelets at different Degrees of Activation. *Scientific Reports* **2016,** *6*.

6. Kim, O. V.; Litvinov, R. I.; Alber, M. S.; Weisel, J. W., Quantitative structural mechanobiology of platelet-driven blood clot contraction. *Nature Communications* **2017,** *8* (1).

7. Sadoul, K.; Lafanechère, L.; Grichine, A., Live imaging of single platelets at work. *Platelets* **2020,** *31* (5), 551-558.

8. Thomas, S. G., The structure of resting and activated platelets. In *Platelets*, 2019; pp 47-77.

9. Kraus, M. J.; Seifert, J.; Strasser, E. F.; Gawaz, M.; Schäffer, T. E.; Rheinlaender, J., Comparative morphology analysis of live blood platelets using scanning ion conductance and robotic dark-field microscopy. *Platelets* **2016,** *27* (6), 541-546.

10. Bandyopadhyay, D.; Baruah, H.; Gupta, B.; Sharma, S., Silver nano particles prevent platelet adhesion on immobilized fibrinogen. *Indian Journal of Clinical Biochemistry* **2012,** *27* (2), 164-170.

11. Lee, D.; Fong, K. P.; King, M. R.; Brass, L. F.; Hammer, D. A., Differential dynamics of platelet contact and spreading. *Biophysical Journal* **2012,** *102* (3), 472-482.

12. Jünger, F.; Olshausen, P. V.; Rohrbach, A., Fast, label-free super-resolution live-cell imaging using rotating coherent scattering (ROCS) microscopy. *Scientific Reports* **2016,** *6*.

13. Park, J. S.; Lee, I. B.; Moon, H. M.; Joo, J. H.; Kim, K. H.; Hong, S. C.; Cho, M., Label-free and live cell imaging by interferometric scattering microscopy. *Chemical Science* **2018,** *9* (10), 2690-2697.

Publications

Journals:

1. **Y. Zheng** *, Y. J. Lim *, H. Lin, T. Xu, C. Longbottom, V. Delghingaro-Augusto, Y. L. Thong, C. R. Parish, E. E. Gardiner, and W. M. Lee. " Combined Scattering, Interferometric and Fluorescence Oblique Illumination for Live Cell Nanoscale Imaging." *ACS Photonics*. *In Press* (2021). **Co-first author*

2. **Y. Zheng**, S. J. Montague, Y. J. Lim, T. Xu, T. Xu, E. E. Gardiner, and W. M. Lee. "Label-free multimodal quantitative imaging flow assay for intrathrombus formation in vitro." *Biophysical Journal* 120, no.5 (2021): 791-804.

3. Z. Zhang, **Y. Zheng**, T. Xu, A. Upadhya, Y. J. Lim, A. Mathews, L. Xie, and W. M. Lee. "Holo-UNet: hologram-to-hologram neural network restoration for high fidelity low light quantitative phase imaging of live cells." *Biomedical Optics Express* 11, no. 10 (2020): 5478-5487.

4. T. Xu, Y. J. Lim, **Y. Zheng**, M. Jung, K. Gaus, E. E. Gardiner, and W. M. Lee. "Modified inverted selective plane illumination microscopy for sub-micrometer imaging resolution in polydimethylsiloxane soft lithography devices." *Lab on a Chip* 20, no. 21 (2020): 3960-3969.

5. A. Upadhya*, **Y. Zheng***, L. Li, and W. M. Lee. "Structured Back focal plane interferometry (SBfpi)." *Scientific Reports* 9, no. 1 (2019): 1-10. **Equal contribution*

Conference proceedings/talks:

1. **Y. Zheng**, S. J. Montague, Y. J. Lim, E. E. Gardiner and W. M. Lee. “Quantification of thrombus kinetics through inhibiting receptor shedding with label-free imaging flow Assay”. Miniaturized System for Chemistry and Life Sciences (μTAS 2021).

2. A. Upadhya*, **Y. Zheng***, L. Li, and W. M. Lee. "Extending tracking range through structured back focal plane interferometry." In *Complex Light and Optical Forces XV*, vol. 11701, p. 1170110. International Society for Optics and Photonics, 2021. **Equal contribution*

3. **Y. Zheng**, S. J. Montague, Y. J. Lim, T. Xu, E. E. Gardiner, and W. M. Lee. "Video Rate, High Contrast Morphological Imaging of Blood Thrombus using Label - Free Coherent Optical Scattering and Interferometry (COSI) Microscopy." In ISTH: Platelets and Megakaryocytes, 2020.

4. **Y. Zheng**, S. J. Montague, Y. J. Lim, T. Xu, E. E. Gardiner, and W. M. Lee. "Coherent Optical Scattering and Interferometry (COSI) Microscopy for Morphological Imaging of Thrombus." In *CLEO: Applications and Technology*, pp. AM1I-4. Optical Society of America, 2020. **(Highlighted talk)**

5. **Y. Zheng**, Y. J. Lim, S. J. Montague, E. E. Gardiner, and W. M. Lee. "Coherent optical scattering and interferometry microscopy for functional imaging of thrombus." In *Microscopy Histopathology and Analytics*, pp. MTh3A-3. Optical Society of America, 2020.

6. **Y. Zheng**, and W. M. Lee. "Label-free optical scattering and interferometry microscopy for functional imaging of thrombus." In *Biophotonics Australasia 2019*, vol. 11202, p. 1120207. International Society for Optics and Photonics, 2019.

7. F. M. Ayyalil, S. J. Montague, S. Hicks, A. Kaur, A. Jahangiri, N. Pati, P. Crispin, **Y. Zheng** *et al.* "Platelet Function in Paroxysmal Nocturnal Haemoglobinuria." (2019): 4884-4884.

Table of Contents

Nomenclature

Adenosine Diphosphate	**ADP**
Atomic Force Microscopy	**AFM**
Acousto-optics	**AODs**
Actin Related Protein 2/3	**Arp 2/3**
Back Focal Plane	**BFP**
Bovine Serum Albumin	**BSA**
Charge-coupled Device	**CCD**
Coherent Brightfield Microscopy	**COBRI**
Collagen-related Peptide	**CRP**
Data Acquisition	**DAQ**
Discrete Dipole Approximation	**DDA**
Digital Holographic Microscopy	**DHM**
Differential Interference Contrast	**DIC**
Darkfield Microscopy	**DM**
Extracellular Matrix	**ECM**
Electromagnetic	**EM**
Extracellular Vesicles	**EVs**
Finite-difference Time-domain	**FDTD**
Fast Fourier Transformation	**FFT**
Field of View	**FOV**
Highly Inclined and Laminated Optical Sheet	**HiLO**
Hexamethyldisilazane	**HMDS**
Green Fluorescent Protein	**GFP**
Grazing Incidence Structured Light Illumination	**GI-SIM**
Galvanometer-mounted Tilting Mirror (GM)	**GM**

Gold Nanoparticles	**GNPs**
Graphics Processing Unit	**GPU**
Illumination Numerical Aperture	**INA**
Interferometric Scattering	**iSCAT**
Optical Path Difference	**OPD**
Phosphate-buffered Saline	**PBS**
Platelet Rich Plasma	**PRP**
Poly-dimethylsiloxane	**PDMS**
Quantitative Phase Microscopy	**QPM**
Red Blood Cells	**RBCs**
Refractive Index	**RI**
Reflectance Interference Contrast Microscopy	**RICM**
Rotational Optical Coherent Scattering	**ROCS**
Region of Interest	**ROI**
Scientific Complementary Metal Oxide Semiconductor	**sCMOS**
Scanning Electron Microscopy	**SEM**
Scanning Ion-conductance Microscopy	**SICM**
Structured Illumination Microscopy	**SIM**
Signal to Noise Ratio	**SNR**
Stochastic Optical Reconstruction Microscopy	**STORM**
Transmission Electron Microscopy	**TEM**
Traction Force Microscopy	**TFM**
Total Internal Reflection Fluorescence Microscope	**TIRF**
Thromboxane	**TxA2**
Vasodilator-stimulated Phosphoprotein	**VASP**
Von Willebrand Factor	**VWF**
Wiskott–Aldrich Syndrome protein	**WASp**

Chapter 1 Harnessing Scattered Light for High-speed and Nanoscopic Imaging

Cytoskeleton remodelling results in membrane protrusions are linked to morphological profiles of motile cells that undergo migration, differentiation, and invasion [1-6]. Identifying membrane protrusions is critical in establishing how cells physically interact with the microenvironment to form cell-cell junctions [7-9] and shape organs, which inform us of their roles in diseases [10-12], and responses to therapeutic drugs [13, 14]. Brightfield, phase contrast, differential contrast, and darkfield microscopy have been the bedrock of cell biology and have identified a wide range of membrane protrusions (lamellipodium, filopodia, and ruffles). In contrast to fluorescence imaging that is heavily influenced by light absorption of the photochemistry of dyes [15, 16] , label-free imaging optimizes the optical sensitivity to refractive index (RI) of the sample itself [17-20] through elastic scattering [21-23]. Most biological cells can be considered as phase-only objects, they absorb very little light and leave a minimal amount of optical scattering signal for high-contrast imaging [17, 24]. Therefore, the contrast of label-free imaging (non-absorptive) is determined by the sensitivity in collecting the weakly scattered light from cells [25, 26]. In biological samples, refractive indices are non-specific and heterogeneously distributed. High refractive index organelles include lipids (droplets and membrane) and actin filaments coincident with membrane protrusions. Maximizing signal from high refractive index organelles using elastic scattered light (non-absorptive) permits a stable biomarker without any concerns in photobleaching and photodamage [27, 28].

The theoretical basis of the Mie scattering [29] serves a key biomarker for high contrast label free imaging. Two main factors limiting the magnitude of scattered light are the particle size and refractive index. Traditional label-free light microscopy is challenging because the RI differences between cytoplasm, extracellular milieu, and immersing solution are small [30, 31]. Imaging nanoscale features such as filopodia and lamellipodia of living cells is more challenging because the scattering signal is much weaker (with 60-700 nm diameter in size [32]), therefore, requires ultra-sensitive detection methods. However, recent developments in detecting scattering signals from weakly scattered samples using interferometry [33-37] have demonstrated single-molecule detection sensitivity down to single proteins [38-41] and viruses [42], paving the way for high-sensitivity imaging of biological samples without labelling [21].

In this chapter, I shall first introduce the concept of light scattering and explain how scattering magnitude is related to particle size and refractive index. I will then discuss the methods evaluating light scattering from biological samples and how scattered light can be used in imaging techniques. I will also review label-free imaging techniques for high contrast cell imaging based on light scattering.

1.1 Light Scattering: Interaction of Light and Matter

1.1.1 Elastic Scattering

The concept of light scattering was firstly proposed by Lord Rayleigh in 1871 when he sought to understand light from the sky, specifically the brightness, colour, and polarization of the atmosphere. He believed that the light we receive from the sun is diverted from its regular course by small, suspended particles in the sky [43]. For the first time, he used the word *scattering* instead of reflection to describe this action of redirecting light from its original direction. In 1899, Rayleigh suggested that the particles are molecules in the air and

succeeded in relating the molecular extinction to the refractive index. This provided the first accurate method of estimating Avogadro's number that describes the number of molecules in a given amount of substance ($N_A = 6.022\times10^{23}$ mol^{-1}) [44].

Light scattering can be described as elastic energy transfer where no energy or wavelength is changed. It can be thought of as redirection of light. One example is a scratched mirror will create a separate reflection of light that deviates from the direct reflected path. When light (incident electromagnetic (EM) wave) encounters and interacts with a scattering particle, as shown in Fig. 1-1, the electron orbits within the particle's constituent molecules are perturbed and forced to oscillate periodically. The oscillation or perturbation of the electron cloud is at the same frequency (ν_o) as the electric field of the incident wave, which will lead to a periodic separation of charges within the molecule (induced dipole moment) [45]. The oscillating induced dipole moment constitutes the source of EM radiation, therefore causing light scattering. Most of the light scattered by the particle is emitted at the identical frequency (ν_o) of the incident light, a process referred to as elastic scattering.

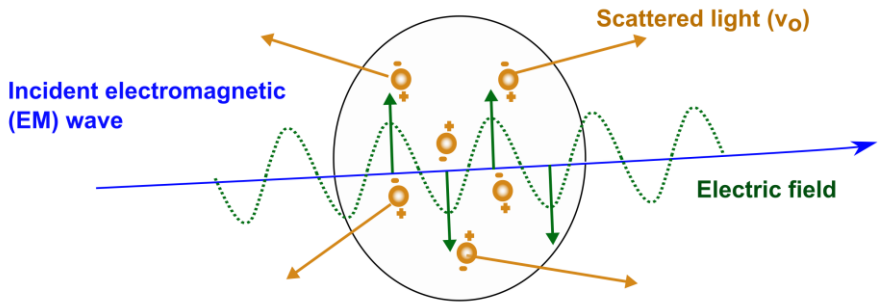

Figure 1-1 Principle of light scattering, where a particle interacts with the incident electromagnetic (EM) field. The oscillating electric field of the incident wave perturbed the electrons orbited the molecule and periodically separated the charges, resulting in scattered light.

Fig. 1-2 shows the formulation of light scattering based on an incident electromagnetic field (Ei) and an object. The object is described as a spherical particle with radius (r) and can be any particle, including biomolecules or chemical compounds, that has a distinct refractive index (N_1) with respect to the medium (N). The incident EM field creates a field inside the molecules (internal field Et) and a diffracted field (scattered field Es). A wide range of analytical approaches is used to calculate the elastic light scattering by single particles, and the most common methods include Rayleigh scattering and Mie theory. Mie theory is the generic name for scattering by a sphere of any size, both small and large, and the common term Rayleigh scattering refers to the Rayleigh limit of Mie scattering due to particles much smaller than the wavelength (λ) of light ($2\pi r/\lambda << 1$). In this thesis, I use the Mie theory to numerically model the scattering properties of various particles and study the influence of illumination conditions in different imaging techniques.

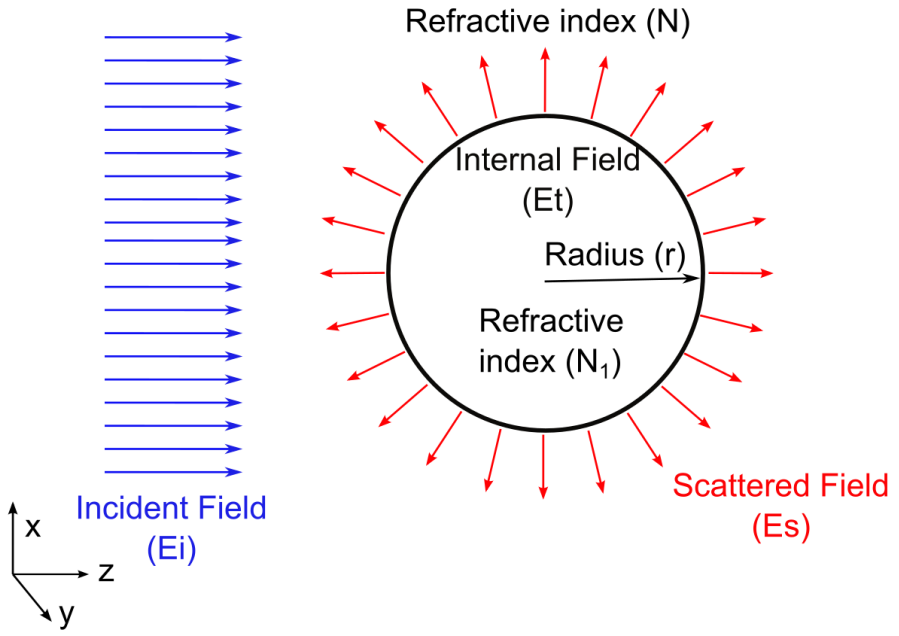

Figure 1-2 A simple model illustrating Mie theory consists of an incident EM field (Ei) and a spherical object (radius r) with a refractive index of N_1. The electrical fields generated inside the object and the scattered light are noted as the internal field (Et) and scattered field (Es), respectively.

In Mie theory [29], the scattering field from the object can be written as a linear combination of the incident field as shown in Eq. 1-1, where $i = \sqrt{(-1)}$, M_{oln} and N_{eln} represent vector spherical harmonics (full equation in Appendix A), and a_n and b_n are the scattering coefficients (Eq. 1-2 and 1-3). The parameters x and m represent the size factor ($x=2\pi Nr/\lambda$) and the relative refractive index ($m=N_1/N$). Riccati-Bessel functions are written as $\xi_n(\rho) = \rho h_n(\rho)$ and $\psi_n(\rho) = \rho j_n(\rho)$.

$$Es = \sum_{n=1}^{\infty} E_n\left(ia_n N_{eln}^{(3)} - b_n M_{oln}^{(3)}\right), with\ E_n = \frac{i^n(2n+1)}{n(n+1)}E_0 \tag{1.1}$$

$$a_n = \frac{m\psi_n(mx)\psi_n'(x) - \psi_n(x)\psi_n'(mx)}{m\psi_n(mx)\xi_n'(x) - \xi_n(x)\psi_n'(mx)} \tag{1.2}$$

$$b_n = \frac{\psi_n(mx)\psi_n'(x) - m\psi_n(x)\psi_n'(mx)}{\psi_n(mx)\xi_n'(x) - m\xi_n(x)\psi_n'(mx)} \tag{1.3}$$

Equation 1.4 describes scattering cross-section (σ_s) using the size factors (x) and the scattering coefficient (a_n and b_n, determined by refractive index and size). These two factors appear to be the dominant factors that affect scattering intensity (a_n and b_n represent the scattering coefficients). In the following section, I shall investigate how *size* and *refractive index* affect the intensity and phase of scattered EM. I shall also discuss the scattering profile of various samples in three-dimensional space based on Mie theory. Full detail of derivation of Eq. 1.1-1.4 can be found in appendix A.

$$\sigma_s = \frac{2}{x^2}\sum_{n=1}^{\infty}(2n+1)(|a_n|^2 + |b_n|^2) \tag{1.4}$$

1.1.2 Scattering Profile and Particle Size

This section investigates how the physical properties (size and refractive index) affect the intensity and phase of scattered EM fields. Refractive index is a dimensionless number that describes the bending of a ray of light when travelling from one medium into a different medium. The refractive index of a material is normally described using a complex number N = N' + jN", where the real part N' describes the ratio of the free-space speed of light to the phase speed of the electromagnetic wave in the medium. In contrast, the imaginary part N" (N"= $\mu_a\lambda/4\pi$) is derived from the absorption coefficient μ_a (cm^{-1}) band indicating the attenuation of the light when passing through the material [46].

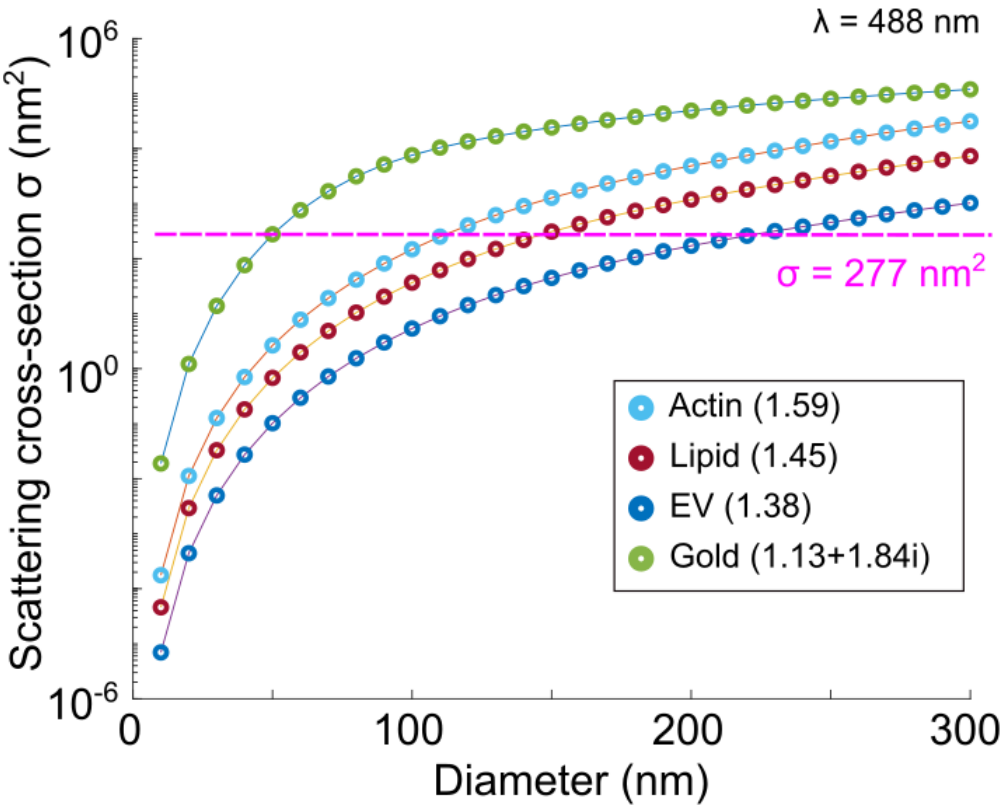

Figure 1-3 Scattering cross-section of molecules made of actin, lipid bilayer, extracellular vesicles, and gold at sizes from 10 nm to 300 nm. The refractive indexes of these molecules are 1.59. 1.45, 1.38 and 1.13+1.84i (λ = 488 nm), respectively. The cross-section is calculated using Mie theory and plotted in log-scale.

To demonstrate the influence of particle size and refractive index on the magnitude of scattering, I calculate the scattering cross-section (from Eq. 1.4) using Mie theory of four types of biomolecules with different RI: actin (1.59) [47], lipid bilayer (1.45) [48] extracellular vesicles (EV, 1.38) [49] and gold (1.13+1.84i, λ = 488 nm) [50], ranging from 10 nm to 300 nm in Fig. 1-3. These four types of molecules represent a heterogeneous group of cell-derived membranous structures [51] and the RI difference in the cytoplasm. Among four types of particles, gold nanoparticles (GNPs) possess a plasmonic effect [52], which is wavelength-dependent and has an imaginary component in RI, while other materials have a fixed RI. As the size of the particle increases, the scattering cross-section expands exponentially, e.g. the scattering cross-sections of 100 nm GNPs and 10 nm GNPs are 1.8×10^{-2} nm^2 and 7.6×10^{4} nm^2, respectively.

I also investigated the magnitude of forward and backward scattering that translates to transmittance-based [53] and reflection-based [26, 34, 54] imaging approaches. To numerically investigate the distribution of scattered light, particles that have similar scattering cross-sections are chosen: gold at 50 nm, actin at 110 nm, lipid bilayer at 145 nm, and EVs at 220 nm. All the particles have a cross-section (σ) $\approx$ 261 $\pm$ 10 nm^2. The axial scattering intensity profile (parallel to incident light) is calculated and plotted in Fig. 1-4 based on Mie theory [29]. All the nanoparticles have similar maximum intensity, while gold exhibits high absorption due to the imaginary component in RI. The GNP poses a strong backward scattering intensity, while other types of particles (actin, lipid, and EV) show a stronger forward scattering component. In all cases, constructive and destructive interferences are observed in the backward direction (bright and dark fringes) only, illustrating that the axial position of the particle can be retrieved using phase information from the backscattered light.

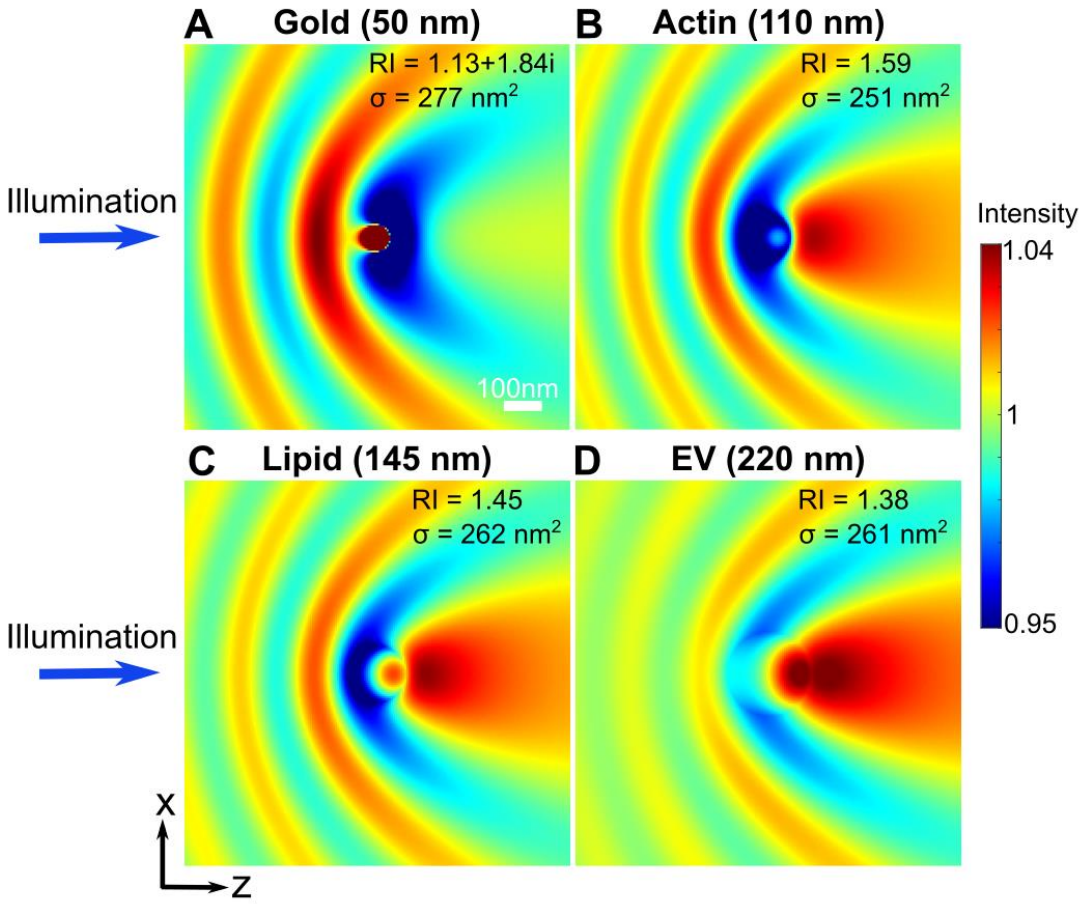

Figure 1-4 Simulation of scattering intensity of four types of molecules at similar scattering cross-section ($\sigma \approx 261 \pm 10$ nm^2), including (A) gold, (B) actin, (C) lipid and (D) extracellular vesicles at 50 nm, 110 nm, 145 nm, and 220 nm respectively. The refractive indexes of these molecules are 1.59. 1.45, 1.38 and 1.13+1.84i (λ = 488 nm). The scattering intensity is simulated using Mie theory, and the plots are in xz plane, with z indicating the direction of incident light.

1.1.3 Modelling Scattering in Biological Sample

Biological cells are more than just a bag of proteins and contain multiple intracellular components (organelle, nucleus). They could exist in different shapes, have various sizes and refractive index, ranging from 1.36 to 1.57, as illustrated in Table 1-1. This section will explain a discrete scattering model constructed to study scattering properties for membrane protrusions in biological cells. Membrane protrusion of cells includes lamellipodium, membrane ruffles, filopodial that are mainly made up of actin. However, these structures can

have strikingly different actin polymerization machinery. For example, the filopodia consist of parallel actin bundles, while the lamellipodia are characterized by a dense network of short, branched actin filaments [55] [56, 57] as shown in Fig. 1-5. Instead of creating a simple spherical scattering model using the existing Mie theory [29], the cell model here is asymmetrical due to the formation of membrane protrusions, indicating numerical approaches for complex shapes are needed.

Table 1-1 refractive index values for organelles in a cell

Structure	Refractive index	Refs
Actin	1.57	47, 58
cytoplasm	1.36-1.39	59
Membrane	1.46-1.54	60
Nucleus	1.355-1.365	61, 62
Mitochondria	1.4-1.142	62

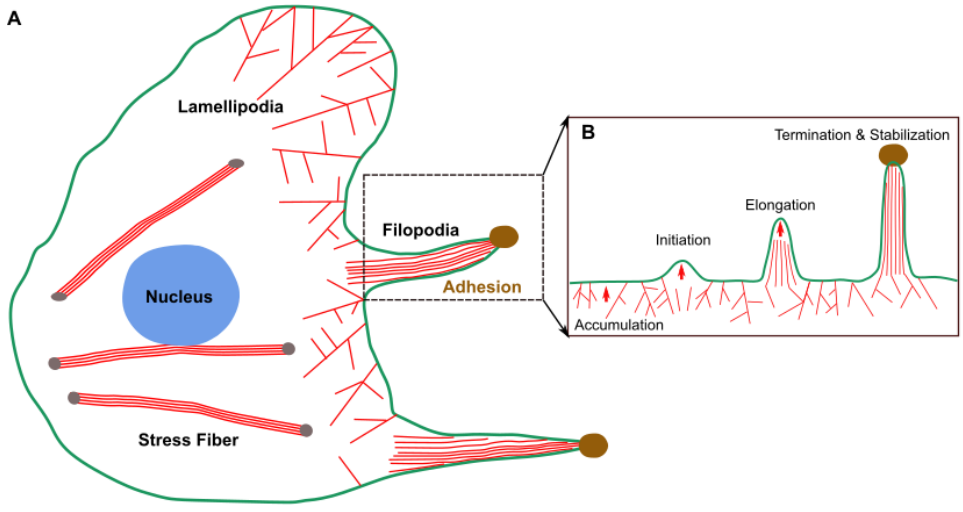

Figure 1-5 (A) Actin distribution during cell migration. Red lines indicate actin filaments. (B) The process of filopodia formation includes actin polymerization and forming of actin bundles.

Several numerical methods have been developed to investigate the scattering properties for particles having an arbitrary shape and/or optical inhomogeneity, including T-matrix that is based on an expansion in vector spherical harmonics [63-65], the finite-difference time-domain (FDTD) method, which solves Maxwell's equations using grids numerically [66, 67], and the discrete dipole approximation (DDA) method that decomposes particles into small sections or dipoles [68, 69]. Here, I choose T-matrix to model the scattering field of biological cells due to the simplicity in cell model construction and minimal requirement in computational power.

T-matrix stands for translation matrix for solving light scattering of non-spherical structures originally formulated by Peter Waterman in 1965 [70]. Similar to Mie theory, T-matrix works by relating the incident field coefficient to the scattering field coefficient of the structure using a translation matrix. The calculation of scattering field coefficient only depends on the particle properties, e.g. composition, size, geometry, and orientation. Consider if the biological cell is composed of small spheres of different sizes, the incident field for each particle is the summation of illumination and the total scattered field from all other particles. Similarly, the incident field coefficient is calculated based on the original incident field coefficient and the summarization of scattered field coefficients. Here, a MATLAB-based T-matrix approach called "CELES" [71] was adopted, which can simulate the scattering field of structures of a larger number of particles ($>10^4$) with non-scientific GPU hardware.

Here, the platelets (essential cell fragments without nucleus) are used as the base model to study the process of platelet activation, where platelets start to change their shape (from discoid to spherical and then flat disk) and adhere on the ligands for hemostasis. During platelet adhesion on rigid surface, the basal layer of the platelet is known to conform to a flat surface. A hemisphere shape is chosen to study the adhesion of platelets because it

could increase contact area with the surface compared with a sphere or ellipsoid shape. The flat bottom allows the adhesion between activated platelet and the ligands, that replicates the platelet activation process. The study of platelet adhesion here focusses on how single platelet adhere onto the injury site and forming a tight seal during hemostasis. The platelet model consists of three components: a hemisphere shell representing the membrane, randomly distributed spheres with random sizing inside the shell representing vesicles and cytoplasm, and long chains of spheres representing filopodia structure composed of the actin filament. The activated platelet that is around 3 μm in diameter and 1.5 μm in height, as shown in Fig. 1-6 A-B. The refractive index and diameter of various spheres used in the model are demonstrated in Fig. 1-6 C.

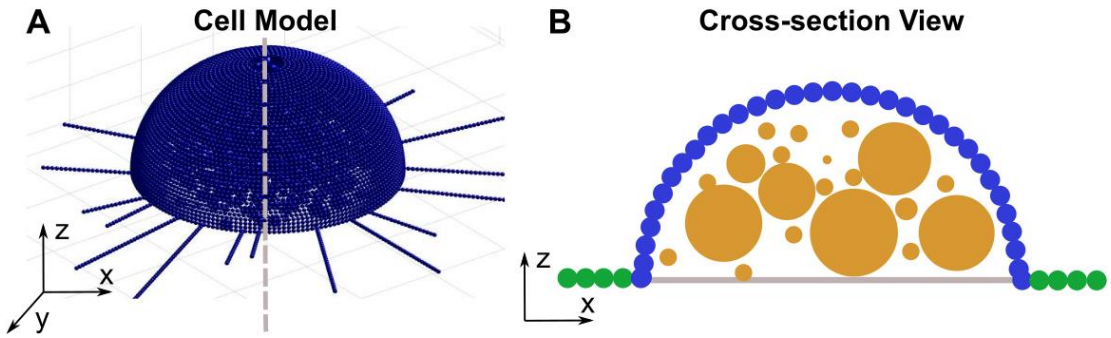

C

Component	Description	Size (d)	RI
Membrane	Hemi-sphere (shell)	50 nm	1.46
Cytoplasm	Randonly distributed spheres	7-300 nm	1.38
Filopodia	Actin	150 nm	1.57

Figure 1-6 Platelet model for studying scattering properties using CELES. 3D (A) and cross-section (B) view of the cell model. (C) Parameters (size and refractive index) of the particles used to construct platelet membrane, cytoplasm, and filopodia.

The simulation results of the electric near-field distribution of the platelet model using CELES [71] are shown in Fig. 1-7. The platelet model is illuminated by a monochromatic incident field (plane wave) along z-direction (Fig. 1-6 A), from the basal layer of the cell to

the apical surface. Fig. 1-7 A shows the electric field at the basal layer of the cell in the xy plane (z = 0) that results from the addition of scattering and internal fields from the cell and the incident field. This detection scheme resembles brightfield detection such as traditional upright microscopy. The fringes around the filopodia structures indicate the incident field is interfering with the scattering field. I also notice the weak imaging contrast around the filopodia region, causing these structures to be hard to resolve. In contrast, I demonstrate the pure scattering field and internal field in Fig. 1-7 B, which resembles the darkfield detection scheme. There is a remarkable increase in imaging contrast (around two folds increase in SNR) with the darkfield detection because all the structures and fine details could be visualized clearly in Fig. 1-7 B. In the next section, I shall explain the concept of imaging contrast in traditional brightfield microscopy, and the methods commonly used to enhance contrast and sensitivity in detecting biomolecules and cell imaging.

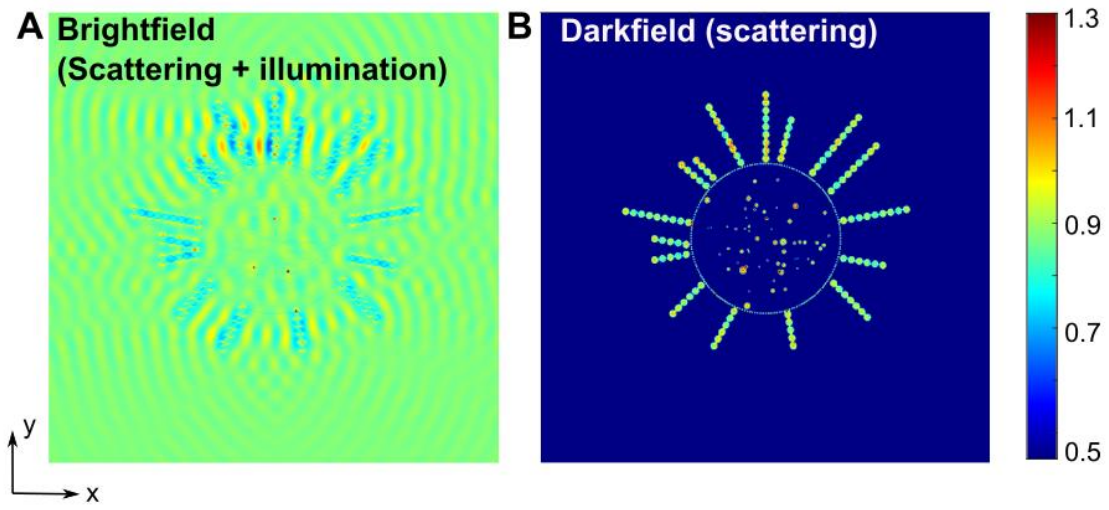

Figure 1-7 Simulated scattering intensity of the platelet model using CELES. Intensity profile in xy plane of brightfield (scattering field and illumination) (A) and darkfield (pure scattering field) (B) are shown, with z-axis indicating the direction of the incident light.

1.2 Enhancing Imaging Contrast with Light Scattering and Interference

The conventional light microscopy that records the scattered light in an optical system also refers to brightfield microscopy, which generally consists of a transillumination light source, a condenser lens, an objective lens, and a detector (eye or camera). White light from a halogen lamp is typically used as the illumination source, and the light scattered from the sample is collected to form an image [72]. The most prominent advantages of light microscopy are non-invasive and fast imaging, which permits imaging of highly dynamic or rapidly evolved activities in biological systems.

To characterize the imaging formation process in light microscopy, we consider the scattered field from the sample as $E_s = E_s e^{i\phi_s}$, and the signal on the detector to be the sum of the illumination and scattered (Eq. 1.5) [36], where $E_i = E_i e^{i\phi_r}$ denotes the complex field of the illumination. If we further break down the resulted light field, we can identify three separated components: illumination ($I_i = |\overline{E_i}|^2$), scattering ($I_s = |\overline{E_s}|^2$) and a cross-term component $2E_r E_s cos\phi$ representing the interference signal of illumination and scattering.

$$I_{det} \propto |\overline{E_i} + \overline{E_s}|^2 = I_i + I_s + 2E_i E_s cos\phi \tag{1.5}$$

Because most biological cells are phase objects and are weakly scattered, the magnitude of scattered light is significantly lower than the background, resulting in low imaging contrast and making traditional brightfield microscopy unsuitable for cell imaging. Therefore, background illumination plays a critical role in imaging contrast. Multiple attempts have been made to improve the imaging contrast, and those methods fall into two categories: minimizing background illumination or boosting the scattering and interference component. In the next section, I shall review the methods that enhance imaging contrast

through modifying the illumination background, including darkfield detection (block background illumination), interferometric scattering (background subtraction), and reflection-based imaging approach.

1.2.1 Darkfield Microscopy

Darkfield refers to a detection method in light microscopy that deliberately detects the scattered light only that was first demonstrated by Joseph Jackson Lister in 1830 [73]. However, the technique remained largely overlooked until Austrian chemists Richard Adolf Zsigmondy and Henry Siedentopf proved their ability to observe fine structures using GNPs in 1902 [74]. The imaging setup consisted of a pair of orthogonally aligned objective and condenser (Fig. 1-9 A), named "ultramicroscope", which allows the observation of pure light scattering in the absence of background illumination. The concept and setup of the ultramicroscope were also adapted in the lightsheet microscopy in 1993 [75]. Zsigmondy was awarded Chemistry Nobel Prize in 1925 in recognition of his achievements, and it was the first time the Nobel Prize was awarded for advances in light microscopy.

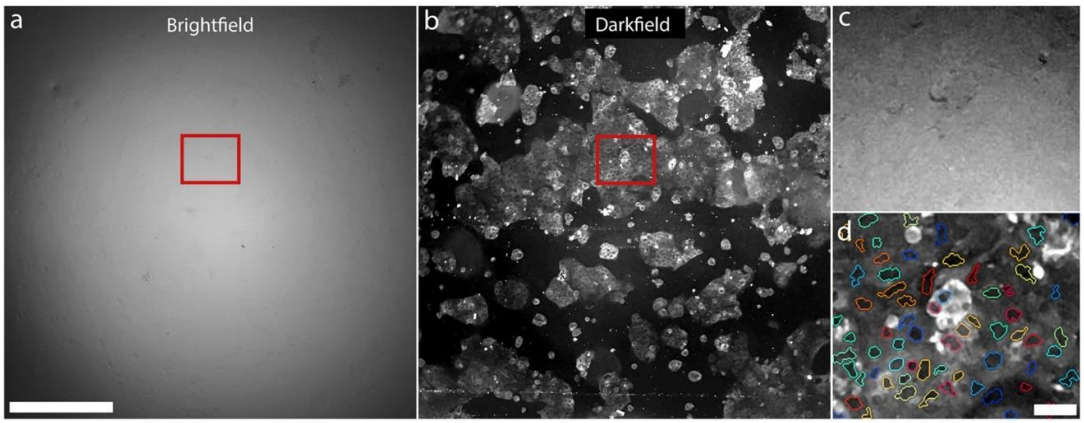

Figure 1-8 Comparison of brightfield (A) and dark field (B) detection using Caco-2 cells. The cells are nearly index-matched in the mounting medium, generating little contrast in brightfield. Scale bar 500 µm. The field of view labelled in a red box is further magnified in (C) and (D). With darkfield detection, cell nuclei can be identified and outlined (processed in MATLAB). Scale bar 50 µm. This figure is reprinted with permission from Orth *et al.* [76] © 2018 Springer Nature.

In darkfield detection, the illumination background is removed so that the detector collects the scattering component only ($E_{det} = E_s$) and the imaging contrast is determined by the magnitude of the scattered light and system noise (Eq. 1.6). The absence of background illumination makes weakly scattered samples visible [77], including objects such as biological cells and imaging probes [26, 78, 79] with high scattering efficiency noble metal nanoparticles [80, 81]. Fig. 1-8 shows an example of Cco-2 cells under brightfield and darkfield imaging settings [76]. The cells in brightfield detection are hardly visible due to the low imaging contrast (Fig. 1-8 A), while the darkfield image indicates the cells are highly confluent (Fig. 1-8 B). The nuclei are also visible in the magnified image (Fig. 1-8 C) and can be recognized in MATLAB, indicating a higher imaging contrast than brightfield detection. To further improve the signal to noise (SNR) ratio in darkfield detection, methods to increase the magnitude of scattered light such as tailoring the oblique illumination angle would be helpful and can be verified using simulation methods (will discuss in chapter 4).

$$c = \frac{E_s}{E_s + E_{noise}} \tag{1.6}$$

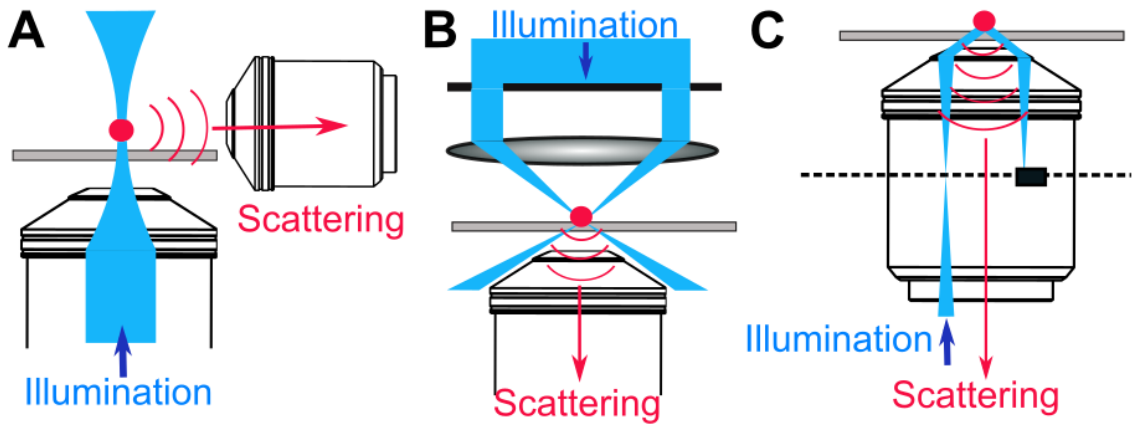

Figure 1-9 Optical configurations of darkfield microscopy. (A) Ultramicroscope that consists of a pair of orthogonally aligned objectives. (B) Partially blocking the illumination using a round stop creates a hollow cone in transmitted light microscopy for darkfield detection. (C) Using oblique illumination and blocking the back-reflection beam in reflection-based microscopy.

Several variants of darkfield detection have been developed in recent years. Except for the ultramicroscopy that separates illumination and detection orthogonally, attempts have been made in both transmission and reflection configurations. In transmitted light microscopes, the illumination is partially blocked by a round light stop before entering a darkfield condenser [82-84], which allows only a hollow cone of light to travel through and illuminates the sample at the in-focal position before being rejected by the collection lens (Fig. 1-9 B). In reflected light microscopes, the back-reflected illumination light is blocked at the back focal plane of the objective, allowing only the scattered light to reach the detector (Fig. 1-9 C). In this configuration, an oblique beam is normally adapted so that the reflection is off-axis and can be easily separated from the scattering component [26, 78, 79] without the need to introduce paired optics (darkfield condenser and objective). However, in both cases, the numerical aperture of the detection objective is partially blocked, either by a darkfield objective (iris diaphragm) or spatial filtering at the Fourier plane that will sacrifice imaging resolution.

1.2.2 Interferometric Scattering

Size and refractive index of the sample are two determinants of the magnitude of the scattered field. Size, in particular, plays an essential role as the pure scattering signal would drop with the sixth power of the particle size [36]. Therefore, when the particle becomes extremely small, the component E_s drops significantly, which is close to the system noise level. In this case, the object cannot be detected under typically darkfield detection. Recently, a new imaging method was introduced that uses background subtraction to extract only the interference component without the illumination background I_r (reference) when the scattered light is negligible ($I_{det} = I_r+2E_rE_s\cos\phi$), namely interferometric scattering (ISCAT) [87]. The concept of this method is to subtract the raw image with a pre-recorded background (image of

empty coverslip). Eq. 1.7 below illustrated imaging contrast through a static subtraction, optimizing the contrast through minimizing E_r in the denominator.

$$c = \frac{I_{det} - I_r}{I_r} = \frac{2E_r E_s cos\phi}{I_r} = 2\frac{E_s}{E_r} cos\phi \tag{1.7}$$

Other subtraction methods are also developed to maximize the detection efficiency, including subtracting subsequent frames [37, 85] and ratiometric subtraction [33, 86]. The ratiometric subtraction appears to reveal the maximum contrast of the scatter but has limitations in temporal resolution due to averaging of frames. The concept of the ratiometric subtraction is shown in Fig. 1-10, where two sequential batches of images (N: number of images) are taken and averaged to obtain two images: $\bar{x}_1$ and $\bar{x}_2$. Both images are then normalized and computed by $\bar{x}_2/\bar{x}_1$.

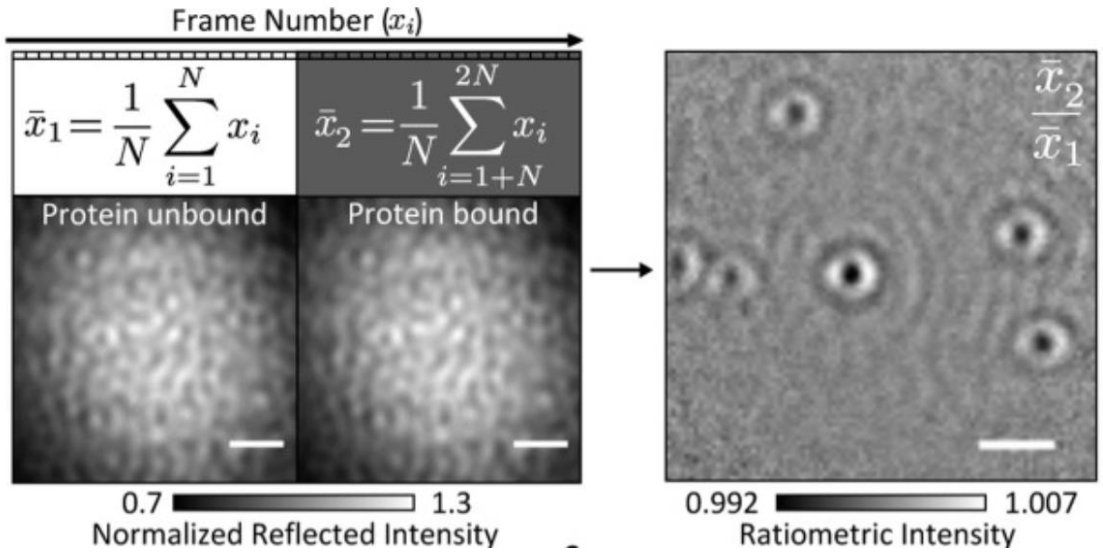

Figure 1-10 Concept of ratiometric subtraction in ISCAT images for detecting weak scatterers. The raw image is processed by dividing the averages of consecutively recorded images. Scale bar = 1μm [33]. This figure is reprinted with permission from Cole *et al.* [21] (https://pubs.acs.org/doi/10.1021/acsphotonics.6b00912) © 2017 American Chemical Society. Further permissions related to the material excerpted should be directed to the ACS.

The background subtraction method has been applied to both transmitted and reflection-based microscopy, namely coherent brightfield (COBRI) [87] and interferometric

scattering (iSCAT) [21, 23, 33-37, 42], respectively. Both methods use coherent laser sources instead of broadband light sources for higher detection sensitivity with widefield illumination. Point-scanning using acousto-optics deflectors (AODs) can also be adopted to minimize speckle noise. Other methods for enhancing imaging contrast includes tailoring the magnitude of the reference by partially blocking the transmitted or reflected light at the Fourier plane [33].

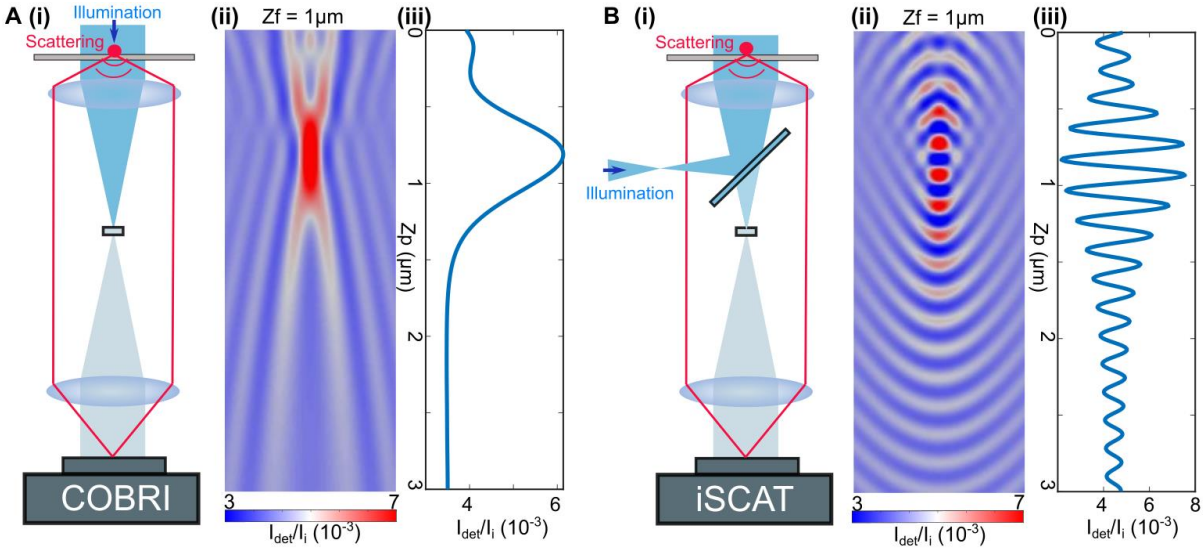

Figure 1-11 Comparison between COBRI and ISCAT. (i) Optical configurations of COBRI (A) and ISCAT (B) that adopts transillumination and reflection-based method, respectively. The block in the light path represents an attenuator that selectively filters the reference. (ii) Simulated axial intensity profile of a 50 nm gold nanoparticle, based on COBRI (A) and ISCAT (B) scheme with focus position z_f = 1 μm. (iii) Intensity plot from the axial intensity profile showing ISCAT has strong oscillations due to fast changes in the phase between reference and the scattered light. The simulation for intensity profile is run using a MATLAB script [88].

However, the detection scheme of these two configurations is completely different: COBRI collects the forward scattered light from the sample that is interfered with the transmitted illumination. In contrast, iSCAT collects the interference of backward scattering and the back-reflected light from the coverslip. Fig. 1-11 demonstrates the simulated axial PSF for both methods from a 50 nm GNP [88], showing the changes in scattering magnitude and phase relations. Because the backscattered light is more prominent than the forward scattering (GNPs in Fig. 1-4), iSCAT detection poses higher contrast than COBRI. iSCAT

detection also demonstrates strong oscillations between positive and negative contrast resulting from the changes in the relative optical path between the reflected (stationary) and scattering light (varying with particle position z_p) [88, 89]. However, this phase relation is not observed in COBRI because of the same phase information between the scattered light and the transmitted illumination. This unique phase correlation in iSCAT could reveal the optical path length between the object and the coverslip, promoting high precision in 3D tracking application [89].

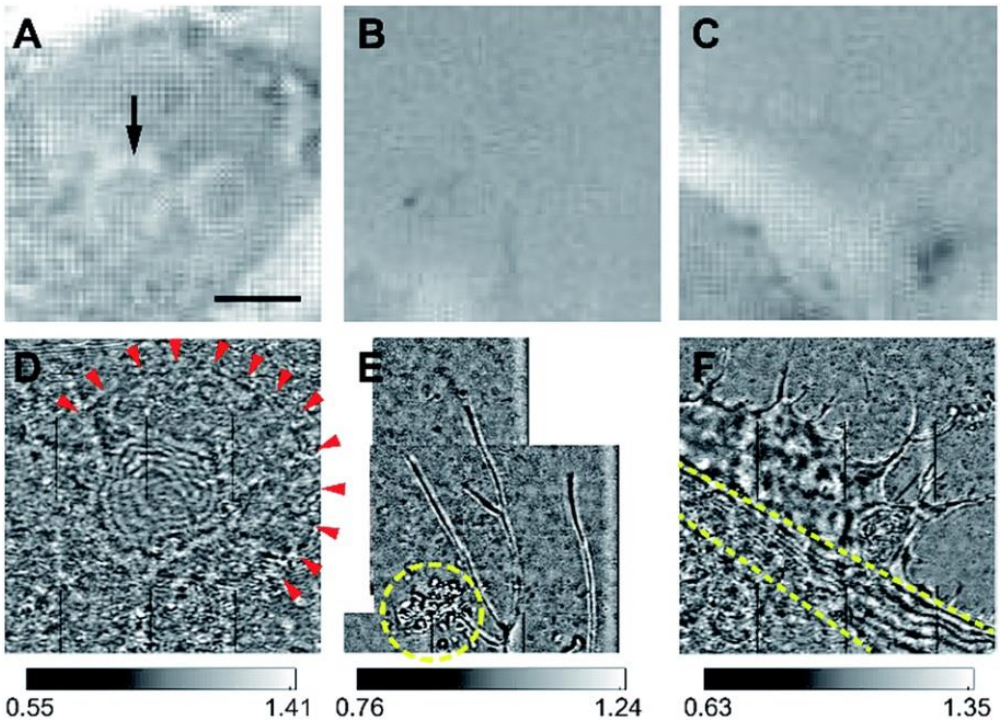

Figure 1-12 Comparison of captured COS-7 cell images using phase-contrast (A-C) and ISCAT (D-F) microscopy. Several cellular features include nucleus (A) and (D), narrow filopodia (B) and (E), and lamellipodia (C) and (F), indicating significantly higher optical contrast. Examples: on the boundary of the nucleus (red arrowheads in D), filopodia branches and debris (yellow circle in E), and cell membrane (between dotted lines in F). Scale bar = 10 μm. This figure is reprinted with permission from Park *et al.* [21] © 2018 Royal society of chemistry.

With ratiometric subtraction, interferometry-based approaches have proven high detection sensitivity in various applications from GNP imaging to viruses [42] and single protein detection [35, 38-40, 90]. Previous studies have shown the imaging of GNPs as small as 2

nm [90] and single protein (BSA) at 65 kDa [38] (1 Da = 1.66×10^{-27} kg). GNPs can be used as inert and stable biological labels to investigate the mobility of proteins and viruses (e.g. microtubules formation [41, 91] and lipid diffusion [92, 93]) because of the high scattering signal that resulted from the plasmonic effects. iSCAT has also been used to reveal intracellular structures in living cells [21]. Fig. 1-12 compares the phase contrast and iSCAT images of a COS-7 cell, revealing cellular details such as the boundary of nucleus, filopodia, and lamellipodia. However, the imaging result shows strong background noise, possibly due to local roughness of the plasma membrane and heterogeneity of cellular corpus that could significantly reduce the imaging quality [35]. Because biological cells are normally larger in size (μm) and have sufficient scattering intensity, interferometric scattering might not be the most suitable approach for cell imaging. In the next section, I shall discuss other interferometry-based methods without background subtraction and post-processing.

1.2.3 Reflection Interference Microscopy

In biological cell imaging, another method to enhance imaging contrast is by optimizing the magnitude of the reference field. The imaging contrast of brightfield detection can be improved when the reference component (E_r) in the denominator is minimized (Eq. 1.8). The simplest method in light microscopy is to collect reflected light instead of transmitted light as the reference. Based on Fresnel coefficients, the light reflected at the glass – water (1.518 to 1.33) interface under normal incidence is about 0.4% of total intensity. Even for a focused or oblique beam, the reflection coefficient is still below 5% when the incident angle is less than 50° (N.A. ≈ 1) as shown in Fig. 1-13 B. Therefore, the magnitude of reference can be optimized by collecting back-reflection from the coverslip and tailoring the illumination angle.

$$c = \frac{E_S + 2E_i E_s cos\phi}{E_r} \tag{1.8}$$

The imaging technique that collects the back-reflection as the reference for the interference component is called 'interference reflection microscopy (IRM), which was firstly introduced by Curtis in 1964 to study cell adhesion [94]. The technique is also known as reflection interference microscopy (RIM) for investigating the adhesion of living cells [95]. In 1975, Ploem introduced the term "reflection interference contrast microscopy" (RICM) for the technique along with an Antiflex objective to enhance imaging contrast [96]. Although these techniques have different names, they all referred to the imaging approach of collecting the interference signal between scattered light from the sample and the reflected light from the coverslip [97].

Traditional RICM uses a monochromatic epi-illumination focused on a coverslip with a semitransparent sample. As shown in Fig. 1-13 A, the incident light (I_0) is partially reflected at the interface between the glass coverslip (n_0) and the aqueous medium (n_1). The partially transmitted light reflects and scatters again at the medium–cell plasma interface (from n_1 to n_2). The reflection coefficients of light at the glass – water (1.518 – 1.33) and water – cell membrane (1.33 – 1.39) interface are plotted in Fig. 1-13 B-C based on the Fresnel equation. Note that the coefficient r_2 is about 10 times lower than r_1, because of the low RI in the cell membrane (~1.36-1.39), indicating reflection from the cell membrane is much weaker and scattered light might contribute more to image formation.

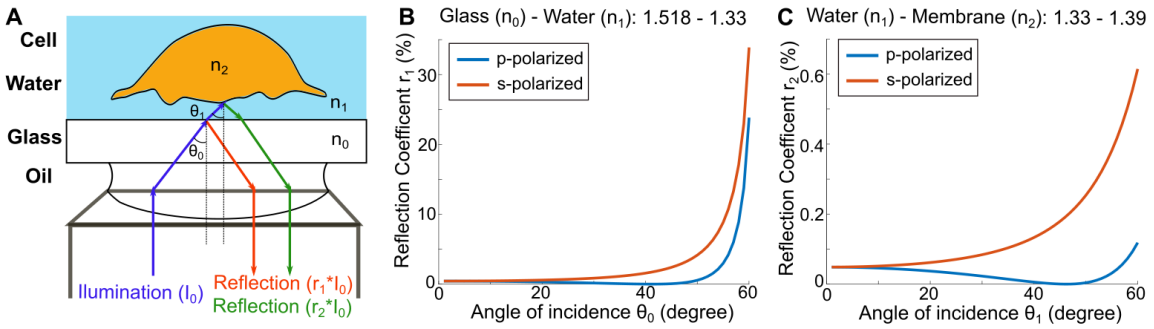

Figure 1-13 (A) Imaging principle of RICM. The illumination (I_0) is reflected twice at the glass (n_0 = 1.518) -water (n_1 = 1.33) interface and the water (n_1 = 1.33) – cell (n_2 = 1.39) interface. The reflection coefficient of these two interfaces (r_1 and r_2) are calculated using the Fresnel equation and plotted in (B) and (C) based on incident angles θ_0 and θ_1.

Removing any unwanted background, such as stray light reflected from different optical surfaces, is critical to enhancing contrast in RICM. To separate stray light and the signal from the sample, a λ/4 waveplate was added on the front of the objective, which will convert the light exiting the objective from linear polarization to circular polarization. The polarization of the reflected light changed from perpendicular to parallel by passing through the λ/4 waveplate again. A crossed analyzer can then block the unwanted stray reflection in the detection path for contrast enhancement.

Another method that enhances the contrast of conventional reflection microscopy is altering the illumination numerical aperture (INA). RICM typically uses a low coherence length source such as high – pressure mercury lamp. To determine the intensity distribution in the image plane, rays of light need to be incoherently summed over the range of angles related to INA. A larger INA could lead to a reduced imaging depth and a larger decay in fringe visibility because the intensity of the interference fringes decays as the axial position moves away from the coverslip. The effect of INA in RICM has been studied by computational [54, 98, 99] and experimental methods [91, 100].

Both iSCAT and RICM work by collecting the interference signal of the back-reflection and back-scattered light. However, the main difference is that the iSCAT uses a high spatial coherence laser source and the subtraction algorithm. The high sensitivity detection of iSCAT demonstrates it is suitable for detecting weakly scattered samples such as single protein and particle at nanometre range. RICM, on the other hand, provides sufficient contrast for cell imaging (HEK 293 and NIH 3T3 cells) compared with the traditional brightfield method [101] (Fig. 1-14), especially on the fine features that are close to the coverslip (filopodia and lamellipodia). Another dominant advantage is RICM can achieve instant imaging without post-processing that permits direct visualization of highly dynamic events in biological systems and might be more suitable for cell imaging.

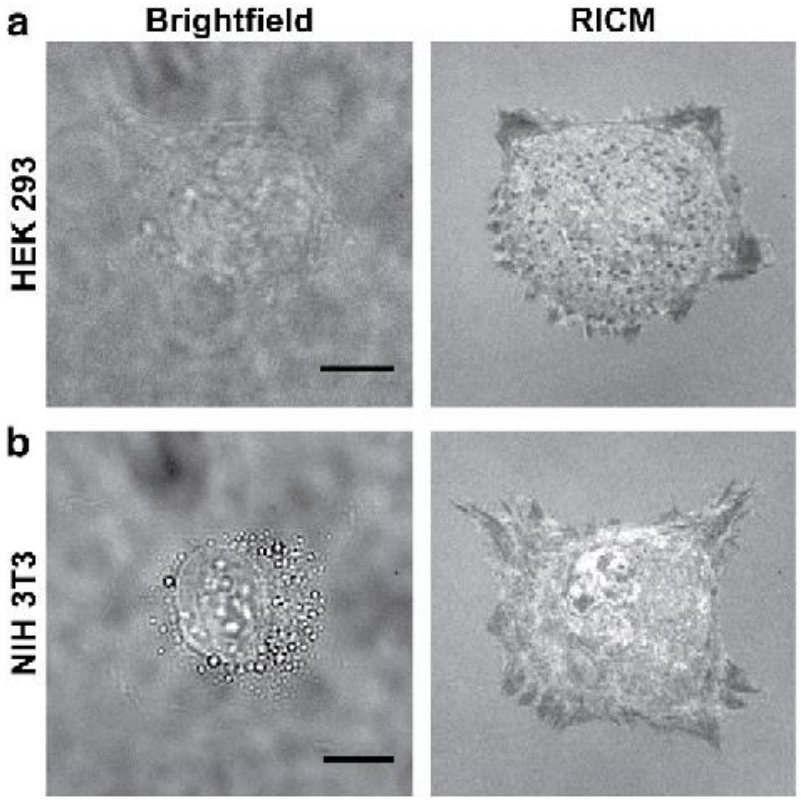

Figure 1-14 Images of HEK 293 and NIH 3T3 cells taken using brightfield and RICM, showing a higher sensitivity and contrast when detecting cellular components such as filopodia and lamellipodia. Scale bar = 10 μm. This figure is reprinted with permission from Jurchenko *et al.* [101] © 2014 Elsevier.

1.3 Conclusion

Label-free imaging techniques utilize optical properties of biological samples and provide non-invasive and fast imaging speed, which is perfect for capturing highly dynamic or rapidly evolving activities within biological systems. Scattering and absorption are the most common approaches and serve as the based principle in modern light microscopy. Biological cells are low in refractive index and have low absorption, they have little light being scattered and are hard to observe in traditional brightfield microscopy. In this chapter, I have reviewed imaging methods that improve imaging contrast and sensitivity in light microscopy through modulating the illumination and detection, including darkfield detection, iSCAT, COBRI and RICM. All the methods can achieve high-speed imaging (>100Hz) and are suitable for morphological studies of dynamic activities such as cell adhesion and migration.

Among all the techniques we reviewed in this chapter, COBRI and iSCAT have the highest imaging sensitivity, down to single protein level. However, the requirement of post-processing and background subtraction can be harder to interpret and time-consuming. RICM and darkfield techniques are free of post-processing, allowing direct visualization of the sample and more suitable for cell imaging. Due to additional interference components presented in RICM, the imaging contrast from finer structures with weaker signals can be boosted compared with darkfield detection (more discussions in chapter 5). In addition, the interference component in iSCAT and RICM permits high axial sensitivity resulting from the optical path difference between reference and scattered light, allowing 3D tracking with high precision. In contrast, signals in COBRI and darkfield cannot provide additional axial information.

The following chapters will discuss how the scattering-based high contrast imaging systems are used in platelet and thrombus imaging (Chapter 2 and 3). Chapter 4 shall describe the label-free imaging system based on the scattering model described in section 1.1.3. Overall, this chapter guides the working imaging principle of the label-free system for platelet and thrombus imaging.

1.4 Contribution

I performed the T-matrix simulation of the cell model using the CELES [71] software with minor modifications (Fig. 1-7). I also performed the simulation used to study the axial profiles of 50 nm GNP from COBRI and iSCAT system (Fig. 1-11) based on the code from [88]. I calculated the reflection ratio in Fig. 1-13 using the equation of Fresnel reflection

.

1.5 References

1. Bergert, M.; Chandradoss, S. D.; Desai, R. A.; Paluch, E., Cell mechanics control rapid transitions between blebs and lamellipodia during migration. *Proceedings of the National Academy of Sciences of the United States of America* **2012,** *109* (36), 14434-14439.

2. Block, J.; Breitsprecher, D.; Kühn, S.; Winterhoff, M.; Kage, F.; Geffers, R.; Duwe, P.; Rohn, J. L.; Baum, B.; Brakebusch, C.; Geyer, M.; Stradal, T. E. B.; Faix, J.; Rottner, K., FMNL2 drives actin-based protrusion and migration downstream of Cdc42. *Current Biology* **2012,** *22* (11), 1005-1012.

3. Giannone, G.; Dubin-Thaler, B. J.; Döbereiner, H. G.; Kieffer, N.; Bresnick, A. R.; Sheetz, M. P., Periodic lamellipodial contractions correlate with rearward actin waves. *Cell* **2004,** *116* (3), 431-443.

4. Ofer, N.; Mogilner, A.; Keren, K., Actin disassembly clock determines shape and speed of lamellipodial fragments. *Proceedings of the National Academy of Sciences of the United States of America* **2011,** *108* (51), 20394-20399.

5. Schneider, I. C.; Hays, C. K.; Waterman, C. M., Epidermal growth factor-induced contraction regulates paxillin phosphorylation to temporally separate traction generation from de-adhesion. *Molecular Biology of the Cell* **2009,** *20* (13), 3155-3167.

6. Asano, Y.; Jiménez-Dalmaroni, A.; Liverpool, T. B.; Marchetti, M. C.; Giomi, L.; Kiger, A.; Duke, T.; Baum, B., Pak3 inhibits local actin filament formation to regulate global cell polarity. *HFSP Journal* **2009,** *3* (3), 194-203.

7. Li, J. X. H.; Tang, V. W.; Brieher, W. M., Actin protrusions push at apical junctions to maintain E-cadherin adhesion. *Proceedings of the National Academy of Sciences of the United States of America* **2020,** *117* (1), 432-438.

8. Cavey, M.; Lecuit, T., Molecular bases of cell-cell junctions stability and dynamics. *Cold Spring Harbor perspectives in biology* **2009,** *1* (5).

9. DeMali, K. A.; Burridge, K., Coupling membrane protrusion and cell adhesion. *Journal of Cell Science* **2003,** *116* (12), 2389-2397.

10. Chang, K.; Baginski, J.; Hassan, S. F.; Volin, M.; Shukla, D.; Tiwari, V., Filopodia and viruses: An analysis of membrane processes in entry mechanisms. *Frontiers in Microbiology* **2016,** *7* (MAR).

11. Zhang, Y.; Chen, X.; Gueydan, C.; Han, J., Plasma membrane changes during programmed cell deaths. *Cell Research* **2018,** *28* (1), 9-21.

12. Caswell, P. T.; Zech, T., Actin-Based Cell Protrusion in a 3D Matrix. *Trends in Cell Biology* **2018,** *28* (10), 823-834.

13. Windus, L. C. E.; Claxton, C.; Allen, C. L.; Key, B.; St. John, J. A., Motile membrane protrusions regulate cell-cell adhesion and migration of olfactory ensheathing glia. *GLIA* **2007,** *55* (16), 1708-1719.

14. Chen, W. T.; Lee, C. C.; Goldstein, L.; Bernier, S.; Liu, C. H. L.; Lin, C. Y.; Yeh, Y.; Monsky, W. L.; Kelly, T.; Dai, M.; Zhou, J. Y.; Mueller, S. C., Membrane proteases as potential diagnostic and therapeutic targets for breast malignancy. *Breast Cancer Research and Treatment* **1994,** *31* (2-3), 217-226.

15. Suhling, K.; French, P. M. W.; Phillips, D., Time-resolved fluorescence microscopy. *Photochemical & Photobiological Sciences* **2005,** *4* (1), 13-22.

16. Schäferling, M., The art of fluorescence imaging with chemical sensors. *Angewandte Chemie - International Edition* **2012,** *51* (15), 3532-3554.

17. Kasprowicz, R.; Suman, R.; O'Toole, P., Characterising live cell behaviour: Traditional label-free and quantitative phase imaging approaches. *International Journal of Biochemistry and Cell Biology* **2017,** *84*, 89-95.

18. Marrison, J.; Räty, L.; Marriott, P.; O'Toole, P., Ptychography-a label free, high-contrast imaging technique for live cells using quantitative phase information. *Scientific Reports* **2013,** *3*.

19. Kim, D.; Lee, S.; Lee, M.; Oh, J.; Yang, S. A.; Park, Y. K., Holotomography: Refractive Index as an Intrinsic Imaging Contrast for 3-D Label-Free Live Cell Imaging. In *Advances in Experimental Medicine and Biology*, 2021; Vol. 1310, pp 211-238.

20. Kim, G.; Lee, M.; Youn, S.; Lee, E.; Kwon, D.; Shin, J.; Lee, S.; Lee, Y. S.; Park, Y., Measurements of three-dimensional refractive index tomography and membrane deformability of live erythrocytes from Pelophylax nigromaculatus. *Scientific Reports* **2018,** *8* (1).

21. Park, J. S.; Lee, I. B.; Moon, H. M.; Joo, J. H.; Kim, K. H.; Hong, S. C.; Cho, M., Label-free and live cell imaging by interferometric scattering microscopy. *Chemical Science* **2018,** *9* (10), 2690-2697.

22. Sjöberg, M.; Mapar, M.; Armanious, A.; Zhdanov, V. P.; Agnarsson, B.; Höök, F., Time-Resolved and Label-Free Evanescent Light-Scattering Microscopy for Mass Quantification of Protein Binding to Single Lipid Vesicles. *Nano Letters* **2021,** *21* (11), 4622-4628.

23. Bae, E.; Bai, N.; Aroonnual, A.; Bhunia, A. K.; Hirleman, E. D., Label-free identification of bacterial microcolonies via elastic scattering. *Biotechnology and Bioengineering* **2011,** *108* (3), 637-644.

24. Poola, P. K.; John, R., Label-free nanoscale characterization of red blood cell structure and dynamics using single-shot transport of intensity equation. *Journal of Biomedical Optics* **2017,** *22* (10).

25. Sandoz, P. A.; Tremblay, C.; Gisou van der Goot, F.; Frechin, M., Image-based analysis of living mammalian cells using label-free 3D refractive index maps reveals new organelle dynamics and dry mass flux. *PLoS Biology* **2019,** *17* (12).

26. Jünger, F.; Olshausen, P. V.; Rohrbach, A., Fast, label-free super-resolution live-cell imaging using rotating coherent scattering (ROCS) microscopy. *Scientific Reports* **2016,** *6*.

27. Wang, Z.; Tangella, K.; Balla, A.; Popescu, G., Tissue refractive index as marker of disease. *Journal of Biomedical Optics* **2011,** *16* (11).

28. He, W.; Zhang, W.; Zhang, J.; Yu, P.; Liu, P.; Yang, G.; Lei, H., Mie resonant scattering-based refractive index sensor using a quantum dots-doped polylactic acid nanowire. *Applied Physics Letters* **2021,** *119* (11).

29. Bohren, C. F., *Absorption and scattering of light by small particles*. 1983.

30. Hauch, K. D.; Ratner, B. D., Chapter II.3.8 - Microscopy for Biomaterials Science. In *Biomaterials Science (Third Edition)*, Ratner, B. D.; Hoffman, A. S.; Schoen, F. J.; Lemons, J. E., Eds. Academic Press: 2013; pp 677-692.

31. Johnson, S. A., Chapter 1 - Phase Contrast Microscopy. In *Biomedical Optical Phase Microscopy and Nanoscopy*, Shaked, N. T.; Zalevsky, Z.; Satterwhite, L. L., Eds. Academic Press: Oxford, 2013; pp 3-18.

32. Pothapragada, S.; Zhang, P.; Sheriff, J.; Livelli, M.; Slepian, M. J.; Deng, Y.; Bluestein, D., A phenomenological particle-based platelet model for simulating filopodia formation during early activation. *International Journal for Numerical Methods in Biomedical Engineering* **2015,** *31* (3), e02702.

33. Cole, D.; Young, G.; Weigel, A.; Sebesta, A.; Kukura, P., Label-Free Single-Molecule Imaging with Numerical-Aperture-Shaped Interferometric Scattering Microscopy. *ACS Photonics* **2017,** *4* (2), 211-216.

34. Ortega-Arroyo, J.; Kukura, P., Interferometric scattering microscopy (iSCAT): new frontiers in ultrafast and ultrasensitive optical microscopy. *Physical Chemistry Chemical Physics* **2012,** *14* (45), 15625-15636.

35. Taylor, R. W.; Mahmoodabadi, R. G.; Rauschenberger, V.; Giessl, A.; Schambony, A.; Sandoghdar, V., Interferometric scattering microscopy reveals microsecond nanoscopic protein motion on a live cell membrane. *Nature Photonics* **2019,** *13* (7), 480-487.

36. Taylor, R. W.; Sandoghdar, V., Interferometric scattering (iSCAT) microscopy and related techniques. In *Label-Free Super-Resolution Microscopy*, Springer: 2019; pp 25-65.

37. Taylor, R. W.; Sandoghdar, V., Interferometric Scattering Microscopy: Seeing Single Nanoparticles and Molecules via Rayleigh Scattering. *Nano Letters* **2019,** *19* (8), 4827-4835.

38. Piliarik, M.; Sandoghdar, V., Direct optical sensing of single unlabelled proteins and super-resolution imaging of their binding sites. *Nature Communications* **2014,** *5*.

39. Ortega Arroyo, J.; Andrecka, J.; Spillane, K. M.; Billington, N.; Takagi, Y.; Sellers, J. R.; Kukura, P., Label-free, all-optical detection, imaging, and tracking of a single protein. *Nano Letters* **2014,** *14* (4), 2065-2070.

40. Young, G.; Hundt, N.; Cole, D.; Fineberg, A.; Andrecka, J.; Tyler, A.; Olerinyova, A.; Ansari, A.; Marklund, E. G.; Collier, M. P.; Chandler, S. A.; Tkachenko, O.; Allen, J.; Crispin, M.; Billington, N.; Takagi, Y.; Sellers, J. R.; Eichmann, C.; Selenko, P.; Frey, L.; Riek, R.; Galpin, M. R.; Struwe, W. B.; Benesch, J. L. P.; Kukura, P., Quantitative mass imaging of single biological macromolecules. *Science* **2018,** *360* (6387), 423-427.

41. Mickolajczyk, K. J.; Geyer, E. A.; Kim, T.; Rice, L. M.; Hancock, W. O., Direct observation of individual tubulin dimers binding to growing microtubules. *Proceedings of the National Academy of Sciences of the United States of America* **2019,** *116* (15), 7314-7322.

42. Kukura, P.; Ewers, H.; Müller, C.; Renn, A.; Helenius, A.; Sandoghdar, V., High-speed nanoscopic tracking of the position and orientation of a single virus. *Nature Methods* **2009,** *6* (12), 923-927.

43. Strutt, J. W., XV. On the light from the sky, its polarization and colour. *The London, Edinburgh, and Dublin Philosophical Magazine and Journal of Science* **1871,** *41* (271), 107-120.

44. Rayleigh, L., XXXIV. On the transmission of light through an atmosphere containing small particles in suspension, and on the origin of the blue of the sky. *The London, Edinburgh, and Dublin Philosophical Magazine and Journal of Science* **1899,** *47* (287), 375-384.

45. Hahn, D. W. J. D. o. M.; Aerospace Engineering, U. o. F., Light scattering theory. **2009**.

46. Jacques, S. L., Optical properties of biological tissues: A review. *Physics in Medicine and Biology* **2013,** *58* (11), R37-R61.

47. Bon, P.; Lécart, S.; Fort, E.; Lévêque-Fort, S., Fast label-free cytoskeletal network imaging in living mammalian cells. *Biophysical Journal* **2014,** *106* (8), 1588-1595.

48. Ardhammar, M.; Lincoln, P.; Nordén, B., Invisible liposomes: Refractive index matching with sucrose enables flow dichroism assessment of peptide orientation in lipid vesicle membrane. *Proceedings of the National Academy of Sciences of the United States of America* **2002,** *99* (24), 15313-15317.

49. Gardiner, C.; Shaw, M.; Hole, P.; Smith, J.; Tannetta, D.; Redman, C. W.; Sargent, I. L., Measurement of refractive index by nanoparticle tracking analysis reveals heterogeneity in extracellular vesicles. *Journal of Extracellular Vesicles* **2014,** *3* (1).

50. Schulz, L. G.; Tangherlini, F. R., Optical Constants of Silver, Gold, Copper, and Aluminum. II. The Index of Refraction n. *J. Opt. Soc. Am.* **1954,** *44* (5), 362-368.

51. Van Niel, G.; D'Angelo, G.; Raposo, G., Shedding light on the cell biology of extracellular vesicles. *Nature Reviews Molecular Cell Biology* **2018,** *19* (4), 213-228.

52. Sharifi, M.; Attar, F.; Saboury, A. A.; Akhtari, K.; Hooshmand, N.; Hasan, A.; El-Sayed, M. A.; Falahati, M., Plasmonic gold nanoparticles: Optical manipulation, imaging, drug delivery and therapy. *Journal of Controlled Release* **2019,** *311-312*, 170-189.

53. Cheng, C. Y.; Liao, Y. H.; Hsieh, C. L., High-speed imaging and tracking of very small single nanoparticles by contrast enhanced microscopy. *Nanoscale* **2019,** *11* (2), 568-577.

54. Wiegand, G.; Neumaier, K. R.; Sackmann, E., Microinterferometry: three-dimensional reconstruction of surface microtopography for thin-film and wetting studies by reflection interference contrast microscopy (RICM). *Applied Optics* **1998,** *37* (29), 6892-6905.

55. Mejillano, M. R.; Kojima, S. I.; Applewhite, D. A.; Gertler, F. B.; Svitkina, T. M.; Borisy, G. G., Lamellipodial versus filopodial mode of the actin nanomachinery: Pivotal role of the filament barbed end. *Cell* **2004,** *118* (3), 363-373.

56. Innocenti, M., New insights into the formation and the function of lamellipodia and ruffles in mesenchymal cell migration. *Cell Adhesion and Migration* **2018,** *12* (5), 401-416.

57. Ridley, A. J., Life at the leading edge. *Cell* **2011,** *145* (7), 1012-1022.

58. Andersen, M.; Nir, S., Van der Waals parameters, refractive indices and dispersion equations of spectrin, actin and other mammalian proteins. *Polymer* **1977,** *18* (9), 867-870.

59. Ross, K. F. A., Measurement of the refractive index of cytoplasmic inclusions in living cells by the interference microscope. *Nature* **1954,** *174* (4435), 836-837.

60. Meyer, R. A., Light scattering from biological cells: Dependence of backscatter radiation on membrane thickness and refractive index. *Applied Optics* **1979,** *18* (5), 585-588.

61. Steelman, Z. A.; Eldridge, W. J.; Weintraub, J. B.; Wax, A., Is the nuclear refractive index lower than cytoplasm? Validation of phase measurements and implications for light scattering technologies. *Journal of Biophotonics* **2017,** *10* (12), 1714-1722.

62. Liu, P. Y.; Chin, L. K.; Ser, W.; Chen, H. F.; Hsieh, C. M.; Lee, C. H.; Sung, K. B.; Ayi, T. C.; Yap, P. H.; Liedberg, B.; Wang, K.; Bourouina, T.; Leprince-Wang, Y., Cell refractive index for cell biology and disease diagnosis: Past, present and future. *Lab on a Chip* **2016,** *16* (4), 634-644.

63. Barber, P. W.; Hill, S. C., *Light Scattering by Particles: Computational Methods*. WORLD SCIENTIFIC: 1990; Vol. Volume 2, p 276.

64. Mishchenko, M. I.; Travis, L. D.; Mackowski, D. W., T-matrix computations of light scattering by nonspherical particles: A review. *Journal of Quantitative Spectroscopy and Radiative Transfer* **1996,** *55* (5), 535-575.

65. Waterman, P. C., Symmetry, unitarity, and geometry in electromagnetic scattering. *Physical Review D* **1971,** *3* (4), 825-839.

66. Shlager, K. L., A Selective Survey of the Finite-Difference Time-Domain Literature. *IEEE Antennas and Propagation Magazine* **1995,** *37* (4), 39-57.

67. Yee, K. S., Numerical Solution of Initial Boundary Value Problems Involving Maxwell's Equations in Isotropic Media. *IEEE Transactions on Antennas and Propagation* **1966,** *14* (3), 302-307.

68. Draine, B. T.; Flatau, P. J., Discrete-dipole approximation for scattering calculations. *Journal of the Optical Society of America A: Optics and Image Science, and Vision* **1994,** *11* (4), 1491-1499.

69. Purcell, E. M.; Pennypacker, C. R. J. T. A. J., Scattering and Absorption of Light by Nonspherical Dielectric Grains. **1973,** *186,* 705-714.

70. Waterman, P. C., Matrix Formulation of Electromagnetic Scattering. *Proceedings of the IEEE* **1965,** *53* (8), 805-812.

71. Egel, A.; Pattelli, L.; Mazzamuto, G.; Wiersma, D. S.; Lemmer, U., CELES: CUDA-accelerated simulation of electromagnetic scattering by large ensembles of spheres. *Journal of Quantitative Spectroscopy and Radiative Transfer* **2017,** *199*, 103-110.

72. Corle, T. R.; Kino, G. S., Chapter 1 - Introduction. In *Confocal Scanning Optical Microscopy and Related Imaging Systems*, Corle, T. R.; Kino, G. S., Eds. Academic Press: Burlington, 1996; pp 1-66.

73. Lister, J. J.; Roget, P. M., XIII. On some properties in achromatic object-glasses applicable to the improvement of the microscope. **1830,** *120*, 187-200.

74. Siedentopf, H.; Zsigmondy, R., Uber Sichtbarmachung und Größenbestimmung ultramikoskopischer Teilchen, mit besonderer Anwendung auf Goldrubingläser. **1902,** *315* (1), 1-39.

75. Voie, A. H.; Burns, D. H.; Spelman, F. A., Orthogonal-plane fluorescence optical sectioning: Three-dimensional imaging of macroscopic biological specimens. *Journal of Microscopy* **1993,** *170* (3), 229-236.

76. Orth, A.; Wilson, E. R.; Thompson, J. G.; Gibson, B. C., A dual-mode mobile phone microscope using the onboard camera flash and ambient light. *Scientific Reports* **2018,** *8* (1).

77. Gage, S. H. J. T. o. t. A. M. S., Modern Dark-Field Microscopy and the History of Its Development. *Transactions of the American Microscopical Society* **1920,** *39* (2), 95-141.

78. Von Olshausen, P.; Rohrbach, A., Coherent total internal reflection dark-field microscopy: Label-free imaging beyond the diffraction limit. *Optics Letters* **2013,** *38* (20), 4066-4069.

79. Enoki, S.; Iino, R.; Morone, N.; Kaihatsu, K.; Sakakihara, S.; Kato, N.; Noji, H., Label-Free Single-Particle Imaging of the Influenza Virus by Objective-Type Total Internal Reflection Dark-Field Microscopy. *PLoS ONE* **2012,** *7* (11).

80. Mirkin, C. A.; Letsinger, R. L.; Mucic, R. C.; Storhoff, J. J., A DNA-based method for rationally assembling nanoparticles into macroscopic materials. *Nature* **1996,** *382* (6592), 607-609.

81. Alivisatos, A. P.; Johnsson, K. P.; Peng, X.; Wilson, T. E.; Loweth, C. J.; Bruchez Jr, M. P.; Schultz, P. G., Organization of 'nanocrystal molecules' using DNA. *Nature* **1996,** *382* (6592), 609-611.

82. Liu, M.; Chao, J.; Deng, S.; Wang, K.; Li, K.; Fan, C., Dark-field microscopy in imaging of plasmon resonant nanoparticles. *Colloids and Surfaces B: Biointerfaces* **2014,** *124*, 111-117.

83. Crut, A.; Maioli, P.; Del Fatti, N.; Vallée, F., Optical absorption and scattering spectroscopies of single nano-objects. *Chemical Society Reviews* **2014,** *43* (11), 3921-3956.

84. Zamora-Perez, P.; Tsoutsi, D.; Xu, R.; Rivera-Gil, P., Hyperspectral-enhanced dark field microscopy for single and collective nanoparticle characterization in biological environments. *Materials* **2018,** *11* (2).

85. Jacobsen, V.; Stoller, P.; Brunner, C.; Vogel, V.; Sandoghdar, V., Interferometric optical detection and tracking of very small gold nanoparticles at a water-glass interface. *Optics Express* **2006,** *14* (1), 405-414.

86. Lebedeva, M. A.; Palmieri, E.; Kukura, P.; Fletcher, S. P., Emergence and Rearrangement of Dynamic Supramolecular Aggregates Visualized by Interferometric Scattering Microscopy. *ACS Nano* **2020,** *14* (9), 11160-11168.

87. Cheng, C.-Y.; Liao, Y.-H.; Hsieh, C.-L., High-speed imaging and tracking of very small single nanoparticles by contrast enhanced microscopy. *Nanoscale* **2019,** *11* (2), 568-577.

88. Dong, J.; Maestre, D.; Conrad-Billroth, C.; Juffmann, T., Fundamental bounds on the precision of iSCAT, COBRI and dark-field microscopy for 3D localization and mass photometry. *Journal of Physics D: Applied Physics* **2021,** *54* (39).

89. Mahmoodabadi, R. G.; Taylor, R. W.; Kaller, M.; Spindler, S.; Mazaheri, M.; Kasaian, K.; Sandoghdar, V., Point spread function in interferometric scattering microscopy (iSCAT). Part I: aberrations in defocusing and axial localization. *Optics Express* **2020,** *28* (18), 25969-25988.

90. Holanová, K.; Vala, M.; Piliarik, M., Optical imaging and localization of prospective scattering labels smaller than a single protein. *Optics and Laser Technology* **2019,** *109*, 323-327.

91. Mahamdeh, M.; Simmert, S.; Luchniak, A.; Schäffer, E.; Howard, J., Label-free high-speed wide-field imaging of single microtubules using interference reflection microscopy. *Journal of Microscopy* **2018,** *272* (1), 60-66.

92. Spindler, S.; Ehrig, J.; König, K.; Nowak, T.; Piliarik, M.; Stein, H. E.; Taylor, R. W.; Garanger, E.; Lecommandoux, S.; Alves, I. D.; Sandoghdar, V., Visualization of lipids and proteins at high spatial and temporal resolution via interferometric scattering (iSCAT) microscopy. *Journal of Physics D: Applied Physics* **2016,** *49* (27).

93. Wu, H. M.; Lin, Y. H.; Yen, T. C.; Hsieh, C. L., Nanoscopic substructures of raft-mimetic liquid-ordered membrane domains revealed by high-speed single-particle tracking. *Scientific Reports* **2016,** *6*.

94. Curtis, A. S., The Mechanism of adhesion of cells to glass. Astudy by interference reflection microscopy. *The Journal of cell biology* **1964,** *20*, 199-215.

95. Barr, V. A.; Bunnell, S. C., Interference Reflection Microscopy. *Current Protocols in Cell Biology* **2009,** *45* (1), 4.23.1-4.23.19.

96. Ploem, J. J. M. p. i. i., infection; pathology, Reflection-contrast microscopy as a tool for investigation of the attachment of living cells to a glass surface. **1975**, 405-421.

97. Weber, I., Reflection interference contrast microscopy. In *Methods in Enzymology*, Academic Press: 2003; Vol. 361, pp 34-47.

98. Gingell, D.; Todd, I., Interference reflection microscopy. A quantitative theory for image interpretation and its application to cell-substratum separation measurement. *Biophysical Journal* **1979,** *26* (3), 507-526.

99. Contreras-Naranjo, J. C.; Ugaz, V. M., A nanometre-scale resolution interference-based probe of interfacial phenomena between microscopic objects and surfaces. *Nature Communications* **2013,** *4*.

100. Mahamdeh, M.; Howard, J., Implementation of interference reflection microscopy for label-free, high-speed imaging of microtubules. *Journal of Visualized Experiments* **2019,** *2019* (150).

101. Jurchenko, C.; Chang, Y.; Narui, Y.; Zhang, Y.; Salaita, K. S., Integrin-generated forces lead to streptavidin-biotin unbinding in cellular adhesions. *Biophysical Journal* **2014,** *106* (7), 1436-1446.

Chapter 2 Platelet Adhesion and Hemostasis

Platelets are the smallest blood cells produced from megakaryocytes that are predominately found in the bone marrow. They play essential roles in thrombosis and haemostasis [1]. Platelets contribute their haemostatic ability through adhesion, activation and aggregation, triggered by vascular injury when the blood vessel becomes exposed. Under static conditions, platelet spreading assays [2, 3] reveal a highly dynamic platelet activation and adhesion process. Platelet adhesion events occur within milliseconds [3] after exposure to adhesive ligands coated on glass surfaces and involve numerous membrane receptors [4-6], intracellular signalling [7-9], and release of cellular contents [10-12].

In this chapter, I will provide a brief overview of the biological motivations of my study in the development of an advanced imaging tool. The aim here is to quantify haemostasis by capturing and imaging platelet shape changes inside and around a thrombus. While the thesis focuses on imaging dynamic platelet shape, it is crucial to discuss the main biochemical receptors involved in platelet adhesion and activation. The role of integrin (αIIbβ3) is critical for platelet shape change because they are intrinsically linked to actin cytoskeleton rearrangement of platelet [9, 13, 14]. Finally, I will review the current imaging techniques used to quantify single platelet activation and adhesion studies, platelet signalling, and biomechanics identified with morphological profiling. However, this chapter only reviews the techniques used for platelet spreading conditions without introducing fluid shear.

2.1 Platelet Adhesion and Activation

Platelets are small anucleate cell fragments produced by megakaryocytes [15, 16]. A healthy person would have a normal platelet count of 150 - 450 $\times 10^9$ per/L. [17-19] Platelets normally circulates, if not activated, for around 7-10 days in the bloodstream [20], before being cleared by macrophages in the spleen and liver. Platelets are one of the smallest cells in the human body (2-3 μm in diameter) [21] and have a thickness of 0.5 - 1 μm. In their resting state [22, 23], platelets play a significant role in primary haemostasis by surveying the blood vessel walls for damage. At the injury site, discoidal platelets encounter sudden changes in fluid shear stress and bind to extracellular matrix ligands by rapidly forming long membrane protrusions. This sudden morphological change allows platelets adhere onto the injury site, forming a mechanical plug (thrombus), and preventing posttraumatic blood loss.

The extracellular matrix (ECM) has a wealth of ligands (e.g. collagen and fibronectin) for rapid platelet adhesion [24, 25]. Current studies have indicated the initial adhesion is being established through platelets binding to collagen fibre [26]. This binding process is mediated through Von Willebrand factor (VWF) and glycoprotein GPIb [27] and then strengthened by various adhesive and other receptors such as GPVI to form a firm adhesion [5]. It has been shown in spreading assays that during the adhesion process, platelets undergo dramatic shape change from resting states (discoid) to prickly sphere [28, 29] that involves the shedding/or release of proteases [30, 31], and release of soluble cargo [12] through granule secretion [10, 32]. The dramatic shape change is induced by the activation of transmembrane integrin αIIbβ3 [8, 9], which is involved in platelet-platelet adhesion through fibrinogen to facilitate aggregation [33]. Next, I shall explain the biological process of the initial steps in haemostasis, including platelet adhesion and activation, and discuss how platelets change their shape to support spreading and adhesion.

2.1.1 Platelet Adhesion Mediated through VWF and GPVI

Vessel wall shear stress (Pa) is determined by the difference in velocity of the blood flow at the centre of the vessel from that at the vessel wall [34]. The high shear at the vessel wall triggers the initial tethering of platelets to the ECM that is mediated by the binding of glycoprotein receptor (GP)Ib to collagen through VWF once the VWF is immobilized in subendothelial connective tissue [35, 36]. Many ligands on the ECM, such as laminin, fibronectin and collagen, are crucial in wound healing because they trigger mechanosensitive pathways in platelets, fibroblasts and macrophages [24]. This section will explain several key proteins and membrane receptors involved in platelet adhesion, activation and aggregation, as shown in Fig. 2-1.

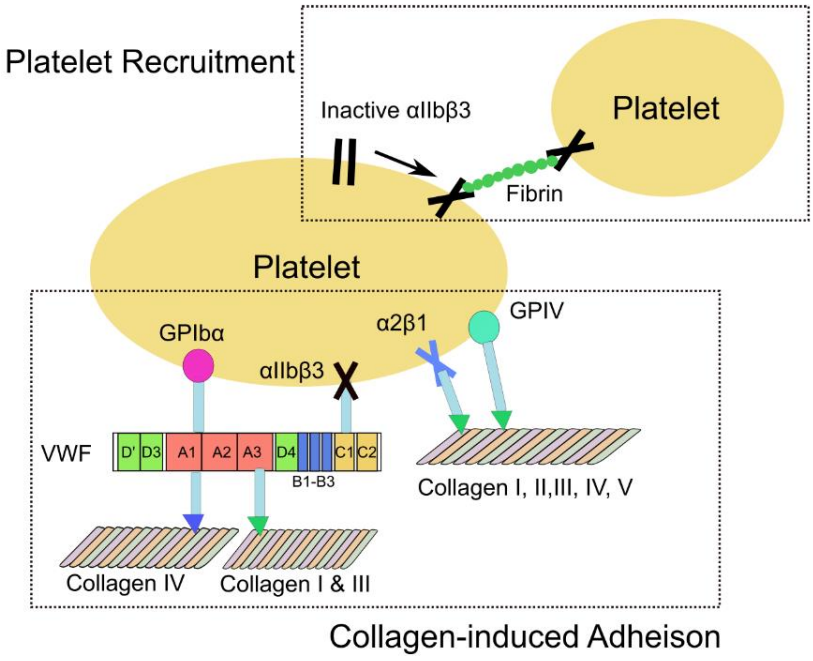

Figure 2-1 The initial steps of the hemostasis process include adhesive ligands (collagen) induced adhesion, platelet activation and recruitment of platelets into a forming aggregate. Platelet adhesion is established through many proteins, including glycoprotein VWF, membrane receptors (e.g. GPIV and GPIb), and integrin (e.g. αIIbβ3). The platelet recruitment into the forming thrombus involves activation of integrin αIIbβ3 and adhere to the fibrin network.

The initial step of hemostasis occurs when flowing platelets bind to collagen fibrils through Von Willebrand factor (VWF) [26] and glycoprotein GPIb [37] as shown in Fig. 2-1. VWF is critical to establish the initial adhesion at injury site [35]. It is an adhesive and mechanosensitive (shear sensitive) glycoprotein [6, 38] that circulates in the blood with two separate compartments: plasma VWF and alpha granules, synthesized by endothelial cells and megakaryocytes, respectively [35]. The mature subunit of VWF is composed of four distinct domains, represented by A-D, repeating two to four times (Fig. 2-1). The A1 domain is the major binding site for the initial platelet adhesion [39] because it binds to both platelet receptor glycoprotein (GP) Ib and collagen type VI [40], which are the major constituents in the subendothelial basement membrane [41].

The binding between GPIb and the A1 domain can be described by a rapid dissociation rate which is insufficient to establish form adhesion [27]. The primary function of the GPIb complex is to recruit or attract platelets to the exposed ECM and lower their motility, which then enables the interaction of other receptors and integrins such as GPVI, αIIbβ3 and α2b1with the thrombogenic surface for stable adhesion [42]. Glycoprotein VI (GPVI) [43] is one of the primary receptors for collagen-platelet binding and mediation of cellular activation that serves as a prerequisite for stable adhesion and coagulant activity on the matrix protein. The role of GPVI is essential in collagen-induced platelet activation and spreading on adhesive ligands [44, 45]. Reduction of platelet attachment and thrombus formation has been observed at sites of arterial injury in FcRγ-chain–deficient [46], GPVI-depleted [47], or GPVI-deficient mice models [48].

Apart from the adhesion established through VWF and GPVI, integrin also plays an essential role in initial adhesion and recruiting platelets into the forming thrombus. Integrins are a family of transmembrane glycoprotein receptors that can transmit and detect changes in

mechanical forces acting on the extracellular matrix. In platelets, the dominant integrin αIIbβ3 constitutes around 17% of total platelet surface proteins [9] and is essential for platelet adhesion and cytoskeleton rearrangement. Upon platelet activation, the intracellular signalling drives the increase in calcium concentration, release of structural proteins (e.g. VASP, talin) and activation of Arp 2/3 complexes that trigger actin reorganization and shape change. Also, the conformational changes of αIIbβ3, from a low to high-affinity state, reveal the RGD binding site [49] and enable binding for adhesive ligands [9] as shown in Fig. 2-1. Integrin αIIbβ3 binds to the C1 domain of VWF that mediates platelet adhesion with collagen fibre. It also binds to fibrinogen, which triggers platelet-platelet adhesion essential in platelet recruitment and clot aggregation. Lacking or dysfunctional αIIbβ3 has been shown to result in absent platelet aggregation, reduced thrombus contraction and significantly reduced fibrinogen uptake in the clot (shown in a mice model lacking β3 integrin that resembles Glanzmann thrombasthenia [50]).

2.1.2 Platelet Activation and Cytoskeleton Rearrangement

Once the integrin is activated, it forms a cluster possibly through direct interaction with myosin II [51], along with the accumulation of actin filaments and forms a focal adhesion plaque [7] with its full complement of enzymes (G-proteins, kinases, proteases and phosphatases) and structural proteins (e.g. VASP, talin, APB, α-actinin and vinculin) [52]. The conglomerate of enzymes recruit WASp/SCAR family members and activate Arp2/3, which supports shape change [52-55] and cytoskeleton rearrangement. There is a dramatic increase in the proportion of actin polymerization during activation and spreading, leading to extreme morphological changes, initially from discoid shape to a spherical structure as actin filaments are fragmented. After that, the membrane of the platelet protrudes due to actin filament assembly, manifesting as lamellipodia and filopodia [56] [57]. The platelet shape change is also a

prerequisite for platelet aggregation. Shape changes of platelets facilitate their adhesion to the site of vascular injury and cohesion with other platelets or erythrocytes, ultimately contributing to the formation of stable aggregates [28, 58, 59].

The cytoskeleton structure plays an essential role in supporting the discoid shape and cell integrity of the resting platelet, especially when exposed to shear and other forces in circulation. It also promotes dynamic and rapid ability to remodel that allows platelets to spread and form aggregates during haemostasis [52, 53, 57]. Actin polymerization and microtubule remodelling are the most important processes promoting cytoskeleton rearrangement. Upon platelet activation, due to the increase in calcium concentration, gelsolin [60, 61] and cofilin [14] are activated, allowing for serving and capping of the actin filament network and enhancing the turnover of the G-actin [52, 62] as shown in Fig. 2-2A. The generation of PI(4,5)P2 and activation GTPase promotes the removal of gelsolin and CapZ from actin filament barbed ends, which provides a large capacity for actin polymerization. Therefore, the actin monomers in the cytoplasm (bound with β-thymosin or profilin) can be connected to the barbed end of the filament [63, 64].

Additionally, new actin filaments are formed due to the activation of Arp2/3 and formin, leading to the protrusive force to form filopodia, lamellipodia and pseudopodia [57]. Therefore, the actin filaments are structured into dendritic arrays or parallel bundles that mediate spreading, adhesion, and resistance to shear stress. Microtubules also undergo structural changes during platelet activation, which allows the platelet to transit from discoid to spherical shape, as shown in Fig. 2-2B. Upon activation, due to the high intracellular calcium concentration that triggers movement of motor protein, there is an enhanced dynein activity with dropped kinesin activity, causing dynein to start to walk and lead to movement and expansion of microtubules [57]. The expanding microtubules then fold and coil into the

centre of the platelet, allowing the spherical shape change [65, 66], which is followed by the depolymerization and formation of the microtubule network in spread platelets [57, 66]. In addition, these cytoskeleton changes and platelets morphology is driven almost solely by transmembrane proteins and surface receptors without the nucleus.

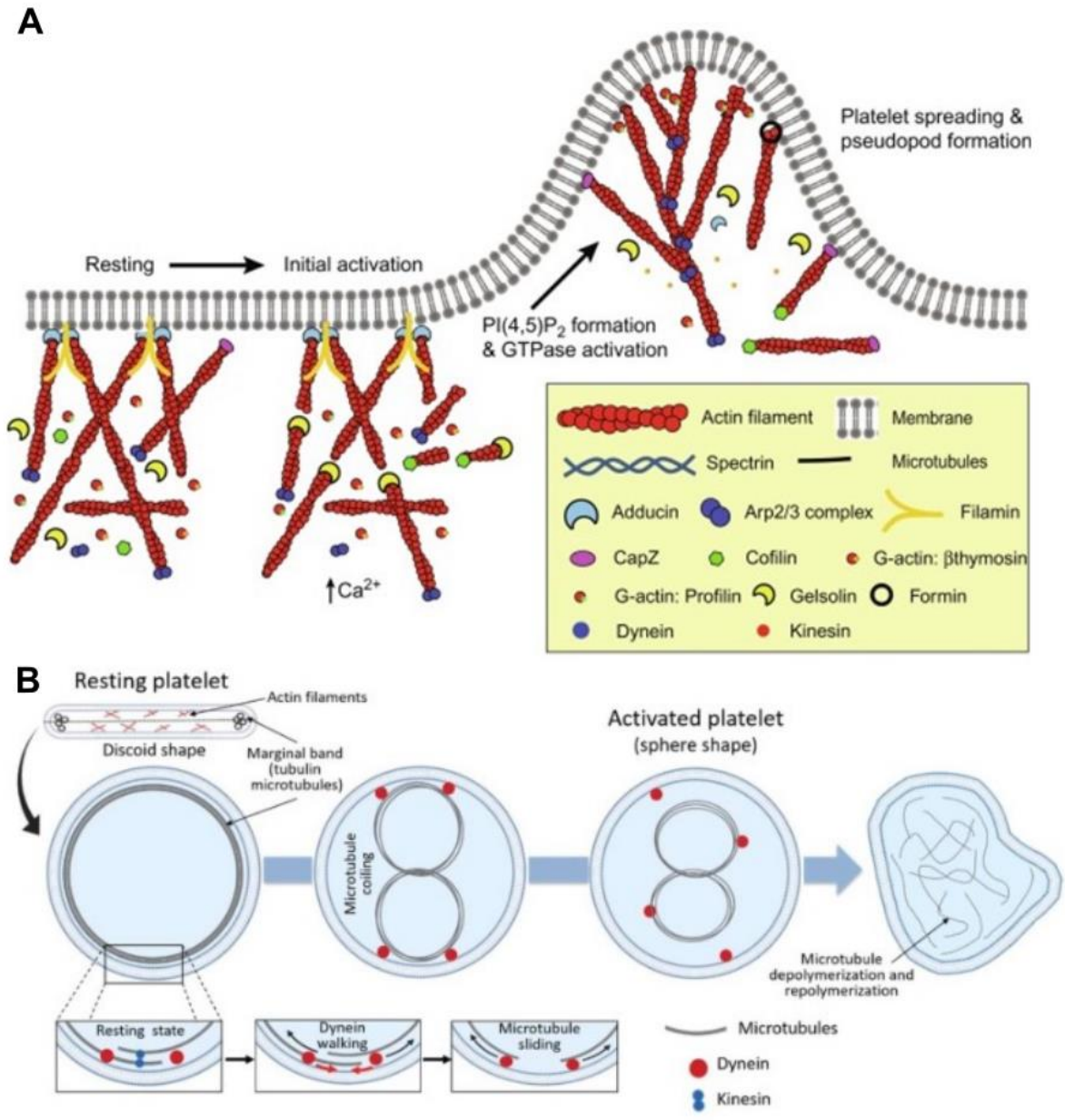

Figure 2-2 Rearrangement of Actin filament (A) and microtubule coiling (B) during platelet spreading and pseudopod formation. Part (A) of this figure is reprinted with permission from Thomas [57] © 2019 Elsevier. Part (B) of this figure is reprinted with permission from Cuenca-Zamora *et al.* [29] © 2019 MDPI.

2.2 Functional Imaging Methods for Single Platelet

In this section, I characterize previous studies of platelet function in spreading assay (single cells perspective) into three groups targeting biochemical signalling, mechanical properties and morphological profiling (Table 2-1). These studies have different needs in imaging techniques, e.g. molecular specificity is key in investigating the interactions of proteins and ligands at single molecule level, while speed and imaging sensitivity are essential in morphological studies. Therefore, I shall review the imaging techniques developed for these three types of studies and discuss how the imaging approaches could help understand platelet function and the hemostasis process. Additionally, all the imaging techniques mentioned in this section are summarized in Table 2-2, which outlines parameters, including the imaging speed, resolution and limitations.

Table 2-1 Quantifications of Biochemical, mechanical, and morphological properties during single platelet adhesion and spreading.

Quantification	**Biochemical**	**Mechanical**	**Morphological**
	• *Integrin* • *Receptor* • *Ligands*	• *Force (N)* • *Viscoelasticity*	• *Membrane protrusion* • *Height/volume* • *Mobility*
Requirement	Specificity Sensitivity	Force sensor Sensitivity	Speed Sensitivity

Platelets spreading assay is the most common method used for studying the function of platelets or receptors. Spreading assays are simple and can be directly tested on a single coverslip without introducing fluid shear. Coverslips are generally coated with immobilized agonists such as collagen, fibrinogen or fibrin, and washed platelets are normally studied here. Washed platelets are free of all plasma components and are ideal for single-cell spreading assays without causing aggregation. Based on protein expression level, spreading assays provide a clear window to morphological profiles of platelets. As seen in previous Fig. 2-1, ligands trigger the activation of platelets, which create extensive protrusions upon adhering

onto a glass surface. These static studies aim to mimic the initial stages of the hemostasis process (adhesion and activation), as shown in Fig. 2-3.

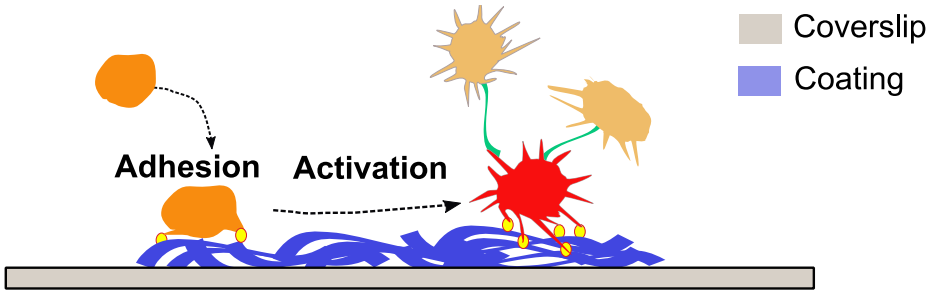

Figure 2-3 Platelet spreading assay mimic the initial stages of the hemostasis process using washed platelets and ligand-coated coverslip (e.g. collagen, fibrin and fibrinogen). In spreading assay, initial platelet adhesion, interaction with coated ligands, activation, and spreading can be investigated with imaging methods.

Recent developments in modern light microscopy techniques have shown significant improvements in imaging speed, resolution [67, 68] and sensitivity [69], which offers great opportunities to visualize dynamic events at single molecular level, but functional imaging of platelets remains challenging. Platelets are produced by fragmentation of the megakaryocyte cytoplasm [15], and they have no nucleus [70, 71]. Therefore, they cannot be transfected to express fluorescently labelled [72] or optogenetically modified proteins unless they are mice derived transgenic cell lines. Thus, fluorescence imaging of live human samples is limited, with membrane dye being the most common method. Labelling of receptors or proteins is often conducted with fixed samples [72]. Additionally, challenges in platelet imaging include a small sample size (3-6 μm diameter [21], with protrusion ranging from 60-700 nm [73]) and imaging speed (activate and adhere to the adhesive ligands within millisecond time interval [3]). Because membrane dye is less specific, recognizing the membrane protrusions (mainly made of actin) could be challenging. In contrast, light scattering uses the refractive index as a biomarker, has inherent advantages in identifying these structures as actin has a much higher index (RI=1.59) than other cellular components (e.g. lipid and cytoplasm). This section will

also discuss platelet imaging with the light scattering techniques introduced in chapter one and how those methods help investigate morphological changes.

2.2.1 Biochemical Signaling

This section reviews the imaging techniques (mainly fluorescence microscopy) that focus on biochemical signalling during platelet adhesion and activation. At the terminus of membrane protrusions, there are significant numbers of membrane-associated receptors that engage with one or more counter-receptors or extracellular matrix proteins. For example, glycoprotein (GP) Ib-IX-V binds VWF, and GPVI binds adhesive ligands, including collagen, fibrin and laminin, that initiate platelet adhesion [5, 26, 44]. Those receptors translate cues from the surrounding vascular environment to mediate molecular signalling pathways, leading to platelet activation, adhesion, and interaction with other cells. Studies of biochemical signalling reveal the process of platelet receptor engagement, triggering phosphorylation [74], activation of intracellular molecules [7, 8, 14], degranulation [10-12] and rearrangement of cytoskeleton [52, 53, 57]. The processes of integrins bind to plasma proteins (fibronectin, cadherins and VWF) [6, 75, 76] and adhesive ligands (collagen, fibrinogen and fibrin) [33, 77] are also investigated. While this thesis does not involve imaging those surface receptors, it is important to contextualise how the membrane protrusions could infer biochemical signalling.

In fluorescence microscopy, epifluorescence, confocal, and total internal reflection fluorescence (TIRF) are the most commonly used techniques to investigate how biochemical signalling leads to morphological changes during platelet adhesion and activation. Fig. 2-4 shows fluorescence images of migrating platelets on fibrin and fibrinogen coated surfaces with and without inhibiting the actin nucleating Arp2/3 complex [54, 78]. By locating the concentration of the Arp2/3 complex, migrating platelets exhibited enriched Arp2/3 at the

leading edge. Inhibiting the Arp2/3 with CK666 (Fig. 2-4 C) also indicates the role of this complex in maintaining the half-moon shape and lamellipodia formation [78].

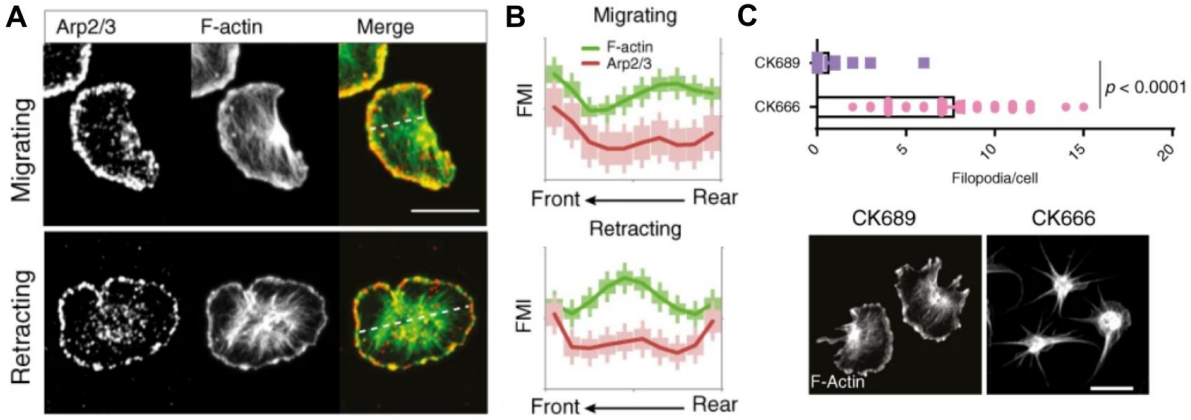

Figure 2-4 (A) Fluorescence images showing the distribution of Arp2/3 and F-actin in migrating and retracting platelet on fibrinogen and fibrin coated substrates. (B) Fluorescence mean intensity (FMI) profiles along short axes of $n = 50$ (migrating) and $n = 53$ (retracting) platelets. Scale bar = 5 µm. (C) Fluorescence images of platelets with Arp2/3 inhibitor (CK666) and control (CK689) and quantification on the number of filopodia formed in each platelet (Mann–Whitney), $n = 41$ cells from three experiments. Scale bar = 5 µm. This figure is reprinted with permission from Nicolai *et al.* [78] © 2020, Springer Nature.

The study of single platelet activation at single molecular level in light microscopy has been extended with the emergence of super-resolution microscopy that can achieve nanometer imaging resolution [67, 68]. Super-resolution approaches such as structured illumination microscopy (SIM), stochastic optical reconstruction microscopy (STORM), and single molecule localization microscopy (SMIM) have been used to investigate morphological features and cytoskeleton rearrangement [29] at nanoscopic resolution. Fig. 2-5 shows the comparison of conventional fluorescence microscopy and dSTORM, revealing nanoscopic imaging of filopodia structure and accurate width measurement. In addition, super-resolution techniques are also used to recognize clusters of actin nodules [79], receptor clustering (GPVI) [80] and distribution of tubulin and actin stress fibres [81, 82] during platelet activation.

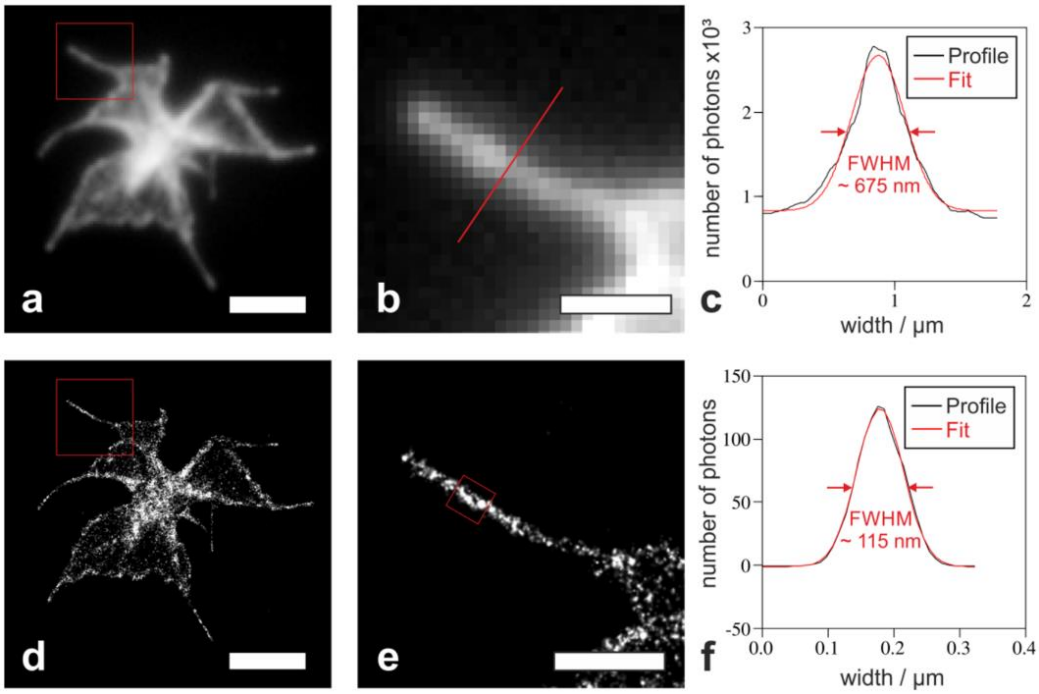

Figure 2-5 Comparison of conventional fluorescence (A) and dSTORM (D) images of a spreading platelet with a spindle-like morphology. The platelet is fixed and labelled with Phalloidin Alex 647. (B) and (E) show the zoom-in view of a single filopodium. (C) and (F) plot the intensity profile of the filopodia and the Gaussian fitting to the profile, indicating the full width half maximum (FWHM) or the width of filopodia to be 675 nm or 115 nm. Scale bar for (A and D) 3 µm and for (B and E) 1 µm. This figure is reprinted with permission from Mayr *et al.* [82] © 2018 MDPI.

Furthermore, the development of Lifeact [83, 84] (stains filamentous actin) mice in live platelets permits localization of actin polymerization and actin nodules during cytoskeleton rearrangement [79]. Structured illumination microscopy (SIM) has shown that the distribution of actin-binding proteins such as talin and vinculin are often found at cell adhesion sites, revealing the enriched concentration of both talin and vinculin at actin nodules [79] (Fig. 2-6). However, the major limitations of super-resolution techniques are the image acquisition time and the computation power required for image reconstruction [67]. Therefore, most single platelet study using super-resolution techniques has been conducted with fixed samples.

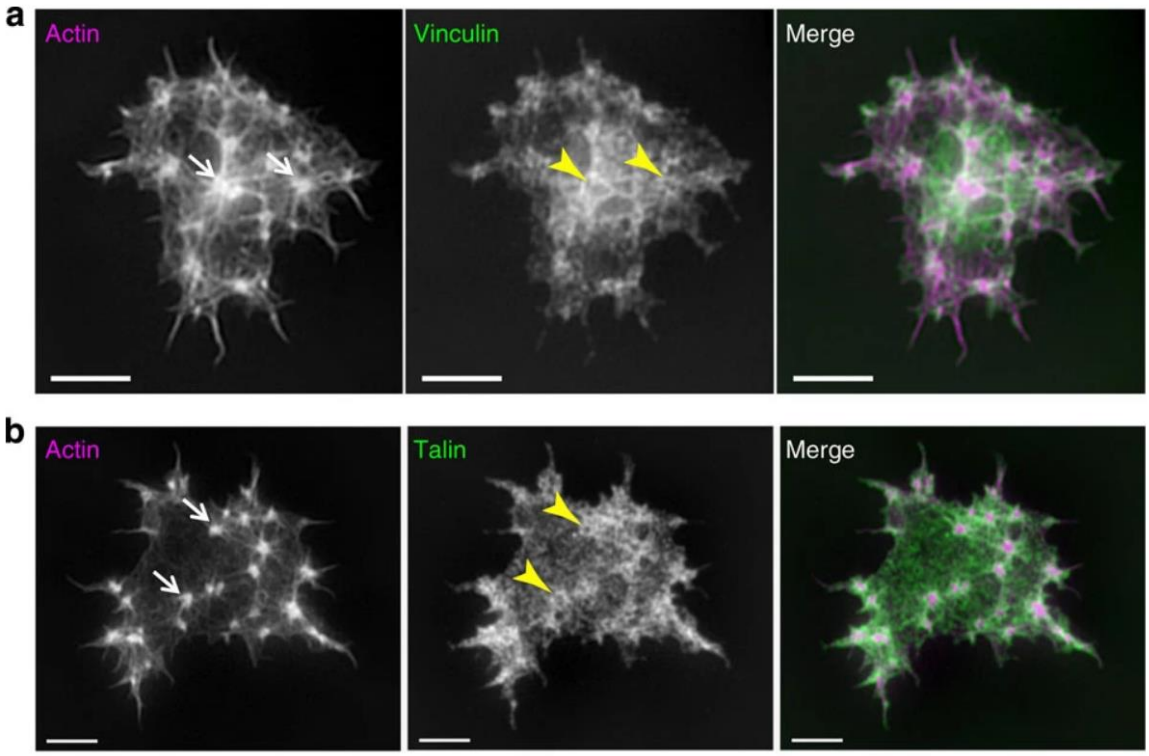

Figure 2-6 Structured illumination microscopy (SIM) images show actin, talin and vinculin distribution in human platelets after activation. Actin, talin and vinculin are labelled using Alexa488-phalloidin, Alexa568-anti-vinculin and Alexa568-anti-talin. The signal from actin/talin and actin/vinculin are merged in the right-hand panel (actin = magenta, vinculin/talin = green), showing localisation of vinculin and talin at actin nodules. Scale bars = 2 μm. This figure is reprinted with permission from Poulter *et al.* [85] © 2015 Springer Nature.

2.2.2 Mechanical Properties

Platelets are mechanosensitive cells and are sensitive to mechanical stimulations such as fluid shear. Biomechanical properties of platelets such as elastic modulus, stiffness, deformability, and contractile forces during platelet spreading and adhesion are closely related to platelet function and are emerging as diagnostic markers for platelet physiology [23, 58, 86]. To quantify these biomechanical properties, a wide array of force transducers (e.g. imaging probe, cantilever and micropipette) have been developed. They are often accompanied by microscopy imaging to monitor both morphological changes (membrane protrusions) and the resulting mechanical forces.

The most straightforward method for measuring forces and elastic modulus includes micropipette aspiration [87, 88] and atomic force microscopy (AFM) [89, 90]. Both techniques require direct contact between the sample and the force probe. Micropipette aspiration works by suctioning part of a single platelet's membrane into a borosilicate glass micropipette (inner diameter 0.5-1.5 μm) [85]. Young's modulus is quantified based on suction force (from micropipette) and membrane deformation (captured by light microscopy). The major limitation of this method is the low throughput, because only one cell can be measured at a time. Manufacturing microfluidics devices with multiple arrays of micropipettes may potentially be helpful to improve the throughput of this technique [91, 92].

AFM adapts a flexible cantilever of 100-200 μm in length, with an integrated pyramidal probe tip 4-8 μm tall contacting the platelet [85] (Fig. 2-7A). As the platelet exerts forces during spreading and activation, it bends the force probe. Therefore, the force of contacting surface (F = -kd) can be quantified by retrieving the deflection of the probe (Fig. 2-7B). Also, the cantilever can be moved by a sensitive piezoelectric transducer, which enables lateral scanning for generating a 2D map, revealing the distribution of mechanical forces of a single platelet (Fig. 2-7 C-D). The major limitation of AFM is that platelets need to be immobilized on either the surface or the probe for force measurement, restricting substrate selection and posing difficulty in sample handling. In addition, platelets are very fragile and can easily be accidentally activated, and the introduction of imaging probes might interfere with the activation process.

Several contact-free methods have been developed to avoid contacting the sample and disrupting the biological process, including scanning conductance ion microscopy (SCIM) [23, 93] and traction force microscopy (TFM) [94]. SCIM is a non-force contact, non-invasive, high-resolution topography technique, which uses a nanopipette to measure the ionic current

between the pipette and the solution. The current changes when the nanopipette approaches the sample surface, allowing reconstruction of the topology of the sample. Mechanical forces can be quantified by the hydrostatic pressure through the nanopipette and the corresponding mechanical responses of the platelet membrane. Similar to AFM techniques, the resolution of SCIM relies on the size and precision of the imaging probe, as the topology is reconstructed through probe scanning, which also means the scanning speed can be a limiting factor in platelet activation.

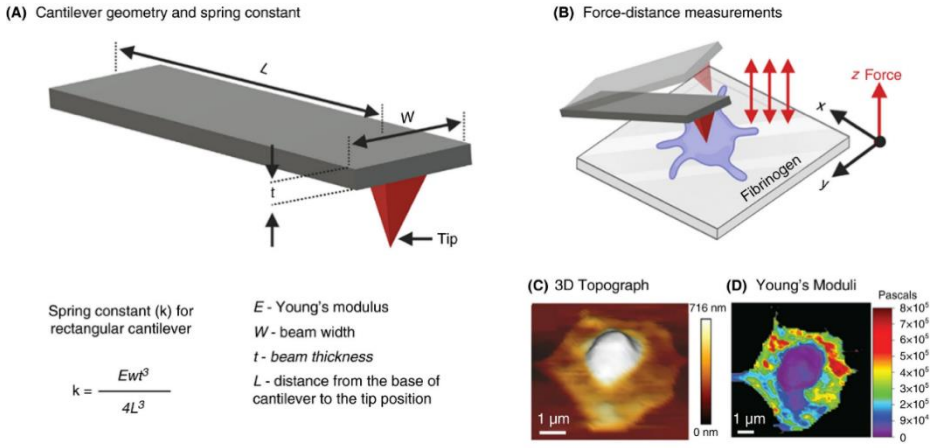

Figure 2-7 (A) Schematic showing the rectangular cantilever with a pyramidal tip equipped in AFM setup and the equation for calculating the spring constant k of the cantilever using beam theory and Young's modulus (E). (B) Example of calibrating 3D topography and Young's modulus of single platelet spreading on fibrinogen coated surface using AFM. This figure is reprinted with permission from Sachs *et al.* [85] © 2020 International Society on Thrombosis and Haemostasis.

TFM uses hydrogel-based substrate with fiducial markers such as fluorescent tracer beads embedded, quantifies force by capturing fluorescence images and tracking the position of the markers over time (Fig. 2-8). Alternative substrates were also developed for contractile force measurement, such as micropillar (elastomeric cylindrical cantilevers) arrays made of polydimethylsiloxane (PDMS). TFM has higher throughput than AFM and SCIM. However, it heavily relies on tracking the position of the tracer with imaging approaches, therefore still

facing the same limitations in resolution and acquisition speed, especially when 3D tracking is needed.

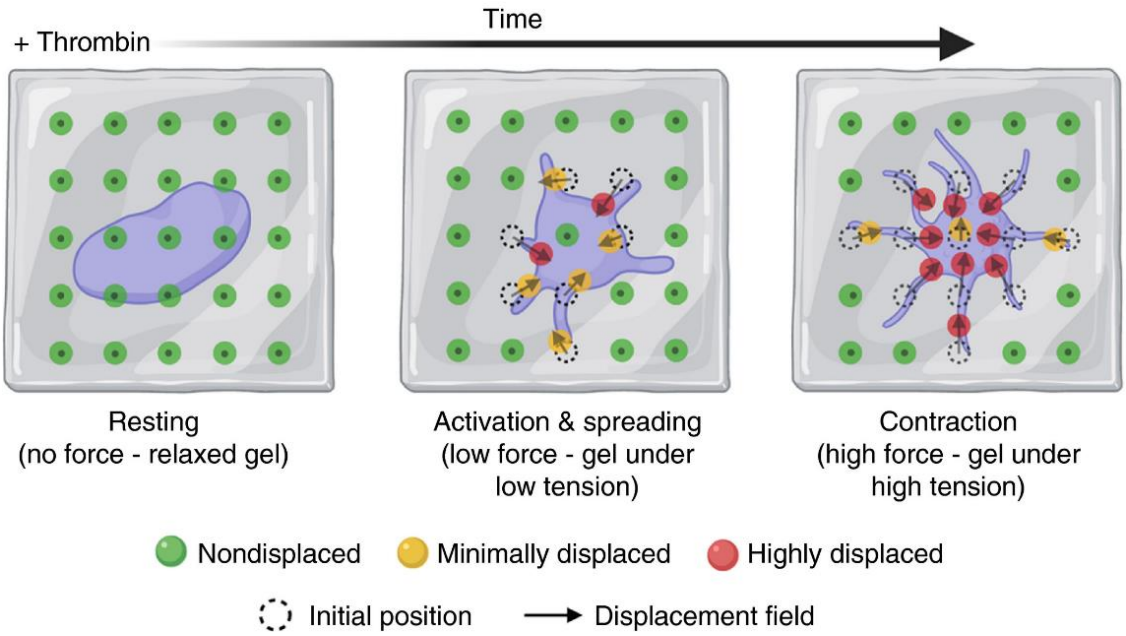

Figure 2-8 Schematic showing the working principle of traction force microscopy. Platelets are seeded on fibrinogen passivated hydrogel surface with embedded microbeads. When platelets are activated, they adhere, spread and interact with the substrate, generating traction forces that exert mechanical tension on the hydrogel, resulting in the displacement of the microbeads. This displacement can be tracked using fluorescence microscopy and compute the traction forces during adhesion and spreading. This figure is reprinted with permission from Sachs *et al*. [85] © 2020 International Society on Thrombosis and Haemostasis.

In conclusion, platelets imaging with force sensors is a powerful approach and allows for measurements of elastic properties, adhesion and contractile forces of adherent platelet. However, micropipette aspiration, AFM and SCIM have low throughput, which only measures one cell at a time, limiting quantification to 1-10 platelets per hour [85]. Also, these techniques are limited by acquisition speed, and therefore not suitable for real-time quantification of platelet spreading and activation.

2.2.3 Morphological Profiling

Lately, specific shape changes of the cell through their membrane protrusion have been characterised [81]. Platelet function has been found to be closely linked with platelet morphology as inhibition of various platelet adhesion receptors resulted in distinct cytoskeletal morphologies. Screening of morphological changes of platelets during spreading and activations using imaging techniques has been used to establish morphological structure-function relationships and could be a potential approach to evaluate platelet function [81]. The main requirement of platelet imaging for morphological profiling is imaging speed as cytoskeleton rearrangement during platelet activation and spreading happen at millisecond timescales [3]. Therefore, imaging techniques that do not require scanning or achieve a fast acquisition rate are preferred for this application. This section will review the imaging techniques used to quantify platelet morphology in terms of fluorescence and label-free based methods.

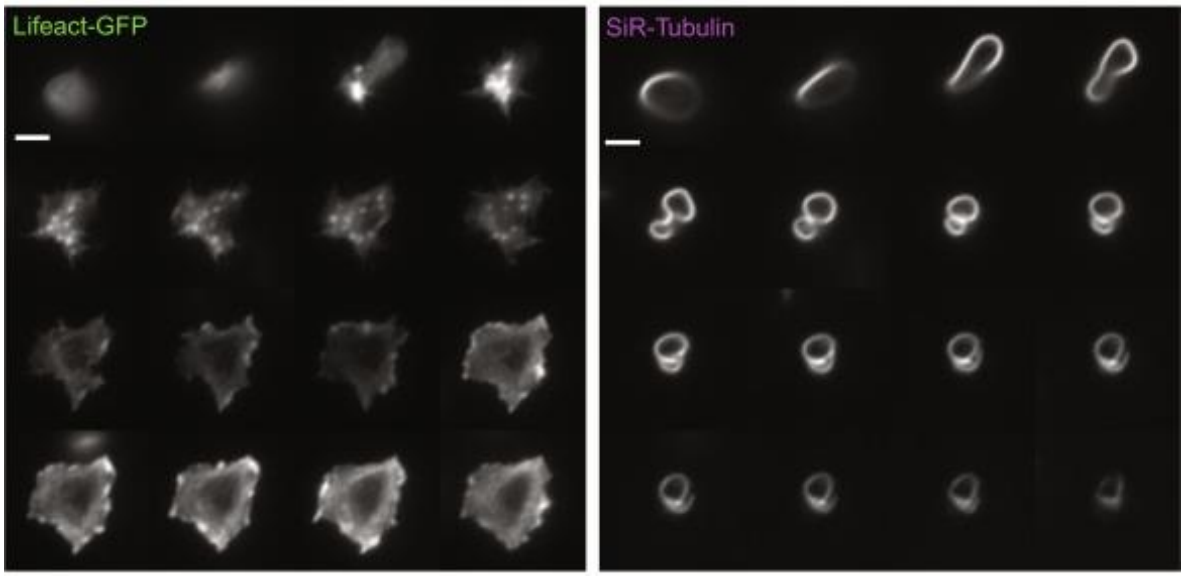

Figure 2-9 Structural changes and cytoskeleton rearrangement of single platelet during spreading. Fluorescence imaging reveals the variations in actin cytoskeleton and microtubule coil that supports the shape change during spreading. This figure is reprinted with permission from Thomas [57] © 2019 Elsevier.

Quantifying morphological changes of single platelets during spreading with fluorescence-based microscopy (epifluorescence [95], TIRF [79, 80] and confocal [11, 96]) normally uses generic membrane dye or specific antibodies targeting cytoskeleton components such as f-actin or microtubule (Fig. 2-9)., The morphological features and activities such as the actin nodules generation, finger-like filopodia interaction showing dynamic membrane ruffling can be observed with fluorescent labelled f-actin and tubulin.

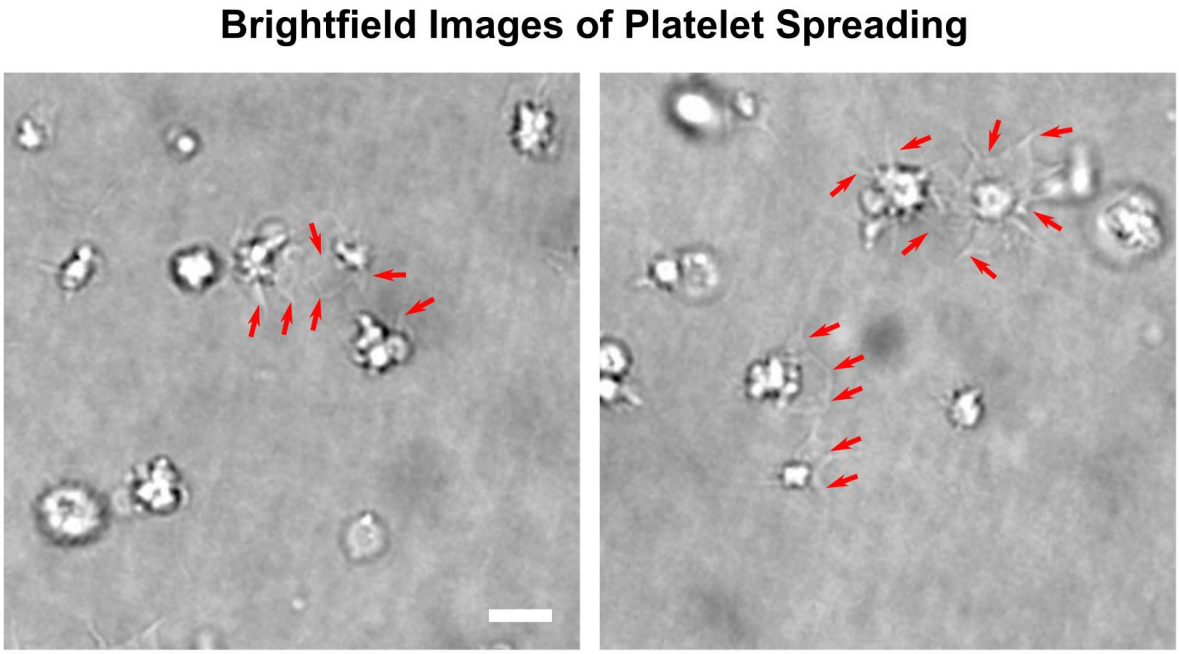

Figure 2-10 Brightfield images of platelet spreading on fibrin coated coverslip. Images captured by an Olympus X71 inverted system, using a 100 X, 1.4 N.A. objective. The red arrows indicate the location of membrane protrusions (filopodia and lamellipodia). Scale bar= 5 μm.

Traditional brightfield microscopy does not provide efficient contrast due to the low scattering cross-section (small size and thickness) and consequently fails to track platelet morphology using label-free methods. In Fig. 2-10, I show the images I took using an Olympus X71 brightfield microscopy (objective: 100X, 1.4 N.A.). The brightfield images capture the platelet spread on fibrin coated surface with platelet membrane protrusions, including filopodia and lamellipodia (highlighted using red arrows). Although these

structures can be recognised, the imaging contrast is poor. Therefore, label-free single platelet imaging is always conducted using imaging methods with higher contrast, including DIC [95] and phase contrast [97]. In this case, the scattering and interference methods (darkfield [23] and RICM [4, 98, 99]) introduced in chapter one would extract platelet morphology at higher contrast.

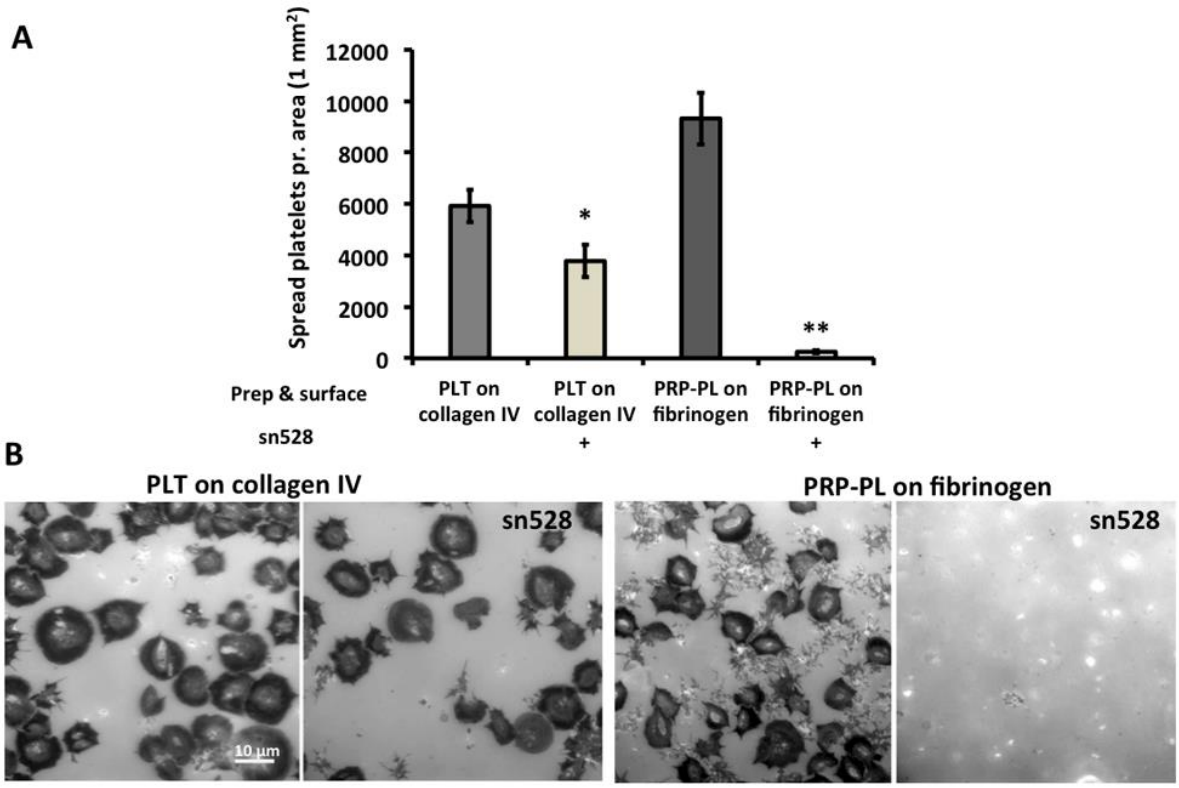

Figure 2-11 Washed platelets (PLT) and platelets rich plasma (PRP-PL) spreading on collagen IV and fibrinogen coated surfaces, with and without the integrin αIIbβ3 inhibitor sn528. (A) Quantification of surface coverage (number of platelets per 1 mm^2). Wilcoxon rank-sum test was used, * p-value < 0.05 and ** p-value < 0.001. N experiments = 4. Error bars = Standard Error. (B) RICM images of the two substrates and treatment. This figure is reprinted with permission from Horev *et al.* [99] © 2020, F1000 Research.

An example of platelet imaging using RICM [99] is shown in Fig. 2-11, morphological features such as filopodia and lamellipodia can be clearly captured, allowing quantifications including surface coverage, shape and protrusion. Fig. 2-11 compares the surface coverage with two distinct adhesive ligands (collagen and fibrinogen) and inhibiting the integrin αIIbβ3 (with sn528), showing the significant reduction of adhesion by inhibiting αIIbβ3 on

fibrinogen substrate [99]. As described in chapter one, RICM enhances the imaging contrast by optimising the reflected background (reference) and improving the interference component. Because of the constructive and destructive interference (Fig. 2-11B), the fringes at membrane protrusions show positive and negative contrast, indicating the distance between the surface and the structures within a few hundred nanometres range [98, 99].

Volumetric imaging of single platelet enables the visualisation of platelet structure in three-dimension with quantifications including volume, thickness and mass. In fluorescence-based confocal microscopy, a series of stacked two-dimensional images need to be collected by axially scanning the sample for three-dimensional reconstruction. Quantifications of volume and thickness can be retrieved using fluorescence intensity, but estimating dry mass is challenging. Additionally, axial scanning could lead to longer acquisition time and increase the risk of photobleaching, which presents challenges for monitoring platelet morphology over time. Quantitative phase microscopy (QPM), on the other hand, retrieves the phase delay of the light passing through the sample, enables reconstruction of volume, thickness and mass in a single-shot [100, 101]. Fig. 2-12 shows an example of volumetric imaging of single platelet using optical diffraction tomography, revealing the differences in RI distribution of resting and activated platelets [102]. From the measurement of RI distribution, the index of single platelets varies within a small region from 1.35 to 1.365, which confirms that platelets have a relatively stable refractive index for label-free imaging. However, QPM techniques do have less sensitivity than RICM as the contrast in the filopodia and lamellipodia region is lower (Fig. 2-12 F and G).

In conclusion, profiling of platelet morphology poses opportunities in platelet diagnostic and drug discovery by extracting the structural features and understanding the meaning behind the morphological profile [22, 81] with the help of regional recognition and

machine learning. Label-free methods such as RICM and QPM enable fast imaging and quantification of shape, volume, thickness, and dry mass without scanning and staining the platelets. Although these methods are less specific for targeted proteins or membrane receptors, we argue that acquisition speed and stability is more critical than molecular specificity for morphological profiling in spreading assay.

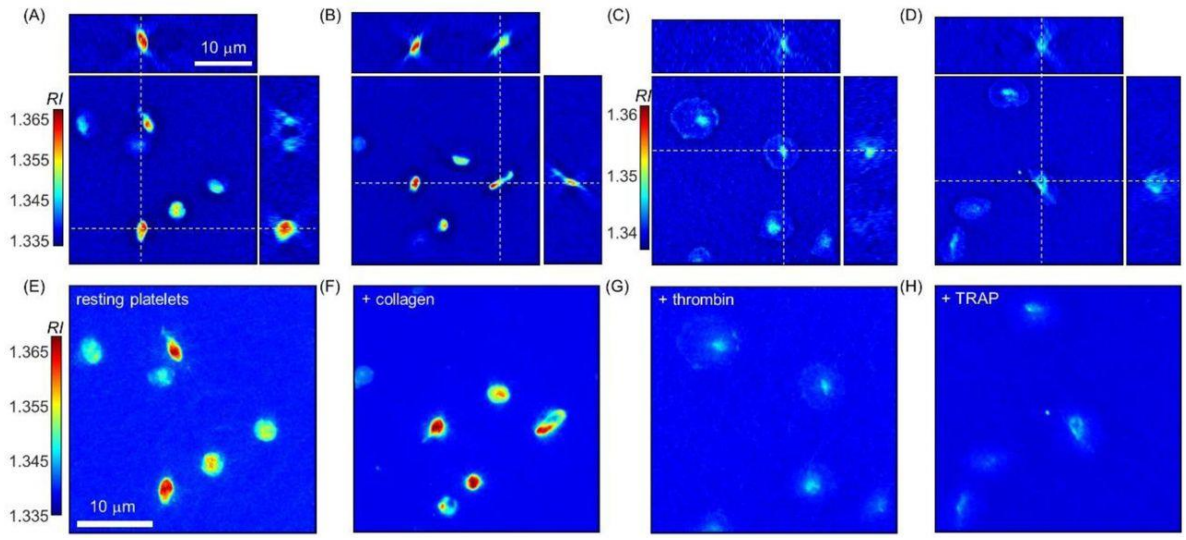

Figure 2-12 Reconstructed 3D refractive index tomograms of resting platelet (A and E) and activated platelets stimulated by collagen (B and F), thrombin (C and G) and thrombin receptor-activating peptide (TRAP) (D and H). The x-y, yz and xz slices are shown in A-D, while the maximum RI projections along the axial direction are shown in E-H. This figure is reprinted with permission from Lee *et al.* [102] © 2019.

2.3 Conclusion

In this chapter, I have briefly introduced the mechanics of platelet adhesion and activation in hemostasis responses. The initial adhesion of platelets and the ECM component (collagen) is mediated through VWF and glycoprotein GPIb [27], and the adhesion site is further secured by various adhesive receptors such as GPVI [5]. These adhesive proteins and agonists trigger platelets activation through various receptor-specific signalling pathways, resulting in rereleasing of granules [10-12] and activation of integrin αIIbβ3 [8, 9, 49] that enables platelet-platelet adhesion through fibrin allows platelet aggregation. Platelets undergo

dramatic shape change during platelets adhesion and activation [52, 53] to support adhesion and granule secretion, driven by cytoskeleton rearrangement and actin polymerization. The morphological profile of single platelet during spreading is significantly affected by adhesive ligands, the function of membrane receptors and the presence of integrin. Capturing morphological information of single platelet during adhesion and activation using high-speed approaches could enable quantification of platelet function and explore possible venues for diagnostic and drug discovery.

Imaging of single platelet is a grand challenge limited by a few factors: detection sensitivity, imaging speed, labelling methods and efficiency, and sample handling [72]. This chapter also reviews the imaging techniques used in single platelet imaging, characterized by quantifications in terms of biochemical, biomechanical and morphological properties. As these quantifications target different biological questions, the suitable imaging techniques need to focus on various aspects, e.g. use high specificity approaches for studying biochemical signalling and high-speed imaging for morphological profiling.

Fluorescence-based microscopy has been heavily used to study biochemical signalling of single platelet at molecular level. These studies have been extended with the emergence of super-resolution microscopy [67, 68] that can achieve nanometer imaging resolution. However, the limitation of super-resolution techniques is the low acquisition speed, which limits the imaging mainly to fixed platelets. Common drawbacks in fluorescence-based microscopy are also related to sample labelling. Since there is no nucleus in platelets, they cannot be transfected. For platelets to express a tagged protein, platelets have to be either purified from genetically modified mice or from differentiation of transfected megakaryocytes [72], which can be challenging and limit the labelling approach in platelet imaging. In addition, in longer-

term imaging (spreading process, >30 minutes), the stability of the fluorescence signal can be suspectable due to photobleaching and phototoxicity.

Label-free methods utilize light scattering and interference that enable the ultra-sensitivity detection of nanoscopic features of single platelet during activation and spreading. Among these label-free methods, RICM [103] has the highest detection sensitivity that resolves nanoscopic features using constructive and destructive interferences for morphological profiling, while QPM enables quantitative measurements of thickness, volume and dry mass [102]. Although these techniques have poor specificity to target desired proteins or membrane receptors, they promote high-speed morphological studies that could be valuable in platelet function assessment.

Most of the techniques reviewed in this chapter focus on single-cell studies where the responses of single platelets are investigated without fluid shear. Single platelet imaging is essential in understanding the signalling pathway, the role of integrins [5, 8, 9, 14], and platelet phenotyping [81] at the initial stage of haemostasis (adhesion and activation). However, the physiological flow also plays an essential role in haemostasis, especially in later stages, such as platelet aggregation and thrombus formation. In the next chapter, I shall discuss the role of flow in haemostasis and the process of thrombus formation. I will also review the techniques for assessing thrombus stability and platelet function.

2.4 Contribution

I took the brightfield image of single platelets (Fig. 2-10) using an Olympus X71 system and a 100X, 1.4 N.A. objective.

Table 2-2 Summary of optical microscopy methods for single platelet imaging

	Imaging method	Quantification	Speed	Resolution	Limitation	Refs
Label -free method	Brightfield	**Biochemical**: • Adhesive ligands **Morphological**: • Shape	>100Hz Only limited by detection camera	Diffraction limited (~λ/2, N.A.≈1.2)	• Low contrast	104
	Phase contrast/ DIC				• No quantitative data	79, 95, 105, 106
	RICM					4, 13, 98, 99, 106
	QPM/ ODT (or holotomography)	**Morphological:** • 3D RI quantification • 3D morphology			• Phase unwrapping problems for thick sample • Axial resolution • Scanning and complex reconstruction are needed for ODT (speed)	102, 107
With imaging probe	Atomic force microscopy (AOM)	**Mechanical**: • Contractile force • Viscoelastic **Morphological**: • 3D morphology	100*100 pixels: 12 Hz	Probing dependent	• Long acquisition time • Hard to glue single platelet to the probe • Might distort shape of the cell or interpret the activation process	108
	Scanning ion conductance microscopy		80*80 pixels: 17 seconds		• Long acquisition time • No direct imaging, resolution depend on the nanopipets	93
Fluorescence-based methods	Epifluorescence	**Biochemical:** • Platelet receptors [65] • Integrin • Granules [11] **Morphological:** • Actin reorganization (LifeAct) [79, 84, 109] **Position Sensing** • Membrane labelling [58, 86, 110]	>100Hz	Diffraction limited (~λ/2, N.A.≈1.2)	• Background/ out of focused light/ SNR	95
	TIRF				• Limited depth of field (~200 nm)	79, 80
	Confocal				• Scanning/ photobleaching	11, 96
	SIM		40*40 μm: 10 Hz [111]	100-120 nm	• Post processing • Long acquisition time – normally used in fixed sample • STORM: Requires highly stable microscope (40,000 frames per final image)	79, 112, 113
	STORM		30*25 μm: 30 seconds [68]	20-30 nm		80-82
	SMIM			50-60 nm		114

2.5 References

1. Chang, Y.; Bluteau, D.; Debili, N.; Vainchenker, W., From hematopoietic stem cells to platelets. *Journal of Thrombosis and Haemostasis* **2007,** *5* (SUPPL. 1), 318-327.

2. Khan, A. O.; Maclachlan, A.; Lowe, G. C.; Nicolson, P. L. R.; Ghaithi, R. A.; Thomas, S. G.; Watson, S. P.; Pike, J. A.; Morgan, N. V., High-throughput platelet spreading analysis: A tool for the diagnosis of platelet-based bleeding disorders. *Haematologica* **2020,** *105* (3), E124-E128.

3. Montague, S. J.; Lim, Y. J.; Lee, W. M.; Gardiner, E. E., Imaging Platelet Processes and Function—Current and Emerging Approaches for Imaging in vitro and in vivo. *Frontiers in Immunology* **2020,** *11*.

4. Hughan, S. C.; Hughes, C. E.; McCarty, O. J. T.; Schweighoffer, E.; Soultanova, I.; Ware, J.; Tybulewicz, V. L. J.; Watson, S. P., GPVI Potentiation of Platelet Activation by Thrombin and Adhesion Molecules Independent of Src Kinases and Syk. **2007,** *27* (2), 422-429.

5. Sarratt, K. L.; Chen, H.; Zutter, M. M.; Santoro, S. A.; Hammer, D. A.; Kahn, M. L., GPVI and alpha2beta1 play independent critical roles during platelet adhesion and aggregate formation to collagen under flow. *Blood* **2005,** *106* (4), 1268-1277.

6. Gogia, S.; Neelamegham, S., Role of fluid shear stress in regulating VWF structure, function and related blood disorders. *Biorheology* **2015,** *52* (5-6), 319-335.

7. Phillips, D. R.; Prasad, K. S. S.; Manganello, J.; Bao, M.; Nannizzi-Alaimo, L., Integrin tyrosine phosphorylation in platelet signaling. *Current Opinion in Cell Biology* **2001,** *13* (5), 546-554.

8. Joo, S. J., Mechanisms of platelet activation and integrin αIIβ3. *Korean Circulation Journal* **2012,** *42* (5), 295-301.

9. Huang, J.; Li, X.; Shi, X.; Zhu, M.; Wang, J.; Huang, S.; Huang, X.; Wang, H.; Li, L.; Deng, H.; Zhou, Y.; Mao, J.; Long, Z.; Ma, Z.; Ye, W.; Pan, J.; Xi, X.; Jin, J., Platelet integrin αiIbβ3: Signal transduction, regulation, and its therapeutic targeting. *Journal of Hematology and Oncology* **2019,** *12* (1).

10. Flaumenhaft, R., Molecular basis of platelet granule secretion. *Arteriosclerosis, Thrombosis, and Vascular Biology* **2003,** *23* (7), 1152-1160.

11. Peters, C. G.; Michelson, A. D.; Flaumenhaft, R., Granule exocytosis is required for platelet spreading: Differential sorting of α-granules expressing VAMP-7. *Blood* **2012,** *120* (1), 199-206.

12. Flaumenhaft, R.; Sharda, A., The life cycle of platelet granules. *F1000Res* **2018,** *7*.

13. Zhang, Y.; Qiu, Y.; Blanchard, A. T.; Chang, Y.; Brockman, J. M.; Ma, V. P. Y.; Lam, W. A.; Salaita, K., Platelet integrins exhibit anisotropic mechanosensing and harness piconewton forces to mediate platelet aggregation. *Proceedings of the National Academy of Sciences of the United States of America* **2017,** *115* (2), 325-330.

14. Falet, H.; Chang, G.; Brohard-Bohn, B.; Rendu, F.; Hartwig, J. H., Integrin αIIbβ3 signals lead cofilin to accelerate platelet actin dynamics. *American Journal of Physiology - Cell Physiology* **2005,** *289* (4 58-4), C819-C825.

15. Penington, D. G.; Olsen, T. E., Megakaryocytes in States of Altered Platelet Production: Cell Numbers, Size and DNA Content. *British Journal of Haematology* **1970,** *18* (4), 447-464.

16. Holinstat, M., Normal platelet function. *Cancer and Metastasis Reviews* **2017,** *36* (2), 195-198.

17. Daly, M. E., Determinants of platelet count in humans. *Haematologica* **2011,** *96* (1), 10-13.

18. Giles, C., The Platelet Count and Mean Platelet Volume. **1981,** *48* (1), 31-37.

19. Ghoshal, K.; Bhattacharyya, M., Overview of platelet physiology: Its hemostatic and nonhemostatic role in disease pathogenesis. *The Scientific World Journal* **2014,** *2014*.

20. Lebois, M.; Josefsson, E. C., Regulation of platelet lifespan by apoptosis. *Platelets* **2016,** *27* (6), 497-504.

21. Frojmovic, M. M.; Milton, J. G., Human platelet size, shape, and related functions in health and disease. *Physiological reviews* **1982,** *62* (1), 185-261.

22. Andreeva, T.; Komsa-Penkova, R.; Langari, A.; Krumova, S.; Golemanov, G.; Georgieva, G. B.; Taneva, S. G.; Giosheva, I.; Mihaylova, N.; Tchorbanov, A.; Todinova, S., Morphometric and nanomechanical features of platelets from women with early pregnancy loss provide new evidence of the impact of inherited thrombophilia. *International Journal of Molecular Sciences* **2021,** *22* (15).

23. Kraus, M. J.; Seifert, J.; Strasser, E. F.; Gawaz, M.; Schäffer, T. E.; Rheinlaender, J., Comparative morphology analysis of live blood platelets using scanning ion conductance and robotic dark-field microscopy. *Platelets* **2016,** *27* (6), 541-546.

24. Bergmeier, W.; Hynes, R. O., Extracellular matrix proteins in hemostasis and thrombosis. *Cold Spring Harbor Perspectives in Biology* **2012,** *4* (2).

25. Watson, S. P., Platelet activation by extracellular matrix proteins in haemostasis and thrombosis. *Current Pharmaceutical Design* **2009,** *15* (12), 1358-1372.

26. Ruggeri, Z. M.; Mendolicchio, G. L., Adhesion mechanisms in platelet function. *Circulation Research* **2007,** *100* (12), 1673-1685.

27. Varga-Szabo, D.; Pleines, I.; Nieswandt, B., Cell adhesion mechanisms in platelets. *Arteriosclerosis, Thrombosis, and Vascular Biology* **2008,** *28* (3), 403-413.

28. Shin, E. K.; Park, H.; Noh, J. Y.; Lim, K. M.; Chung, J. H., Platelet shape changes and cytoskeleton dynamics as novel therapeutic targets for anti-thrombotic drugs. *Biomolecules and Therapeutics* **2017,** *25* (3), 223-230.

29. Cuenca-Zamora, E. J.; Ferrer-Marín, F.; Rivera, J.; Teruel-Montoya, R., Tubulin in Platelets: When the Shape Matters. *International Journal of Molecular Sciences* **2019,** *20* (14).

30. Gardiner, E. E., Proteolytic processing of platelet receptors. *Research and Practice in Thrombosis and Haemostasis* **2018,** *2* (2), 240-250.

31. Montague, S. J.; Andrews, R. K.; Gardiner, E. E., Mechanisms of receptor shedding in platelets. *Blood* **2018,** *132* (24), 2535-2545.

32. Golebiewska, E. M.; Poole, A. W., Platelet secretion: From haemostasis to wound healing and beyond. *Blood Reviews* **2015,** *29* (3), 153-162.

33. Kattula, S.; Byrnes, J. R.; Wolberg, A. S., Fibrinogen and Fibrin in Hemostasis and Thrombosis. *Arteriosclerosis, Thrombosis, and Vascular Biology* **2017,** *37* (3), e13-e21.

34. Casa, L. D. C.; Deaton, D. H.; Ku, D. N., Role of high shear rate in thrombosis. *Journal of Vascular Surgery* **2015,** *61* (4), 1068-1080.

35. Peyvandi, F.; Garagiola, I.; Baronciani, L., Role of von Willebrand factor in the haemostasis. *Blood Transfusion* **2011,** *9* (SUPPL. 2), s3-s8.

36. Hassan, M. I.; Saxena, A.; Ahmad, F., Structure and function of von Willebrand factor: The protein that is deficient and/or abnormal in inherited von Willebrand disease. *Blood Coagulation and Fibrinolysis* **2012,** *23* (1), 11-22.

37. Adam, F.; Guillin, M. C.; Jandrot-Perrus, M., Glycoprotein Ib-mediated platelet activation: A signalling pathway triggered by thrombin. *European Journal of Biochemistry* **2003,** *270* (14), 2959-2970.

38. Arce, N. A.; Cao, W.; Brown, A. K.; Legan, E. R.; Wilson, M. S.; Xu, E. R.; Berndt, M. C.; Emsley, J.; Zhang, X. F.; Li, R., Activation of von Willebrand factor via mechanical unfolding of its discontinuous autoinhibitory module. *Nature Communications* **2021,** *12* (1).

39. Zhang, X.; Halvorsen, K.; Zhang, C. Z.; Wong, W. P.; Springer, T. A., Mechanoenzymatic cleavage of the ultralarge vascular protein von willebrand factor. *Science* **2009,** *324* (5932), 1330-1334.

40. Hoylaerts, M. F.; Yamamoto, H.; Nuyts, K.; Vreys, I.; Deckmyn, H.; Vermylen, J., Von Willebrand factor binds to native collagen VI primarily via its A1 domain. *Biochemical Journal* **1997,** *324* (1), 185-191.

41. Madri, J. A.; Dreyer, B.; Pitlick a, F.; Furthmayr, H., The collagenous components of the subendothelium. Correlation of structure function function. *Laboratory Investigation* **1980,** *43* (4), 303-315.

42. Savage, B.; Almus-Jacobs, F.; Ruggeri, Z. M., Specific synergy of multiple substrate-receptor interactions in platelet thrombus formation under flow. *Cell* **1998,** *94* (5), 657-666.

43. Moroi, M.; Jung, S. M., Platelet glycoprotein VI: Its structure and function. *Thrombosis Research* **2004,** *114* (4), 221-233.

44. Kato, K.; Kanaji, T.; Russell, S.; Kunicki, T. J.; Furihata, K.; Kanaji, S.; Marchese, P.; Reininger, A.; Ruggeri, Z. M.; Ware, J., The contribution of glycoprotein VI to stable platelet adhesion and thrombus formation illustrated by targeted gene deletion. *Blood* **2003,** *102* (5), 1701-1707.

45. Lockyer, S.; Okuyama, K.; Begum, S.; Le, S.; Sun, B.; Watanabe, T.; Matsumoto, Y.; Yoshitake, M.; Kambayashi, J.; Tandon, N. N., GPVI-deficient mice lack collagen responses and are protected against experimentally induced pulmonary thromboembolism. *Thrombosis Research* **2006,** *118* (3), 371-380.

46. Konishi, H.; Katoh, Y.; Takaya, N.; Kashiwakura, Y.; Itoh, S.; Ra, C.; Daida, H., Platelets activated by collagen through immunoreceptor tyrosine-based activation motif play pivotal role in initiation and generation of neointimal hyperplasia after vascular injury. *Circulation* **2002,** *105* (8), 912-916.

47. Massberg, S.; Gawaz, M.; Grüner, S.; Schulte, V.; Konrad, I.; Zohlnhöfer, D.; Heinzmann, U.; Nieswandt, B., A crucial role of glycoprotein VI for platelet recruitment to the injured arterial wall in vivo. *Journal of Experimental Medicine* **2003,** *197* (1), 41-49.

48. Konstantinides, S.; Ware, J.; Marchese, P.; Almus-Jacobs, F.; Loskutoff, D. J.; Ruggeri, Z. M., Distinct antithrombotic consequences of platelet glycoprotein Ibα and VI deficiency in a mouse model of arterial thrombosis. **2006,** *4* (9), 2014-2021.

49. Sánchez-Cortés, J.; Mrksich, M., The Platelet Integrin αIIbβ3 Binds to the RGD and AGD Motifs in Fibrinogen. *Chemistry and Biology* **2009,** *16* (9), 990-1000.

50. Hodivala-Dilke, K. M.; McHugh, K. P.; Tsakiris, D. A.; Rayburn, H.; Crowley, D.; Ullman-Culleré, M.; Ross, F. P.; Coller, B. S.; Teitelbaum, S.; Hynes, R. O., β3-integrin-deficient mice are a model for Glanzmann thrombasthenia showing placental defects and reduced survival. *Journal of Clinical Investigation* **1999,** *103* (2), 229-238.

51. Kovacsovics, T. J.; Hartwig, J. H., Thrombin-induced GPIb-IX centralization on the platelet surface requires actin assembly and myosin II activation. *Blood* **1996,** *87* (2), 618-629.

52. Bearer, E. L.; Prakash, J. M.; Li, Z., Actin dynamics in platelets. In *International Review of Cytology*, 2002; Vol. 217, pp 137-182.

53. Pantaloni, D.; Le Clainche, C.; Carlier, M. F., Mechanism of actin-based motility. *Science* **2001,** *292* (5521), 1502-1506.

54. Li, Z.; Kim, E. S.; Bearer, E. L., Arp2/3 complex is required for actin polymerization during platelet shape change. *Blood* **2002,** *99* (12), 4466-4474.

55. Higgs, H. N.; Pollard, T. D., Regulation of actin filament network formation through Arp2/3 complex: Activation by a diverse array of proteins. In *Annu Rev Biochem*, 2001; Vol. 70, pp 649-676.

56. Sandmann, R.; Köster, S., Topographic Cues Reveal Two Distinct Spreading Mechanisms in Blood Platelets. *Scientific Reports* **2016,** *6*.

57. Thomas, S. G., 3 - The Structure of Resting and Activated Platelets. In *Platelets (Fourth Edition)*, Michelson, A. D., Ed. Academic Press: 2019; pp 47-77.

58. Kim, O. V.; Litvinov, R. I.; Alber, M. S.; Weisel, J. W., Quantitative structural mechanobiology of platelet-driven blood clot contraction. *Nature Communications* **2017,** *8* (1).

59. Jackson, S. P., The growing complexity of platelet aggregation. *Blood* **2007,** *109* (12), 5087-5095.

60. Barkalow, K.; Witke, W.; Kwiatkowski, D. J.; Hartwig, J. H., Coordinated regulation of platelet actin filament barbed ends by gelsolin and capping protein. *Journal of Cell Biology* **1996,** *134* (2), 389-399.

61. Vasconcellos, C. A.; Lind, S. E., Coordinated inhibition of actin-induced platelet aggregation by plasma gelsolin and vitamin D-binding protein. *Blood* **1993,** *82* (12), 3648-3657.

62. Offermanns, S., Activation of platelet function through G protein-coupled receptors. *Circulation Research* **2006,** *99* (12), 1293-1304.

63. Xue, B.; Leyrat, C.; Grimes, J. M.; Robinson, R. C., Structural basis of thymosin-β4/profilin exchange leading to actin filament polymerization. *Proceedings of the National Academy of Sciences of the United States of America* **2014,** *111* (43), E4596-E4605.

64. Yarmola, E. G.; Bubb, M. R., Effects of profilin and thymosin β4 on the critical concentration of actin demonstrated in vitro and in cell extracts with a novel direct assay. *Journal of Biological Chemistry* **2004,** *279* (32), 33519-33527.

65. Diagouraga, B.; Grichine, A.; Fertin, A.; Wang, J.; Khochbin, S.; Sadoul, K., Motor-driven marginal band coiling promotes cell shape change during platelet activation. *Journal of Cell Biology* **2014,** *204* (2), 177-185.

66. Patel-Hett, S.; Richardson, J. L.; Schulze, H.; Drabek, K.; Isaac, N. A.; Hoffmeister, K.; Shivdasani, R. A.; Bulinski, J. C.; Galjart, N.; Hartwig, J. H.; Italiano Jr, J. E., Visualization of microtubule growth in living platelets reveals a dynamic marginal band with multiple microtubules. *Blood* **2008,** *111* (9), 4605-4616.

67. Galbraith, C. G.; Galbraith, J. A., Super-resolution microscopy at a glance. *Journal of Cell Science* **2011,** *124* (10), 1607-1611.

68. Huang, B.; Bates, M.; Zhuang, X., Super-resolution fluorescence microscopy. *Annu Rev Biochem* **2009,** *78*, 993-1016.

69. Kukura, P.; Ewers, H.; Müller, C.; Renn, A.; Helenius, A.; Sandoghdar, V., High-speed nanoscopic tracking of the position and orientation of a single virus. *Nature Methods* **2009,** *6* (12), 923-927.

70. Melchinger, H.; Jain, K.; Tyagi, T.; Hwa, J., Role of Platelet Mitochondria: Life in a Nucleus-Free Zone. *Frontiers in Cardiovascular Medicine* **2019,** *6*.

71. Patel, S. R.; Hartwig, J. H.; Italiano Jr, J. E., The biogenesis of platelets from megakaryocyte proplatelets. *Journal of Clinical Investigation* **2005,** *115* (12), 3348-3354.

72. Sadoul, K.; Lafanechère, L.; Grichine, A., Live imaging of single platelets at work. *Platelets* **2020,** *31* (5), 551-558.

73. Pothapragada, S.; Zhang, P.; Sheriff, J.; Livelli, M.; Slepian, M. J.; Deng, Y.; Bluestein, D., A phenomenological particle-based platelet model for simulating filopodia formation during early activation. *International Journal for Numerical Methods in Biomedical Engineering* **2015,** *31* (3), e02702.

74. Golden, A.; Brugge, J. S., Thrombin treatment induces rapid changes in tyrosine phosphorylation in platelets. *Proceedings of the National Academy of Sciences of the United States of America* **1989,** *86* (3), 901-905.

75. Cho, J.; Mosher, D. F., Role of fibronectin assembly in platelet thrombus formation. *Journal of Thrombosis and Haemostasis* **2006,** *4* (7), 1461-1469.

76. Dunne, E.; Spring, C. M.; Reheman, A.; Jin, W.; Berndt, M. C.; Newman, D. K.; Newman, P. J.; Ni, H.; Kenny, D., Cadherin 6 has a functional role in platelet aggregation and thrombus formation. *Arteriosclerosis, thrombosis, and vascular biology* **2012,** *32* (7), 1724-1731.

77. Farndale, R. W., Collagen-induced platelet activation. *Blood Cells, Molecules, and Diseases* **2006,** *36* (2), 162-165.

78. Nicolai, L.; Schiefelbein, K.; Lipsky, S.; Leunig, A.; Hoffknecht, M.; Pekayvaz, K.; Raude, B.; Marx, C.; Ehrlich, A.; Pircher, J.; Zhang, Z.; Saleh, I.; Marel, A. K.; Löf, A.; Petzold, T.; Lorenz, M.; Stark, K.; Pick, R.; Rosenberger, G.; Weckbach, L.; Uhl, B.; Xia, S.; Reichel, C. A.; Walzog, B.; Schulz, C.; Zheden, V.; Bender, M.; Li, R.; Massberg, S.; Gaertner, F., Vascular surveillance by haptotactic blood platelets in inflammation and infection. *Nature Communications* **2020,** *11* (1).

79. Poulter, N. S.; Pollitt, A. Y.; Davies, A.; Malinova, D.; Nash, G. B.; Hannon, M. J.; Pikramenou, Z.; Rappoport, J. Z.; Hartwig, J. H.; Owen, D. M.; Thrasher, A. J.; Watson, S. P.; Thomas, S. G., Platelet actin nodules are podosome-like structures dependent on Wiskott–Aldrich syndrome protein and ARP2/3 complex. *Nature Communications* **2015,** *6* (1), 7254.

80. Poulter, N. S.; Pollitt, A. Y.; Owen, D. M.; Gardiner, E. E.; Andrews, R. K.; Shimizu, H.; Ishikawa, D.; Bihan, D.; Farndale, R. W.; Moroi, M.; Watson, S. P.; Jung, S.

M., Clustering of glycoprotein VI (GPVI) dimers upon adhesion to collagen as a mechanism to regulate GPVI signaling in platelets. *Journal of Thrombosis and Haemostasis* **2017,** *15* (3), 549-564.

81. Lickert, S.; Sorrentino, S.; Studt, J. D.; Medalia, O.; Vogel, V.; Schoen, I., Morphometric analysis of spread platelets identifies integrin αIIbβ3-specific contractile phenotype. *Scientific Reports* **2018,** *8* (1).

82. Mayr, S.; Hauser, F.; Peterbauer, A.; Tauscher, A.; Naderer, C.; Axmann, M.; Plochberger, B.; Jacak, J., Localization microscopy of actin cytoskeleton in human platelets. *International Journal of Molecular Sciences* **2018,** *19* (4).

83. Riedl, J.; Crevenna, A. H.; Kessenbrock, K.; Yu, J. H.; Neukirchen, D.; Bista, M.; Bradke, F.; Jenne, D.; Holak, T. A.; Werb, Z.; Sixt, M.; Wedlich-Soldner, R., Lifeact: A versatile marker to visualize F-actin. *Nature Methods* **2008,** *5* (7), 605-607.

84. Riedl, J.; Flynn, K. C.; Raducanu, A.; Gärtner, F.; Beck, G.; Bösl, M.; Bradke, F.; Massberg, S.; Aszodi, A.; Sixt, M.; Wedlich-Söldner, R., Lifeact mice for studying F-actin dynamics. *Nature Methods* **2010,** *7* (3), 168-169.

85. Sachs, L.; Denker, C.; Greinacher, A.; Palankar, R., Quantifying single-platelet biomechanics: An outsider's guide to biophysical methods and recent advances. *Research and Practice in Thrombosis and Haemostasis* **2020,** *4* (3), 386-401.

86. Myers, D. R.; Qiu, Y.; Fay, M. E.; Tennenbaum, M.; Chester, D.; Cuadrado, J.; Sakurai, Y.; Baek, J.; Tran, R.; Ciciliano, J. C.; Ahn, B.; Mannino, R. G.; Bunting, S. T.; Bennett, C.; Briones, M.; Fernandez-Nieves, A.; Smith, M. L.; Brown, A. C.; Sulchek, T.; Lam, W. A., Single-platelet nanomechanics measured by high-throughput cytometry. *Nature Materials* **2017,** *16* (2), 230-235.

87. McGrath, B.; Mealing, G.; Labrosse, M. R., A mechanobiological investigation of platelets. *Biomechanics and Modeling in Mechanobiology* **2011,** *10* (4), 473-484.

88. Hochmuth, R. M., Micropipette aspiration of living cells. *Journal of Biomechanics* **2000,** *33* (1), 15-22.

89. Lam, W. A.; Chaudhuri, O.; Crow, A.; Webster, K. D.; Li, T. D.; Kita, A.; Huang, J.; Fletcher, D. A., Mechanics and contraction dynamics of single platelets and implications for clot stiffening. *Nature Materials* **2011,** *10* (1), 61-66.

90. García, R.; Pérez, R., Dynamic atomic force microscopy methods. *Surface Science Reports* **2002,** *47* (6-8), 197-301.

91. Mak, M.; Erickson, D., A serial micropipette microfluidic device with applications to cancer cell repeated deformation studies. *Integrative Biology (United Kingdom)* **2013,** *5* (11), 1374-1384.

92. Myrand-Lapierre, M. E.; Deng, X.; Ang, R. R.; Matthews, K.; Santoso, A. T.; Ma, H., Multiplexed fluidic plunger mechanism for the measurement of red blood cell deformability. *Lab on a Chip* **2015,** *15* (1), 159-167.

93. Seifert, J.; Rheinlaender, J.; Lang, F.; Gawaz, M.; Schäffer, T. E., Thrombin-induced cytoskeleton dynamics in spread human platelets observed with fast scanning ion conductance microscopy. *Scientific Reports* **2017,** *7* (1).

94. Beussman, K. M.; Mollica, M. Y.; Leonard, A.; Miles, J.; Hocter, J.; Song, Z.; Stolla, M.; Han, S. J.; Emery, A.; Thomas, W. E.; Sniadecki, N. J., Black Dots: High-Yield Traction Force Microscopy Reveals Structural Factors Contributing to Platelet Forces. *Acta Biomaterialia* **2021**.

95. Paknikar, A. K.; Eltzner, B.; Köster, S., Direct characterization of cytoskeletal reorganization during blood platelet spreading. *Progress in Biophysics and Molecular Biology* **2019,** *144*, 166-176.

96. Kahr, W. H. A.; Pluthero, F. G.; Elkadri, A.; Warner, N.; Drobac, M.; Chen, C. H.; Lo, R. W.; Li, L.; Li, R.; Li, Q.; Thoeni, C.; Pan, J.; Leung, G.; Lara-Corrales, I.; Murchie, R.; Cutz, E.; Laxer, R. M.; Upton, J.; Roifman, C. M.; Yeung, R. S. M.; Brumell, J. H.; Muise, A. M., Loss of the Arp2/3 complex component ARPC1B causes platelet abnormalities and predisposes to inflammatory disease. *Nature Communications* **2017,** *8*.

97. Agbani, E. O.; Van Den Bosch, M. T. J.; Brown, E.; Williams, C. M.; Mattheij, N. J. A.; Cosemans, J. M. E. M.; Collins, P. W.; Heemskerk, J. W. M.; Hers, I.; Poole, A. W., Coordinated membrane ballooning and procoagulant spreading in human platelets. *Circulation* **2015,** *132* (15), 1414-1424.

98. Zarka, R.; Horev, M. B.; Volberg, T.; Neubauer, S.; Kessler, H.; Spatz, J. P.; Geiger, B., Differential Modulation of Platelet Adhesion and Spreading by Adhesive Ligand Density. *Nano Letters* **2019,** *19* (3), 1418-1427.

99. Horev, M. B.; Zabary, Y.; Zarka, R.; Sorrentino, S.; Medalia, O.; Zaritsky, A.; Geiger, B., Differential dynamics of early stages of platelet adhesion and spreading on collagen IV- and fibrinogen-coated surfaces. *F1000Res* **2020,** *9*, ISF-449.

100. Park, Y. K.; Depeursinge, C.; Popescu, G., Quantitative phase imaging in biomedicine. *Nature Photonics* **2018,** *12* (10), 578-589.

101. Stanly, T. A.; Suman, R.; Rani, G. F.; O'Toole, P. J.; Kaye, P. M.; Hitchcock, I. S., Quantitative Optical Diffraction Tomography Imaging of Mouse Platelets. *Frontiers in Physiology* **2020,** *11*.

102. Lee, S.; Jang, S.; Park, Y., Measuring three-dimensional dynamics of platelet activation using 3-D quantitative phase imaging. *bioRxiv* **2019**, 827436.

103. Barr, V. A.; Bunnell, S. C., Interference Reflection Microscopy. *Current Protocols in Cell Biology* **2009,** *45* (1), 4.23.1-4.23.19.

104. Sauter, A.; Richter, G.; Micoulet, A.; Martinez, A.; Spatz, J. P.; Appel, S., Effective polyethylene glycol passivation for the inhibition of surface interactions of peripheral blood mononuclear cells and platelets. *Biointerphases* **2013,** *8* (1), 1-12.

105. Kulkarni, S.; Jackson, S. P., Platelet factor XIII and calpain negatively regulate integrin αIIbβ3 adhesive function and thrombus growth. *Journal of Biological Chemistry* **2004,** *279* (29), 30697-30706.

106. Lee, D.; Fong, K. P.; King, M. R.; Brass, L. F.; Hammer, D. A., Differential dynamics of platelet contact and spreading. *Biophysical Journal* **2012,** *102* (3), 472-482.

107. Zouaoui Boudejltia, K.; de Sousa, D. R.; Uzureau, P.; Yourassowsky, C.; Perez-Morga, D.; Courbebaisse, G.; Chopard, B.; Dubois, F., Quantitative analysis of platelets aggregates in 3D by digital holographic microscopy. *Biomedical Optics Express* **2015,** *6* (9), 3556-3563.

108. Ando, T.; Kodera, N.; Takai, E.; Maruyama, D.; Saito, K.; Toda, A., A high-speed atomic force microscope for studying biological macromolecules. *Proceedings of the National Academy of Sciences of the United States of America* **2001,** *98* (22), 12468-12472.

109. Urban, A. E.; Quick, E. O.; Miller, K. P.; Krcmery, J.; Simon, H. G., Pdlim7 regulates Arf6-dependent actin dynamics and is required for platelet-mediated thrombosis in mice. *PLoS ONE* **2016,** *11* (10).

110. Kim, O. V.; Nevzorova, T. A.; Mordakhanova, E. R.; Ponomareva, A. A.; Andrianova, I. A.; Minh, G. L.; Daminova, A. G.; Peshkova, A. D.; Alber, M. S.; Vagin, O.; Litvinov, R. I.; Weisel, J. W., Fatal dysfunction and disintegration of thrombin-stimulated platelets. *Haematologica* **2019,** *104* (9), 1866-1878.

111. Markwirth, A.; Lachetta, M.; Mönkemöller, V.; Heintzmann, R.; Hübner, W.; Huser, T.; Müller, M., Video-rate multi-color structured illumination microscopy with simultaneous real-time reconstruction. *Nature Communications* **2019,** *10* (1).

112. Westmoreland, D.; Shaw, M.; Grimes, W.; Metcalf, D. J.; Burden, J. J.; Gomez, K.; Knight, A. E.; Cutler, D. F., Super-resolution microscopy as a potential approach to diagnosis of platelet granule disorders. *Journal of Thrombosis and Haemostasis* **2016,** *14* (4), 839-849.

113. Yadav, S.; Storrie, B., The cellular basis of platelet secretion: Emerging structure/function relationships. *Platelets* **2017,** *28* (2), 108-118.

114. Mao, H.; Diekmann, R.; Liang, H. P. H.; Cogger, V. C.; Le Couteur, D. G.; Lockwood, G. P.; Hunt, N. J.; Schüttpelz, M.; Huser, T. R.; Chen, V. M.; McCourt, P. A. G., Cost-efficient nanoscopy reveals nanoscale architecture of liver cells and platelets. *Nanophotonics* **2019**.

Chapter 3 Platelet-rich Thrombus Formation

The composition of a thrombus includes platelets, fibrin mesh, and red blood cells that are known to determine its mechanical properties [1-3]. Thrombus stability is vital to maintaining thrombus function, and the biophysical properties of platelets, i.e. the extent of adhesiveness, rate of aggregation and dissociation, are all important biophysical markers of an unstable thrombus. An unstable thrombus can lead to significant health outcomes such as excessive bleeding [4], or embolization [5]. These complications are the most common causes of myocardial infarction, ischemic stroke, deep vein thrombosis, and other cardiovascular diseases [5-7].

In this chapter, I will first discuss the influence of high fluid shear stress in thrombus formation and focus on the unfolding process of the Von Willebrand factor (VWF) [8-10]. More importantly, I shall focus on platelet-rich thrombi known as "white clots" [11] formed under high fluid shear. Platelets play a significant role in these high shear-induced clots, along with fibrin fibres that form as part of the coagulation cascade (thrombin, fibrinogen [12, 13]). An increase in activated and aggregating platelets would recruit additional platelets and thereby influence the stability of a thrombus [14, 15]. In addition, I shall briefly discuss the relationship of thrombus stability with the "core-shell" hierarchy [16]. Under the core-shell framework, the thrombus structure is described as a tightly-packed platelet core that forms on the injury site and is topped by a loosely-packed shell of platelet aggregates. The existing core-shell framework has been derived primarily from electron microscopy, without fluorescence labelling, which has identified and classified the packing density and morphology of platelets

in formed thrombi. However, these studies were conducted using fixed samples, which do not preserve the dynamic processes of platelet aggregation and thrombus formation.

Microfluidics techniques promote different chamber designs to capture thrombus dynamics [17, 18], mimic stenotic vessel [19], and quantify micromechanics of forming clots [20, 21]. In the second section of the chapter, I shall discuss the fabrication techniques (microfluidics [22, 23] and soft lithography [24]), which have been widely applied to mimic the microenvironment of blood vessels in *in-vitro* studies. I will then elaborate on advanced imaging approaches that enable the in-depth study of thrombus structure and stability under fluid shear conditions. This section will also cover the challenges of thrombus imaging and the possible imaging approaches to studying thrombus stability.

3.1 Role of Fluid Shear in Platelet Studies

Early studies on platelet activation and aggregation were conducted in the absence of shear forces [25, 26] as it was assumed that soluble factors served as the primary mechanism for triggering haemostasis, and shear flow had a minor contribution [27]. Studies that focused on platelet spreading on the surface enabled the investigation of the role of membrane receptors and adhesive ligands in platelet adhesion, shape change, spreading, and aggregation [28, 29]. These studies without flow conditions have been meaningful in understanding membrane binding mechanisms and processes. However, it was recognized later that shear forces are also directly involved in platelet activation, beyond simply transporting platelet and proteins to the site of injury on the vessel [30-32]. In addition, some of the findings from non-flow assays were different to those under shear conditions, such as the studies of clotting behaviour using implant devices [33].

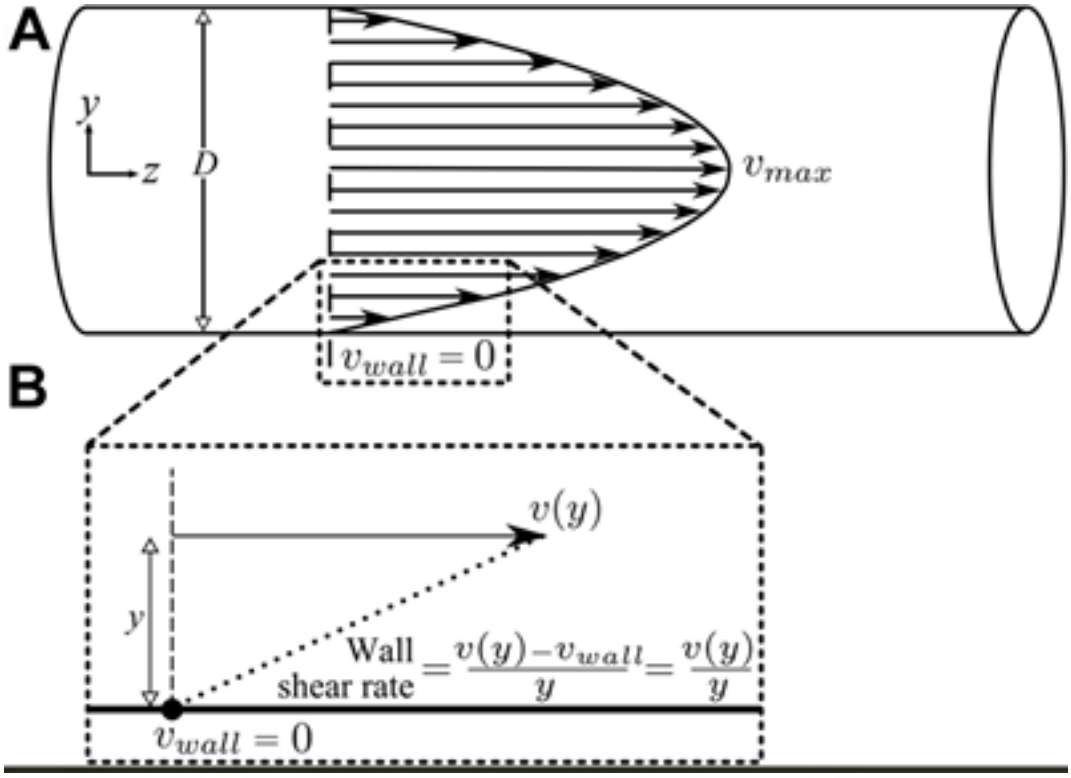

Figure 3-1 Fluid shear and velocity profile in a straight tube. (A) Poiseuille flow in the tube (diameter D) can be described as a parabolic velocity profile with zero velocity at the wall (vwall=0). The arrows indicate the velocity vector as a function of distance (y) across the vessel. (B) The shear rate is defined as the near-wall velocity (v) divided by the distance from the wall (y). This figure is reprinted with permission from Casa *et al.* [34] © 2015 Elsevier.

Shear forces are produced by the fluid layers of blood passing by each other at different velocities, and this gradient of velocities within a flow is described using shear rate, as shown in Fig. 3-1 [34]. The velocity profile is characterized by a parabolic curve with zero velocity at the wall and maximum velocity at the centre of the tube. The wall shear rate is defined as the slope or gradient of the parabolic curve, and the wall shear stress is the force per unit area exerted by the near-wall fluid on the vessel wall (shear stress = viscosity × shear rate). The presence of fluid shear forces can influence the behaviour of adhesive ligands and proteins on the platelet membrane. VWF is the most well-known component, mediating the initial adhesion of platelet and collagen [8, 9, 35].

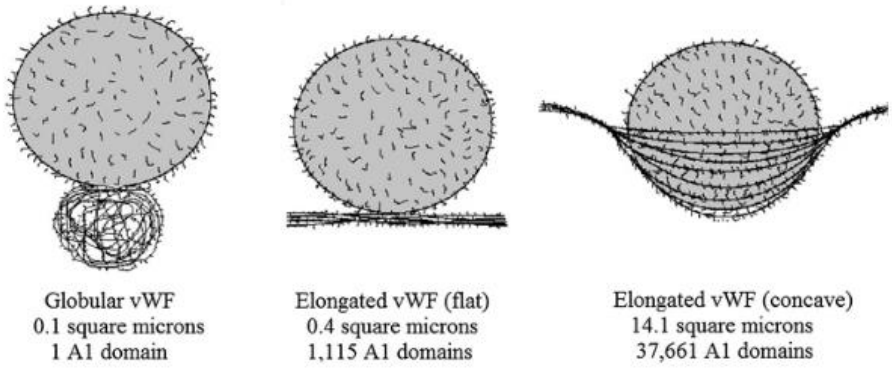

Figure 3-2 Structural change of VWF from a globular form to a flat and concave elongated form at a high shear rate and the change in binding site on the A1 domain when in contact with the platelets. For each form, the maximum contact area (in square microns, um^2) and the maximum number of A1 domains which can come in contact with platelets is shown (with receptor density of 2664 domains/μm^2).

During thrombus formation, VWF is proposed to function as a mechanical flow sensor. Studies of individual VWF concatemer have revealed that the A1 domain can interact and bind to GPIbα under mechanical forces [36-38]. Early hypotheses suggest that VWF exists in a coiled or globular conformation due to monomeric self-association under low flow shear stress [39]. In this conformation, the binding site on the A1 domain is believed to be hidden and inaccessible for platelet adhesion [40-42]. The structural change of VWF from its globular confirmation to the elongation form unmasks the active binding site and activate the VWF for platelet binding (as shown in Fig. 3-2). However, recent single molecule results [43] suggested that the free-VWF does not stretch significantly in solution as previously thought. Bergal *et al* [43] demonstrated that the change in VWF length distribution is two orders of magnitude less than the previously reported values (0.17 vs 13 μm), indicating the elongation of the VWF might not be sufficient to activate the binding sites on the A1 domain.

In recent studies, Fu *et al.* [44] tethered the VWF concatemer to a surface and measured VWF response to shear flow at the single molecule level. They revealed that the activation of the A1 domain for platelet adhesion requires a minimum tension when exposed to flow

condition. Fig. 3-3 illustrates GPIbα binding and extension of VWF molecule under different flow conditions. As shown in Fig. 3-3 A, the extension of VWF is observed but no GPIbα binding occurred below 720 dyn cm^{-2}. At 720–1280 dyn cm^{-2} shear stress, binding of GPIbα is observed at the upstream regions of the extended VWF near the tether where tensile force is high [44]. The relation between tension force and GPIbα binding along a single, long VWF concatemers are also quantified as shown in Fig 3-3 B, illustrating a sigmoidal dependence of the number of bound GPIbα molecules per μm of VWF and the tensile force [44]. GPIbα binding only reach plateau when the tension is about above 35 pN, showing that the tensile force promotes the switch from low-affinity state of the A1 domain in VWF to a high-affinity state.

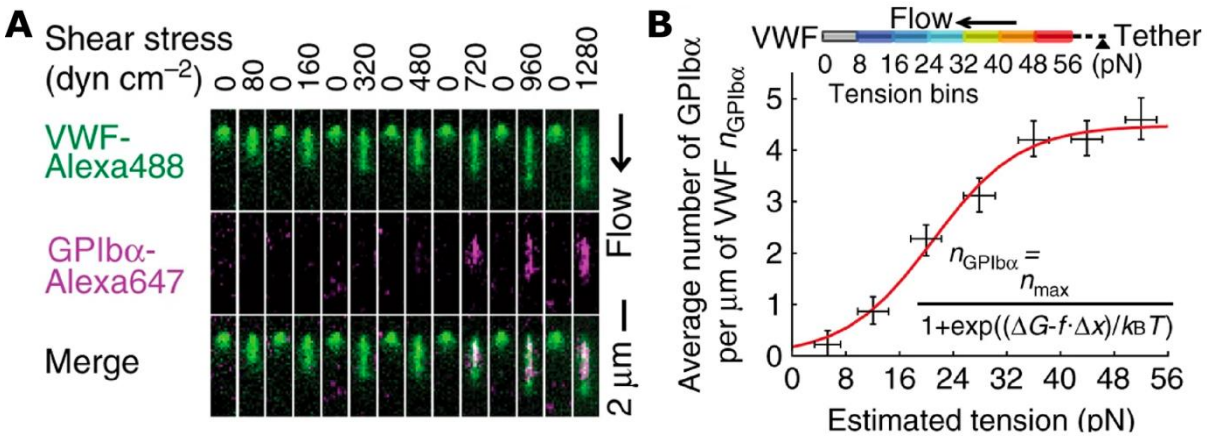

Figure 3-3 Tension-regulated VWF binding to GPIbα. (A) Representative time-lapse fluorescence images showing VWF extension and reversible GPIbα binding during cycling between stasis and a range of wall shear stresses. VWF and GPIbα are labelled using Alexa 488 and Alexa 647 respectively. (B) average number of GPIbα per μm binds along the extended VWF concatemers at 1280 dyn cm^{-2}. Data are mean for 103 concatemers that were long enough to include all seven tension bins. The data points are fitted using a two-state model fit using the inset formula. This figure is reprinted with permission from Fu *et al*. [44] © 2017 Springer Nature.

Additionally, membrane protrusions or tethers that are pulled from the surface of the platelets under hemodynamic drag force also play a critical role in initiating platelet-matrix and platelet-platelet adhesive interactions (Fig. 3-4). These structures are smooth cylinders of

lipid bilayer that can develop up to 30 μm in length [45]. Membrane tethers can reduce the pulling forces imposed on adhesive bonds formed between platelets and the membrane [10], increasing the probability of preserving adhesion under high fluid shear. Membrane tethers are also critical for keeping platelets close to each other (Fig. 3-4 B), which helps facilitate autocrine and paracrine stimulation through locally generated agonists. Membrane tethers restrict the distance between platelets, resulting in a higher concentration of activating signals within the local region of a developing thrombus.

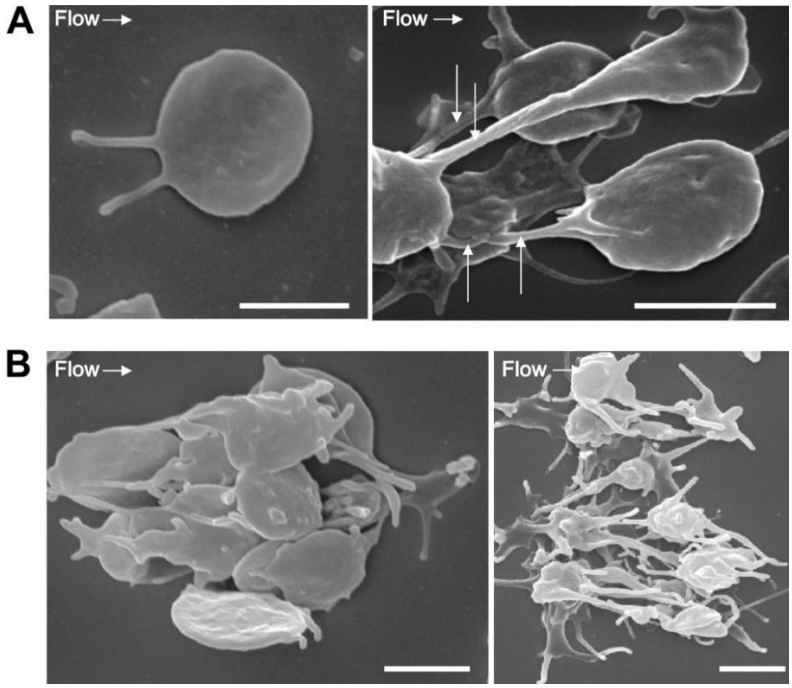

Figure 3-4 Scanning electron microscopy showing platelets forming tethers during adhesion to immobilized VWF at 1800 s^{-1} shear rate. Scale bar = 2 μm. This figure is reprinted with permission from Jackson [46] © 2007 Elsevier.

3.2 Thrombus Structure and Stability

The formed thrombus contracts under high fluid shear and can shed small or large emboli (detachment of platelets or platelet aggregates). Detached pieces of the platelet aggregates can occlude downstream blood vessels in the lungs or brain, causing life-threatening diseases, including pulmonary embolism and ischemic stroke [47]. Mechanical

stability of an intravascular thrombus reflects the effectiveness of hemostasis at the sites of the injured vessel and the possibility of pathological blood vessel obstruction. The stability of a thrombus is determined by its structures and the mechanical properties of its components (e.g. platelets, collagen, and fibrin network). Individual platelets and fibrin networks that make up a forming clot are high heterogenous, and platelet activation levels [46, 48], platelet morphology [46, 49], cytosolic calcium [50], and α-granule secretion [51] are not uniform throughout a hemostatic plug. This heterogeneity in platelet morphology and fibrin formation is captured using scanning electron microscopy and shown in Fig. 3-5, showing images at the extravascular side of the vessel, the boundary of the injury site, and luminal surfaces.

As shown in Fig. 3-5, most platelets on the luminal surface retain a discoid shape or only change shape minimally and develop few membrane protrusions, indicating minimal activation. Platelets at the boundary of the injury site are squeezed tightly together and appear as small spheroid bodies ~0.5 - 1 μm with long protrusions. In contrast, the extravascular portion differs dramatically from intravascular components, both in platelet morphology and fibrin concentration. Platelets at the extravascular site have the highest packing density on the extensive fibrin network that uniformly fills the hole created by the injury. Small islands of platelets are also formed and are interconnected by fibrin fibres. The heterogeneity in platelet morphology results from the highly activated platelets at the extravascular surface, indicated by P-selection expression [52, 53].

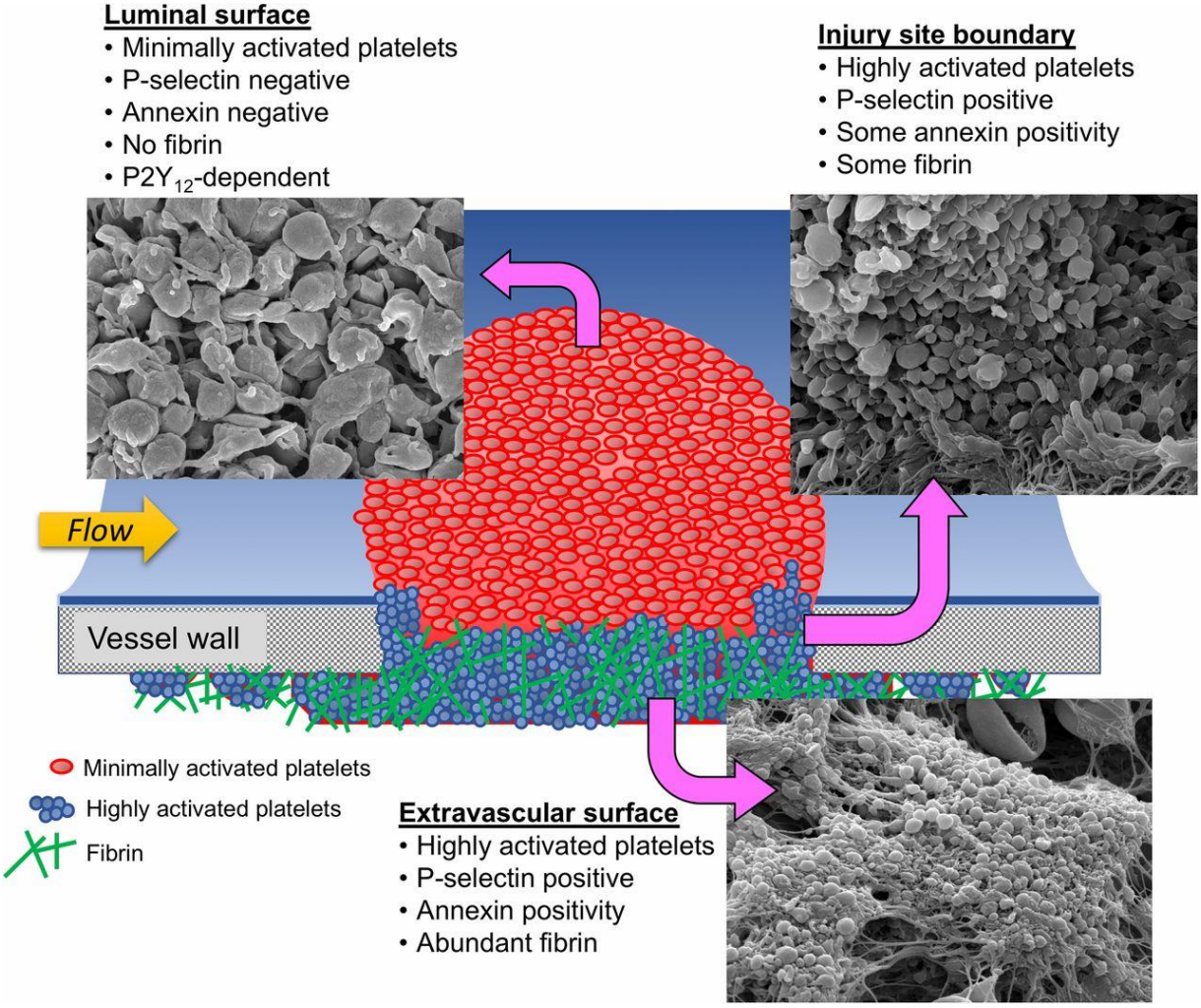

Figure 3-5 Scanning electron microscopy images showing spatial heterogeneity of platelet activation and fibrin network at the extravascular surface, injury site boundary, and luminal surface, respectively. The differences in platelet activation level, protein expressions (P2Y12 and p-selectin) are also summarized and illustrated. This figure is reprinted with permission from Tomaiuoli *et al.* [53] © 2019 National Academy of Sciences.

The heterogeneity in platelet behaviour produces an organized thrombus structure that consists of regions that differ in platelet activation state, packing density, and stability [16, 54, 55]. This structural behaviour is known as the "core-shell" theory, which proposes that a forming thrombus consists of an inner core and outer shell, and a change in behaviour is observed passing between the two regions (Fig. 3-6). Consistent with the observations from SEM images, in vitro studies also showed the distribution of P-selectin signal indicates the different platelet activation states within thrombi from a side view perspective [56]. During

platelet activation, P-selectin translocates from intracellular granules to the external membrane, and the extent of P-selectin expression reflects the level of platelet activation [57]. The inner core expresses a high P-selectin signal, which indicates that it consists of tightly packed, highly activated platelets. The low signal from the outer shell indicates that the zone consists of loosely packed and less activated platelets.

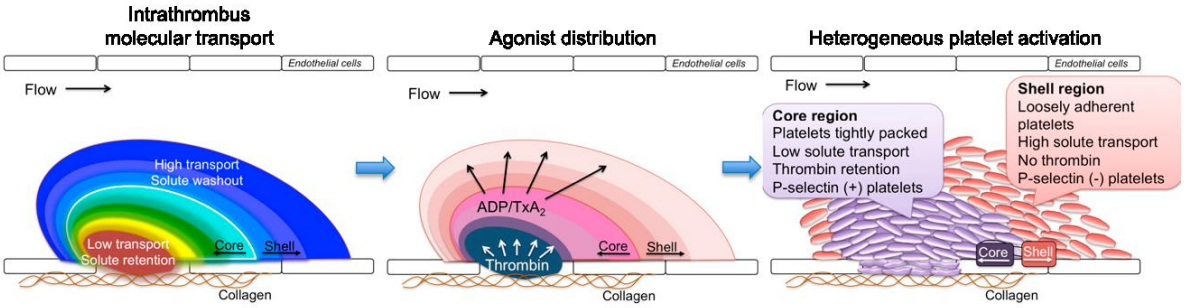

Figure 3-6 Thrombus core-shell model showing differences between the core and shell regions for intrathrombus molecular transport rates, platelet agonist distribution and platelet activation. This figure is reprinted with permission from Stalker [58] © 2014 Elsevier.

The difference in platelet activation within a forming thrombus is due to the distribution of platelet agonists and the different elements of the platelet-signalling network. Although collagen mainly exists at the vascular wall, other components such as thrombin, adenosine diphosphate (ADP) and thromboxane A2 (TxA2) are located throughout the thrombus. The distribution of formed fibrin indicates that thrombin is primarily generated at the site of vascular injury, where the inner core is located [16, 54, 59]. The high thrombin concentration results in a dense fibrin network with highly activated platelet closely packed together (Fig. 3-6). As thrombin diffuses outwards, it is expected to have less of an impact on the platelets further from the vessel wall (in the outer shell). The outer shell region is more affected by TxA2 and ADP as they are small enough to diffuse outward from the core.

3.3 Assessing Thrombus Formation and Stability

A stable thrombus must balance the processes of clotting and fibrinolysis. The imbalance in one direction can cause bleeding or embolization. The opposite direction can lead to thrombosis, the most common source of myocardial infarction, ischemic stroke, deep vein thrombosis, and other cardiovascular diseases [60]. The stability of the thrombus is affected by many variables such as platelet dysfunction, coagulation, and flow conditions. To assess the stability of a thrombus, two factors should be considered: (1) ***adhesiveness*** of the thrombus core, which is determined by the strength of attachment between platelets and ligands, and (2) ***porosity*** (structures) of the forming thrombus, which determines detachment of single platelet or micro-aggregates [5]. As shown in Fig. 3-7, a less stable thrombus structure, consisting of a porous fibrin network with sparse platelet contact, can lead to the detachment of a series of small fragments. Additionally, the unstable core, formed by looser and weaker attachment between platelets and collagen, can lead to embolization of larger fragments or the whole thrombus.

In-vitro flow assays utilize nano-scale fabrication approaches and high-resolution imaging techniques to assess thrombus stability and platelet function in real-time. These approaches are used to mimic the micro-environment of the blood vessel and physiological blood flow conditions. However, nearly all flow assays assess thrombus stability by quantifying the extent of platelet detachment by measuring the change in mass/volume, and these studies do not investigate platelet adhesiveness or their interaction with collagen at the thrombus core. In the section, I will first review the fabrication techniques for microfluidic devices used to study thrombus behaviour under flow conditions. I will discuss volumetric imaging approaches used to quantify thrombus stability and imaging methods which could possibly be used to investigate the adhesiveness of the thrombus core.

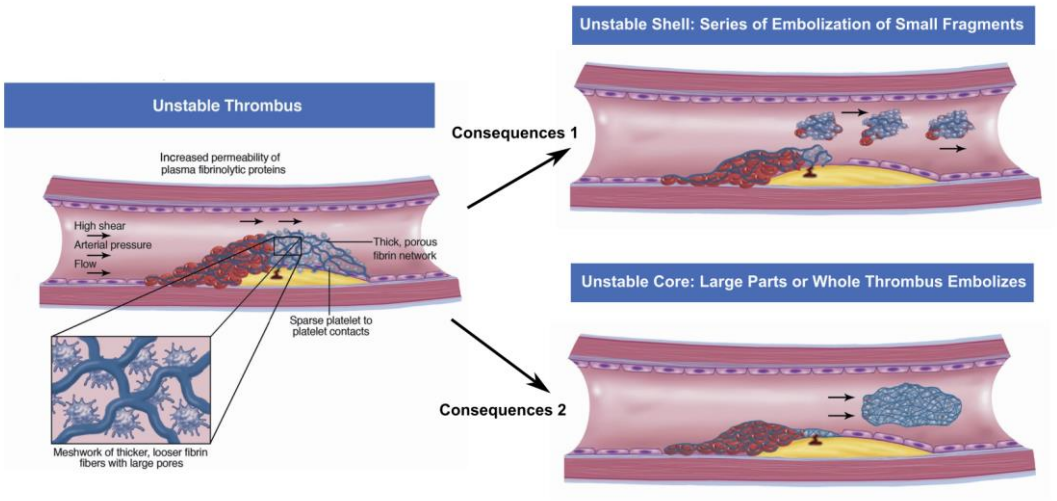

Figure 3-7 Structural features which should be considered when assessing thrombus stability include adhesiveness of the core and porosity of the thrombus. An unstable structure will cause embolization of a series of small fragments, and a less adhesive core will lead to embolization of larger parts or whole thrombus. This figure is edited and reprinted with permission from Gorog *et al*. [5] © 2017 Elsevier.

3.4.1 Microfluidics Design for Thrombus Imaging

This section is not meant to be an exhaustive review of microfluidic devices, which has previously been done [23, 61]. I mainly review channels developed to investigate thrombus formation and stability with high-resolution imaging methods.

Microfluidics systems are the most common method of conducting *in-vitro* platelet or thrombus imaging under flow. Microfluidics assays require several components, including microfluidic chips containing micro-channels, a fluidics pump to precisely control the applied shear stress, and an imaging system to visualize the activity inside the channel (Fig. 3-8 A). *In-vitro* studies of platelet activation and thrombus formation often utlise micro-channels 50 – 100 μm in width [62, 63] with adhesive ligands (collagen [23] or fibrin [64]) coated on the bottom surface to initiate thrombus formation and mimic injured blood vessel walls. Physiological flow conditions in microfluidics application are generally introduced by a syringe pump that

pulls or pushes blood or platelet-rich plasma (PRP) through the channel at a constant shear rate determined by the velocity and viscosity of the sample.

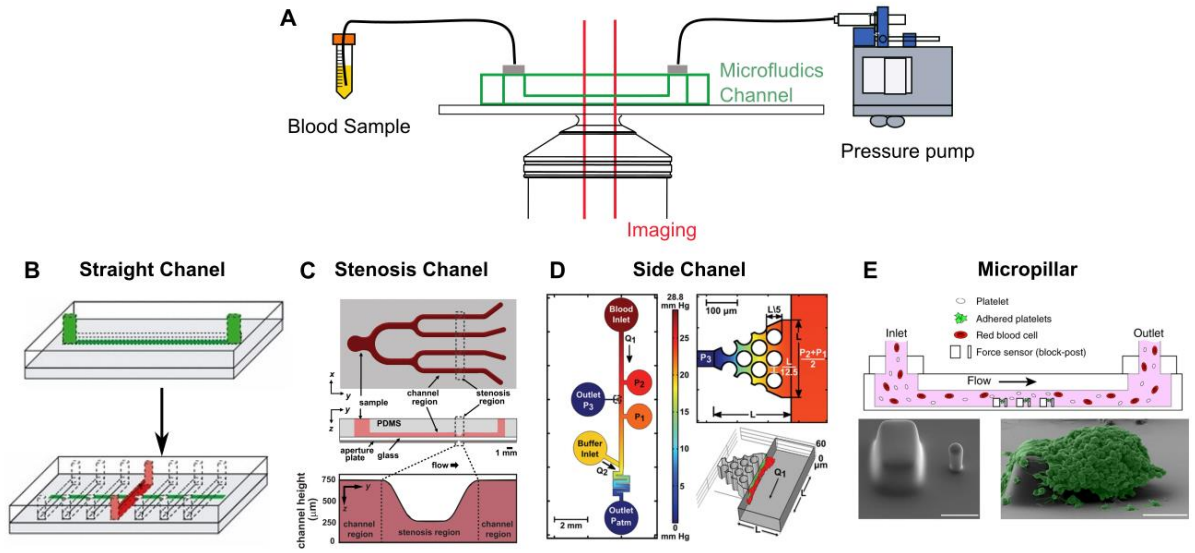

Figure 3-8 (A) Microfluidics system consists of a microfluidics channel, a pressure pump, blood sample, and an imaging system to capture the dynamic process. Typically created using soft lithography, the microfluidics channel be in the form of a straight channel (B), stenosis channels (C), side channels (D) for structural study and micropillar (E) for contractile force measurements. Figure B is reprinted with permission from Diamond *et al.* [65] © 2008 John Wiley and Sons. Figure C is reprinted with permission from Li *et al.* [19] © 2014 PLOS. Figure D is reprinted with permission from Muthard and Diamond [17] © 2012 Wolters Kluwer Health, Inc. Figure E is reprinted with permission from Ting *et al.* [20] © 2019 Springer Nature.

The simplest structure for conducting microfluidics is directly employing a glass capillary tube as a straight channel [66]. A more complex channel structure is typically realized using soft lithography [24], which imprints the desired structures on a polydimethylsiloxane (PDMS) polymer and assembles the channel by binding the PDMS to a glass slide [22]. The flexibility to alter channel designs using soft lithography enables channel designs to recapitulate pathological vessel geometries, including simple straight channel [18, 65] (Fig. 3-8 B) and stenotic channels (Fig. 3-8 C) representing vessels with stagnation points [19]. Besides engineering the shape of the channel, multiple approaches have been developed to pattern the coating of the adhesive ligands. For example, the collagen fibre has been patterned

orthogonally to the flow direction [65, 67] to study the influence of collagen orientation on thrombus activity. The collagen fibre was also coated on the sidewall of the channel [17], allowing imaging to visualise the side view of the thrombus structure and corroborating the core-shell theory (Fig. 3-8 D).

In addition, previous work has also developed methods to investigate the effects of contractile forces (Fig. 3-8 E), including patterning the adhesive ligand (fibrinogen) [68] and developing a micro-pillar layer [20, 21]. In both cases, the patterned structure acts like force sensors where the contraction forces can be quantified through the deformation of micropillars or the displacement of coated ligands.

3.4.2 Quantifying Thrombus Stability through Volumetric Imaging

Monitoring thrombus formation and stability with imaging methods is typically conducted by checking the size of the platelet aggregate over time. As thrombi have a larger and complex structure than single platelets, a larger field of view is more critical than imaging resolution and sensitivity. Super-resolution techniques are less suitable as they sacrifice acquisition time for the expanded FOVs. Fig. 3-9 and Table 3-1 provide an overview of the imaging techniques used for thrombus imaging. The most straightforward approaches used to visualize a thrombus structure include brightfield [20, 69, 70], DIC [71], and epi-fluorescence [20, 69] microscopy due to their fast acquisition speed and simple sample preparation. These methods capture the process of thrombus formation and embolization and indicate the surface coverage. However, they cannot provide any quantitative information on platelet detachment, which poses a challenge for studying thrombus stability and embolization.

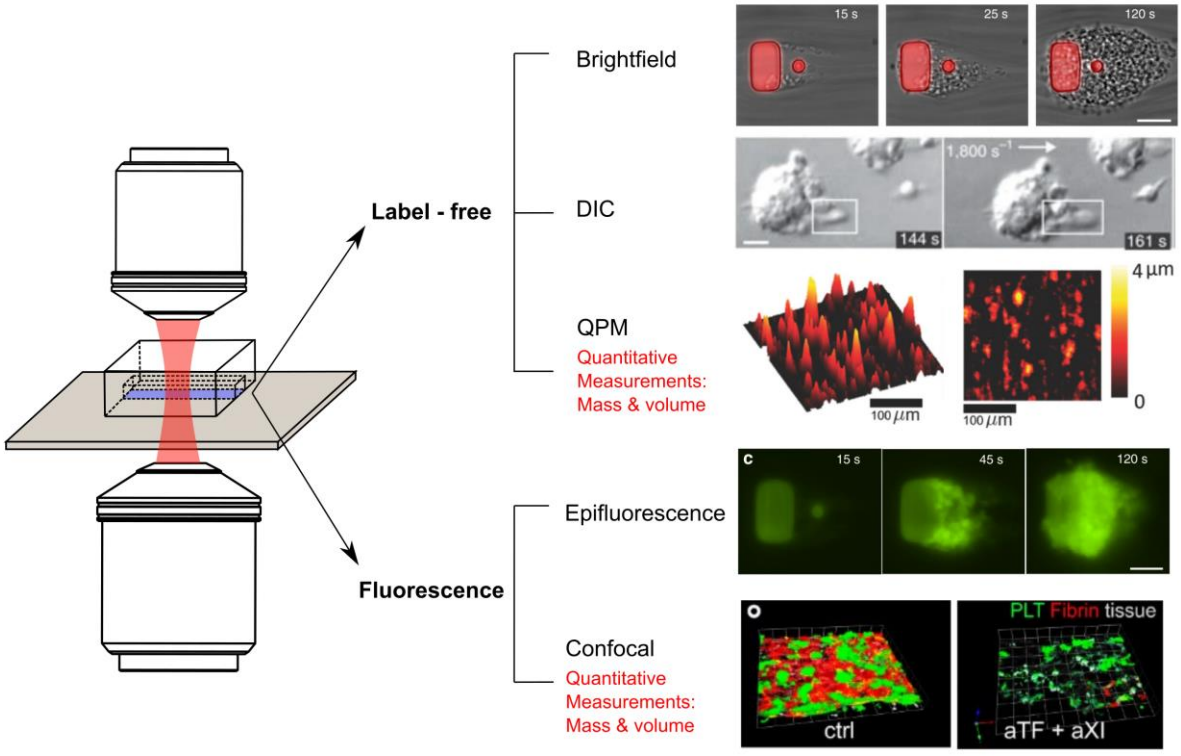

Figure 3-9 Overview of imaging methods for assessing thrombus stability, including label-free and fluorescence methods. The DIC images are reprinted from Nesbitt *et al.* [49] © 2009 Springer Nature. The QPM images are reproduced from He *et al.*[18] © Wiley-VCH GmbH. The brightfield and epifluorescence images are reprinted with permission from Ting *et al.* [20] © 2019 Springer Nature. The confocal images are reprinted with permission from Marchese *et al.* [72] © 2021 MDPI.

Quantifying platelet detachment is typically conducted by tracking the total platelet mass or volume [73, 74] through thrombus formation under flow stress using volumetric imaging approaches such as confocal microscopy and quantitative phase microscopy. In 3D confocal microscopy, thrombus morphology information such as height and volume over the course of thrombus formation is provided by summing up the fluorescence intensity attributed to platelet-specific fluorescent markers [72] as shown in Fig. 3-10. The evolution of a thrombus and the initial steps of adhesion, activation, signalling, and recruitment can also be studied by labelling membrane receptors and surface proteins. However, the accuracy and precisions of fluorescence microscopy approaches are limited by the antibodies or probes used, which may have variable affinities and efficiencies for binding to the platelet membrane. Because these

reagents can potentially interfere with platelet activation or aggregation processes and receptor function, these approaches may not be suitable for live-cell imaging. Furthermore, a scanning laser system increases the risk of photobleaching and phototoxicity [75, 76], increasing uncertainty in quantitative measurements. Lastly, accurate quantification of thrombus volume may be hampered by the dynamic range of the photodetector, as saturation of the fluorescence signal will result in the direct relationship between signal and volume being lost with further increases to thrombus volume [63].

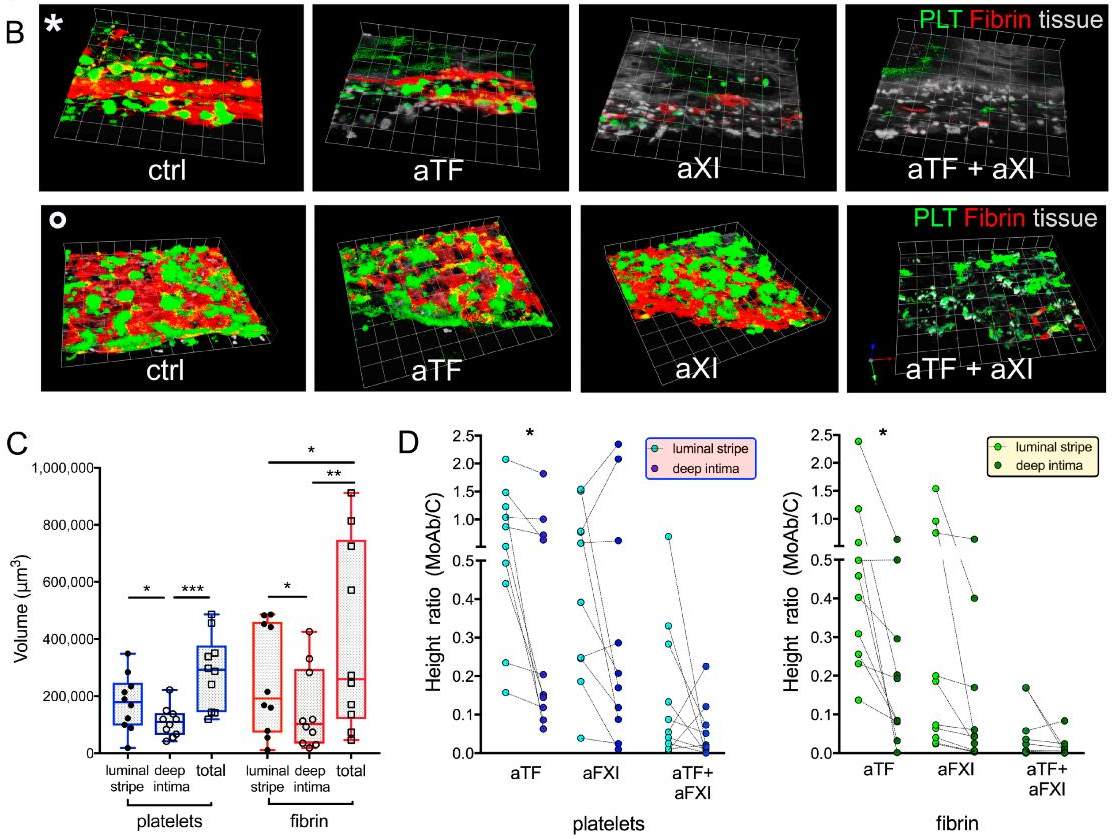

Figure 3-10 (A) Confocal images showing thrombus formation over intima in the presence of aTF and/or aFXI. (B) Quantification of thrombus volume, fibrin strand deposition from fluorescence signal. This figure is reprinted with permission from Marchese *et al.* [72] © 2021 MDPI.

Several label-free methods have been developed for quantitative imaging of platelet adhesion and thrombus formation [18, 71]. Because there is no nucleus in platelets, the refractive index of platelets is likely to be stable and uniform [63]. Phase imaging based on optical path

and refractive index differences can be an excellent choice for platelet imaging. Digital holography microscopy (DHM) [77, 78], a form of QPM that quantifies height, volume, and mass based on the phase shift of the incident light has been used to quantitatively measure volume the of thrombi during formation and embolization (Fig. 3-11) under different shear rates [18, 71]. Since DHM imaging does not require scanning, it enables a fast capture rate that is only limited by the acquisition rate of the camera. This allows DHM to offer real-time and stable quantification of thrombus morphology without fluorescence labelling.

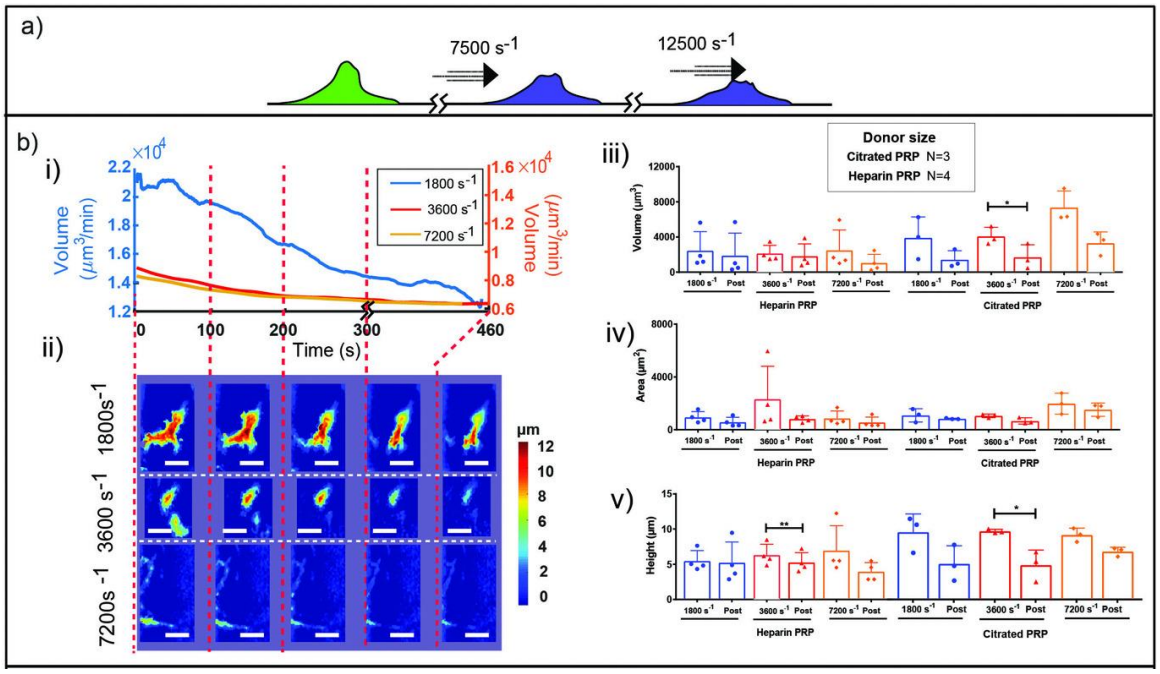

Figure 3-11 Testing thrombus stability at different shear rates by monitoring thrombus volume using QPM. (A) thrombus stability is tested by exerting high flow shear on the forming thrombus (buffer flowing at 7500 s-1 for 5 minutes and then 12500 s-1 for 2 minutes). (B) (i) Trace of thrombus volume during stability test, thrombus formed under the shear rate of 1800 s-1, 3600 s-1, and 7200 s-1 are shown here. (ii) Heightmaps of the thrombus at selected time points. Quantification of thrombus volume (iii), surface area (iv), and peak height (v) of the thrombus formed from all donors. This figure is reproduced from He *et al.* [18] © 2018 John Wiley-VCH GmbH.

QPM approaches have limited optical sectioning capabilities because the optical path difference is generated by the summation of phase shift across the depth of the sample. One of the significant constraints is that the interacting surface between platelets and the adhesive

ligands cannot be imaged once the initial layer of platelets has aggregated. Previous efforts have been made to acquire accurate three-dimensional images using phase imaging. Tomographic phase microscopy (TPM) [79-81] introduces tilted scanning in the illumination path that can reconstruct the three-dimensional refractive index of the sample using a galvanometer-based scanning mirror or AOM. However, because a large amount of data is needed to reconstruct a single image, the imaging speed and post-processing remain challenging. To date, TPM has not been used for thrombus imaging, possibly because of the imaging speed.

3.4.3 Imaging through the Adhesion Site

Monitoring platelet-ligand adhesion with adhesive ligands during thrombus formation could provide extra information on thrombus stability, as it determines the strength of the attachment of the thrombus to the substrate. Previous studies have used confocal microscopy to capture single platelets interacting with fibrin fibre during thrombus formation [82]. As shown in Fig. 3-12, single platelets could adhere to fibrin, become activated, form long protrusions, and bind the fibrin fibre at a mean rate of 0.003 ± 0.002 μm/s. However, the major limitation of the study is the absence of fluid shear. In fact, none of the current studies focus on studying platelet interactions with collagen/fibrin at the thrombus core during thrombus formation under the influence of fluid shear [68, 82]. To selectively visualize the adherent platelets under high flow shear, the two key parameters which need to be controlled for are the depth of the imaging field and acquisition speed. The imaging depth needs to cover only the thickness of the fibre and a few layers of adherent platelets (~3-4 μm) to selectively image the thrombus core. Methods such as confocal and tomographic phase microscopy have depth sectioning, but they are limited in imaging speed (~10s for one tomogram [79], maximum 30 FPS for one confocal image [83]). In contrast, widefield techniques

that permit high-speed imaging and depth sectioning, including highly inclined thin illumination (HILO) [84, 85], and GI-SIM [86] could be used in this application. These methods provide a tunable imaging depth (0.2-2.5 μm) by altering the oblique angle of the illumination beam and restricting the depth of field to the platelets at the thrombus core only.

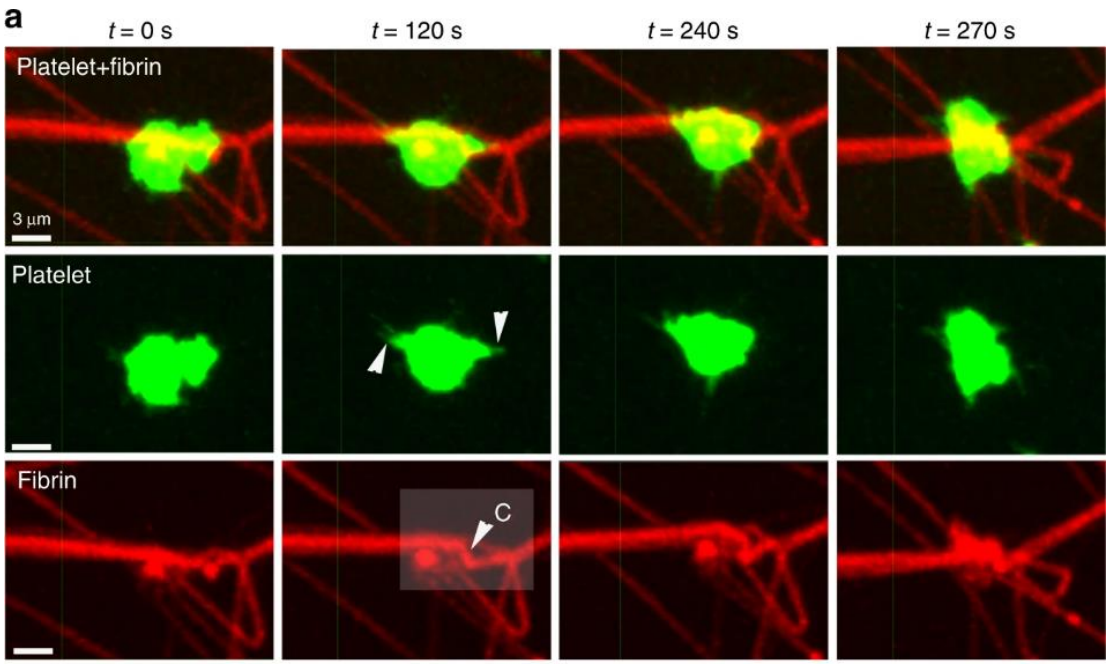

Figure 3-12 Time-lapse images from confocal microscopy show that contracting platelets can bend, kink, and accumulate on a single fibrin fibre locally. Platelets and fibrin are labelled in green and red, respectively. Scale bar = 3 μm. This figure is reprinted with permission from Kim *et al.* [82] © 2017 Springer Nature.

3.4 Conclusion

In this chapter, I have reviewed the influence of fluid shear on platelet aggregation and thrombus formation, focusing on the dynamics of VWF unfolding and membrane tethering under high shear stress. These findings suggest that flow conditions are critical when assessing hemostasis and investigating platelet dysfunction. Under high flow shear, fragments of platelets or platelet aggregates (emboli) might detach from an unstable thrombus, leading to acute conditions, e.g. stroke. To understand thrombus stability, studies on

thrombus structure (following the core-shell hierarchy) using electron and fluorescence microscopy have revealed a heterogeneous distribution of platelet activation levels [46, 48], platelet morphology [46, 49], cytosolic calcium [50], and α-granule secretion. This heterogeneous distribution is represented by a closely packed, highly activated thrombus core and a loosely packed shell structure. We argue that two factors contribute towards thrombus stability and need to be considered in such studies: (1) adhesiveness of the core, (2) porosity (structure) of the thrombus as the former investigates the firmness of adhesion between the thrombus and substrate and the later examines the detachment of the platelet aggregate. However, the majority of the *in-vitro* flow assays monitor thrombus stability by tracking the changes in thrombus volume and platelet detachment [18, 72]. None of the studies focus on the adhesion site between the thrombus core and the adhesive agonists.

In the following chapters, I shall introduce our methods of oblique illumination, which we have used to study the platelet interaction at the thrombus core under flow shear. Instead of collecting fluorescence signals, we propose a label-free technique that uses scattered light within the thrombus core region (~4 μm depth) and investigates platelet motility as a marker for platelet adhesiveness. The imaging method and platelet adhesiveness study will be discussed in chapter 4, 5, and 7.

Table 3-1 Summary of optical microscopy methods for platelet aggregation and thrombus imaging

	Imaging method	Quantification	Speed	Resolution	Limitation	Refs
Label -free method	Brightfield	• Visualization of effect	>100Hz Only limited by detection camera	Diffraction limited (~λ/2, N.A. ≈1.22)	• Low contrast	87
	Phase contrast/ DIC				• No quantitative data	49
	QPM/ ODT (or holotomography)	**Morphological:** • 3D RI quantification • Volume • Mass			• Phase unwrapping problems for thick sample • Cannot measure the adhesion site • Scanning and complex reconstruction are needed for ODT (speed)	18, 71
Fluorescence-based methods	Epifluorescence	**Biochemical:** • Platelet receptors • Interaction at adhesion site during thrombus formation **Morphological:** • Volume	>100Hz	Diffraction limited (~λ/2, N.A. ≈1.22)	• Background/ out of focused light/ SNR • No sectioning	20
	Confocal				• Low speed and relatively small FOV for 3D imaging • Photobleaching due to scanning	72, 82

3.5 References

1. Gersh, K. C.; Nagaswami, C.; Weisel, J. W., Fibrin network structure and clot mechanical properties are altered by incorporation of erythrocytes. *Thrombosis and Haemostasis* **2009,** *102* (6), 1169-1175.

2. Krasokha, N.; Theisen, W.; Reese, S.; Mordasini, P.; Brekenfeld, C.; Gralla, J.; Slotboom, J.; Schrott, G.; Monstadt, H., Mechanical properties of blood clots - A new test method. *Materialwissenschaft und Werkstofftechnik* **2010,** *41* (12), 1019-1024.

3. Weisel, J. W., The mechanical properties of fibrin for basic scientists and clinicians. *Biophysical Chemistry* **2004,** *112* (2-3 SPEC. ISS.), 267-276.

4. Mihalko, E.; Brown, A. C., Clot Structure and Implications for Bleeding and Thrombosis. *Seminars in Thrombosis and Hemostasis* **2020,** *46* (1), 96-97.

5. Gorog, D. A.; Fayad, Z. A.; Fuster, V., Arterial Thrombus Stability: Does It Matter and Can We Detect It? *Journal of the American College of Cardiology* **2017,** *70* (16), 2036-2047.

6. Gorog, D. A., Potentiation of thrombus instability: a contributory mechanism to the effectiveness of antithrombotic medications. *Journal of Thrombosis and Thrombolysis* **2018,** *45* (4), 593-602.

7. Heptinstall, S., Hemostasis and thrombosis: Basic principles and clinical practice, 4th edition. *Platelets* **2001,** *12* (5), 319.

8. Colace, T. V.; Diamond, S. L., Direct observation of von Willebrand factor elongation and fiber formation on collagen during acute whole blood exposure to pathological flow. *Arteriosclerosis, Thrombosis, and Vascular Biology* **2013,** *33* (1), 105-113.

9. Schneider, S. W.; Nuschele, S.; Wixforth, A.; Gorzelanny, C.; Alexander-Katz, A.; Netz, R. R.; Schneider, M. F., Shear-induced unfolding triggers adhesion of von Willebrand factor fibers. *Proceedings of the National Academy of Sciences of the United States of America* **2007,** *104* (19), 7899-7903.

10. Dopheide, S. M.; Maxwell, M. J.; Jackson, S. P., Shear-dependent tether formation during platelet translocation on von Willebrand factor. *Blood* **2002,** *99* (1), 159-167.

11. Koupenova, M.; Kehrel, B. E.; Corkrey, H. A.; Freedman, J. E., Thrombosis and platelets: An update. *European Heart Journal* **2017,** *38* (11), 785-791.

12. Palta, S.; Saroa, R.; Palta, A., Overview of the coagulation system. *Indian Journal of Anaesthesia* **2014,** *58* (5), 515-523.

13. Periayah, M. H.; Halim, A. S.; Saad, A. Z. M., Mechanism action of platelets and crucial blood coagulation pathways in Hemostasis. *International Journal of Hematology-Oncology and Stem Cell Research* **2017,** *11* (4), 319-327.

14. Jackson, S. P.; Nesbitt, W. S.; Westein, E., Dynamics of platelet thrombus formation. *Journal of Thrombosis and Haemostasis* **2009,** *7* (SUPPL. 1), 17-20.

15. Packham, M. A., Role of platelets in thrombosis and hemostasis. *Canadian Journal of Physiology and Pharmacology* **1994,** *72* (3), 278-284.

16. Welsh, J. D.; Stalker, T. J.; Voronov, R.; Muthard, R. W.; Tomaiuolo, M.; Diamond, S. L.; Brass, L. F., A systems approach to hemostasis: 1. The interdependence of thrombus architecture and agonist movements in the gaps between platelets. *Blood* **2014,** *124* (11), 1808-1815.

17. Muthard, R. W.; Diamond, S. L., Blood clots are rapidly assembled hemodynamic sensors: Flow arrest triggers intraluminal thrombus contraction. *Arteriosclerosis, Thrombosis, and Vascular Biology* **2012,** *32* (12), 2938-2945.

18. He, X.; Montague, S. J.; Tao, X.; Gardiner, E. E.; Lee, W. M., Quantifying Embolism: Label-Free Volumetric Mapping of Thrombus Structure and Kinesis in a Microfluidic System with Optical Holography. *Advanced Biosystems* **2018,** *2* (10).

19. Li, M.; Hotaling, N. A.; Ku, D. N.; Forest, C. R., Microfluidic thrombosis under multiple shear rates and antiplatelet therapy doses. *PLoS ONE* **2014,** *9* (1).

20. Ting, L. H.; Feghhi, S.; Taparia, N.; Smith, A. O.; Karchin, A.; Lim, E.; John, A. S.; Wang, X.; Rue, T.; White, N. J.; Sniadecki, N. J., Contractile forces in platelet aggregates under microfluidic shear gradients reflect platelet inhibition and bleeding risk. *Nature Communications* **2019,** *10* (1).

21. Chen, Z.; Lu, J.; Zhang, C.; Hsia, I.; Yu, X.; Marecki, L.; Marecki, E.; Asmani, M.; Jain, S.; Neelamegham, S.; Zhao, R., Microclot array elastometry for integrated measurement of thrombus formation and clot biomechanics under fluid shear. *Nature Communications* **2019,** *10* (1).

22. Duffy, D. C.; McDonald, J. C.; Schueller, O. J. A.; Whitesides, G. M., Rapid prototyping of microfluidic systems in poly(dimethylsiloxane). *Analytical Chemistry* **1998,** *70* (23), 4974-4984.

23. Westein, E.; De Witt, S.; Lamers, M.; Cosemans, J. M. E. M.; Heemskerk, J. W. M., Monitoring in vitro thrombus formation with novel microfluidic devices. *Platelets* **2012,** *23* (7), 501-509.

24. Qin, D.; Xia, Y.; Whitesides, G. M., Soft lithography for micro- and nanoscale patterning. *Nature Protocols* **2010,** *5* (3), 491-502.

25. Leytin, V. L.; Ljubimova, E. V.; Sviridov, D. D.; Repin, V. S.; Smirnov, V. N., Time-response changes in the thrombogenicity of platelets spread on a collagen-coated surface. *Thrombosis Research* **1980,** *20* (3), 335-341.

26. Koteliansky, V. E.; Leytin, V. L.; Sviridov, D. D.; Repin, V. S.; Smirnov, V. N., Human plasma fibronectin promotes the adhesion and spreading of platelets on surfaces coated with fibrillar collagen. *FEBS Letters* **1981,** *123* (1), 59-62.

27. Feghhi, S.; Sniadecki, N. J., Mechanobiology of platelets: Techniques to study the role of fluid flow and platelet retraction forces at the micro- and nano-scale. *International Journal of Molecular Sciences* **2011,** *12* (12), 9009-9030.

28. Feuerstein, I. A.; Ratner, B. D., Adhesion and aggregation of thrombin prestimulated human platelets: evaluation of a series of biomaterials characterized by ESCA. *Biomaterials* **1990,** *11* (2), 127-132.

29. Frojmovic, M.; Longmire, K.; van de Ven, T. G., Long-range interactions in mammalian platelet aggregation. II. The role of platelet pseudopod number and length. *Biophysical Journal* **1990,** *58* (2), 309-318.

30. Yeh, C.; Eckstein, E. C., Transient lateral transport of platelet-sized particles in flowing blood suspensions. *Biophysical Journal* **1994,** *66* (5), 1706-1716.

31. Eckstein, E. C.; Bilsker, D. L.; Waters, C. M.; Kippenhan, J. S.; Tilles, A. W., Transport of Platelets in Flowing Blood. In *Annals of the New York Academy of Sciences*, 1987; Vol. 516, pp 442-452.

32. Sixma, J. J.; de Groot, P. G., Regulation of Platelet Adhesion to the Vessel Wall. In *Annals of the New York Academy of Sciences*, 1994; Vol. 714, pp 190-199.

33. Spijker, H. T.; Graaff, R.; Boonstra, P. W.; Busscher, H. J.; Van Oeveren, W., On the influence of flow conditions and wettability on blood material interactions. *Biomaterials* **2003,** *24* (26), 4717-4727.

34. Casa, L. D. C.; Deaton, D. H.; Ku, D. N., Role of high shear rate in thrombosis. *Journal of Vascular Surgery* **2015,** *61* (4), 1068-1080.

35. Wellings, P. J.; Ku, D. N., Mechanisms of Platelet Capture Under Very High Shear. *Cardiovascular Engineering and Technology* **2012,** *3* (2), 161-170.

36. Kim, J.; Zhang, C. Z.; Zhang, X.; Springer, T. A., A mechanically stabilized receptor-ligand flex-bond important in the vasculature. *Nature* **2010,** *466* (7309), 992-995.

37. Kim, J.; Hudson, N. E.; Springer, T. A., Force-induced on-rate switching and modulation by mutations in gain-of-function von Willebrand diseases. *Proceedings of the National Academy of Sciences of the United States of America* **2015,** *112* (15), 4648-4653.

38. Ju, L.; Dong, J. F.; Cruz, M. A.; Zhu, C., The N-terminal flanking region of the A1 domain regulates the force-dependent binding of von willebrand factor to platelet glycoprotein Ibα. *Journal of Biological Chemistry* **2013,** *288* (45), 32289-32301.

39. Ulrichts, H.; Vanhoorelbeke, K.; Girma, J. P.; Lenting, P. J.; Vauterin, S.; Deckmyn, H., The von Willebrand factor self-association is modulated by a multiple domain interaction. *Journal of Thrombosis and Haemostasis* **2005,** *3* (3), 552-561.

40. De Luca, M.; Facey, D. A.; Favaloro, E. J.; Hertzberg, M. S.; Whisstock, J. C.; McNally, T.; Andrews, R. K.; Berndt, M. C., Structure and function of the von Willebrand factor A1 domain: Analysis with monoclonal antibodies reveals distinct binding sites involved in recognition of the platelet membrane glycoprotein Ib-IX-V complex and ristocetin-dependent activation. *Blood* **2000,** *95* (1), 164-172.

41. Di Stasio, E.; De Cristofaro, R., The effect of shear stress on protein conformation: Physical forces operating on biochemical systems: The case of von Willebrand factor. *Biophysical Chemistry* **2010,** *153* (1), 1-8.

42. Vergauwe, R. M. A.; Uji-I, H.; De Ceunynck, K.; Vermant, J.; Vanhoorelbeke, K.; Hofkens, J., Shear-stress-induced conformational changes of von Willebrand factor in a water-glycerol mixture observed with single molecule microscopy. *Journal of Physical Chemistry B* **2014,** *118* (21), 5660-5669.

43. Bergal, H. T.; Jiang, Y.; Yang, D.; Springer, T. A.; Wong, W. P., Conformation of von Willebrand factor in shear flow revealed with stroboscopic single-molecule imaging. *Blood* **2022**.

44. Fu, H.; Jiang, Y.; Yang, D.; Scheiflinger, F.; Wong, W. P.; Springer, T. A., Flow-induced elongation of von Willebrand factor precedes tension-dependent activation. *Nature Communications* **2017,** *8* (1).

45. Reininger, A. J.; Heijnen, H. F. G.; Schumann, H.; Specht, H. M.; Schramm, W.; Ruggeri, Z. M., Mechanism of platelet adhesion to von Willebrand factor and microparticle formation under high shear stress. *Blood* **2006,** *107* (9), 3537-3545.

46. Maxwell, M. J.; Westein, E.; Nesbitt, W. S.; Giuliano, S.; Dopheide, S. M.; Jackson, S. P., Identification of a 2-stage platelet aggregation process mediating shear-dependent thrombus formation. *Blood* **2007,** *109* (2), 566-576.

47. Lyaker, M. R.; Tulman, D. B.; Dimitrova, G. T.; Pin, R. H.; Papadimos, T. J., Arterial embolism. *Int J Crit Illn Inj Sci* **2013,** *3* (1), 77-87.

48. DeCortin, M. E.; Brass, L. F.; Diamond, S. L., Core and shell platelets of a thrombus: A new microfluidic assay to study mechanics and biochemistry. *Research and Practice in Thrombosis and Haemostasis* **2020,** *4* (7), 1158-1166.

49. Nesbitt, W. S.; Westein, E.; Tovar-Lopez, F. J.; Tolouei, E.; Mitchell, A.; Fu, J.; Carberry, J.; Fouras, A.; Jackson, S. P., A shear gradient-dependent platelet aggregation mechanism drives thrombus formation. *Nature Medicine* **2009,** *15* (6), 665-673.

50. Dubois, C.; Panicot-Dubois, L.; Gainor, J. F.; Furie, B. C.; Furie, B., Thrombin-initiated platelet activation in vivo is vWF independent during thrombus formation in a laser injury model. *J Clin Invest* **2007,** *117* (4), 953-960.

51. Hechler, B.; Nonne, C.; Eckly, A.; Magnenat, S.; Rinckel, J. Y.; Denis, C. V.; Freund, M.; Cazenave, J. P.; Lanza, F.; Gachet, C., Arterial thrombosis: Relevance of a model with two levels of severity assessed by histologic, ultrastructural and functional characterization. *Journal of Thrombosis and Haemostasis* **2010,** *8* (1), 173-184.

52. Muthard, R. W.; Diamond, S. L., Side view thrombosis microfluidic device with controllable wall shear rate and transthrombus pressure gradient. *Lab on a Chip* **2013,** *13* (10), 1883-1891.

53. Tomaiuolo, M.; Matzko, C. N.; Poventud-Fuentes, I.; Weisel, J. W.; Brass, L. F.; Stalker, T. J., Interrelationships between structure and function during the hemostatic

response to injury. *Proceedings of the National Academy of Sciences of the United States of America* **2019,** *116* (6), 2243-2252.

54. Stalker, T. J.; Traxler, E. A.; Wu, J.; Wannemacher, K. M.; Cermignano, S. L.; Voronov, R.; Diamond, S. L.; Brass, L. F., Hierarchical organization in the hemostatic response and its relationship to the platelet-signaling network. *Blood* **2013,** *121* (10), 1875-1885.

55. Shen, J.; Sampietro, S.; Wu, J.; Tang, J.; Gupta, S.; Matzko, C. N.; Tang, C.; Yu, Y.; Brass, L. F.; Zhu, L.; Stalker, T. J., Coordination of platelet agonist signaling during the hemostatic response in vivo. *Blood Advances* **2017,** *1* (27), 2767-2775.

56. Muthard, R. W.; Welsh, J. D.; Brass, L. F.; Diamond, S. L., Fibrin, y'-Fibrinogen, and Transclot Pressure Gradient Control Hemostatic Clot Growth During Human Blood Flow Over a Collagen/Tissue Factor Wound. **2015,** *35* (3), 645-654.

57. Merten, M.; Thiagarajan, P., P-selectin expression on platelets determines size and stability of platelet aggregates. *Circulation* **2000,** *102* (16), 1931-1936.

58. Stalker, T. J.; Welsh, J. D.; Tomaiuolo, M.; Wu, J.; Colace, T. V.; Diamond, S. L.; Brass, L. F., A systems approach to hemostasis: 3. Thrombus consolidation regulates intrathrombus solute transport and local thrombin activity. *Blood* **2014,** *124* (11), 1824-1831.

59. Swieringa, F.; Spronk, H. M. H.; Heemskerk, J. W. M.; van der Meijden, P. E. J., Integrating platelet and coagulation activation in fibrin clot formation. *Research and Practice in Thrombosis and Haemostasis* **2018,** *2* (3), 450-460.

60. Weisel, J. W.; Litvinov, R. I., Fibrin formation, structure and properties. *Sub-Cellular Biochemistry* **2017,** *82*, 405-456.

61. Herbig, B. A.; Yu, X.; Diamond, S. L., Using microfluidic devices to study thrombosis in pathological blood flows. *Biomicrofluidics* **2018,** *12* (4).

62. Hastings, S. M.; Griffin, M. T.; Ku, D. N., Hemodynamic studies of platelet thrombosis using microfluidics. *Platelets* **2017,** *28* (5), 427-433.

63. Montague, S. J.; Lim, Y. J.; Lee, W. M.; Gardiner, E. E., Imaging Platelet Processes and Function—Current and Emerging Approaches for Imaging in vitro and in vivo. *Frontiers in Immunology* **2020,** *11*.

64. De Witt, S. M.; Swieringa, F.; Cavill, R.; Lamers, M. M. E.; Van Kruchten, R.; Mastenbroek, T.; Baaten, C.; Coort, S.; Pugh, N.; Schulz, A.; Scharrer, I.; Jurk, K.; Zieger, B.; Clemetson, K. J.; Farndale, R. W.; Heemskerk, J. W. M.; Cosemans, J. M. E. M., Identification of platelet function defects by multi-parameter assessment of thrombus formation. *Nature Communications* **2014,** *5*.

65. Neeves, K. B.; Maloney, S. F.; Fong, K. P.; Schmaier, A. A.; Kahn, M. L.; Brass, L. F.; Diamond, S. L., Microfluidic focal thrombosis model for measuring murine platelet deposition and stability: PAR4 signaling enhances shear-resistance of platelet aggregates. *Journal of Thrombosis and Haemostasis* **2008,** *6* (12), 2193-2201.

66. Olanrewaju, A.; Beaugrand, M.; Yafia, M.; Juncker, D., Capillary microfluidics in microchannels: From microfluidic networks to capillaric circuits. *Lab on a Chip* **2018,** *18* (16), 2323-2347.

67. Bang, H.; Lee, W. G.; Park, J.; Yun, H.; Lee, J.; Chung, S.; Cho, K.; Chung, C.; Han, D. C.; Chang, J. K., Active sealing for soft polymer microchips: Method and practical applications. *Journal of Micromechanics and Microengineering* **2006,** *16* (4), 708-714.

68. Myers, D. R.; Qiu, Y.; Fay, M. E.; Tennenbaum, M.; Chester, D.; Cuadrado, J.; Sakurai, Y.; Baek, J.; Tran, R.; Ciciliano, J. C.; Ahn, B.; Mannino, R. G.; Bunting, S. T.; Bennett, C.; Briones, M.; Fernandez-Nieves, A.; Smith, M. L.; Brown, A. C.; Sulchek, T.; Lam, W. A., Single-platelet nanomechanics measured by high-throughput cytometry. *Nature Materials* **2017,** *16* (2), 230-235.

69. Vandendries, E. R.; Hamilton, J. R.; Coughlin, S. R.; Furie, B.; Furie, B. C., Par4 is required for platelet thrombus propagation but not fibrin generation in a mouse model of thrombosis. *Proceedings of the National Academy of Sciences* **2007,** *104* (1), 288.

70. Herfs, L.; Swieringa, F.; Jooss, N.; Kozlowski, M.; Heubel-Moenen, F. C. J.; van Oerle, R.; Machiels, P.; Henskens, Y.; Heemskerk, J. W. M., Multiparameter microfluidics assay of thrombus formation reveals increased sensitivity to contraction and antiplatelet agents at physiological temperature. *Thrombosis Research* **2021,** *203*, 46-56.

71. Baker-Groberg, S. M.; Phillips, K. G.; McCarty, O. J. T., Quantification of volume, mass, and density of thrombus formation using brightfield and differential interference contrast microscopy. *Journal of Biomedical Optics* **2013,** *18* (1).

72. Marchese, P.; Lombardi, M.; Mantione, M. E.; Baccellieri, D.; Ferrara, D.; Chiesa, R.; Alfieri, O.; Foglieni, C., Confocal blood flow videomicroscopy of thrombus formation over human arteries and local targeting of p2x7. *International Journal of Molecular Sciences* **2021,** *22* (8).

73. Satoh, H.; Delbridge, L. M. D.; Blatter, L. A.; Bers, D. M., Surface: Volume relationship in cardiac myocytes studied with confocal microscopy and membrane capacitance measurements: Species-dependence and developmental effects. *Biophysical Journal* **1996,** *70* (3), 1494-1504.

74. Hardie, N. A.; MacDonald, G.; Rubel, E. W., A new method for imaging and 3D reconstruction of mammalian cochlea by fluorescent confocal microscopy. *Brain Research* **2004,** *1000* (1-2), 200-210.

75. Boudreau, C.; Wee, T. L.; Duh, Y. R.; Couto, M. P.; Ardakani, K. H.; Brown, C. M., Excitation light dose engineering to reduce photo-bleaching and photo-toxicity. *Scientific Reports* **2016,** *6*.

76. Carlton, P. M.; Boulanger, J.; Kervrann, C.; Sibarita, J. B.; Salamero, J.; Gordon-Messer, S.; Bressan, D.; Haber, J. E.; Haase, S.; Shao, L.; Winoto, L.; Matsuda, A.; Kner, P.; Uzawa, S.; Gustafsson, M.; Kam, Z.; Agard, D. A.; Sedat, J. W., Fast live simultaneous multiwavelength four-dimensional optical microscopy. *Proceedings of the National Academy of Sciences of the United States of America* **2010,** *107* (37), 16016-16022.

77. He, X.; Nguyen, C. V.; Pratap, M.; Zheng, Y.; Wang, Y.; Nisbet, D. R.; Williams, R. J.; Rug, M.; Maier, A. G.; Lee, W. M., Automated Fourier space region-recognition filtering for off-axis digital holographic microscopy. *Biomed Opt Express* **2016,** *7* (8), 3111-3123.

78. Kemper, B.; Von Bally, G., Digital holographic microscopy for live cell applications and technical inspection. *Applied Optics* **2008,** *47* (4), A52-A61.

79. Choi, W.; Fang-Yen, C.; Badizadegan, K.; Oh, S.; Lue, N.; Dasari, R. R.; Feld, M. S., Tomographic phase microscopy. *Nature Methods* **2007,** *4* (9), 717-719.

80. Jin, D.; Zhou, R.; Yaqoob, Z.; So, P. T. C., Tomographic phase microscopy: Principles and applications in bioimaging [Invited]. *Journal of the Optical Society of America B: Optical Physics* **2017,** *34* (5), B64-B77.

81. Kuś, A.; Dudek, M.; Kemper, B.; Kujawińska, M.; Vollmer, A., Tomographic phase microscopy of living three-dimensional cell cultures. *Journal of Biomedical Optics* **2014,** *19* (4).

82. Kim, O. V.; Litvinov, R. I.; Alber, M. S.; Weisel, J. W., Quantitative structural mechanobiology of platelet-driven blood clot contraction. *Nature Communications* **2017,** *8* (1).

83. Jonkman, J.; Brown, C. M., Any way you slice it—A comparison of confocal microscopy techniques. *Journal of Biomolecular Techniques* **2015,** *26* (2), 54-65.

84. Fiolka, R., Clearer view for TIRF and oblique illumination microscopy. *Optics Express* **2016,** *24* (26), 29556-29567.

85. Tokunaga, M.; Imamoto, N.; Sakata-Sogawa, K., Highly inclined thin illumination enables clear single-molecule imaging in cells. *Nature Methods* **2008,** *5* (2), 159-161.

86. Guo, Y.; Li, D.; Zhang, S.; Yang, Y.; Liu, J. J.; Wang, X.; Liu, C.; Milkie, D. E.; Moore, R. P.; Tulu, U. S.; Kiehart, D. P.; Hu, J.; Lippincott-Schwartz, J.; Betzig, E.; Li, D., Visualizing Intracellular Organelle and Cytoskeletal Interactions at Nanoscale Resolution on Millisecond Timescales. *Cell* **2018,** *175* (5), 1430-1442.e17.

87. Van Geffen, J. P.; Brouns, S. L. N.; Batista, J.; McKinney, H.; Kempster, C.; Nagy, M.; Sivapalaratnam, S.; Baaten, C. C. F. M. J.; Bourry, N.; Frontini, M.; Jurk, K.; Krause, M.; Pillitteri, D.; Swieringa, F.; Verdoold, R.; Cavill, R.; Kuijpers, M. J. E.; Ouweh, W. H.; Downes, K.; Heemskerk, J. W. M., High-throughput elucidation of thrombus formation reveals sources of platelet function variability. *Haematologica* **2019,** *104* (6), 1256-1267.

Chapter 4 Coherent Optical Light Scattering and Interferometry (COSI)

In the previous chapters, I have outlined label-free imaging methods using scattered light and interferometry (chapter 1), imaging of single platelets spreading (chapter 2), and thrombus formation under fluid shear (chapter 3). This chapter will detail the experimental efforts to develop a comprehensive label-free imaging system with sufficient resolution to study the morphodynamics of platelets (membrane protrusions) and thrombi. Here, we develop a scattering-based light microscopy for the simultaneous detection of scattered light and reflection interference signals, termed Coherent Optical Scattering and Interferometry (COSI). As the scattering alone does not reveal biochemical signals or volumetric information, we extend the COSI system to accommodate other imaging modalities that can capture fluorescence and volume simultaneously. In the following sections, I shall discuss the following variants of the COSI system we have developed: COSI-F for single platelet migration and COSI-QPM thrombus formation studies.

4.1 Scattering Light Microscopy

Real-time functional imaging of platelets and thrombus is limited by (1) resolution and sample size, (2) imaging speed (rapid activation), (3) labelling methods and efficiency (nucleus free and without transfection, can only rely on membrane dyes for live-cell study), and (4) sample handling (samples are easily activated) [1]. To overcome these limitations, we focus on developing a label-free imaging method such that minimal scanning can provide high-speed imaging. Among the techniques introduced in chapter 1.2, we select darkfield (pure scattering) detection as the base imaging system for platelet membrane protrusion

imaging due to its high contrast (without illumination background). Also, because the darkfield detection collects the scattered light from the cell only, it could recognize the high refractive index components (actin, RI = 1.57 [2]) that contributed to the scattered light.

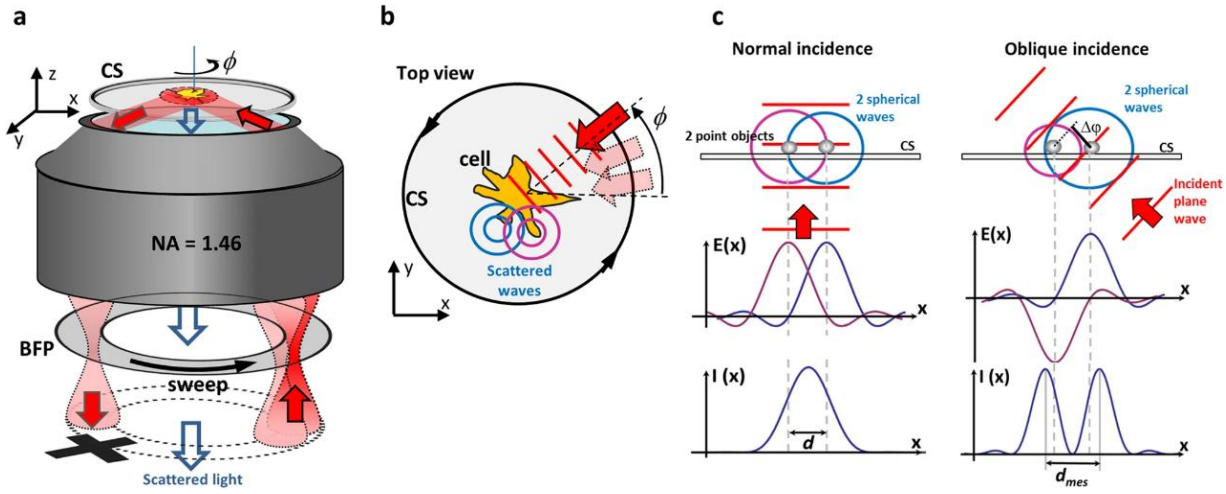

Figure 4-1 Experimental setup and imaging principle of ROCS microscopy. (A) The laser beam is focused and scanned along a circle in the back focal plane of the objective, introducing total internal reflection (TIR) illumination of the sample. The reflected beam at the coverslip is blocked by a diaphragm enabling darkfield detection. (B) Top view showing the azimuthal scanning pattern in the x-y plane. (C) The resolution enhancement of two adjacent scatterers using oblique illumination and constructive interference. This figure is reprinted with permission from Junger *et al*. [3] © 2016 Springer Nature.

A recently developed darkfield detection method, rotational optical coherent scattering microscopy (ROCS), takes advantage of a high N.A. objective lens (N.A. >1.33) and a coherent laser source for high-resolution live-cell imaging [3-7]. In ROCS microscopy, the laser beam is projected at the total internal reflection (TIR, ≈ 70°) [4] or highly inclined thin illumination (HILO, ≈ 56°) [6] angle and circularly scanned around the optical axis (in Fig. 4-1 A). The illumination reflects from the coverslip at the glass-water interface and is blocked by a diaphragm at the Fourier plane, only allowing the pure scattering to be collected at the detector, enabling darkfield detection. The coherent oblique illumination enhances imaging resolution because the scattered light from adjacent scatterers induces a phase delay ($\Delta\varphi \approx \pi$) and can be resolved by constructive interference [3] (Fig. 4-1 C).

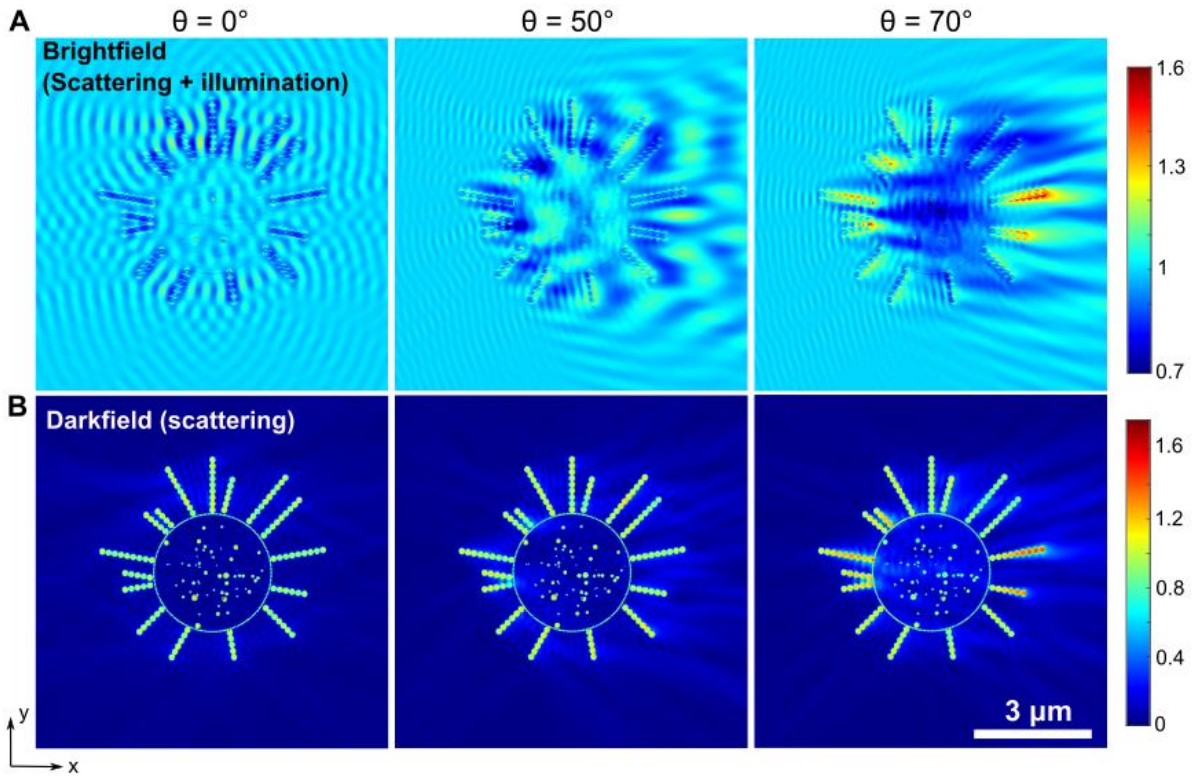

Figure 4-2 Simulation of the (A) brightfield and (B) darkfield intensity of the cell model at three different oblique illumination angles (θ = 0°, 50°, 70° respectively) in the x-y plane. The simulation is performed using CELES [8], the brightfield refers to the interference signal of scattered light and illumination, and the darkfield refers to the scattered light only. All the images are simulated at a fixed azimuthal angle (ϕ=0°) with the illumination is projected on the z-axis.

ROCS collects the scattered light under oblique (HiLO or TIR) illumination, which could alter the scattering field based on simulation results from Mie theory as shown in Fig. 1-4 (the difference in magnitude of scattered light in forward and backward direction). Here, Fig. 4-2 shows how the scattering field would vary when the cell is illuminated under oblique angles (θ = 0°, 50° and 70° respectively) using the model introduced in chapter 1.1.3. The brightfield (interference of scattered light and illumination) and darkfield detections (pure scattered light) are shown in Fig. 4-2 A and B, respectively. In our model, we identify that oblique angle could influence detection sensitivity. In Fig. 4-2, we show that by changing the oblique angle from 0° to 70°, the scattering signal increase by about 40%, allowing the observation of scattering signal from membrane protrusions (resembling filopodia). However,

without azimuthal scanning, we observe imaging artefacts arising from uneven intensity distribution and the presence of background signal are shown to be more severe for brightfield detection.

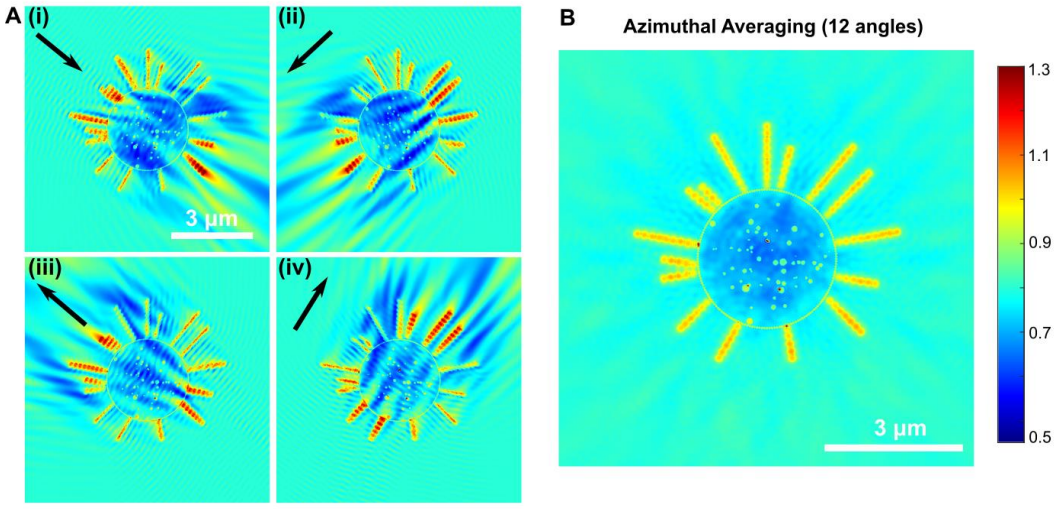

Figure 4-3 Simulation of the (A) brightfield of the cell model at four different azimuthal illumination angles (with fixed oblique angle θ = 70°) in the x-y plane. (B) Summing and averaging of the brightfield signal from 12 azimuthal angles from 0 to 2π. The simulation is performed using CELES [8]. The brightfield refers to the interference signal of scattered light and illumination.

The azimuthal averaging is introduced to remove the imaging artifacts from the oblique illumination. In this method, a series of images are captured at one scanning cycle covering a 2π azimuthal angle and averaged by acquisition time. Azimuthal averaging has been used in several microscopy methods such as TIRF [9-11] and glazing incidence structured illumination (GI-SIM) [12] to remove imaging artifacts from oblique illumination. To demonstrate the effectiveness of the method, we show the simulation results of the brightfield detection at four different azimuthal angles (φ = 60°, 150°, 240°, and 330° respectively) in Fig. 4-3 A. The black arrow demonstrates the direction of azimuthal angles (oblique illumination θ = 70°). In Fig. 4-3 B, we sum and average the electric field at 12 azimuthal

angles (in a 2π cycle) and show that the imaging artifacts and uneven intensity distribution could be corrected.

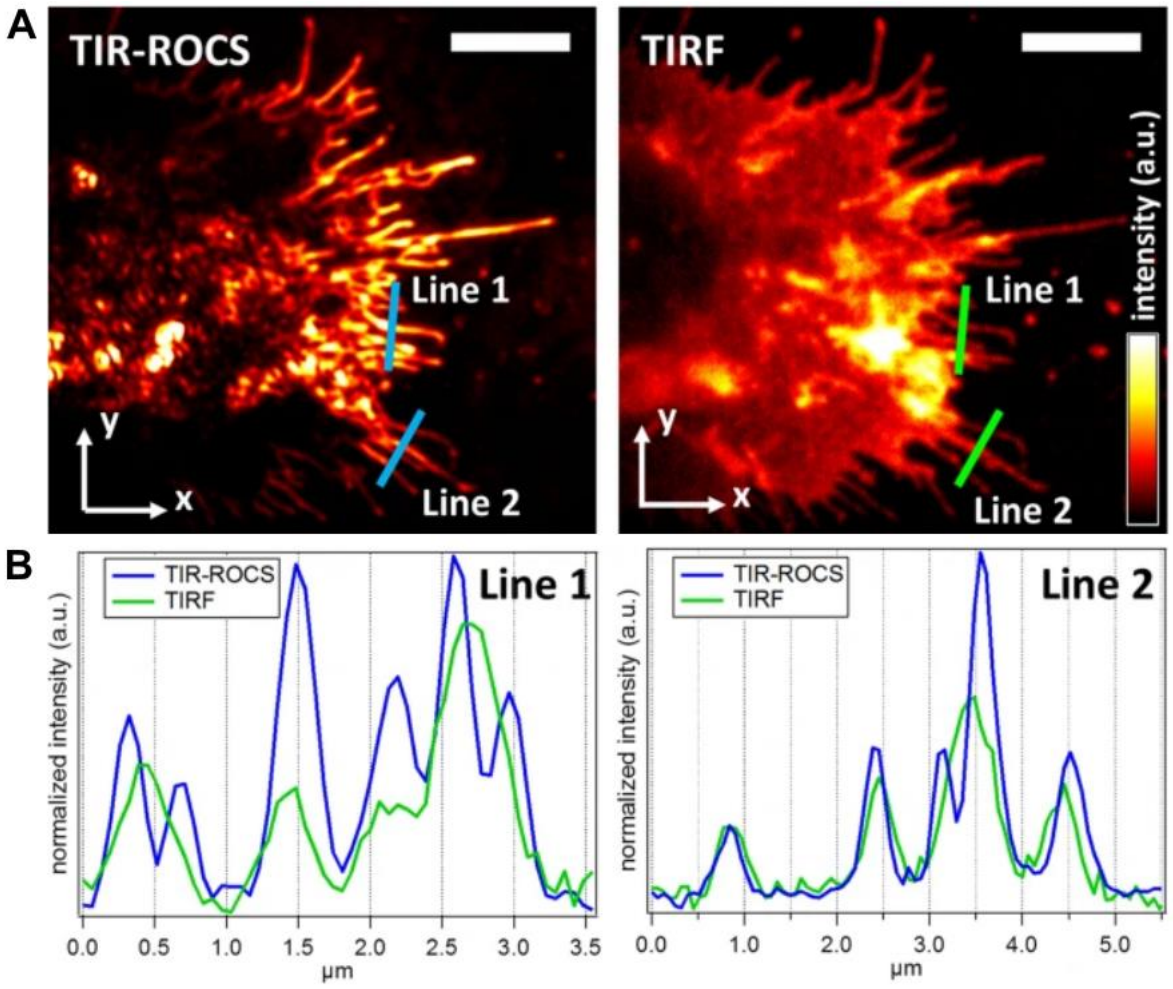

Figure 4-4 (A) Images from ROCS microscopy show the scattered light and fluorescence signal of a living mouse-macrophage. The scattering signal is captured with a 488 nm laser at 20 ms exposure. The fluorescence signal is from a membrane dye (WGA-staining) and captured at 5 seconds exposure. Both images were taken at TIR angle. (B) Comparison of the intensities along with line profiles as indicated in (A). This figure is reprinted with permission from Junger *et al.* [3] © 2016 Springer Nature.

ROCS microscopy has shown superior imaging contrast in live-cell imaging, as demonstrated in Fig. 4-4 A, where both the scattering and fluorescence signal of a macrophage (~ 20 μm) at TIR illumination are compared for the same field of view [4, 5]. Junger *et al.* [3] has shown that the scattered light from ROCS provides significantly higher contrast and resolution than the fluorescence signal, especially for tiny structures, e.g. the

branches of filopodia (Fig. 4-4 B). This is consistent with our numerical model. The ability for ROCS to pick up weak signals from fine structures could provide opportunities in platelet imaging for membrane protrusion studies. However, ROCS has not been used in imaging highly motile cells with smaller sizes (platelets, ~ 3-6 μm).

In the following section, I shall detail our efforts in developing the label-free imaging system by tailoring the ROCS microscopy for platelet imaging. I will introduce the steps taken to build the setup and the modifications to expand imaging modalities for platelet and thrombus imaging.

4.2 Coherent Optical Scattering and Interferometry (COSI)

This section will explain the design, selection of optical components, and control system of the imaging system we build for platelets and thrombus imaging based on the ROCS microscopy. Coherent Optical Scattering and Interferometry (COSI) is developed to integrate interferometric imaging with ROCS. As explained earlier, the resolution enhancement from ROCS microscopy is generated from the interference of the coherently scattered light. In the first part of the section, I shall demonstrate the effect of spatial coherence of the laser source in scattering signal detection. I will then discuss the reflection optics chosen for reflection-based microscopy to avoid unwanted reflection. After that, I will explain the objective selection and illumination angle calibration for the COSI system. In the last part, I will explain the steps to design the control system that synchronizes the galvanometer mirror and detection camera for azimuthal scanning.

4.2.1 Optics

4.2.1.1 Spatial coherence of the laser source

Understanding and quantifying the spatial coherence of the illumination are critical to the selection of the light source for the imaging system. Traditional microscopy methods (darkfield and RICM) use a broadband source (e.g. halogen lamp) with lower spatial coherence than a laser source used in ROCS. Here, we test how the spatial coherence of the light source could affect imaging resolution. To vary the spatial coherence of the illumination, we place a rotational diffuser (LSR-3005, Optotune) after the laser source. Before we conduct imaging, we test the fringe visibility [13] with and without the diffuser by a double-slit experiment. Fig. 4-5 A shows the fringes produced by the double split. Significantly disrupted fringes are observed when adding the diffuser into the system, with the fringe visibility reduced from 0.95 to 0.14 (from Eq. 4.1).

$$V = \frac{I_{max} - I_{min}}{I_{max} + I_{min}} \tag{4.1}$$

In Fig. 4-5 B, we demonstrate the scattered light from adjacent 200 nm (in diameter) polystyrene beads when using high (V=0.95) and low (V=0.14) coherence sources. We observe that the signal to noise (SNR) ratio is reduced by 30% with the lower coherence, and the adjacent beads cannot be resolved, indicating lower imaging resolution. Similar phenomenons are also observed in ROCS microscopy [4]. Therefore, compared with the traditional darkfield microscopy that uses a low coherence light source (halogen lamp), the laser source in the ROCS and COSI system could enhance imaging resolution.

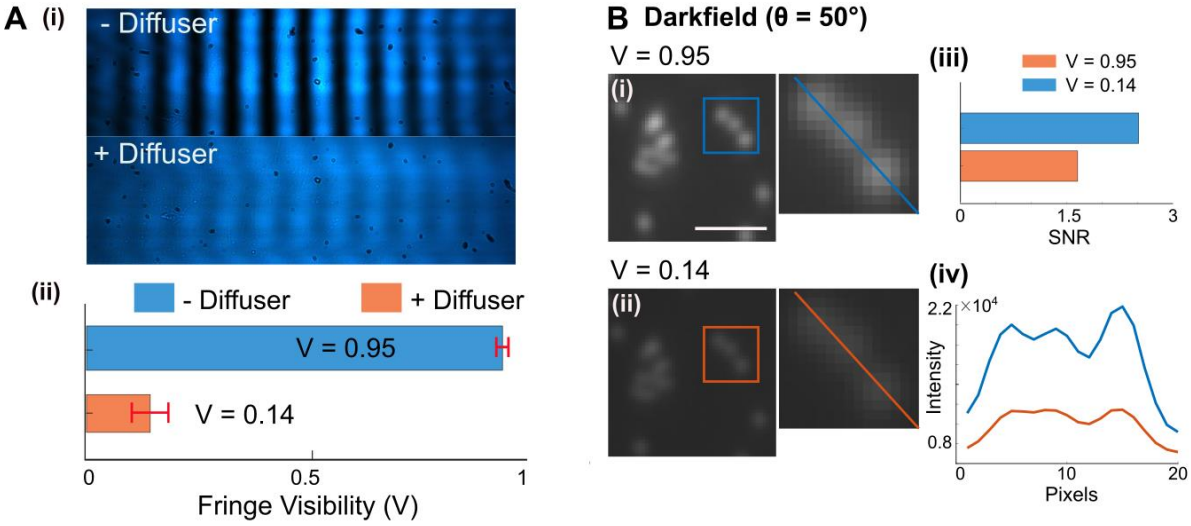

Figure 4-5 (A) (i) Fringe visibility of a laser source with/without adding the rotational diffuser. The fringes are captured by placing a customized double slit at the Fourier plane after the diffuser. The camera is placed about 0.8 meters away from the double slit. (ii) Plot of the visibility of the fringes with/without the diffuser (B) Scattering detection of 200 nanometre polystyrene particles (ii) with and (i) without adding the diffuser. The SNR and intensity across three adjacent beads are plotted in (iii) and (iv). Scale bar = 1 μm

4.2.1.2 Parasitic reflection from optical train

The background intensity in reflection-based microscopy methods is critical for high sensitivity detection because the magnitude of the background can significantly influence the SNR ratio. Theoretically, the background intensity originates from the back-reflected light from the coverslip (oil-medium interference). However, unwanted signals such as reflections from optics might also contribute to background intensity. In RICM, the unwanted reflection is filtered using polarization optics and an Antiflex objective that only allows collection of reflection from the coverslip, which could improve imaging contrast and optimize background intensity [14]. However, to incorporate reflectance interference in a ROCS system, it is crucial to remove parasitic reflectance surfaces.

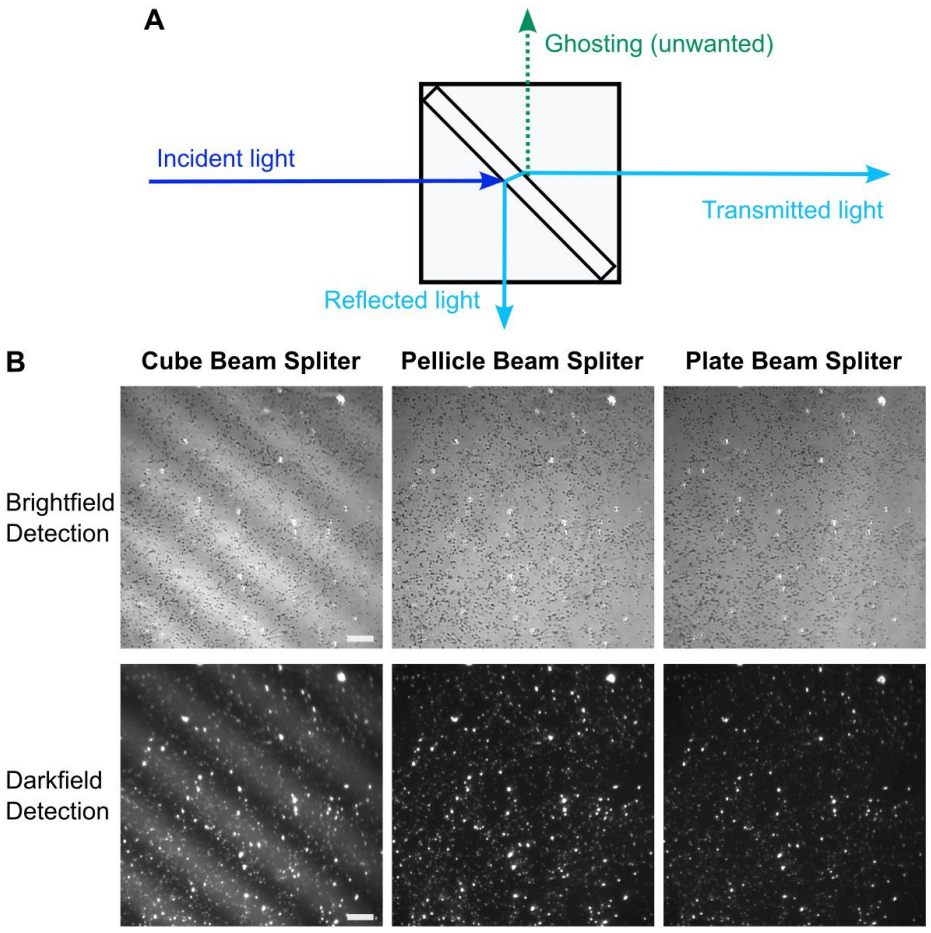

Figure 4-6 (A) Illustration of ghosting reflection caused by cube beam splitter. (B) Brightfield and scattering images of 40 nanometer gold nanoparticles with three different types of beam splitters (cube, pellicle, and plate) are shown. The brightfield and scattering images are taken at an oblique angle of 22° and 60°, respectively. The splitting ratio of the cube and plate beam splitter is the same 50:50 (R:T), and the splitting ratio of the pellicle beam splitter is 45:55 (R:T). Scale bar = 5 μm.

Here, we test different types of beam splitters because we identify ghosting reflections that could affect the scattering detection. A similar problem is identified and reported in the iSCAT techniques [15]. Ghosting reflection refers to the unwanted light reflection to the orthogonal direction that possibly caused by surface coating and thickness of the beam splitter as illustrated in Fig 4-6 A. Three types of beam splitters are tested that showed the effect of ghosting: cube (BS013, Thorlabs), plate (BSW10R, Thorlabs), and pellicle (BP145B1, Thorlabs) at different illumination angles (22° and 60°) in Fig. 4-6 B. Other optics in the imaging system remain the same, and only the beam splitter was changed out for

testing. When using a cube beam splitter, inclined fringes (showing as dark and light bands) that results from the interference of ghosting reflection and scattered signal are observed in both brightfield and darkfield detection. However, no interference artifacts are observed with the pellicle and platelet beam splitter, indicating that ghosting is minimal in both cases. Therefore, in reflection-based imaging techniques, a plate or pellicle beam splitter is recommended to avoid ghost reflection when detecting scattering signals.

4.2.1.3 Objective

In darkfield detection, a minimum N.A. of 1.45 of the detection objective is typically required to reach TIR illumination [16]. Here, we use a 60X 1.49 N.A. (APON60XOTIRF, Olympus) in the COSI system to access the full illumination range from HILO to TIR. However, an objective with lower N.A. can also be adopted for darkfield detection under oblique illumination if the reflected circular pattern can be blocked by the diaphragm at the Fourier plane. We also tested a 60X 1.42 NA (PLAPON60XO, Olympus) in the imaging system, which could reach a maximum oblique angle of around 60°, allowing detection of scattered light at HiLO illumination. In interference detection, the reflected light is collected at a lower illumination angle (~20°), which means an objective with lower N.A. could be used for standalone interference detection.

4.2.2 Illumination Angle

To calibrate the illumination angle, we first generate a circular scanning pattern at the back focal plane of the objective. We then relay the BFP of the objective to a CCD with a 4f configuration and capture the light being reflected from the coverslip to visualize the scanning pattern. By varying the voltage applied to the galvanometer mirror, a circular ring with a different radius (indicating the scanning pattern) is expected. The brightness of the

ring shows the amount of light being reflected. In Fig. 4-7 A-B, we demonstrate the maximum intensity projection of the scanning pattern at different galvanometer voltages for an oil-air and oil-water interface, respectively. The sudden jump in reflected intensity indicates the critical angle where total internal reflection (TIR) is reached [17]. As the oil-water interface has a less significant refractive index difference, the critical angle is larger ($\theta_{critical}$ = 61.4°) than the oil-air interface ($\theta_{critical}$ =41.2°), and a higher voltage (larger ring) is needed to reach TIR illumination Fig. 4-7 B.

$$\theta_{critical} = \arcsin\left(\frac{n_2}{n_1}\right) \tag{5.1}$$

To calibrate the galvanometer voltage and illumination angle, we measure the radius of the scan pattern on the CCD at corresponding voltages as shown in Fig. 4-7 C. We then calculate that the theoretical maximum angle with the objective using Eq. 5.2 (θ_{max} =78.98°). By substituting the calculated critical angle, maximum angle, and the measured scan radius, into Eq. 5.3, the illumination angle θ can be estimated [11, 17]. The relation of the scan radius and illumination angle is plotted in Fig. 4-7 D.

$$\theta_{maximum} = \arcsin\left(\frac{NA}{n_2}\right) \tag{5.2}$$

$$r = f_{obj} n_1 sin\theta \tag{5.3}$$

After the illumination angle is determined, the aperture of the diaphragm is fixed to filter out the reflected light from the coverglass under HiLO and TIRF angles. Because the diaphragm blocks the back focal plane of the objective and reduces detection N.A., the aperture is set at the maximal position at detection N.A. = 1.27 (illumination angle = 57°). The imaging depth at various illumination angles is also measured and can be found in Appendix C.

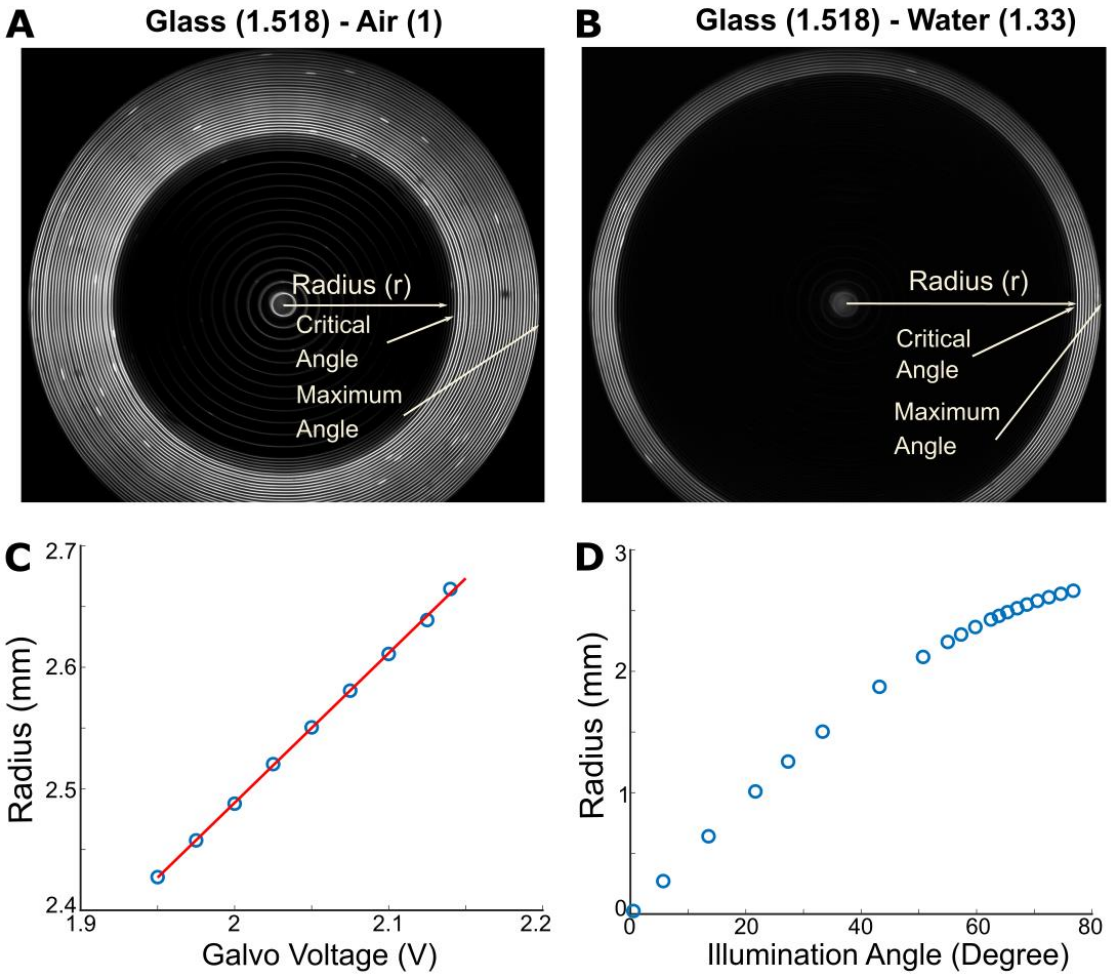

Figure 4-7 Calibrating the illumination angle of the oblique beam by visualizing the reflected beam at the Fourier plane using a separate CCD camera. The reflected beam at (A) the glass to water interface and (B) the glass to water interface with a camera at the conjugate plane of the back focal plane. Total internal reflection is reached when a sudden jump in intensity is presented. The scanning radius is measured for angle calibration. (C) Plot showing the linear relation between galvanometer voltage and scanning radius (D) Calculated illumination angle at different scanning radius.

4.2.3 Optoelectronic Control

The control system is designed to synchronize the capture rate of the sCOMS (PCO edge 4.2) and the scanning frequency of the galvanometer mirror. We develop a customised user interface (UI) written in MATLAB, as shown in Fig. 4-8 A, where we can generate continuous sinusoidal waveforms for rotation scanning. The signal generated is then sent to

the data acquisition card (PCIe-6374, National Instrument) that outputs voltages for galvanometer scanning (analogue output) and triggers the camera acquisition (Fig. 4-8 B).

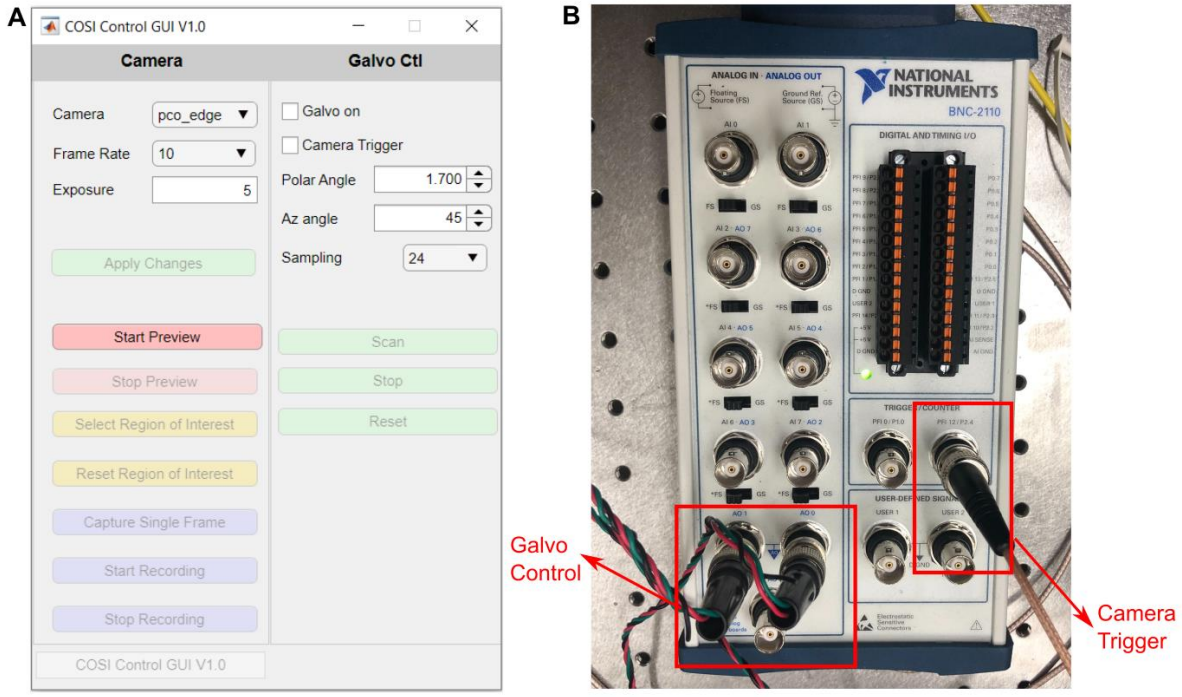

Figure 4-8 (A) Customized graphic user interface (GUI) for COSI control system, designed using MATLAB. (B) Image of the NI controller for synchronizing the galvanometer scanning and camera triggering.

The scan radius of the scanning pattern is determined by the sinusoidal (sine or cosine) wavefront amplitude. A 5V TTL signal is generated simultaneously to trigger camera capture, where the acquisition begins when the rising edge is detected and stops when the falling edge is identified (Fig. 4-9). The sinusoidal signal is generated at 300 Hz (24 data points for each azimuthal scan) for a camera acquisition rate of 30 Hz. One trigger can include up to 10 scanning cycles, and the duty cycle of the trigger signal determines the exposure time of the camera. The MATLAB code for controlling the galvanometer and camera can be found in Appendix D.

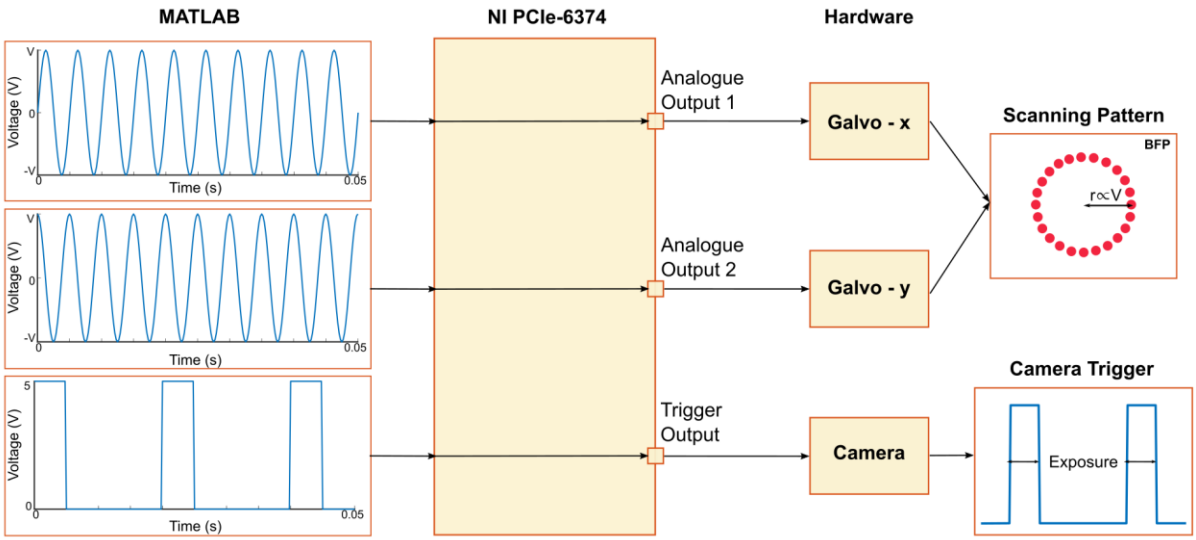

Figure 4-9 Block diagram showing the working principle of the control system. The sin sinusoids are generated, giving output to the two-axis galvanometer mirror for the radical scanning pattern, with V controlling the scanning radius at the back focal plane. A 5V TTL triggers the camera capture, where the duty cycle of the TTL controls the exposure of the camera.

4.2.4 COSI Setup

The COSI imaging system is constructed on an inverted microscopy platform (RAMM, ASI) using a linearly polarized 488 nm laser (Stradus 488-150), as shown in Fig. 4-10. A two-axis galvanometer mirror (GVS212/M, Thorlabs) is conjugated to the imaging plane of the system so that the laser beam is focused on the back focal plane of the objective lens (Olympus, 60X, NA 1.49, oil immersion) to allow for wide-field illumination. The scattering signal and the back reflection from the coverslip are separated from the illumination using a 50/50 plate beam splitter (BSW10R, Thorlabs) and further magnified with a beam expander (around 1.33 time) before being collected by an sCOMS (PCO edge 4.2). A diaphragm is placed at the conjugate plane of the BFP to block the reflected beam from the coverslip. To achieve oblique illumination and azimuthal averaging, the galvanometer mirror azimuthally scans around the optical axis at the back focal plane of the objective (the scan pattern is shown in the inset image in Fig. 4-10 A). We also synchronize

the capture rate of the sCOMS and the scanning frequency with a data acquisition card (PCIe-6374, National Instrument) so that one full cycle of azimuthal scan can be captured and averaged simultaneously.

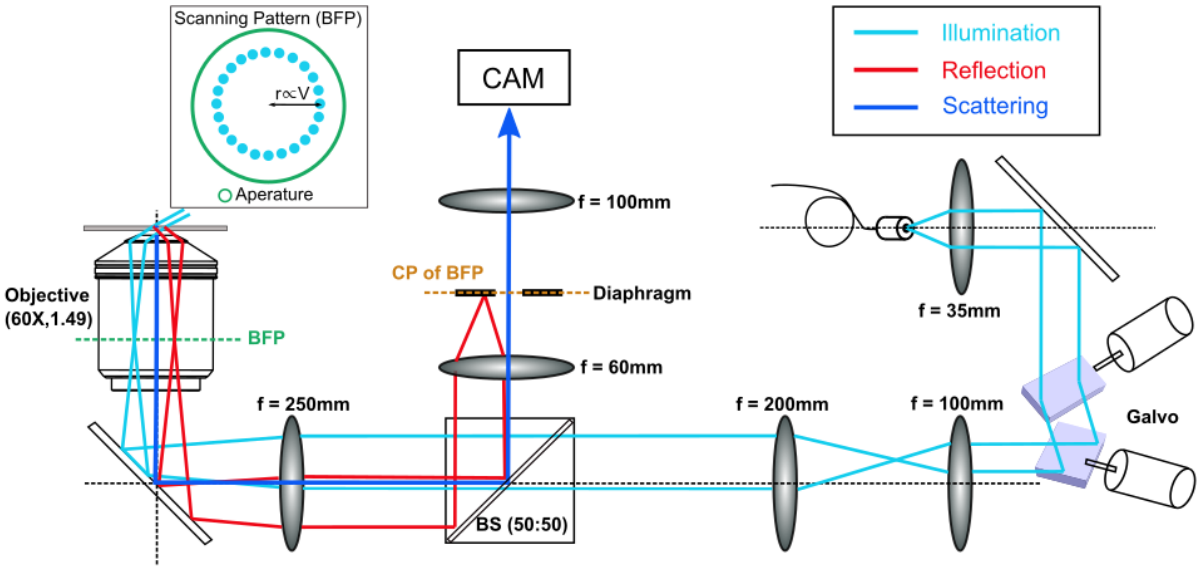

Figure 4-10 Imaging setup of the COSI system. The colours represent the beam of illumination, reflection and scattering as indicated in the legend. The diaphragm is placed at the conjugate plane (CP) of the back focal plane (BFP) of the objective, enabling scattering and interference detection based on oblique illumination angle.

Apart from the darkfield detection at HILO and TIRF angles, we collect the interference signal of reflected light and scattered light at a lower illumination angle (<50°), the interference component could be used to enhance imaging contrast and sensitivity. The interference detection has not been studied previously, and it is the main difference between COSI and ROCS microscopy.

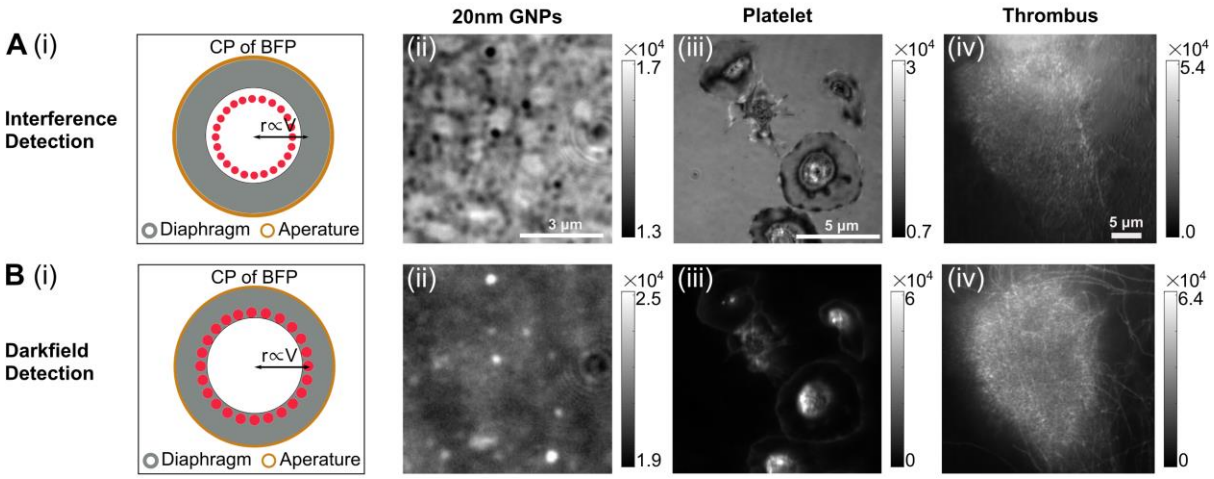

Figure 4-11 Switching between interference and darkfield detection while fixing the aperture of the diaphragm at the conjugate plane (CP) of the back focal plane (BFP) of the objective. (A) The reflected beam is passed and interfered with the scattered light at a lower illumination angle resulting in interference detection. (B) The reflected beam is blocked when the laser is illuminating at HILO or TIRF angles, enabling darkfield detection. Images of 20 nm GNPs, activated platelets, and a thrombus at two detection schemes are shown for comparison.

The concept of this imaging method is illustrated in Fig. 4-11. By increasing the oblique illumination angle, the radius of the scanning pattern increases. Therefore, promoting two detection schemes with a diaphragm at a fixed aperture: interference detection (back-reflection passes through the diaphragm) and darkfield detection (the diaphragm blocks back-reflection). We term this method as Coherent Optical Scattering and Interferometry (COSI) because it uses pure scattered light and interference signals to enhance contrast. Here, we show samples at three different size scales: 20 nm GNPs, single platelets (~5 μm), and a thrombus (~30 μm) in Fig. 4-11. For weakly scattered samples (20 nm GNP, scattering cross-section ~ 1.32 nm^2), we observe that interference detection offers better imaging contrast from destructive interference. The bright-dark contrast from the interference signal in platelet imaging also provides rich axial information. In contrast, scattering detection shows better imaging contrast for samples at a larger scale or with high scattering intensity, as shown in

Fig. 4-11 (iv). Details of imaging contrast and sensitivity (in lateral and axial detection) will be further compared and discussed in Chapter 6.

4.3 Variants of COSI System

The COSI system achieves scattering and interference detection together, and both enable high contrast morphological profiling of single platelets and access to axial information. However, one of the limitations is the lack of capability to study biochemical signalling during platelet adhesion and activation. Therefore, we adopt dual-camera detection to address this limitation to capture the fluorescence signal simultaneously. We name this variant of the COSI system as **C**oherent **O**ptical **S**cattering, **I**nterference and **F**luorescence (COSI-F) microscopy. As the detection path is separated from the scattering/interference detection, the numerical aperture of the fluorescence signal will not be blocked by the diaphragm, allowing high contrast fluorescence imaging at HILO and TIRF angles.

In addition to COSI-F, we integrated an additional volume/dry mass mapping imaging tool to study thrombus stability. We adopt QPM to monitor the detachment of platelet or platelet aggregates during the embolization test while the COSI system captures the motility of the adhesive platelet at the thrombus core. The integrated system is termed **C**oherent **O**ptical **S**cattering, **I**nterference and **Q**uantitative **P**hase **M**icroscopy (COSI-QPM). In this section, I shall introduce the setups of the two variants of the COSI system and how these imaging systems are used for platelet and thrombus imaging.

4.3.1 COSI - F

Reflection interference contrast microscopy (RICM) is a method that is well used to study membrane interactions with the ECM. It has been combined with fluorescence microscopy for investigating the role of integrin or membrane receptors in actin

polymerization [18], cell migration [19], and immune responses [20]. The combination of RICM (or iSCAT) with fluorescence microscopy (TIRF) is typically done using two separate illumination sources and with complicated optics (Antiflex objective) [21, 22]. To ease the requirement of additional optics and illuminations, we can integrate the interference detection with fluorescence signal in the COSI system by adding a dichroic mirror and a camera. The interference detection in COSI shares the same imaging concepts as the traditional RICM. However, using a laser source will provide higher detection sensitivity while the scanning process eliminates the speckle noise.

The COSI-F system integrates the fluorescence signal into the COSI system by separating the scattered light and fluorescence using a dichroic mirror (FF505-SDi01-25x36, Semrock) and a CCD (Retiga 4000R, QImaging) for detection (Fig. 4-12). With the excitation laser at 488nm, COSI is suitable for detecting green fluorescent (emission wavelength > 510 nm), for example, Alexa Fluor 488, Oregon green and green fluorescent protein (GFP). The dual camera detection separates the scattering and fluorescence detections, retaining the maximum detection N.A. of the fluorescence signal. The CCD is directly placed after the tube lens and the dichroic mirror without a beam expander to preserve the maximum fluorescence signal. However, the trend-off here is the lower magnification (83 X) compared with the scattering /interference detection (~138 X). To achieve simultaneous detection of interference, pure scattering and fluorescence signal, the galvanometer mirror is switched between two voltages, producing azimuthal scanning patterns at two oblique angles: 22° and 60°. The detection camera is synchronized and captures the interference and scattering signal at 22° and 60°, respectively. The fluorescence signal is always collected at 60° (HILO) for maximum imaging contrast (quantifications of imaging contrast are shown in Chapter 6).

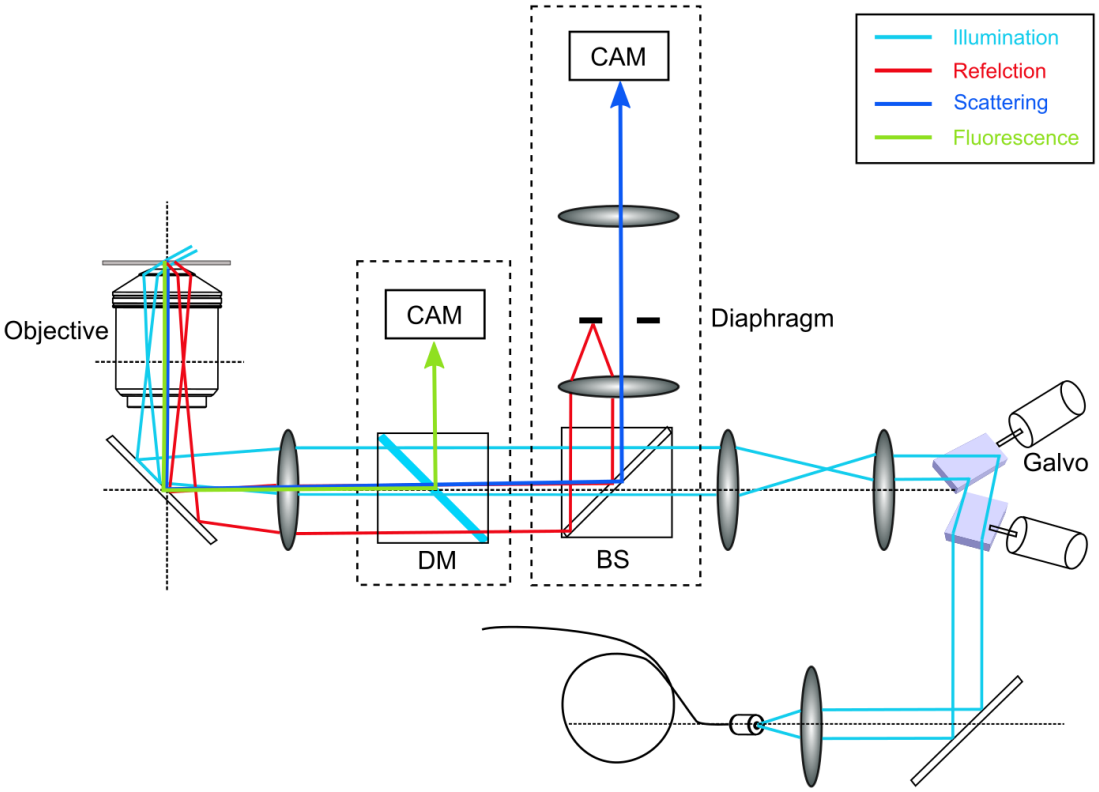

Figure 4-12 Imaging setup of the COSI-F system. The colours represent the beam of illumination, reflection, fluorescence, and scattering indicated in the legend. An additional camera and a short-pass dichromic mirror are added for simultaneous fluorescence detection to enable the COSI-F setup.

Chapter 6 will further explore the detection sensitivity of scattering, interference, and fluorescence signals. Because the detection schemes of COSI-F depend on the oblique angle of the scanning pattern, the effects of angle in imaging sensitivity and imaging contrast will also be discussed. The second part of chapter 6 demonstrates high contrast multiplex imaging that quantifies filopodia and lamellipodium formation, surface interaction (scavenging fibrin(ogen) coating) and morphological profiling of the migrating platelets.

4.3.2 COSI – QPM

As explained in chapter 3.4.2, most thrombus stability studies use volumetric imaging approaches to monitor the total volume or dry mass of the thrombus over time during embolization. Volumetric imaging is normally done using 3D fluorescence microscopy or

quantitative phase microscopy (QPM). The volumetric information is quantified by the total fluorescence counts in fluorescence-based approaches. In contrast, QPM works by measuring the phase delay of the light (due to change in refractive index) when passing through the sample (principles of QPM is in Appendix B). For most of the biological cells, the change in refractive index corresponds to a linear increase in dry biomass (proteins and nucleic acids without water) that falls within a very narrow range of approximately $\alpha = 1.8 \times 10^{-4}$ m^3/kg (= 0.18 $\mu m^3/pg$) [23, 24]. Therefore, QPM can be a reliable method to retrieve the dry mass of biological samples compared with fluorescence-based approaches because photobleaching is not a limiting factor.

However, the limitation of these volumetric studies is that none of them selectively focus on thrombus core [25, 26]. With the COSI system, we could alter the depth of the imaging field by adjusting the illumination angle to collect the signal from the thrombus core only (~4 μm that covers the thickness of collagen fibre and a few layers of adhesive platelets). Therefore, we combined the COSI imaging system with a QPM setup to comprehensively study thrombus stability under flow shear.

The COSI system is built on a QPM system previously developed by Dr Xuefei He [25]. To integrate QPM into the COSI system, a 632.8 nm HeNe laser (HeNe laser, TEM_{00} mode, JDS Uniphase, 1144p-3581) is split into two arms by a standard dual fibre splitter: one passing through a series of optics (reference arm) and one pass through the sample (object arm). Two illuminating beams share the same microscope objective (Olympus, 60X, NA 1.49, oil immersion). The object arm is focused onto the back focal plane (BFP) of a transmission objective (10X, air) to ensure the illumination beams approximate idea plane waves as much as possible once they reach the sample plane (Fig. 4-13). The reference and object arm are then re-combined by a 50/50 beamsplitter (Thorlabs, BS013) to form the interference pattern

that is digitally recorded with an sCMOS camera (Thorlabs Quantalux CS2100M-USB). The intensity of the transmitted beam through the sample is adjusted using natural density filters (Thorlabs NEK02) so that it reaches nearly equal intensity to the reference beam.

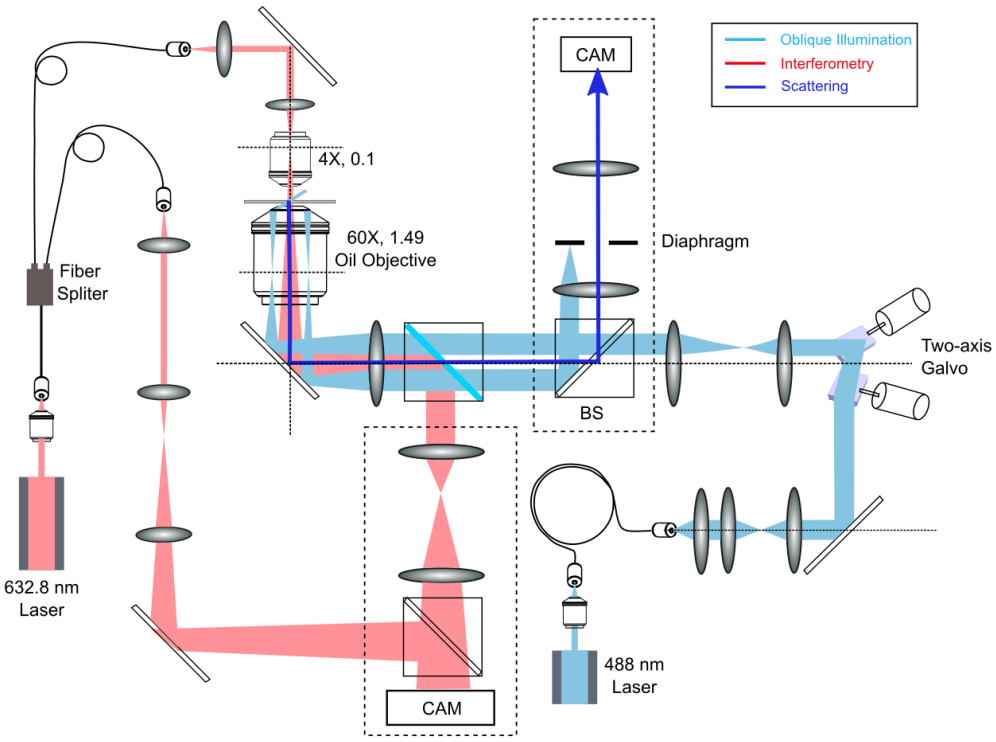

Figure 4-13 The imaging setup of the COSI-QPM setup. A separate illumination (red) is added to enable off-axis interferometry.

Chapter 7 will describe how we use the COSI-QPM system to study thrombus stability by tracing the adhesive platelet activity and the total thrombus mass. The formed thrombus contracts under high shear forces and can shed emboli of various sizes. Monitoring dry mass variation of the thrombus during embolization quantifies the number and size of the emboli, while the activity of the adhesive platelets indicates the adhesiveness (or motility) of the thrombus core. By combining the spatial-temporal information of activity and mass variation of a developing thrombus under (patho)physiological shear rates, we evaluate thrombus stability with the impact of a metalloproteinase inhibitor.

4.4. Conclusion

In this chapter, I have explained the rationale and steps we have taken to build the label-free imaging system based on rotational optical coherent scattering (ROCS) microscopy. ROCS microscopy produces a circular scanning pattern and collects the pure scattered light by blocking the reflected light at the Fourier plane. To understand the scattering properties of the biological samples with this illumination method, we use the cell model built in chapter 1 to test scattering intensity using oblique illumination and azimuthal scanning.

In the second part of this chapter, I explain how we build the COSI system and how the system is different from ROCS microscopy. I start by introducing the key optical elements (laser, beam splitter, and objective) that would influence the optical resolution and imaging artefacts by demonstrating the effect of spatial coherence of the illumination source and the performance of three types of beam splitters. I then discuss how we control the galvanometer mirror using a DAQ card for scanning and methods to calibrate the oblique angle by recording the reflected pattern at the BFP of the objective. With the selection of optical components and the designed control system, I describe the COSI setup with two distinct detection schemes: interference (of the reflected beam and scattered light) and scattering (pure scattered light). These two detection schemes can be easily switched by changing the oblique illumination angle, with 5°-50° to be interference detection and >55° to be scattering detection. The interference detection is an add-on compared with the ROCS microscopy, and it shares the same imaging principle with RICM. However, unlike RICM requires the Antiflex objective, the implementation of COSI in any laser scanning system is straightforward because the scanning pattern is the key element.

The limitation of the COSI system is that it cannot support investigations in biochemical signalling or volumetric imaging. The former prevents the study of integrin or

membrane receptors during platelet adhesion and activation while the latter restricts the study on thrombus stability. Therefore, in the last part of the chapter, I introduce two variants of the COSI system: COSI-F and COSI-QPM for comprehensive functional imaging of single platelet and thrombus.

The COSI-F system integrates fluorescence (epi, HILO and TIRF), interference, and scattering detection using a single objective, single illumination scheme. Chapter 6 will first compare the imaging contrast and sensitivity between three modalities using nanoparticles ranging from 20 nm to 100 nm. The high contrast imaging and axial fluctuations of membrane ruffles will also be demonstrated during platelets migration and scavenging fibrin fibres. The COSI-QPM system integrates a QPM into the COSI system, providing extra information on the adhesiveness of the thrombus core. Chapter 7 will show how we use this system to study thrombus stability with the effect of the metalloproteinase inhibitor that inhibits the shedding of membrane ligands.

4.5 Contribution

Dr Xuefei He initially developed the QPM system. I integrated the QPM setup into the COSI system with some modifications to the original setup. I performed the simulation on the scattering field of the cell model (in section 4.1) using the CELES software [8] with minor modifications to the code.

4.6 References

1. Sadoul, K.; Lafanechère, L.; Grichine, A., Live imaging of single platelets at work. *Platelets* **2020,** *31* (5), 551-558.

2. Bon, P.; Lécart, S.; Fort, E.; Lévêque-Fort, S., Fast label-free cytoskeletal network imaging in living mammalian cells. *Biophysical Journal* **2014,** *106* (8), 1588-1595.

3. Jünger, F.; Olshausen, P. V.; Rohrbach, A., Fast, label-free super-resolution live-cell imaging using rotating coherent scattering (ROCS) microscopy. *Scientific Reports* **2016,** *6*.

4. Ruh, D.; Mutschler, J.; Michelbach, M.; Rohrbach, A., Superior contrast and resolution by image formation in rotating coherent scattering (ROCS) microscopy. *Optica* **2018,** *5* (11), 1371-1381.

5. Jünger, F.; Rohrbach, A., Strong cytoskeleton activity on millisecond timescales upon particle binding revealed by ROCS microscopy. *Cytoskeleton* **2018,** *75* (9), 410-424.

6. Koch, M. D.; Rohrbach, A., Label-free Imaging and Bending Analysis of Microtubules by ROCS Microscopy and Optical Trapping. *Biophysical Journal* **2018,** *114* (1), 168-177.

7. Von Olshausen, P.; Rohrbach, A., Coherent total internal reflection dark-field microscopy: Label-free imaging beyond the diffraction limit. *Optics Letters* **2013,** *38* (20), 4066-4069.

8. Egel, A.; Pattelli, L.; Mazzamuto, G.; Wiersma, D. S.; Lemmer, U., CELES: CUDA-accelerated simulation of electromagnetic scattering by large ensembles of spheres. *Journal of Quantitative Spectroscopy and Radiative Transfer* **2017,** *199*, 103-110.

9. Boulanger, J.; Gueudry, C.; Münch, D.; Cinquin, B.; Paul-Gilloteaux, P.; Bardin, S.; Guérin, C.; Senger, F.; Blanchoin, L.; Salameroa, J., Fast high-resolution 3d total internal reflection fluorescence microscopy by incidence angle scanning and azimuthal averaging. *Proceedings of the National Academy of Sciences of the United States of America* **2014,** *111* (48), 17164-17169.

10. Ellefsen, K. L.; Dynes, J. L.; Parker, I.; Waigh, T., Spinning-spot shadowless TIRF microscopy. *PLoS ONE* **2015,** *10* (8).

11. Oheim, M.; Salomon, A.; Weissman, A.; Brunstein, M.; Becherer, U., Calibrating Evanescent-Wave Penetration Depths for Biological TIRF Microscopy. *Biophysical Journal* **2019,** *117* (5), 795-809.

12. Guo, Y.; Li, D.; Zhang, S.; Yang, Y.; Liu, J. J.; Wang, X.; Liu, C.; Milkie, D. E.; Moore, R. P.; Tulu, U. S.; Kiehart, D. P.; Hu, J.; Lippincott-Schwartz, J.; Betzig, E.; Li, D., Visualizing Intracellular Organelle and Cytoskeletal Interactions at Nanoscale Resolution on Millisecond Timescales. *Cell* **2018,** *175* (5), 1430-1442.e17.

13. Deng, Y.; Chu, D., Coherence properties of different light sources and their effect on the image sharpness and speckle of holographic displays. *Scientific Reports* **2017,** *7* (1).

14. Weber, I., [2] Reflection interference contrast microscopy. In *Methods in Enzymology*, Academic Press: 2003; Vol. 361, pp 34-47.

15. Gemeinhardt, A.; McDonald, M. P.; König, K.; Aigner, M.; Mackensen, A.; Sandoghdar, V., Label-free imaging of single proteins secreted from living cells via iscat microscopy. *Journal of Visualized Experiments* **2018,** *2018* (141).

16. Fish, K. N., Total internal reflection fluorescence (TIRF) microscopy. *Current Protocols in Cytometry* **2009,** (SUPPL.50), 12.18.1-12.18.13.

17. Soubies, E.; Schaub, S.; Radwanska, A.; Van Obberghen-Schilling, E.; Blanc-Feraud, L.; Aubert, G. In *A framework for multi-angle TIRF microscope calibration*, Proceedings - International Symposium on Biomedical Imaging, 2016; pp 668-671.

18. Case, L. B.; Waterman, C. M., Adhesive F-Actin waves: A novel Integrin-Mediated adhesion complex coupled to ventral actin polymerization. *PLoS ONE* **2011,** *6* (10).

19. Brockman, J. M.; Blanchard, A. T.; Pui-Yan, V.; Derricotte, W. D.; Zhang, Y.; Fay, M. E.; Lam, W. A.; Evangelista, F. A.; Mattheyses, A. L.; Salaita, K., Mapping the 3D orientation of piconewton integrin traction forces. *Nature Methods* **2018,** *15* (2), 115-118.

20. Yu, Y.; Fay, N. C.; Smoligovets, A. A.; Wu, H. J.; Groves, J. T., Myosin IIA modulates T cell receptor transport and CasL phosphorylation during early immunological synapse formation. *PLoS ONE* **2012,** *7* (2).

21. Simmert, S.; Abdosamadi, M. K.; Hermsdorf, G.; Ffer, E. S., LED-based interference-reflection microscopy combined with optical tweezers for quantitative three-dimensional microtubule imaging. *Optics Express* **2018,** *26* (11), 14499.

22. Mahamdeh, M.; Howard, J., Implementation of interference reflection microscopy for label-free, high-speed imaging of microtubules. *Journal of Visualized Experiments* **2019,** *2019* (150).

23. Baker-Groberg, S. M.; Phillips, K. G.; McCarty, O. J. T., Quantification of volume, mass, and density of thrombus formation using brightfield and differential interference contrast microscopy. *J. Biomed. Opt.* **2013,** *18* (1).

24. Zangle, T. A.; Teitell, M. A., Live-cell mass profiling: An emerging approach in quantitative biophysics. *Nat. Med.* **2014,** *11* (12), 1221-1228.

25. He, X.; Montague, S. J.; Tao, X.; Gardiner, E. E.; Lee, W. M., Quantifying Embolism: Label-Free Volumetric Mapping of Thrombus Structure and Kinesis in a Microfluidic System with Optical Holography. *Advanced Biosystems* **2018,** *2* (10).

26. Marchese, P.; Lombardi, M.; Mantione, M. E.; Baccellieri, D.; Ferrara, D.; Chiesa, R.; Alfieri, O.; Foglieni, C., Confocal blood flow videomicroscopy of thrombus formation over human arteries and local targeting of p2x7. *International Journal of Molecular Sciences* **2021,** *22* (8).

Chapter 5 Light Scattering for Platelet Spreading Assay

Publication relevant to this chapter:

Y. Zheng, S. J. Montague, Y. J. Lim, T. Xu, T. Xu, E. E. Gardiner, and W. M. Lee. "Label-free multimodal quantitative imaging flow assay for intrathrombus formation in vitro." *Biophysical Journal* 120, no.5 (2021): 791-804.

5.1 Introduction

This chapter studies single platelet adhesion and activation in spreading assay using the scattering detection from the COSI system (chapter 4.2). With the scattering signal from platelets during spreading, we investigate the motility and activity of the membrane protrusions (filopodia and lamellipodia) that is commonly done using DIC [1, 2] and RICM [3, 4] imaging systems. In the second part of this chapter, we demonstrated for the first time, single platelet adhesion and migration along with collagen fibre and being recruited into a forming thrombus under fluid shear. The capability to track single platelet under flow highlights the high spatial-temporal resolution of the COSI system.

Traditional labelling strategies focus on the molecular responses of the platelets, i.e. intracellular signalling [3, 5], actin reorganization [6, 7], and calcium release [8, 9]. The label-free imaging approaches monitor displacement over time (velocity, μm/s) of the whole cell in the context of the microenvironment [10]. During activation, the adherent platelets form lamellipodia and ruffles, which are thin sheet-like membrane protrusions composed of branched actin filaments [11]. Actin filaments are known to possess a relatively high refractive index [12] than the other cellular component (e.g. cytoplasm, and lipid bilayer), resulting in a

higher scattering signal in a platelet. Traditional darkfield microscopy (DM) equipped with a darkfield condenser utilises the pure scattered light from the platelet and has shown significant imaging contrast [13] as shown in Fig. 5-1 B. However, the imaging resolution of the DM is not optimised compared with the images from SICM because the edges of filopodia and lamellipodia look blurred.

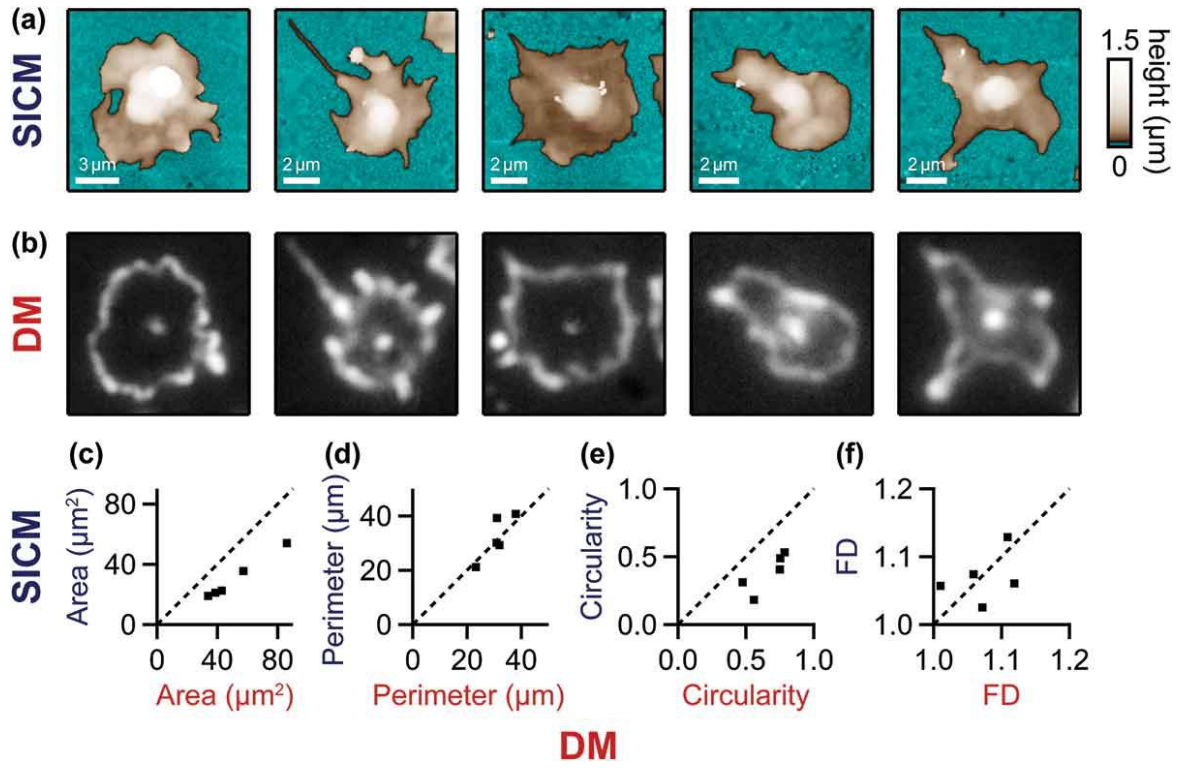

Figure 5-1 Comparison of (A) SICM and (B) darkfield (DM) images of spreading platelets. (C) Area, perimeter, circularity and fractal dimension (FD) measurements for the platelets (left axis in black and bottom axis in red represent quantifications from SICM and DM, respectively). The darkfield microscopy used in this study is a standard upright system with a halogen lamp, darkfield condenser and objective of 100X, 1.32 NA (Leitz Laborlux). This figure is reprinted with permission from Kraus *et al*. [13] © 2016 Taylor & Francis.

This chapter demonstrates platelet imaging with the scattering signal from the COSI system, which also works in darkfield detection. Compared with traditional darkfield microscopy, COSI presents three distinct advantages: (1) simplified optics components, (2) better imaging resolution and (3) depth of field. As we explained in Chapter 4, COSI reaches darkfield by oblique illumination blocking the reflected beam at Fourier plane, which means

the complementary illumination (darkfield condenser and darkfield objective) is not needed. With the oblique illumination, the depth of field can also be adjusted by altering the illumination angle (More details on imaging depth calibration can be found in Appendix C). The spatial coherence of the illumination is another essential factor to consider. COSI uses a high spatial coherence laser source, enabling high contrast imaging with better resolution (chapter 4.2.1.1).

5.2 Monitoring Platelet Motility in Spreading Assay

Quantitative phase imaging (QPM) has been used to study the refractive index of the biological samples based on the optical path difference (OPD) because OPD can be directly related to the refractive index (n) and thickness (t) (OPD $\approx \Delta n \times t$) [12]. Fig. 5-2 shows that the refractive index of actin filament and tubulin microtubule at membrane protrusion can be estimated based on the measured OPD and an estimated microtubule diameter. Actin has larger values and higher dispersion in OPD than microtubules because the stress fibres could form bundles (lead to differences in thickness). Similarly, the correlation between the scattered light and the refractive index can also trace the high index components in spreading platelets. Among all the intracellular components, cytoskeleton structures mainly consist of actin (RI=1.57) [14] and microtubule (RI=2.81) [15], posing the highest refractive index. Therefore, a strong scattering signal is expected from the cytoskeletal fibres. Tracking the high contrast scattered light could quantify the rate of cytoskeleton activity and the motility during platelet activation and spreading.

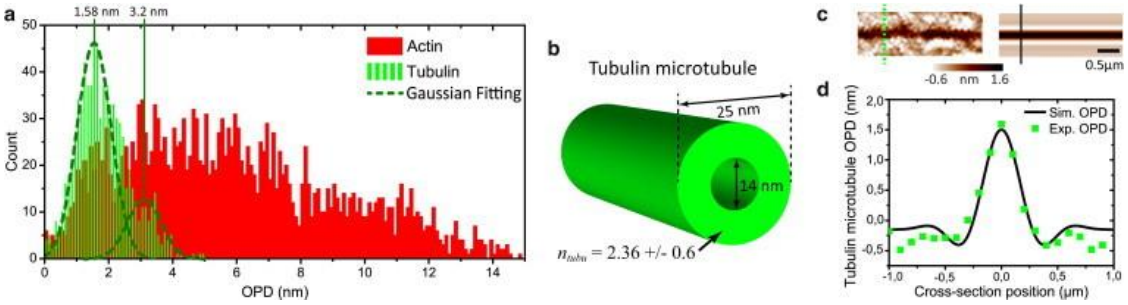

Figure 5-2 Quantifying refractive index of actin filament and tubulin microtubule using optical path difference (OPD) measurements. (A) OPD measurement of actin and microtubule fibres in cytoskeletal structure. (B-C) The diameter of the microtubule is estimated using simulation to calculate the mean refractive index. This figure is reprinted with permission from Bon *et al.* [12] © 2014 Elsevier.

Therefore, we adopted a differential method that quantifies the positional change by subtracting between two subsequent frames on the top of the scattering detection. It quantifies subtle intensity changes in membrane shape (lamellipodia and ruffles) due to cytoskeleton rearrangement at high temporal resolution (30Hz). For simplicity, we refer the measurement to platelet **activity** that quantified the rate of membrane shape fluctuation of platelet movement (μm/s). To verify the contribution of cytoskeleton rearrangement to platelet activity, we demonstrate measurements using an actin polymerization inhibitor. We also show that the COSI system can capture spatial membrane fluctuations of lamellipodia and ruffles of cells during adhesion, spreading and aggregation in static (no flow) conditions.

5.2.1 Backscattering Signal from Fixed Platelets

Before conducting imaging experiments on live platelets, the backscattering light of fixed platelets under oblique illumination (illumination angle 52^o, depth 4 μm) stained with phalloidin is collected to visualize actin filaments as shown in Fig. 5-3 A and Fig. 5-3 B. The backscattering images in Fig. 5-3 C show maximum intensity along the membrane where ruffling and protrusions appear (Fig. 5-3 C and 5-3 D). This is consistent with the previous cell migration studies using phase contrast, fluorescence and EM microscopy [16], indicating a

high amount of optical phase delay (destructive interference) from actin filaments. The fluorescence imaging suggests that the membrane ruffling and protrusions are associated with densely packed bundles of actin filaments [16, 17]. However, other sources of light scattering inside the platelets are not actin-related. In Fig. 5-3 E, the backscattering signal from the inside of the platelet does not correlate with the fluorescence signal (Fig. 5-3 F), which might reflect contributions from other intracellular entities, including degranulation [18]. Apart from the scattered signal from the platelets, vertical interference fringes in the background are also observed in Fig. 5-3 A, which could relate to the unwanted reflection such as reflection from the sample and residual ghost reflection. Similar effects are not observed after the system is optimised (see results in Chapter 6 and 7) by changing the beam splitter and designing the synchronization system. Methods such as background subtraction can be used in the future to remove the fringes in the background and improve the imaging quality.

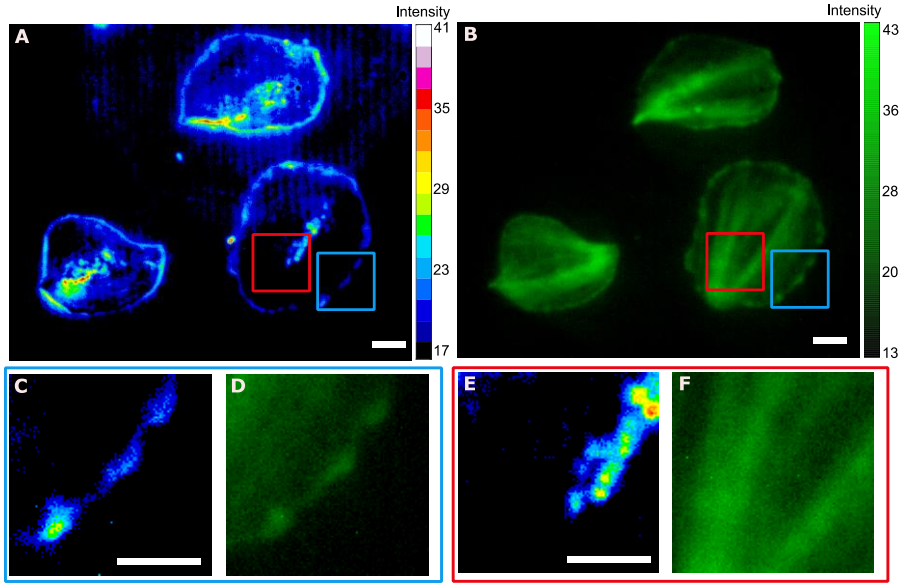

Figure 5-3 Comparisons of COSI scattering signal to F–actin fluorescence signal. (A) Scattering and (B) fluorescence signal of fixed permeabilized platelets stained with phalloidin to visualize F-actin after 45 minutes spreading on fibrin-coated coverslips. (C) - (D) Magnified regions from scattering and fluorescence signal (blue boxes) showing the scattering signal is clearly visible along the membrane ruffling (i.e. regions with newly polymerized actin filaments). (E) - (F) Magnified regions (red boxes) from scattering and fluorescence signal showing region within the platelet. Scale Bar = 2 μm.

5.2.2 Quantifying Platelet Activity

There are various methods to quantify the motion of cells during adhesion and migration. For example, kymographs are graphic representations of spatial position over time, which tracks the subcellular component qualitatively [19]. However, it cannot quantitatively track the changes of cellular structures over time. Here we adopted a differential method that calculates the differences in intensity signals between successive imaging frames [10, 20]. The change in intensity defines the rate of change in cytoskeleton activity and motility as platelet activity, and we refer this quantification as platelet activity. The concept is demonstrated in Fig. 5-4, showing the subtraction of intensity ($\Delta I(t)$) images at each digital pixel along a 2D matrix between two sequential frames separated by Δt [10]. In contrast to existing kymography [21], this differential method between two frames highlights the physical change that platelets exhibit and removes static background signal. However, this differential measurement is extremely sensitive to the synchronization of galvo mirror and camera during scanning and capture. To minimise these effects of the optical system, we use a NI DAQ system (as explained in chapter 4) to precisely control the scanning speed and camera trigger and ensure the synchronization of the system. We also use fast capture rate (> 30 FPS) when using the differential method and moving average when processing the data to minimise the effect of laser fluctuations and drifting. Fig. 5-4 A illustrates this concept with a simplified diagram of a pixelated image of a platelet that has rearranged its cytoskeleton across a given time interval (Δt).

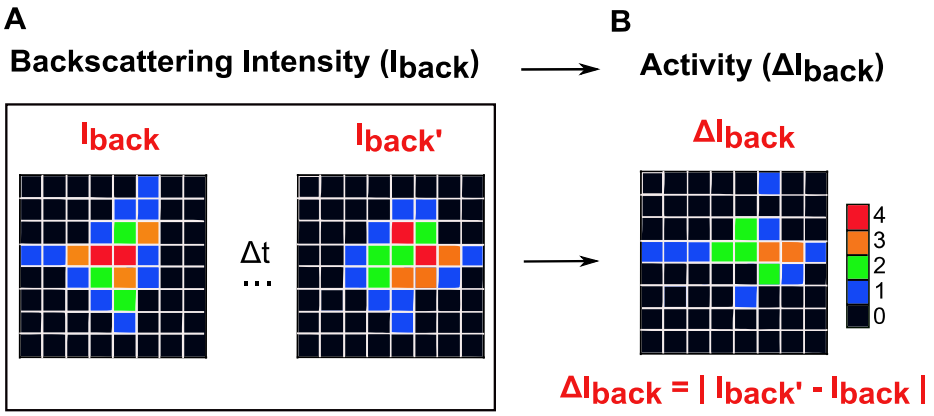

Figure 5-4 Platelet activity quantification. (A) Simplified diagram of a pixelated image of a single platelet with a grid representing individual pixels on the camera. At given Δt, the intensity of the platelet changed from I_{back} to I_{back}' due to the change in refractive index (resulting from cytoskeleton rearrangement). (B) Activity ΔI_{back} is quantified as the absolute intensity distribution difference between I_{back}' and I_{back}.

Here we provide an example of using the differential method to study platelet motility and activity. If we quantify the time-dependent spatial-temporal interaction of single platelets under flow conditions at 0.1 second time intervals with a spatial resolution for each pixel to be 40 nm based on the optical magnification of 263x. So, for a single pixel shift, the spatiotemporal resolution is 40 nm/0.1 s = 0.4 μm/s. We show two subsequent scattering intensities (I_{back}) of a platelet during spreading after 20 minutes of loading the washed platelets (protocol in Appendix E) onto agonist coated surface (without flow shear). In Fig. 5-5, we compare three agonists: collagen related peptide (CRP), collagen fibre and fibrin. We plot two sequential frames during spreading in between 200 milliseconds to calculate platelet activity. The single platelet activity on CRP, collagen, and fibrin was around 3.6 - 4.4 μm/s (Fig. 5-5), which shows the minimised effect of coated agonist in platelet activity during spreading.

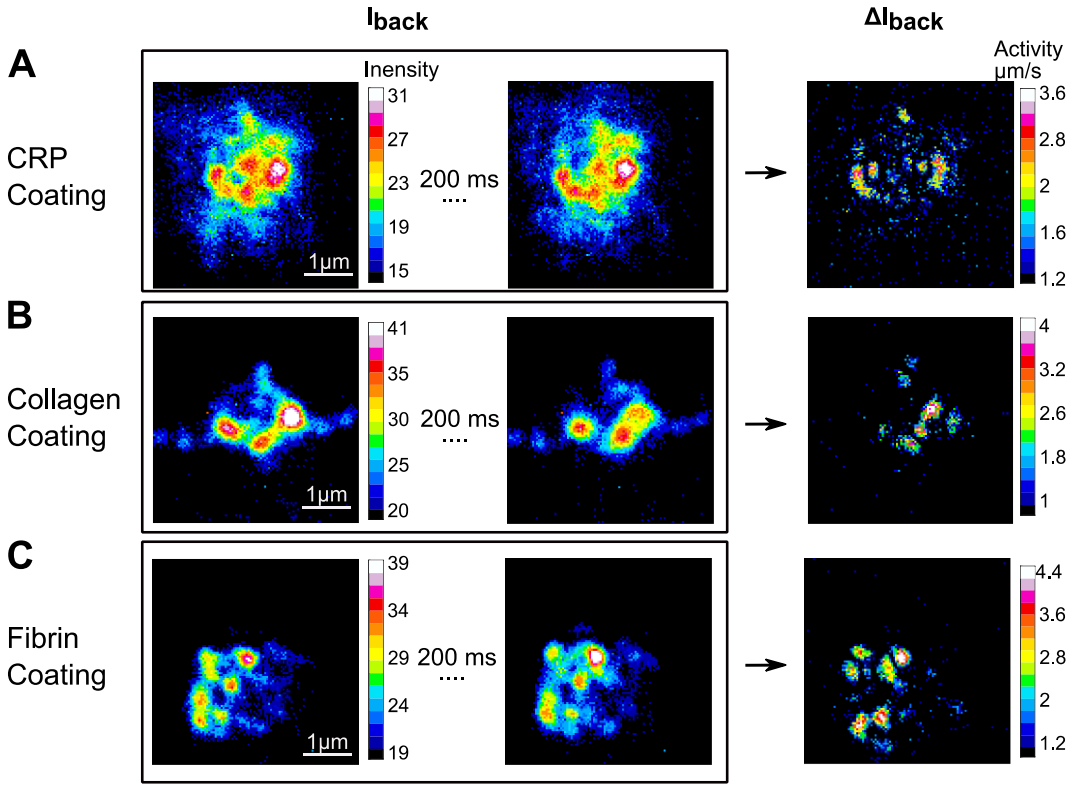

Figure 5-5 Comparison of backscattered signal and platelet activity of spreading platelets on different coatings without flow (static). (A) collagen related peptide (CRP) coating, (B) collagen fiber coating and (C) fibrin coating. Two images of the spreading platelet are taken 200 ms apart (I_{back}) with the activity map (ΔI_{back}) shown in right panels.

5.2.3 Platelet Activity with Actin Polymerization Inhibitor

We then move to validate the contribution of cytoskeleton rearrangement via actin polymerization in platelet activity, especially along the membrane protrusion region. We carry out imaging experiments using platelets treated with cytochalasin D, which inhibits actin polymerization and prevents active cytoskeletal rearrangement and platelet shape change [22]. We compare the activity map between platelets that had adhered and spread on CRP-coated coverslips after treatment with PBS (control), 1% DMSO (vehicle) or 10 μM cytochalasin D.

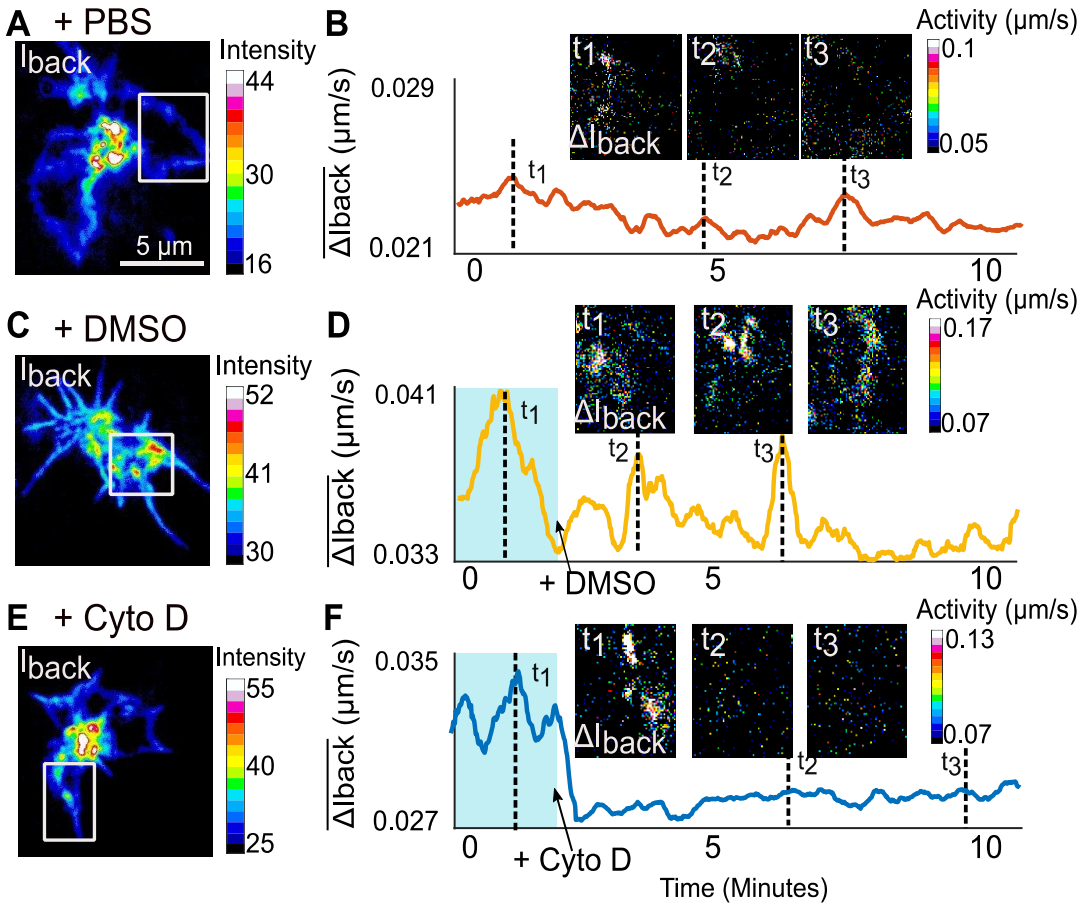

Figure 5-6 (A) Backscattering signal of a single platelet spreading on CRP coated surface. PBS is added during platelet spreading. (B) Top and bottom panels show the activity map and time series plots of averaged activity variations (Δt = 1 second) within the lamellipodia rich region shown in (A). Backscattering signal, activity map and time series plots of single platelet spreading when 1% DMSO solution (C-D) or 10 μM Cytochalasin D (E-F) is added. Activity measurements are shown as averaged activity across all pixels with a moving average of 30 seconds.

Membrane ruffling and extensions are observed prior to the addition of each reagent, and with spreading platelets, the majority of the cytoskeleton rearrangement are primarily associated with the formation of lamellipodia, which is consistent with the fixed platelet images (Fig. 5-3). By tracking platelet activity during spreading, we then focus on quantifying activity around the lamellipodia as shown in the solid white box in Fig. 5-6 A, C and E. The average activity (μm/s) along lamellipodia is monitored over 20 minutes and plotted in a time series in Fig. 5-6 B, D and F. The results show that platelets treated with

PBS showed minimal activity changes in the first 5 minutes (0.024 μm/s to 0.0215 μm/s). DMSO treated platelets show a decrease from 0.041 μm/s to 0.033 μm/s in the first three minutes before returning to 0.038 μm/s. In contrast, platelets treated with cytochalasin D show a sudden drop from 0.034 μm/s to 0.027 μm/s and remain low with minimal changes across the experiment duration. These single platelets results compare well with conduction ion microscopy, which showed cytochalasin D treatment could inhibit morphological changes by 75% (shape and height change at platelet membrane). The results indicate that activity from COSI can be used to detect membrane fluctuations resulting from cytoskeleton rearrangement and that disruption of actin polymerization abrogates membrane movement, ruffling and protrusions down to nanometre μm/s levels.

5.2.4 Platelet Activity during Aggregation

We then investigate the platelet activity during aggregation, where two platelets adhere and form an aggregate. Note this experiment is done without introducing the fluid shear. In Fig. 5-7, we track two individual platelets forming a micro-aggregate on a CRP-coated surface. Fig. 5-7 B shows the activity map of two platelets that begin to interact and also aggregate (t_1 to t_4) on a CRP-coated surface. The mean scattered intensity increases about 12% from 0.086 to 0.096 concomitant with the aggregation process (Fig. 5-7 A), as the second platelet introduces more mass to the aggregate. In contrast, the platelet activity shows a remarkable increase by 30% upon encountering the second platelet at t_3 (0.021 μm/s to 0.032 μm/s) and then decaying down to 0.025 μm/s when the aggregate stabilized, which indicates the platelet activity is independent on the total mass. This experiment shows that the activity measurement can quantify subtle transient changes within platelet-platelet macroaggregates.

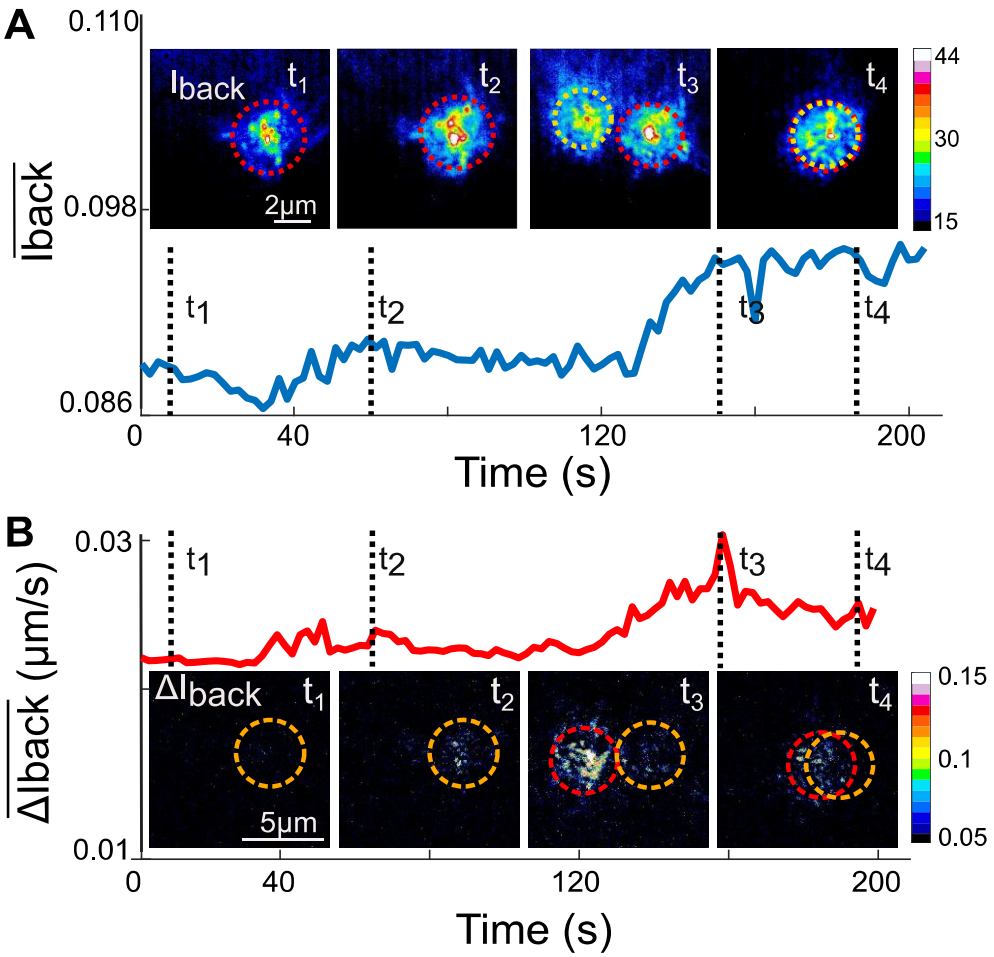

Figure 5-7 Backscattering signal of two platelets interacting and aggregating on the CRP coated surface. Top and bottom panels show the time series plot of (A) backscattering signal and (B) averaged activity (Δt = 2 seconds) and the activity map at indicated time points. Two interacting platelets are circled in red and orange.

In contrast, we also show the platelet activity of single platelet spreading on the collagen-related peptide (CRP) 20 minutes after loading in Fig. 5-8. Using a time interval of 2 seconds (Δt), the activity of a single platelet was observed to fluctuate at around 0.022 ±0.005 μm/s over 3 minutes. While there are some noticeable activity spikes, the overall movement of the platelet appears to be relatively minor.

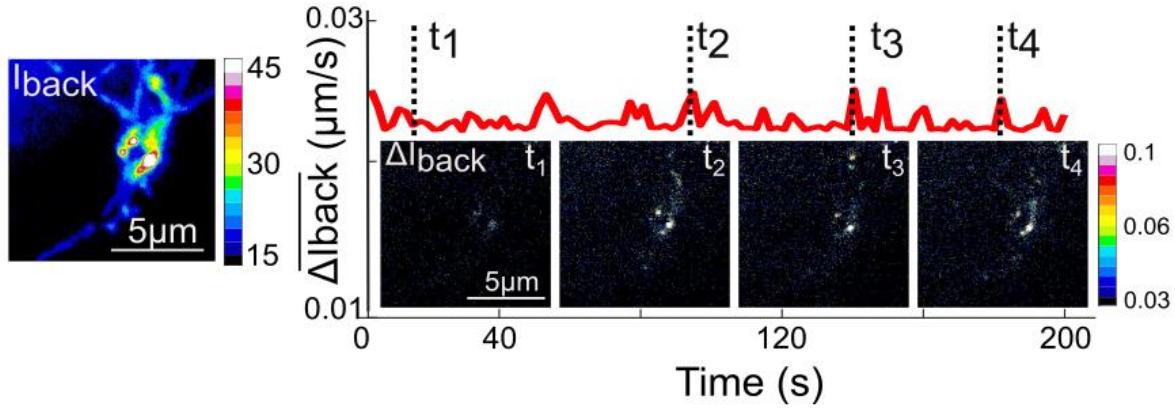

Figure 5-8 Averaged activity (Δt = 2 seconds) and the activity map of single platelet spreading on the CRP coated surface at indicated time points (t1-t4).

5.3 Visualizing of Single Platelet Adhesion Under Flow

The process of platelet adhesion and interaction with collagen/fibrin fibres under flow conditions whilst a whole intact thrombus is being formed has not been shown at single platelet level. In this section, we show for the first time, platelet adhesion events under flow conditions and quantifications of platelet motility during thrombus formation.

The initial platelet adhesion events during thrombus formation under flow are captured using the scattering signal in the COSI system, as shown in Fig. 5-9. The microfluidics channel (customized straight channel) is pre-coated with collagen fibres (100 μg/ml) overnight at 4 °C, and the PRP is flowing at 1800 s^{-1} flow rate. Here, we demonstrate two events captured by the COSI system at 30 FPS: (1) platelet migration and (2) recruitment. In ROI 1, a platelet firstly adhered onto the collagen fibre and then migrated along the fibre followed by the flow direction before being recruited into a forming thrombus. While in ROI 2, the platelet was directly adhered to and recruited to the forming thrombus. These results confirmed that the backscattering signal in COSI can capture single platelet migration,

especially at a highly dynamic microenvironment, because platelet attachment and recruitment occurred within milliseconds.

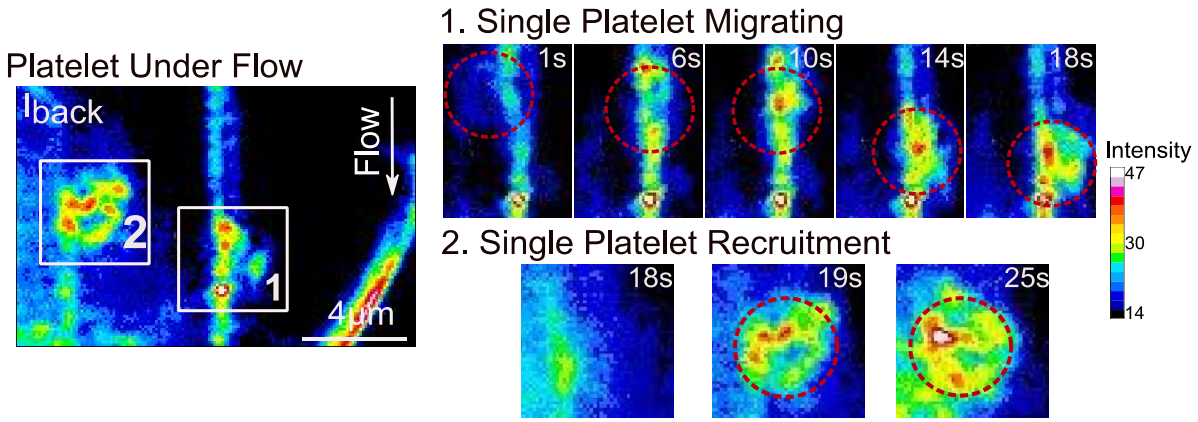

Figure 5-9 Backscattering signal of single platelets under flow in a microfluidic channel where platelet migrates the collagen fibre in ROI 1 and adhere to a collagen fibre in ROI 2. The time-lapse images are captured and shown.

Next, we move to investigate platelet activity or motility during adhesion and recruitment. The presence of fluid shear can alter VWF bonding and affect adhesive platelet behaviour. Here, we compare the adhesive platelet spreading dynamics with collagen fibres under both static and flow conditions in Fig. 5-10. At an imaging depth of ~ 4μm, the scattering component of COSI permits direct imaging of the precise location of individual collagen fibres and platelets. Fig. 5-10 A and B show the raw scattered light image of a platelet adhering to a single collagen fibre and activity map of the platelet, which shows minimal spreading (membrane protrusions) with around 0.55 μm/s (averaged activity). However, with exposure to fluid shear stress of 1800 s^{-1} Fig. 5-10 C-E, we observe an ~2-fold increase in activity of up to 7 μm/s compared to platelets in static conditions (3.2 μm/s).

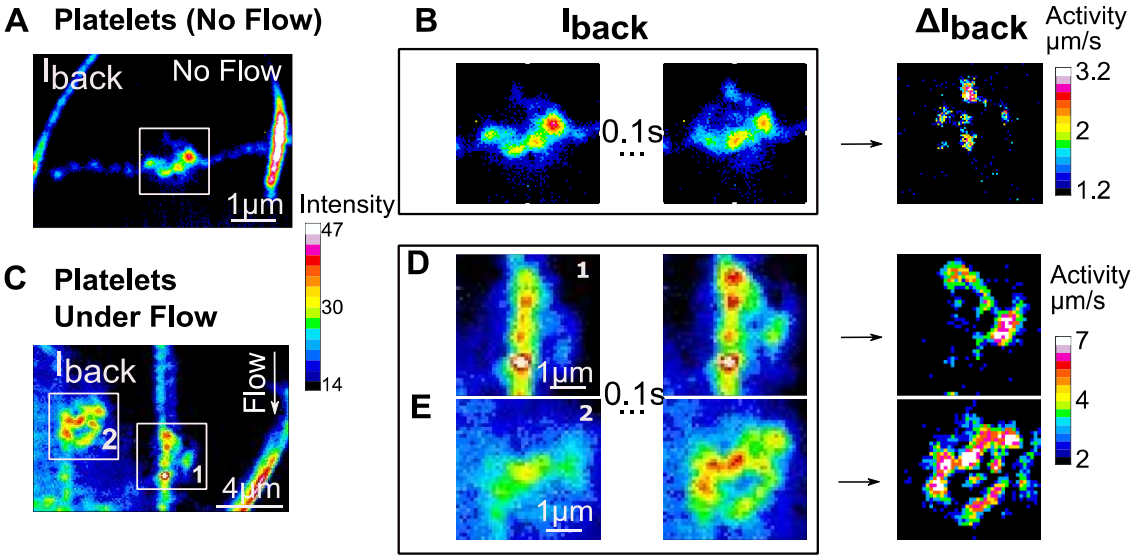

Figure 5-10 Single platelet activity on a coated collagen fibre at Δt = 0.1 second with and without flow conditions. (A) Single platelet spreading on a collagen-coated coverslip (static). (B) Two images of the spreading platelet (Δt = 0.1 seconds) and the activity map are shown (right). (C) Backscattering signal of single platelets under flow in a microfluidic channel where platelets move along the collagen fibre in ROI 1 or adhere to a collagen fibre in ROI 2. Two images in ROI 1 (D) and ROI 2 (E) with activity maps are shown. Shear rate=1800 s^{-1}.

5.4 Conclusion

This chapter conclusively demonstrates that the scattering component in the COSI system achieves high contrast imaging and spatial-temporal resolution that can capture membrane ruffling and protrusion events in single platelets at an adhesion site. We show that the COSI system can extract the platelet activity (motility) during spreading and adhesion with the differential method. By inhibiting actin polymerization, we demonstrate that the platelet activity drops significantly, indicating the activity measurements along the membrane ruffling are directly related to the cytoskeleton (actin) rearrangement. This is due to the high refractive index of actin (~1.57 [12], compared with cytoplasm ≈ 1.38 [23] and lipid ≈ 1.45 [24]) and the high concentration of branched actin at protrusions.

On the other hand, actin organization and cytoskeleton rearrangement may not be the only contributing factors triggering variations in scattering signals in the other regions rather than membrane protrusion. As the central portion of the platelet is presumably flat on the surface of the substrate, as shown by SEM images [25], it would appear that the strong scattering signal emanates from other intracellular components such as granules, organelles and lysosomes. However, it would be difficult to prove one way over the other at this stage without specifically staining for granule proteins. Future work using platelets that lack α-granules isolated either from Grey Platelet Syndrome patients or the murine equivalent Nbeal2-deficient mice may help define the source of light scattering in platelets.

The COSI imaging approach could also help address where procoagulant platelets, characterized as having amplified surface area, sustained calcium rises, and phosphatidylserine (PS) exposure, are located in newly formed or embolizing thrombi. Procoagulant platelets accelerate coagulation [26] for the formation of fibrin-rich thrombi, and these platelets seem to be mechanically translocated to the periphery via thrombus contraction [27]. This platelet subpopulation would be ideally targeted by antithrombotic therapies. As COSI and other refractive index-based imaging tools do not require the uptake of membrane-permeable dyes, or fluorophore-conjugated antibodies, which can disrupt the function of important platelet receptors or surface molecules [28], these tools are ideal to be developed for utility in clinical and drug evaluation settings.

To study platelet motility during spreading and cytoskeleton rearrangement, we first used the scattering detection in the COSI system to quantify membrane ruffling and filopodia protrusions. The main advantage of pure scattering detection versus interference detection (or RICM) is the selective depth of field and higher imaging contrast for morphological studies. The interference detection measures axial membrane displacements of isolated single cells in

the range of hundreds of nanometers above the coverslip, but the interference component (e.g. fringes and negative contrast) might be hard to interpret for complex biological structures with multiple scattering mediators and lateral cell motility. In the next chapter, I shall demonstrate single platelet imaging with scattering and interference signals for simultaneously quantifying platelet morphology and measuring axial displacement.

5.5 Contribution

The platelet experiments were designed along with Dr Samantha Montage. Dr Samantha J. Montage, Ms Simone Brysland and Dr Yean Jin Lim did the work related to platelet preparation. Mr Tao Xu fabricated microfluidic devices. I calibrated the imaging performance of COSI along with Mr Tienan Xu, performed all the experiments, and interpreted the results.

5.6 References

1. Kulkarni, S.; Jackson, S. P., Platelet factor XIII and calpain negatively regulate integrin αIIbβ3 adhesive function and thrombus growth. *Journal of Biological Chemistry* **2004,** *279* (29), 30697-30706.

2. McCarty, O. J. T.; Calaminus, S. D. J.; Berndt, M. C.; Machesky, L. M.; Watson, S. P., von Willebrand factor mediates platelet spreading through glycoprotein Ib and αIIbβ3 in the presence of botrocetin and ristocetin, respectively. *Journal of Thrombosis and Haemostasis* **2006,** *4* (6), 1367-1378.

3. Zhang, Y.; Qiu, Y.; Blanchard, A. T.; Chang, Y.; Brockman, J. M.; Ma, V. P. Y.; Lam, W. A.; Salaita, K., Platelet integrins exhibit anisotropic mechanosensing and harness piconewton forces to mediate platelet aggregation. *Proc. Natl. Acad. Sci. U.S.A.* **2017,** *115* (2), 325-330.

4. Lee, D.; Fong, K. P.; King, M. R.; Brass, L. F.; Hammer, D. A., Differential dynamics of platelet contact and spreading. *Biophys. J.* **2012,** *102* (3), 472-482.

5. Nicolai, L.; Schiefelbein, K.; Lipsky, S.; Leunig, A.; Hoffknecht, M.; Pekayvaz, K.; Raude, B.; Marx, C.; Ehrlich, A.; Pircher, J.; Zhang, Z.; Saleh, I.; Marel, A. K.; Löf, A.; Petzold, T.; Lorenz, M.; Stark, K.; Pick, R.; Rosenberger, G.; Weckbach, L.; Uhl, B.; Xia, S.; Reichel, C. A.; Walzog, B.; Schulz, C.; Zheden, V.; Bender, M.; Li, R.; Massberg, S.; Gaertner, F., Vascular surveillance by haptotactic blood platelets in inflammation and infection. *Nature Communications* **2020,** *11* (1).

6. Mayr, S.; Hauser, F.; Peterbauer, A.; Tauscher, A.; Naderer, C.; Axmann, M.; Plochberger, B.; Jacak, J., Localization microscopy of actin cytoskeleton in human platelets. *International Journal of Molecular Sciences* **2018,** *19* (4).

7. Lickert, S.; Sorrentino, S.; Studt, J. D.; Medalia, O.; Vogel, V.; Schoen, I., Morphometric analysis of spread platelets identifies integrin αiIbβ3-specific contractile phenotype. *Scientific Reports* **2018,** *8* (1).

8. Liu, E. C. K.; Abell, L. M., Development and validation of a platelet calcium flux assay using a fluorescent imaging plate reader. *Analytical Biochemistry* **2006,** *357* (2), 216-224.

9. Nesbitt, W. S.; Harper, I. S.; Schoenwaelder, S. M.; Yuan, Y.; Jackson, S. P., A live cell micro-imaging technique to examine platelet calcium signaling dynamics under blood flow. In *Methods in Molecular Biology*, 2012; Vol. 788, pp 73-89.

10. Jünger, F.; Rohrbach, A., Strong cytoskeleton activity on millisecond timescales upon particle binding revealed by ROCS microscopy. *Cytoskeleton* **2018,** *75* (9), 410-424.

11. Monzel, C.; Sengupta, K., Measuring shape fluctuations in biological membranes. *J. Phys. D Appl. Phys.* **2016,** *49* (24).

12. Bon, P.; Lécart, S.; Fort, E.; Lévêque-Fort, S., Fast label-free cytoskeletal network imaging in living mammalian cells. *Biophys. J.* **2014,** *106* (8), 1588-1595.

13. Kraus, M. J.; Seifert, J.; Strasser, E. F.; Gawaz, M.; Schäffer, T. E.; Rheinlaender, J., Comparative morphology analysis of live blood platelets using scanning ion conductance and robotic dark-field microscopy. *Platelets* **2016,** *27* (6), 541-546.

14. Andersen, M.; Nir, S., Van der Waals parameters, refractive indices and dispersion equations of spectrin, actin and other mammalian proteins. *Polymer* **1977,** *18* (9), 867-870.

15. Mershin, A.; Kolomenski, A. A.; Schuessler, H. A.; Nanopoulos, D. V., Tubulin dipole moment, dielectric constant and quantum behavior: Computer simulations, experimental results and suggestions. *BioSystems* **2004,** *77* (1-3), 73-85.

16. Borm, B.; Requardt, R. P.; Herzog, V.; Kirfel, G., Membrane ruffles in cell migration: Indicators of inefficient lamellipodia adhesion and compartments of actin filament reorganization. *Exp. Cell. Res.* **2005,** *302* (1), 83-95.

17. Neto, J. C.; Agero, U.; Gazzinelli, R. T.; Mesquita, O. N., Measuring optical and mechanical properties of a living cell with defocusing microscopy. *Biophys. J.* **2006,** *91* (3), 1108-1115.

18. White, J. G.; Estensen, R. D., Degranulation of discoid platelets. *Am. J. Clin. Pathol.* **1972,** *68* (2), 289-302.

19. Jakobs, M. A.; Dimitracopoulos, A.; Franze, K., Kymobutler, a deep learning software for automated kymograph analysis. *eLife* **2019,** *8*.

20. Ruh, D.; Mutschler, J.; Michelbach, M.; Rohrbach, A., Superior contrast and resolution by image formation in rotating coherent scattering (ROCS) microscopy. *Optica* **2018,** *5* (11), 1371-1381.

21. Mangeol, P.; Prevo, B.; Peterman, E. J. G., KymographClear and KymographDirect: Two tools for the automated quantitative analysis of molecular and cellular dynamics using kymographs. *Mol. Biol. Cell.* **2016,** *27* (12), 1948-1957.

22. Casella, J. F.; Flanagan, M. D.; Lin, S., Cytochalasin D inhibits actin polymerization and induces depolymerization of actin filaments formed during platelet shape change. *Nature* **1981,** *293* (5830), 302-305.

23. Przibilla, S.; Dartmann, S.; Vollmer, A.; Ketelhut, S.; Greve, B.; Von Bally, G.; Kemper, B., Sensing dynamic cytoplasm refractive index changes of adherent cells with quantitative phase microscopy using incorporated microspheres as optical probes. *Journal of Biomedical Optics* **2012,** *17* (9).

24. Ardhammar, M.; Lincoln, P.; Nordén, B., Invisible liposomes: Refractive index matching with sucrose enables flow dichroism assessment of peptide orientation in lipid vesicle membrane. *Proceedings of the National Academy of Sciences of the United States of America* **2002,** *99* (24), 15313-15317.

25. Gaertner, F.; Ahmad, Z.; Rosenberger, G.; Fan, S.; Nicolai, L.; Busch, B.; Yavuz, G.; Luckner, M.; Ishikawa-Ankerhold, H.; Hennel, R.; Benechet, A.; Lorenz, M.; Chandraratne, S.; Schubert, I.; Helmer, S.; Striednig, B.; Stark, K.; Janko, M.; Böttcher, R. T.; Verschoor, A.; Leon, C.; Gachet, C.; Gudermann, T.; Mederos y Schnitzler, M.; Pincus, Z.; Iannacone, M.; Haas, R.; Wanner, G.; Lauber, K.; Sixt, M.; Massberg, S.,

Migrating Platelets Are Mechano-scavengers that Collect and Bundle Bacteria. *Cell* **2017,** *171* (6), 1368-1382.e23.

26. Agbani, E. O.; Poole, A. W., Procoagulant platelets: Generation, function, and therapeutic targeting in thrombosis. *Blood* **2017,** *130* (20), 2171-2179.

27. Nechipurenko, D. Y.; Receveur, N.; Yakimenko, A. O.; Shepelyuk, T. O.; Yakusheva, A. A.; Kerimov, R. R.; Obydennyy, S. I.; Eckly, A.; Léon, C.; Gachet, C.; Grishchuk, E. L.; Ataullakhanov, F. I.; Mangin, P. H.; Panteleev, M. A., Clot contraction drives the translocation of procoagulant platelets to thrombus surface. *Arterioscler. Thromb. Vasc. Biol.* **2019,** *39* (1), 37-47.

28. Bergstrand, J.; Xu, L.; Miao, X.; Li, N.; Öktem, O.; Franzén, B.; Auer, G.; Lomnytska, M.; Widengren, J., Super-resolution microscopy can identify specific protein distribution patterns in platelets incubated with cancer cells. *Nanoscale* **2019,** *11* (20), 10023-10033.

Chapter 6 COSI-F for Platelet Migration Assay

Publication relevant to this chapter:

Y. Zheng *, Y. J. Lim *, H. Lin, T. Xu, C. Longbottom, V. Delghingaro-Augusto, Y. L. Thong, C. R. Parish, E. E. Gardiner, and W. M. Lee. " Combined Scattering, Interferometric and Fluorescence Oblique Illumination for Live Cell Nanoscale Imaging." *In Press* (2021).
**Co-first author*

6.1 Introduction

This chapter will demonstrate platelet migration assay on adhesive ligands coated substrates (fibrinogen and fibrin) and morphological profiling of the migrating platelets using the COSI-F system described in chapter 4. Previous studies in cell-surface interaction and biochemical signalling often combine fluorescence (TIRF) and interferometry (iSCAT and RICM) that use two separate illuminations [1, 2]. In contrast, COSI-F uses a single objective oblique rotational illumination scheme that facilitates simultaneous scattering, interferometric, and fluorescence imaging of living cells at the nanoscale. The imaging contrast and sensitivity of the different detection schemes are firstly calibrated using gold nanoparticles (GNPs) from 20-100 nm. We demonstrate that the COSI-F system can detect GNPs at 20 nm without any forms of post-processing. I will also show multiplex imaging by quantifying spatial-temporal formation of filopodia and lamellipodium of adherent human platelets with different agonists (fibrin, fibrinogen). Profiling the morphological features and tracking the axial membrane fluctuations of a migrating platelet will be explained in the last part of this chapter.

Nanoscale label free imaging such as ROCS (introduced in Chapter 4) has emerged as an important tool to avoid photobleaching and achieve 3D quantitative imaging[3]. The current hallmark of ROCS lies in the ability to extract nanoscale scattering that results in either inverted intensity (brightfield-BF) or bright intensity (darkfield-DF), all of which occurs at > 50° oblique angles[4-6]. While BF and DF ROCS obtains high contrast images based on scattered light from the sample, ROCS does not contain axial positional information of the sample. That said, elastic scattered light from nanoparticles and biological molecules [7] do not degrade or saturate over time [7-9]. However, label free imaging does not provide the molecular identity of molecules and cellular structures. Lately, interferometric signals has been instrumental at tracking axial positions of purified proteins [8-10] and membrane protrusions [11]. Lately, the combinations of ROCS with total internal reflection fluorescence microscopy-TIRF [6] as well as interference scattering (iSCAT) with fluorescence confocal [4] have begun to play an important role for nanoscopic correlative imaging. The complementary elements of fluorescence and label free nanoscale imaging permit quantitative 3D spatial temporal detail of individual cellular components that will define the next generation of nanoscopy to study cell migration.

In this chapter, I will demonstrate for the first time, three imaging modalities (scattering, interferometry and fluorescence) combined in an oblique illumination system using a single laser source, a diaphragm and 2 cameras. While ROCS and HILO are constructed on an oblique scanning system, quantitative interferometric imaging has not been reported to use an oblique illumination system before [12]. Furthermore, BF and DF ROCS improve imaging contrast of scatterers but do not produce visible interference intensity fringes that is present in interferometric imaging such as iSCAT [4-6, 13] or reflection interference contrast microscopy (RICM) [14-18]. Images from these interferometric techniques display characteristic varying interference fringes produced from scattered and reflecting

light from the sample and glass surface. Here, the new interferometric imaging is achieved based on the ROCS platform. At 22° oblique angle for a rotating beam, distinctive intensity fringes [19] can be retrieved which can be used to quantify axial position of scatterers (nanoparticles, organelle in living cells).

In the following sections, I shall first outline the optical design (scanning angle and Fourier amplitude filter) necessary to obtain the combined scattering, interferometry and fluorescence imaging (COSI-F). Secondly, the calibration experiments were carried out to measure and compare the imaging sensitivity of interferometric, scattering and fluorescence signal using 20 nm, 100 nm and 200 nm nanoparticles along axial and lateral direction [8]. The combined imaging platform is then applied to study two cell types that actively migrate in response to vessel injury. Thirdly, the COSI-F system is used to examine platelets that are thought to generate filipodium protrusions that spans several platelet lengths (~ 5-10 μm) [20, 21, 22] to form a biomechanical plug [23, 24]. Platelet can direct their migration to scavenge adhesive molecules bound to a stiff substrate [25], that links their role as cellular scavengers to collect molecular agents. We used fluorescence imaging to study real-time platelet migration on glass surfaces coated with fluorophore-labelled fibrinogen and crossed-linked fibrinogen-fibrin, in the presence and absence of Bovine serum albumin (BSA)- common protein in blood. In this biological imaging experiment, we focused on correlating the spatial organization of membrane, organelles in subcellular regions of cells [26-28] along edge of cell membrane (leading and rear edge) [29] that orchestrates cell migration. Combined oblique imaging with interference and scattering permits us to quantify membrane fluctuations of migrating cells platelets and endothelial cells at the leading and rear edge and leverage fluorescence to identifying surface molecules or intracellular organelle that regulate cell migration.

6.2 Platelet Migration Assay

Cells direct their movement [30] and modulate the strength of adhesion [31, 32] in response to external fluid stimuli (fluid shear, osmotic pressure), [33] [34] or biochemical agonists in the extra-cellular matrix (ECM) [35], to fulfil their respective biological function in immune surveillance [36], wound healing [37] [32], or thrombus/clot formation [25]. Among different cell types, platelet presents an imaging challenge for light microscopy [38]. Platelets are nucleus-free cells that serve as a mechanical model system [30] to study the modulation of actin-rich membrane protrusions directed by clustering transmembrane proteins during ligand binding. Due to their small size (2-3 μm) and rapid activation, a high-speed microscopy imaging system is required to image platelets at the sub-cellular level. The platelet membrane contains a wide range of mechanosensitive transmembrane receptors such as glycoprotein (GP) Ib-IX-V, ion channels [39] and fibrinogen-binding integrin ($\alpha_{IIb}\beta_3$)[40]. Transmembrane receptors coordinate between intracellular signalling pathways and extracellular signals so to remodel its cytoskeleton and form membrane protrusions. Platelet-specific cytoskeleton remodelling results membrane protrusion and membrane receptor clustering has important consequence in context of clot formation [41] and vasculature surveillance[25, 30, 42, 43].

6.3 Method

6.3.1 Fibrinogen/Fibrin Coating

The coating of fibrin and fibrinogen are critical in platelet migration. Previous study have shown that substrate adhesiveness can influence the migration and shape of the activated platelets, and the presence of free calcium is required for platelet polarisation [25]. Here, we use bovine serum albumin (BSA) to lower the substrate adhesiveness of fibrin/fibrinogen and investigate the effect of BSA in platelet migration. The fibrin/fibrinogen

coating protocol is adapted and modified [25]. Coverslips (#1) are firstly immersed in 20% NHO_3 for 1 hour and washed with distilled water (ddH_2O). The acid-washed coverslips are then immersed in ddH_2O for another hour and rinsed again with ddH_2O. The cleaned coverslips are then dried on a coverslip rack. Before fibrin/fibrinogen coating, a layer of Hexamethyldisilazane (HMDS) is silanised on the coverslip by vapour deposition to create a hydrophobic surface for protein binding. The dried coverslips are plasma cleaned for 4 minutes and then placed in a vacuum desiccator with a vial containing 1 ml of HMDS solution at room temperature. The desiccator is connected to a vacuum pump in a fume hood to deposit the HMDS vapour for 40 minutes. The effectiveness of HMDS coating is verified by checking the contact angle of the surface.

After the HMDS coating, a customized PDMS chamber (radius 10 mm, depth 6mm) is placed on the coverslip and 200 ul fibrin (300 μg/ml fibrinogen, 12 mg/ml BSA, 2U/ml thrombin, and 1 mM $CaCl_2$ supplemented in modified Tyrode's buffer, pH=7.4) or fibrinogen solution (300 μg/ml fibrinogen and 12 mg/ml BSA supplemented in modified Tyrode's buffer) is loaded into the chamber. These solutions are used immediately after mixing. For control experiments, modified Tyrode's buffer (pH=7.4) is added instead of BSA. The fibrin and fibrinogen coverslips are coated for 30 minutes and 1 hour at room temperature, respectively and then washed with modified Tyrode's buffer (pH=7.4) three times before use.

Washed platelets (protocol in Appendix E) is supplemented in modified Tyrode's buffer (pH=7.4) with 1 mg/ml BSA, 200 μM $CaCl_2$, 4μM U46619 and 10 μM ADP at final concentration of 10^7 platelets/ml. The imaging chamber is incubated at 37 °C for 40 minutes to allow platelet adhesion and migration before imaging. Note that incubation at 37 °C is recommended but not a determinant factor for migration. Platelet migration is also observed at room temperature but at a much slower speed and shorter trajectory.

6.3.2 Morphological Profiling of Single Platelet during Migration

The processing of quantifying morphological features is illustrated in Fig. 6-1. The fluorescence and scattering images are firstly overlapped to recognize migrating platelets. The criteria used to check if a platelet is migrating is to confirm a dark region associated with the platelet. The area of the dark region needs to be larger than half of a platelet size. We then crop scattering images of the migrating and non-migrating platelets into a small field of views (500×500 pixels) using Fiji (ImageJ). We put them into a different group for shape analysis using a cell profiler.

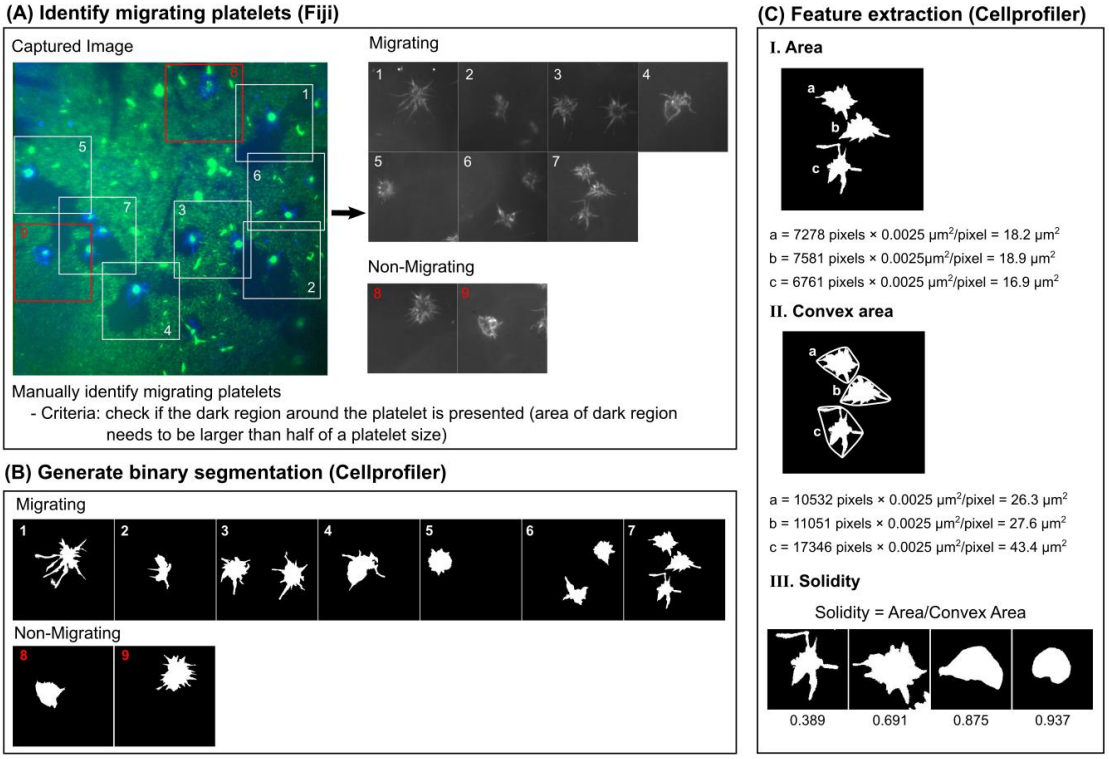

Figure 6-1 Quantifies platelet morphological features using Fiji (ImageJ) and Cellprofiler. (A) The migrating platelets are first identified using the overlapping fluorescence (green) image and scattering (blue) signal. The criteria for migration is to check if there is a dark region associated with the platelet, and the area of the dark region needs to be larger than half of a platelet size. The migrating and non-migrating platelets are then cropped into a small field of views (500×500 pixels) and put into different groups for shape analysis. (B) After that, the binary segmentation is generated using Cellprofiler, and the morphological features (area, convex area, and solidity) are calculated. (C) These quantifications are illustrated and explained with examples.

The total number of platelets being processed is 937, including 427 on the fibrin surface (288 platelets with BSA, 139 without BSA) and 510 on the fibrinogen surface (318 platelets with BSA, 192 without BSA). To generate binary segmentation of the platelets, the following modules are used in the processing: rescale intensity, identify primary object (platelet, with adaptive threshold, otsu method), identify secondary object (filopodia associated with the identified platelet, adaptive threshold, robust background method). The processed data is reviewed and edited manually if two objects touch each other. Morphological features of the platelet are calculated using the "measure object size and shape" module in the Cellprofiler. As shown in Fig. 6-1 C, the area is calculated as the product of the number of pixels covered in the object and the actual pixel size of the COSI-F system (0.025 μm^2/pixel). The convex area is the convex hull area that encloses the object, and the solidity is defined as the object area/convex area. In Fig. 6-1 C, we demonstrate the filopodia rich shape platelet can have a solidity of 0.39-0.7 while the round or half-moon shape platelets are around 0.85-0.94.

6.3.3 Tracking Intensity along Lamellipodia during Migration

To track the intensity on the lamellipodia of the platelet, a binary mask showing only the edge of the platelet is generated based on the scattering signal using ImageJ (auto local threshold function with Nilblack [44] algorithm and radius = 8). Because the membrane ruffles during migration and causes lamellipodia shifts in the lateral position, a stack of binary masks that corresponds to the lateral part of the edge at a different time point is generated to filter the intensity at lamellipodia only. After that, 14 regions on the lamellipodia are manually selected in the binarized image and then converted to ROIs using the BIOP image analysis plugin. The ROIs are selected on the interference image to quantify mean intensity. Because of varying intensity in scattered signals, the cell outline might appear discontinuous in some

frames after binarization and creating multiple small ROIs in one frame, and a separate MATLAB script is used to re-calculate mean intensity when multiple ROIs are presented.

6.4 COSI-F: Combinatorial Imaging

To effectively switch between interferometric, scattering and fluorescence microscopy, we need to simply switch between the scanning angles as shown in Fig. 6-2 A, where we projected 3 annular scanning illumination paths (red, blue and green) implemented on a single high numerical aperture (NA) objective lens of 1.49. The interference of back-reflection and the scattered light is collected here is at an illumination angle of 20°-35° (~N.A. = 1.49). This differs from ROCS where the authors retrieved the interference signal at a much larger angle (N.A. = 1.2 and 1.46). During imaging, a single laser beam (wavelength, λ= 488 nm) is directed onto a two-axis galvanometer and conjugated onto the back focal plane of the objective lens. The two-axis galvanometer allows precise adjustment to different scanning radii which in turn selects the imaging mode (Scattering, Interferometric, and Fluorescence). While fluorescence imaging (green) can be obtained from any azimuthal scanning pattern [45, 46], interferometric and scattering-only images [5, 16] are separated by two scanning radii (red, blue). Experimentally, this can be determined and preset, as shown in Fig. 6-2 A on conjugated back focal planes (BFP). Here, interference contrast is maximized without using specialized partially reflective mirror [16]. As shown in Fig. 6-2 B, at higher azimuthal oblique angles (>50°), one can choose between brightfield and darkfield ROCS by opening (BF) or closing (DF) the diaphragm placed in the BFP to remove reflected intensities (*i.e.* from coverglass and particles). Using the oblique illumination angle alone, we can achieve interferometric imaging at an oblique angle θ of 22° and scattering mode at an illumination angle greater than 50° (Figure 6-2 B). The iris diaphragm has zero transmittance on the edge and will not induce phase shift.

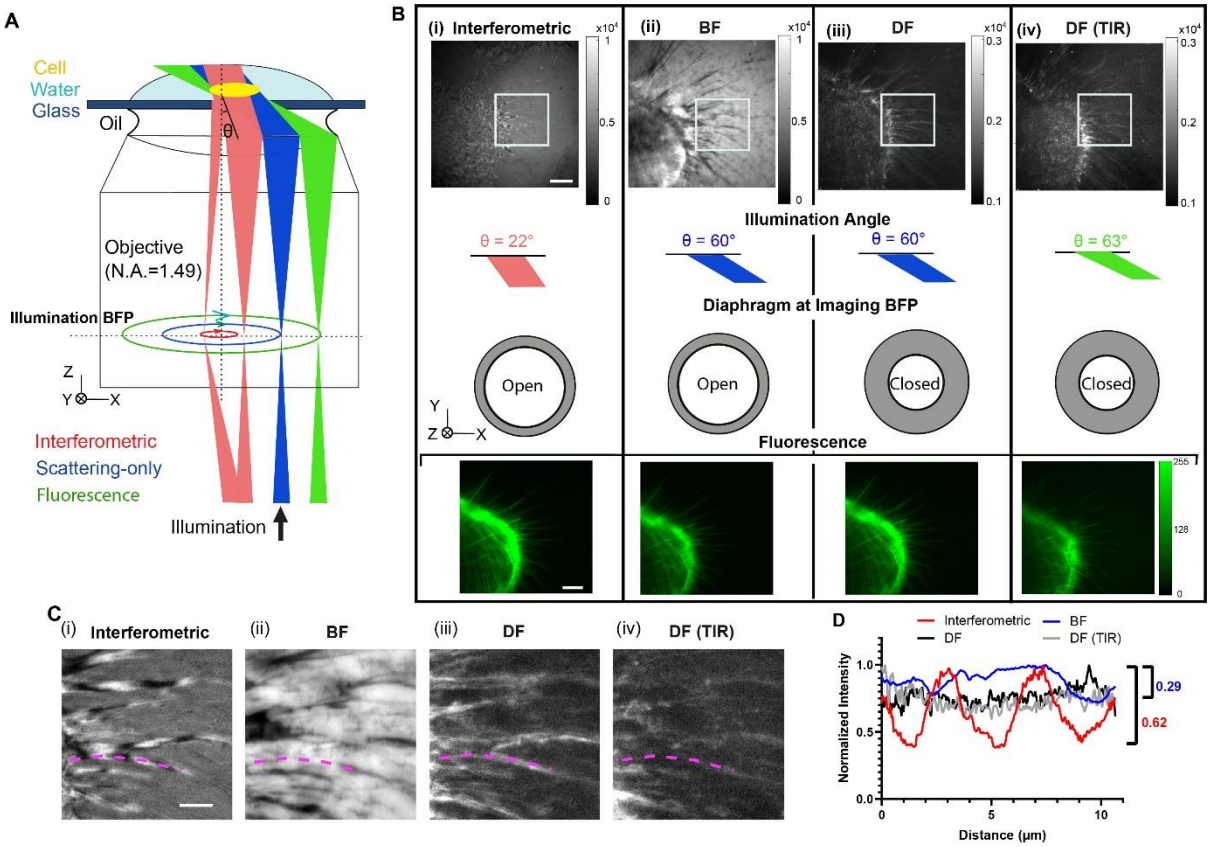

Figure 6-2 (A) An oblique beam (with angle θ corresponding to optical axis) is radically scanning at back focal plane (BFP) of the 1.49 NA objective. When θ = 10° to 40° (red), the interference of back-reflection from the coverslip and scattered light will be collected by the detector, and when θ > 50° (green), the back-reflection will be blocked by a diaphragm at the imaging BFP that only allow pure scattering to be detected (darkfield). The fluorescence signal (blue) will be collected simultaneously at corresponding angles without blocking due to the dual camera detection scheme. (B) Label-free and fluorescent imaging using interferometric, BF, DF and TIR ROCS imaging of HMVEC cells (labelled with Alexa Fluor 488 conjugated Phalloidin). Scale bar = 5 μm. The illumination angles (22°, 60° (HiLo) and 63° (TIRF)) and diaphragm opening at the imaging BFP are illustrated for each modality. (C) Zoomed views of the highlighted filopodia region in (B, i-iv) for each modality and (D) plot of the fringe intensity profile along a filopodium indicated in D (i-iv) (magenta dashed line). Scale bar = 2 μm.

We firstly tested the combined imaging of fixed HMVEC cells adhered on a glass coverslip. Fig. 6-2 B (i) to (iv) shows a sequence of interferometric, scattering (BF and DF ROCS) and fluorescence images of F-actin (phalloidin)-labelled HMVEC cells under different oblique illumination angles from 22° to 63°. While changing from 55° to 60°, we observed the inversion of scattering and background signal (Fig. 6-2 B (i, ii)) from brightfield to darkfield. Fluorescence images taken at oblique illumination angles (θ = 60°, 63°)

displayed increased contrast than at θ = 22°. Fig. 6-2 C shows the magnified view of filopodia indicated in Fig. 6-2 B and Fig. 6-2 D, the measured intensities along the marked filopodium protrusion. Restricting the diaphragm diameter leads to contrast inversion of filopodia from BF to DF ROCS (θ = 60°). In BF and DF ROCS, interference intensity fringe are no longer observed. In interferometric ROCS, interference intensity fringes are distributed along a filopodia (Fig. 6-2 D). We then quantify the intensity fringe against the intensity signal from BF and DF ROCS is shown in (Fig. 6-2 D) after normalizing the intensities. This comparison informs us that the intensity variations of interference fringes from interferometric ROCS is distinctively different from that of BF and DF ROCS.

Interferometric scattering signals, shown in Fig. 6-2 C (i) and D provided a negative contrast because of the cosine term in the interferometric component $2E_rE_scos\phi$, where Er, is the reflected electric field from the coverslip, E_s is scattering electric field from the sample and ϕ is the relative phase difference between E_r and E_s. Scattering cross-section of the sample (Es) will scale nonlinearly with particle size, where E_r will scale with just reflecting angle. In other words, a smaller object will thereby have lower scattering (E_s) and E_r changes with just angle. As with any interference signal, the balance of E_r and E_s are necessary for high fringe contrast. Because of sample variability, the visibility of the interference fringes in an interferometric scattering signal requires the balancing between E_r and E_s as shown in Fig. 6-4.

We next investigated detection limit of each imaging mode, interferometric, scattering and fluorescence using gold and polymer nanoparticles. We choose a range of GNPs with a mean diameter of 20± 6.3 nm, 40± 8.9 nm, and 60± 17 nm and fluorescence beads of 200 nm. The nanoparticle diameters are chosen because the cross-section of gold scales exponentially below 100 nm, modelled in Fig. 6-3, which influences the scattering intensity (I_s).

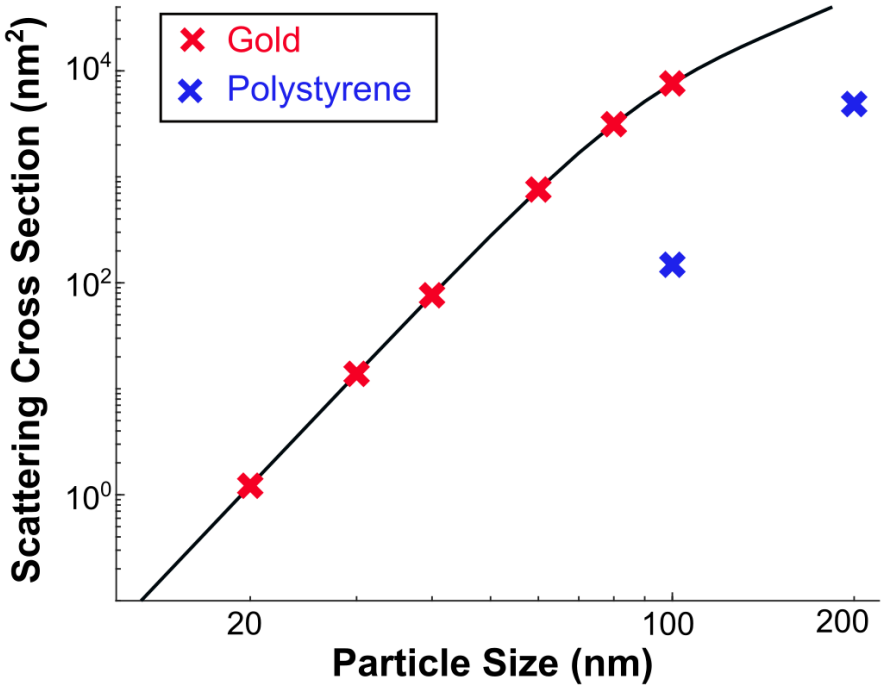

Figure 6-3 Scattering cross-section of gold (20 nm, 30 nm, 40nm, 60nm, 80 nm, and 100 nm) and polystyrene particles (100 nm and 200 nm), calculated using Mie theory. The calculation of scattering cross-section is based on illumination wavelength of 488 nm, the refractive index of the medium, and particles to be 1.33, 1.1271+1.8382i (gold) and 1.59 (polystyrene), respectively. The plot is on a log-log scale.

Fig. 6-4 A to D compares imaging contrasts of interference, scattering, and fluorescence using signal to noise ratio (SNR) by scanning oblique angle from 5.7° to 76.8 °. The method for SNR calculation can be found in Appendix C. Fig. 6-4 A and B shows GNPs with 20nm, 40nm, and 60 nm under various oblique illumination angle. We only compare the interference and scattering signals for GNPs. SNR results for 20 nm GNPs with a low scattering cross-section of 1.32 nm^2 (~1.6% of total surface area) are much higher in interference detection than scattering imaging. Fig. 6-4 A show that scattering signal (Is) exhibit an SNR of 0.08 ± 0.022, whereas the interference SNR ($\frac{\mathrm{Is}.2E\_rE\_\cos\phi}{\mathrm{Ir}}$) [47] is about 37% higher (0.11 ± 0.022).

Conversely, we show that an increase of the scattering cross-section by orders of magnitudes, ~ 81.3 nm^2 (40 nm gold nanoparticle) and 791 nm^2 (60 nm gold nanoparticle)

results in dominant scattering SNR when compared with interference SNR as shown in Fig. 6-4 B. Fig. 6-4 B showed that scattering SNR reached a value of 3.25 ± 0.97 to 0.566 ± 0.05 which are higher than the value of interference SNR that hovers around 0.278 ± 0.05 to 0.60 ± 0.27. Our finding shows that interference SNR ($2E_rE_scos\phi$) [47] significantly improves imaging contrast when particles have a small scattering cross-section of around 1.32 nm^2.

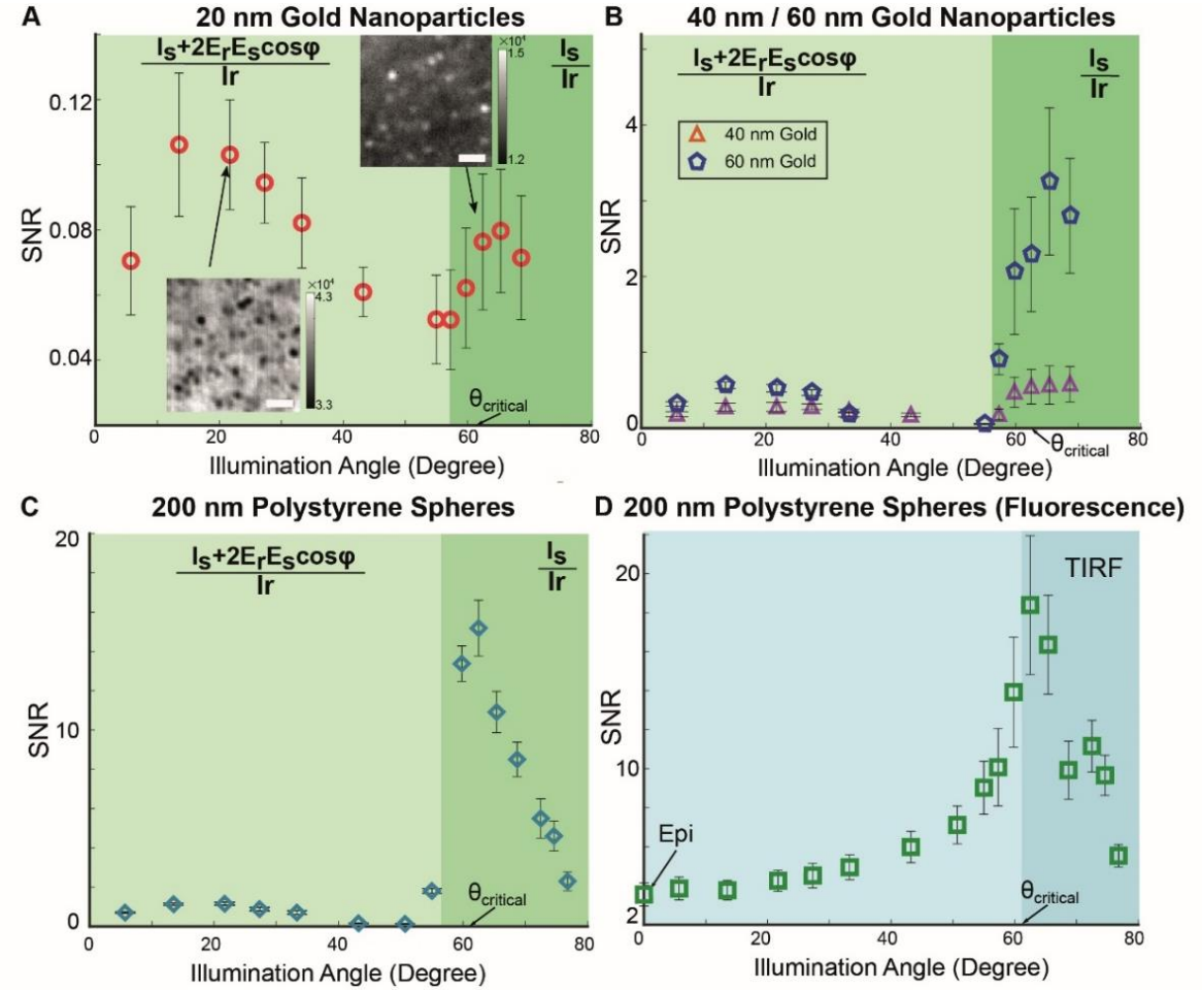

Figure 6-4 Quantification of signal to noise ratio of nanoparticles ranging from 20 – 200nm (diameter) with scattering and fluorescence detection. SNR of (A) 20 nm, (B) 40 nm and 60 nm gold nanoparticles and (C) 200 nm polystyrene using scattering detection under different illumination angles ranging from 5° to 70°, where the diaphragm is set to block back-reflection at 57°, and the critical angle is at 63°. Inlet images in (A) are interference and pure scattering signals of the particles at 22° and 63°, respectively. Scale bar = 1 μm. (D) SNR of the 200 nm polystyrene with fluorescence detection, where the critical angle is at 63°. Error bar = standard derivation from the measurement of at least 50 nanoparticles.

Next, we compare particles size with a diameter of 200 nm. Fig. 6-4 C and D compare the interference, scattering, and fluorescence SNR of 200 nm polystyrene beads with a scattering cross-section of 4866 nm^2 (over the third power of magnitude higher than observed for 20 nm GNPs). Scattering SNR in 200 nm polystyrene beads has a value of 15.19 ± 1.42 that is close to 10-fold higher than interference SNR with a value of 1.13 ± 0.05.

Interferometric SNR in SIF would naturally possess axial information that can be used to retrieve a 3D point-spread function [48]. This permits interferometric signals to track gold nanoparticles axially [15, 48] that can be developed for tracking cell membrane protrusions [49]. To calibrate this, we investigate axial interference SNR using the same GNPs sizing from 20 nm, 60 nm, and 100 nm as well as 100 nm polystyrene. All the particles are fixed on a thin coverglass, which is placed on a piezo nanostage (P-736, Physik Instrument) as shown in Fig. 6-5 A. The sample is illuminated obliquely at 22^o is swept axially through the objective focus at an interval of 10 nm step sizes. As shown in Fig. 6-5 B and C, for 60 nm and 100 nm GNPs (higher scattering cross section of 7620 nm^2 and 81.3 nm^2), the axial interferometric intensity displays a characteristic sinusoidal intensity gradient. On the other hand, when scattering cross section is reduced by an order of magnitude to ~1.32 nm^2, the intensity gradient followed a parabolic curve as presented Fig. 6-5 D. The parabolic curve in 20 nm gold nanoparticles indicate that destructive interference ($cos\phi$) [47] is responsible for high axial resolution for nanometer gold scatterers. Axial interference SNR for membrane tracking used the linear region calibrated with 100 nm polystyrene sphere that has a refractive index close to actin (~1.57) [50]. In summary, Fig. 6-5 B to E shows that the total axial tracking distance of COSI-F for all particle sizes ranges between 0.67 to 0.7 μm.

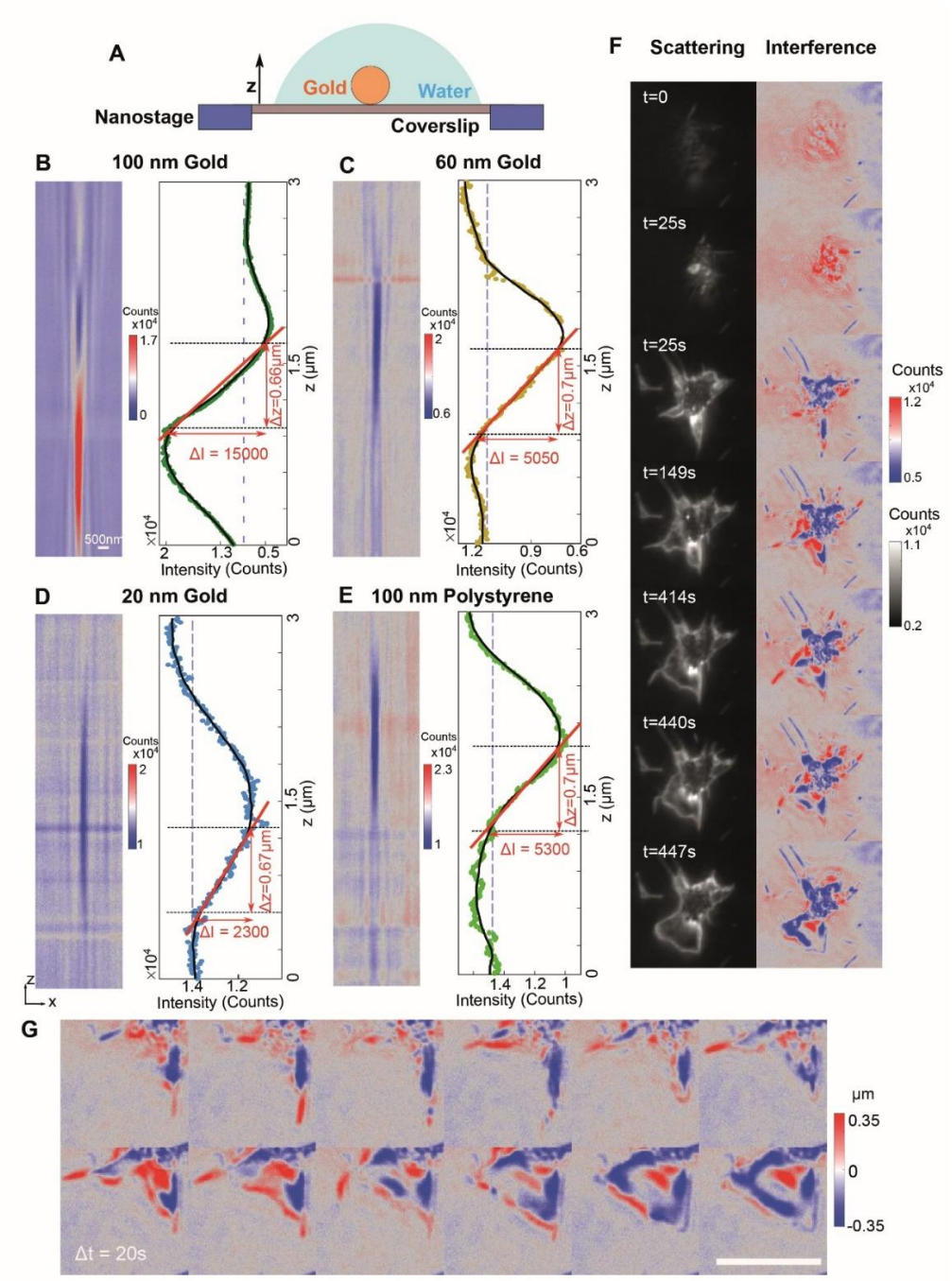

Figure 6-5 Calibrating axial intensity profile and displacement with nanoparticles from 20 nm to 100 nm. (A) To record the intensity profile of gold/polystyrene nanoparticles, we first dried the particles on a coverslip and then immersed them in water. The coverslip was placed on a piezo nanostage that allows axial sweeping of the sample across the focus at 10 nm steps. The axial intensity map along with the line profile of GNPs at (B) 100 nm, (C) 60nm and (D) 20nm, and (E) polystyrene nanoparticles at 100 nm are plotted as scattered plot, the black line indicates the moving average of 30 points. The red line represents the relation between intensity (ΔI) and axial displacement (Δz). (F) Simultaneous recording of both scattering and interference for 447 seconds showing early platelet adhesion, filopodia and lamellipodia formation and spreading on fibrin surfaces. Scale bar = 5 μm. (G) Axial displacements of the membrane protrusions at 20 seconds time intervals.

6.5 Imaging of Single Platelet Migrating at Nanoscale

Recent live imaging studies of platelets have showed different biomechanical actions associated with platelet membrane protrusions. Platelet filopodium was observed to make "hand over hand" actions on fibrin fibers[51]. Platelet have been seen to migrate with formed lamellipodium when exposure to pathogens on coated fibrinogen surfaces. We previously demonstrated that high speed label-free platelet imaging, with rotating coherent scattering (ROCS) [5, 52] ,captured unlabelled platelet generating rodlike-extension filopodia instead of thin-sheet lamellipodia to directly attach onto single collagen fibril under arterial fluid shear [41, 53]. ROCS alone is insufficient to investigate other platelet morphodynamics along the axial direction as well as membrane surface signalling processes. We now overcome the limitation by using combined fluorescence, interferometric and scattering imaging to study platelet lateral and axial membrane protrusions dynamics on glass surfaces coated with fibrinogen or fibrin (cross-linked fibrinogen).

For each coated surface, we either add or omit BSA to study platelet migration (detailed in method section). We first evaluate simultaneous scattering and interference COSI-F on platelet arriving onto fibrin coated surfaces. Unlike traditional RICM imaging, COSI-F can capture platelet adhesion from initial contact to initial stages of spreading and adhesion on fibrin-coated glass surfaces. Fig. 6-6 F shows the simultaneous recording of both scattering and interference signals for 447 seconds. While interference signals only occur close to the coverslip, the scattering signal in COSI-F suppresses the background to capture floating platelets before adhesion at high contrast (without post-processing). The scattering signal is sufficiently high for automated segmentation and tracking. The interference signal is used to quantify axial displacements on those membrane protrusions, as shown in Fig. 6-5 G

at 5 second time intervals. Fig. 6-5 G tracks the first instances of filopodia formation during adhesion before a lamellipodium is formed.

To visualize migrating tracks with and without BSA, we label fibrinogen and fibrin with fluorescence label (Alexa Fluor 488) using previously published protocols [25, 30]. Here, migrating tracks are shown by a lost in fluorescence due to uptake of fibrin or fibrinogen coating on glass surfaces. The tracks are imaged using fluorescence imaging.

Fig. 6-6 A(i) to (iv) shows that combining scattering and fluorescence signal, using BSA treated sample, adherent platelets are seen to internalized fibrinogen and fibrin. A bright fluorescence spot is located intracellularly in the platelet using the fluorescence signal. Using the scattering and interference signals, platelets' cellular morphology in 3D can be quantified using standard cell segmentation and profiling tools in an open-source program Cellprofiler [54]. We sorted the imaged platelets (n_{fibrin}=427 and $n_{fibrinogen}$ 510) against two different classifiers, namely area (μm^2) and solidarity. Area is meant to show cell spreading. For platelets with a larger spread could indicate flat membrane protrusion resembling lamellipodium. Solidarity is defined by irregularity along the cell boundaries. Platelets with many filopodium protrusion (finger-like) would score low on the solidarity point.

Fig. 6-6 B (i) show the classifiers (area and solidarity) and the percentage of migrating platelets on fibrin and fibrinogen coated surfaces. The results show that no migration is observed without the inclusion of BSA (no visible tracking due to loss of fluorescence). Overall, Fig. 6-6 B (i) show around four folds more platelets migrating under fibrin coated. Conversely, platelets would generally migrate on fibrinogen coated surfaces. Using the classifiers, we can further separate the morphological profiles of the migrating and non-migrating platelets as shown in Fig. 6-6 B ii) and iii). Platelets on fibrin coated surfaces show comparatively smaller surface area than the fibrinogen coated surfaces. On the other

hand, there is no significant variation amongst the migrating and non-migrating platelets on the solidity scoring. Overall, this meant that the platelet adhesion under spreading conditions would generate highly heterogeneous morphology profiles. Such heterogenous membrane protrusion differs from our previous observation of platelet under flow on collagen matrix where scattering imaging only displayed filopodia formation and could have important implication of thrombus-based fibrinolysis. We then carry out automated axial tracking of lamellipodium of a migrating platelet on fibrin coated surface with scattering and interference signal, as shown in Fig. 6-6 C (i). The fluctuation in intensity indicates a peak to peak height displacement of around 0.13 μm, as demonstrated in Fig. 6-6 C (ii). In Fig. 6-6 C (iii), we compared both the leading and rear edge of the migrating platelet by plotting the overall axial fluctuations. The leading edge showed a normal distribution of membrane displacement entered at 0 (*i.e.* no protrusion or retraction). However, the rear edge exhibited unequal membrane fluctuations of -0.13 μm (retraction) to 0.13 μm (extension), shown as two peaks in Fig. 6-3 C, (iii). The heterogeneity of membrane fluctuations may reflect unequal membrane tension during cell migration. Out of phase fluctuations indicate asynchronous behaviour of cell migration inferring differences in adhesion strength [55] between the leading and rear edge.

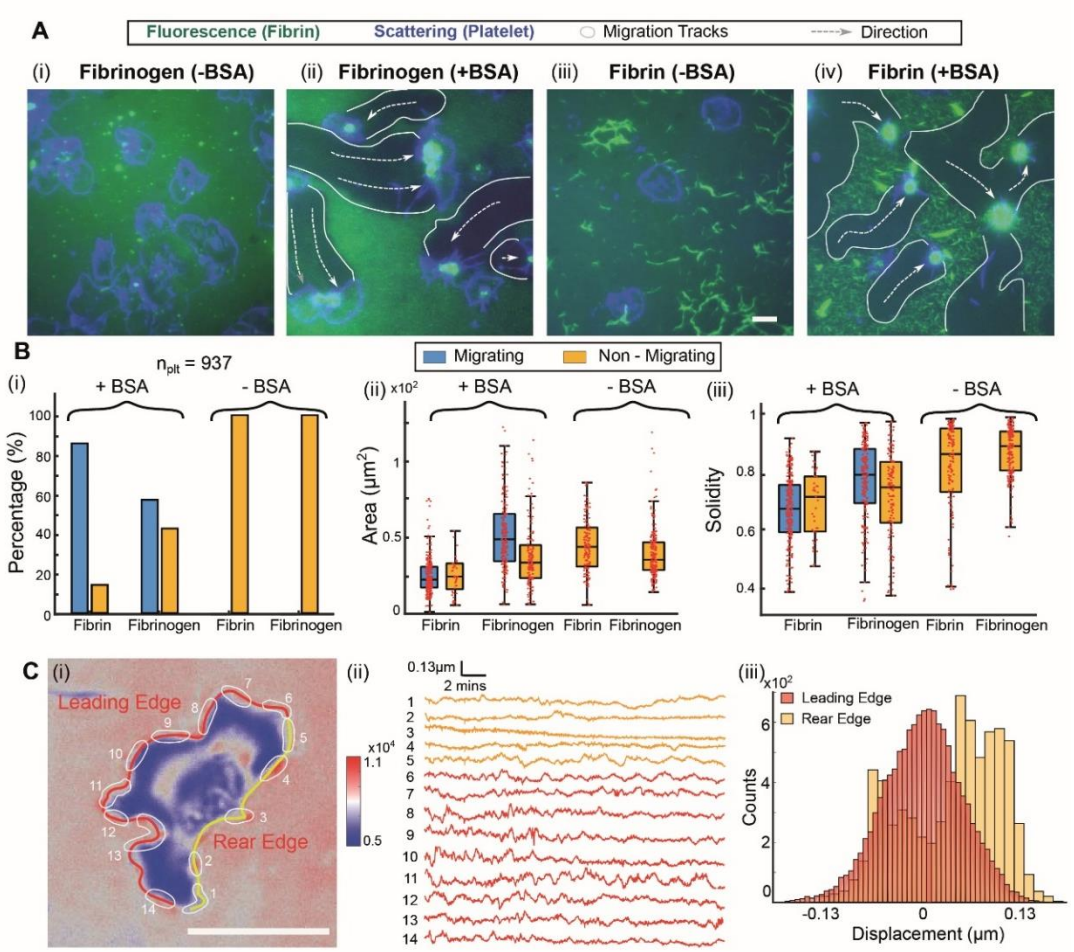

Figure 6-6 Tracking platelet migration on fibrin/fibrinogen coated surface. (A) Combined fluorescence and scattering signal of single platelet migration on fibrin and fibrinogen coated surfaces with/without BSA. The Green channel and blue channels are fluorescence and scattering signals, respectively. The trajectory of platelet movement is highlighted with white border with a white arrow indicating the predicted direction of migration. (B) Quantification of platelet migration and morphology (area and solidity) with four types of coating. Platelet morphology is quantified through Cellprofiler. The number of platelets quantified was n = 427 and n = 510 for fibrin and fibrinogen coated surfaces. (C) (i) Interference signal of a migrating platelet on the fibrin-coated surface. (ii) The axial displacement along the leading edge and the rear edge is tracked during 25 minutes of spreading, with orange and red representing the rear and leading edge, respectively. (iii) Histogram showing the counts on the axial displacement of the rear and leading edge.

6.6 Conclusion

This chapter demonstrates GNPs and platelet imaging using the COSI-F system. We show the detection sensitivity down to 20 nm GNPs without post-processing with the interference detection. We then used platelets migration assay to show multiplex imaging of scattering, interference, and fluorescence signal that simultaneously tracks migration, morphology, and axial fluctuation. We observed the leading edge of the platelet has more axial fluctuation than the rare edge, possibly due to the high concentration of the Arp2/3 complex that affects actin polymerization. COSI-F also detect a folded filopodium to form the edge of a lamellipodium (Fig. 6-6). These filopodia and lamellipodia structure changes could relate to actin filament organization during cytoskeleton rearrangement, but the mechanism remains unclear. Future studies investigating the role of integrins and membrane proteins would be helpful to interpret the behaviour of these membrane activities.

For a single laser line, COSI-F has the potential to incorporate multiplex fluorescence, scattering, and interference signals, all of which can be used to report on the spatial organization of intracellular organelles [56], ligand or lipid coating on substrates surface [57], membrane receptor [58], intracellular calcium flux [59], actin polymerization [60] along with continuous track morphological changes of the cell membrane and protrusion in the context of those biochemical signals. Based on the high contrast imaging observed, COSI-F will significantly impact studies that aim to elucidate nanoscale membrane curvatures [61], membrane pores[62], transmembrane protein [63], surface receptors[64], and external mechanical forces[65]. These factors would influence the formation of membrane protrusion (lamellipodia, ruffles, filopodia).

A weakness in the interference COSI-F here is based on a simple thin-film model [66], which can apply for platelets that do not have a complex internal morphology. For more

complex cells, the interference signal will be difficult to interpret. As one can already notice, the signal from the pseudo nucleus shows complex intensity changes. To map out more complex intensity changes, one must move the re-calibrate axial using a non-coverslip adhesion probe [15]. Since COSI-F do not use any form of post-processing, we postulate that detection sensitivity could be further enhanced by using standard ratiometric subtraction.

6.7 Contribution

I built the COSI-F system and performed the experimental work related to GNP and platelets. Dr Yean Jin Lim develop live cell imaging chamber and conducted intracellular imaging on endothelial cells. Ms Yee Lin Thong prepared washed platelet sample. The data analysis is done with Mr Hanqi Lin (Intensity tracking) and Ms Carmen Longbottom (Cell profiler).

6.8 References

1. Simmert, S.; Abdosamadi, M. K.; Hermsdorf, G.; Ffer, E. S., LED-based interference-reflection microscopy combined with optical tweezers for quantitative three-dimensional microtubule imaging. *Optics Express* **2018,** *26* (11), 14499.

2. Mahamdeh, M.; Howard, J., Implementation of interference reflection microscopy for label-free, high-speed imaging of microtubules. *Journal of Visualized Experiments* **2019,** *2019* (150).

3. Schermelleh, L.; Ferrand, A.; Huser, T.; Eggeling, C.; Sauer, M.; Biehlmaier, O.; Drummen, G. P. C., Super-resolution microscopy demystified. *Nature Cell Biology* **2019,** *21* (1), 72-84.

4. Hsiao, Y.-T.; Tsai, C.-N.; Cheng, C.-Y.; Hsieh, C.-L., Molecularly Specific and Functional Live Cell Imaging by Label-Free Interference Microscopy. *ACS Photonics* **2022,** *9* (7), 2237-2245.

5. Ruh, D.; Mutschler, J.; Michelbach, M.; Rohrbach, A., Superior contrast and resolution by image formation in rotating coherent scattering (ROCS) microscopy. *Optica* **2018,** *5* (11), 1371-1381.

6. Jünger, F.; Ruh, D.; Strobel, D.; Michiels, R.; Huber, D.; Brandel, A.; Madl, J.; Gavrilov, A.; Mihlan, M.; Daller, C. C.; Rog-Zielinska, E. A.; Römer, W.; Lämmermann, T.; Rohrbach, A., 100 Hz ROCS microscopy correlated with fluorescence reveals cellular dynamics on different spatiotemporal scales. *Nature Communications* **2022,** *13* (1), 1758.

7. Boyer, D.; Tamarat, P.; Maali, A.; Lounis, B.; Orrit, M., Photothermal Imaging of Nanometer-Sized Metal Particles Among Scatterers. *Science* **2002,** *297* (5584), 1160-1163.

8. Young, G.; Kukura, P., Interferometric Scattering Microscopy. *Annual Review of Physical Chemistry* **2019,** *70* (1), 301-322.

9. Cotte, Y.; Toy, F.; Jourdain, P.; Pavillon, N.; Boss, D.; Magistretti, P.; Marquet, P.; Depeursinge, C., Marker-free phase nanoscopy. *Nature Photonics* **2013,** *7* (2), 113-117.

10. Piliarik, M.; Sandoghdar, V., Direct optical sensing of single unlabelled proteins and super-resolution imaging of their binding sites. *Nature Communications* **2014,** *5* (1), 4495.

11. Taylor, R. W.; Mahmoodabadi, R. G.; Rauschenberger, V.; Giessl, A.; Schambony, A.; Sandoghdar, V., Interferometric scattering microscopy reveals microsecond nanoscopic protein motion on a live cell membrane. *Nature Photonics* **2019,** *13* (7), 480-487.

12. Dominika, J.; Kristyna, H.; Milan, V.; Marek, P. In *Interferometric scattering (iSCAT) microscopy with optimized reference wave*, Proc.SPIE, 2019.

13. Junger, F.; Rohrbach, A., Strong cytoskeleton activity on millisecond timescales upon particle binding revealed by ROCS microscopy. *Cytoskeleton (Hoboken)* **2018,** *75* (9), 410-424.

14. Taylor, R. W.; Sandoghdar, V., Interferometric Scattering Microscopy: Seeing Single Nanoparticles and Molecules via Rayleigh Scattering. *Nano Letters* **2019,** *19* (8), 4827-4835.

15. Gholami Mahmoodabadi, R.; Taylor, R. W.; Kaller, M.; Spindler, S.; Mazaheri, M.; Kasaian, K.; Sandoghdar, V., Point spread function in interferometric scattering microscopy (iSCAT). Part I: aberrations in defocusing and axial localization. *Opt. Express* **2020,** *28* (18), 25969-25988.

16. Cole, D.; Young, G.; Weigel, A.; Sebesta, A.; Kukura, P., Label-Free Single-Molecule Imaging with Numerical-Aperture-Shaped Interferometric Scattering Microscopy. *ACS Photonics* **2017,** *4* (2), 211-216.

17. Young, G.; Hundt, N.; Cole, D.; Fineberg, A.; Andrecka, J.; Tyler, A.; Olerinyova, A.; Ansari, A.; Marklund, E. G.; Collier, M. P.; Chandler, S. A.; Tkachenko, O.; Allen, J.; Crispin, M.; Billington, N.; Takagi, Y.; Sellers, J. R.; Eichmann, C.; Selenko, P.; Frey, L.; Riek, R.; Galpin, M. R.; Struwe, W. B.; Benesch, J. L. P.; Kukura, P., Quantitative mass imaging of single biological macromolecules. *Science* **2018,** *360* (6387), 423-427.

18. Radler, J.; Sackmann, E., Imaging Optical Thicknesses and Separation Distances of Phospholipid-Vesicles at Solid-Surfaces. *J Phys Ii* **1993,** *3* (5), 727-748.

19. Mann, C.; Yu, L.; Lo, C. M.; Kim, M., High-resolution quantitative phase-contrast microscopy by digital holography. *Opt Express* **2005,** *13* (22), 8693-8.

20. Pleines, I.; Eckly, A.; Elvers, M.; Hagedorn, I.; Eliautou, S.; Bender, M.; Wu, X.; Lanza, F.; Gachet, C.; Brakebusch, C.; Nieswandt, B., Multiple alterations of platelet functions dominated by increased secretion in mice lacking Cdc42 in platelets. *Blood* **2010,** *115* (16), 3364-3373.

21. Pierre, H. M.; Marie-Blanche, O.; Nicolas, R.; Nicolas Le, L.; Alexander, T. H.; Clare, W.; Ximena, S.; Stéphane, L.; Arnaud, D.; Amir, K. B.; Jeanette, L. C. M.; Helen, P.; Craig, E. H.; Andrew, B. H.; Robert, A. S. A.; Diego, M.; Martine, J.-P.; Christian, G.; Steve, P. W., Immobilized fibrinogen activates human platelets through glycoprotein VI. *Haematologica* **2018,** *103* (5), 898-907.

22. Montague, S. J.; Hicks, S. M.; Lee, C. S.-M.; Coupland, L. A.; Parish, C. R.; Lee, W. M.; Andrews, R. K.; Gardiner, E. E., Fibrin exposure triggers αIIbβ3-independent platelet aggregate formation, ADAM10 activity and glycoprotein VI shedding in a charge-dependent manner. *Journal of Thrombosis and Haemostasis* **2020,** *18* (6), 1447-1458.

23. Kaneva, V. N.; Dunster, J. L.; Volpert, V.; Ataullahanov, F.; Panteleev, M. A.; Nechipurenko, D. Y., Modeling Thrombus Shell: Linking Adhesion Receptor Properties and Macroscopic Dynamics. *Biophys J* **2021,** *120* (2), 334-351.

24. Sandmann, R.; Koster, S., Topographic Cues Reveal Two Distinct Spreading Mechanisms in Blood Platelets. *Sci Rep* **2016,** *6*, 22357.

25. Gaertner, F.; Ahmad, Z.; Rosenberger, G.; Fan, S.; Nicolai, L.; Busch, B.; Yavuz, G.; Luckner, M.; Ishikawa-Ankerhold, H.; Hennel, R.; Benechet, A.; Lorenz, M.; Chandraratne, S.; Schubert, I.; Helmer, S.; Striednig, B.; Stark, K.; Janko, M.; Böttcher, R. T.; Verschoor, A.; Leon, C.; Gachet, C.; Gudermann, T.; Mederos y Schnitzler, M.; Pincus, Z.; Iannacone, M.; Haas, R.; Wanner, G.; Lauber, K.; Sixt, M.; Massberg, S.,

Migrating Platelets Are Mechano-scavengers that Collect and Bundle Bacteria. *Cell* **2017,** *171* (6), 1368-1382.e23.

26. Cunniff, B.; McKenzie, A. J.; Heintz, N. H.; Howe, A. K., AMPK activity regulates trafficking of mitochondria to the leading edge during cell migration and matrix invasion. *Mol Biol Cell* **2016,** *27* (17), 2662-74.

27. Campello, S.; Lacalle, R. A.; Bettella, M.; Manes, S.; Scorrano, L.; Viola, A., Orchestration of lymphocyte chemotaxis by mitochondrial dynamics. *J Exp Med* **2006,** *203* (13), 2879-86.

28. Lopez-Domenech, G.; Covill-Cooke, C.; Ivankovic, D.; Halff, E. F.; Sheehan, D. F.; Norkett, R.; Birsa, N.; Kittler, J. T., Miro proteins coordinate microtubule- and actin-dependent mitochondrial transport and distribution. *EMBO J* **2018,** *37* (3), 321-336.

29. Ridley, Anne J., Life at the Leading Edge. *Cell* **2011,** *145* (7), 1012-1022.

30. Nicolai, L.; Schiefelbein, K.; Lipsky, S.; Leunig, A.; Hoffknecht, M.; Pekayvaz, K.; Raude, B.; Marx, C.; Ehrlich, A.; Pircher, J.; Zhang, Z.; Saleh, I.; Marel, A.-K.; Löf, A.; Petzold, T.; Lorenz, M.; Stark, K.; Pick, R.; Rosenberger, G.; Weckbach, L.; Uhl, B.; Xia, S.; Reichel, C. A.; Walzog, B.; Schulz, C.; Zheden, V.; Bender, M.; Li, R.; Massberg, S.; Gaertner, F., Vascular surveillance by haptotactic blood platelets in inflammation and infection. *Nature Communications* **2020,** *11* (1), 5778.

31. Yeoman, B.; Shatkin, G.; Beri, P.; Banisadr, A.; Katira, P.; Engler, A. J., Adhesion strength and contractility enable metastatic cells to become adurotactic. *Cell Reports* **2021,** *34* (10), 108816.

32. Mattila, P. K.; Lappalainen, P., Filopodia: molecular architecture and cellular functions. *Nature Reviews Molecular Cell Biology* **2008,** *9* (6), 446-454.

33. Yamada, K. M.; Sixt, M., Mechanisms of 3D cell migration. *Nature Reviews Molecular Cell Biology* **2019,** *20* (12), 738-752.

34. Lee, H. J.; Diaz, M. F.; Price, K. M.; Ozuna, J. A.; Zhang, S.; Sevick-Muraca, E. M.; Hagan, J. P.; Wenzel, P. L., Fluid shear stress activates YAP1 to promote cancer cell motility. *Nature Communications* **2017,** *8* (1), 14122.

35. Fassett, J.; Tobolt, D.; Hansen, L. K., Type I Collagen Structure Regulates Cell Morphology and EGF Signaling in Primary Rat Hepatocytes through cAMP-dependent Protein Kinase A. *Molecular Biology of the Cell* **2006,** *17* (1), 345-356.

36. Dustin, M. L., The Immunological Synapse. *Cancer Immunology Research* **2014,** *2* (11), 1023-1033.

37. Guerrero-Juarez, C. F.; Dedhia, P. H.; Jin, S.; Ruiz-Vega, R.; Ma, D.; Liu, Y.; Yamaga, K.; Shestova, O.; Gay, D. L.; Yang, Z.; Kessenbrock, K.; Nie, Q.; Pear, W. S.; Cotsarelis, G.; Plikus, M. V., Single-cell analysis reveals fibroblast heterogeneity and myeloid-derived adipocyte progenitors in murine skin wounds. *Nature Communications* **2019,** *10* (1), 650.

38. Montague, S. J.; Lim, Y. J.; Lee, W. M.; Gardiner, E. E., Imaging Platelet Processes and Function—Current and Emerging Approaches for Imaging in vitro and in vivo. *Frontiers in Immunology* **2020,** *11* (78).

39. MAHAUT-SMITH, M. P., The unique contribution of ion channels to platelet and megakaryocyte function. *Journal of Thrombosis and Haemostasis* **2012,** *10* (9), 1722-1732.

40. Andrews, R. K.; Gardiner, E. E.; Shen, Y.; Whisstock, J. C.; Berndt, M. C., Glycoprotein Ib–IX–V. *The International Journal of Biochemistry & Cell Biology* **2003,** *35* (8), 1170-1174.

41. Schurr, Y.; Sperr, A.; Volz, J.; Beck, S.; Reil, L.; Kusch, C.; Eiring, P.; Bryson, S.; Sauer, M.; Nieswandt, B.; Machesky, L.; Bender, M., Platelet lamellipodium formation is not required for thrombus formation and stability. *Blood* **2019,** *134* (25), 2318-2329.

42. Sorrentino, S.; Conesa, J. J.; Cuervo, A.; Melero, R.; Martins, B.; Fernandez-Gimenez, E.; de Isidro-Gomez, F. P.; de la Morena, J.; Studt, J.-D.; Sorzano, C. O. S.; Eibauer, M.; Carazo, J. M.; Medalia, O., Structural analysis of receptors and actin polarity in platelet protrusions. *Proceedings of the National Academy of Sciences* **2021,** *118* (37), e2105004118.

43. Allen, R. D.; Zacharski, L. R.; Widirstky, S. T.; Rosenstein, R.; Zaitlin, L. M.; Burgess, D. R., Transformation and motility of human platelets: details of the shape change and release reaction observed by optical and electron microscopy. *Journal of Cell Biology* **1979,** *83* (1), 126-142.

44. Nichele, L.; Persichetti, V.; Lucidi, M.; Cincotti, G., Quantitative evaluation of ImageJ thresholding algorithms for microbial cell counting. *OSA Continuum* **2020,** *3* (6), 1417-1427.

45. Tokunaga, M.; Imamoto, N.; Sakata-Sogawa, K., Highly inclined thin illumination enables clear single-molecule imaging in cells. *Nature Methods* **2008,** *5* (2), 159-161.

46. Axelrod, D., Total internal reflection fluorescence microscopy in cell biology. *Traffic* **2001,** *2* (11), 764-774.

47. Taylor, R. W.; Sandoghdar, V., Interferometric Scattering (iSCAT) Microscopy and Related Techniques. In *Label-Free Super-Resolution Microscopy*, Astratov, V., Ed. Springer International Publishing: Cham, 2019; pp 25-65.

48. Dong, J.; Maestre, D.; Conrad-Billroth, C.; Juffmann, T., Fundamental bounds on the precision of iSCAT, COBRI and dark-field microscopy for 3D localization and mass photometry. *Journal of Physics D: Applied Physics* **2021,** *54* (39), 394002.

49. Park, J.-S.; Lee, I.-B.; Moon, H.-M.; Ryu, J.-S.; Kong, S.-Y.; Hong, S.-C.; Cho, M., Fluorescence-Combined Interferometric Scattering Imaging Reveals Nanoscale Dynamic Events of Single Nascent Adhesions in Living Cells. *The Journal of Physical Chemistry Letters* **2020,** *11* (23), 10233-10241.

50. Bon, P.; Lécart, S.; Fort, E.; Lévêque-Fort, S., Fast Label-Free Cytoskeletal Network Imaging in Living Mammalian Cells. *Biophysical Journal* **2014,** *106* (8), 1588-1595.

51. Kim, O. V.; Litvinov, R. I.; Alber, M. S.; Weisel, J. W., Quantitative structural mechanobiology of platelet-driven blood clot contraction. *Nature Communications* **2017,** *8* (1), 1274.

52. Zhang, P.; Ma, G.; Dong, W.; Wan, Z.; Wang, S.; Tao, N., Plasmonic scattering imaging of single proteins and binding kinetics. *Nature Methods* **2020,** *17* (10), 1010-1017.

53. Zheng, Y.; Montague, S. J.; Lim, Y. J.; Xu, T.; Xu, T.; Gardiner, E. E.; Lee, W. M., Label-free multimodal quantitative imaging flow assay for intrathrombus formation in vitro. *Biophysical Journal* **2021,** *120* (5), 791-804.

54. Jones, T. R.; Carpenter, A. E.; Lamprecht, M. R.; Moffat, J.; Silver, S. J.; Grenier, J. K.; Castoreno, A. B.; Eggert, U. S.; Root, D. E.; Golland, P.; Sabatini, D. M., Scoring diverse cellular morphologies in image-based screens with iterative feedback and machine learning. *Proceedings of the National Academy of Sciences* **2009,** *106* (6), 1826-1831.

55. Barnhart, E.; Lee, K.-C.; Allen, G. M.; Theriot, J. A.; Mogilner, A., Balance between cell−substrate adhesion and myosin contraction determines the frequency of motility initiation in fish keratocytes. *Proceedings of the National Academy of Sciences* **2015,** *112* (16), 5045-5050.

56. Guo, Y.; Li, D.; Zhang, S.; Yang, Y.; Liu, J.-J.; Wang, X.; Liu, C.; Milkie, D. E.; Moore, R. P.; Tulu, U. S.; Kiehart, D. P.; Hu, J.; Lippincott-Schwartz, J.; Betzig, E.; Li, D., Visualizing Intracellular Organelle and Cytoskeletal Interactions at Nanoscale Resolution on Millisecond Timescales. *Cell* **2018,** *175* (5), 1430-1442.e17.

57. Axelrod, D., Chapter 9 Total Internal Reflection Fluorescence Microscopy. In *Methods in Cell Biology*, Taylor, D. L.; Wang, Y.-L., Eds. Academic Press: 1989; Vol. 30, pp 245-270.

58. Eckert, A. F.; Gao, P.; Wesslowski, J.; Wang, X.; Rath, J.; Nienhaus, K.; Davidson, G.; Nienhaus, G. U., Measuring ligand-cell surface receptor affinities with axial line-scanning fluorescence correlation spectroscopy. *eLife* **2020,** *9*, e55286.

59. Jiang, Y.; Zhou, Y.; Bao, X.; Chen, C.; Randolph, L. N.; Du, J.; Lian, X. L., An Ultrasensitive Calcium Reporter System via CRISPR-Cas9-Mediated Genome Editing in Human Pluripotent Stem Cells. *iScience* **2018,** *9*, 27-35.

60. Kraning-Rush, C. M.; Carey, S. P.; Califano, J. P.; Smith, B. N.; Reinhart-King, C. A., The role of the cytoskeleton in cellular force generation in 2D and 3D environments. *Physical Biology* **2011,** *8* (1), 015009.

61. Groves, J. T.; Parthasarathy, R.; Forstner, M. B., Fluorescence Imaging of Membrane Dynamics. *Annual Review of Biomedical Engineering* **2008,** *10* (1), 311-338.

62. Shin, W.; Ge, L.; Arpino, G.; Villarreal, S. A.; Hamid, E.; Liu, H.; Zhao, W.-D.; Wen, P. J.; Chiang, H.-C.; Wu, L.-G., Visualization of Membrane Pore in Live Cells Reveals a Dynamic-Pore Theory Governing Fusion and Endocytosis. *Cell* **2018,** *173* (4), 934-945.e12.

63. Kanchanawong, P.; Shtengel, G.; Pasapera, A. M.; Ramko, E. B.; Davidson, M. W.; Hess, H. F.; Waterman, C. M., Nanoscale architecture of integrin-based cell adhesions. *Nature* **2010,** *468* (7323), 580-584.

64. Poulter, N. S.; Pollitt, A. Y.; Davies, A.; Malinova, D.; Nash, G. B.; Hannon, M. J.; Pikramenou, Z.; Rappoport, J. Z.; Hartwig, J. H.; Owen, D. M.; Thrasher, A. J.; Watson, S. P.; Thomas, S. G., Platelet actin nodules are podosome-like structures dependent on Wiskott–Aldrich syndrome protein and ARP2/3 complex. *Nature Communications* **2015,** *6* (1), 7254.

65. Oakes, P. W.; Bidone, T. C.; Beckham, Y.; Skeeters, A. V.; Ramirez-San Juan, G. R.; Winter, S. P.; Voth, G. A.; Gardel, M. L., Lamellipodium is a myosin-independent mechanosensor. *Proceedings of the National Academy of Sciences* **2018,** *115* (11), 2646-2651.

66. Dejardin, M.-J.; Hemmerle, A.; Sadoun, A.; Hamon, Y.; Puech, P.-H.; Sengupta, K.; Limozin, L., Lamellipod Reconstruction by Three-Dimensional Reflection Interference Contrast Nanoscopy (3D-RICN). *Nano Letters* **2018,** *18* (10), 6544-6550.

Chapter 7 Intra-thrombus Stability and Embolization in Flow Assay

Publication relevant to this chapter:

Y. Zheng, S. J. Montague, Y. J. Lim, T. Xu, T. Xu, E. E. Gardiner, and W. M. Lee. "Label-free multimodal quantitative imaging flow assay for intrathrombus formation in vitro." *Biophysical Journal* 120, no.5 (2021): 791-804.

7.1 Introduction

This chapter will describe the steps we have taken to investigate thrombus formation and stability using the COSI-QPM system introduced in chapter 4.3.2. When assessing thrombus stability, two factors: (1) adhesiveness of the thrombus core and (2) stability of the thrombus structure, are critical to consider (chapter 3.4). To gain access to both information of the thrombus during formation and embolization, we used the COSI-QPM system that quantifies platelet activity (μm/s) and dry mass (pg) simultaneously to evaluate thrombus stability under fluid shear. The platelet activity quantifies the membrane fluctuation (cytoskeleton rearrangement) of the platelets adhered on the collagen fibre that could relate to the motility of the adherent platelets. The dry mass of the thrombus traces the detachment of platelet aggregates and monitors the stability of the thrombus structure. By combining the spatial-temporal imaging of both the surface driven activity of adherent platelets and dry mass changes of a developing thrombus under (patho)physiological shear rates, we evaluate intra-thrombus stability and basal surface activity of the thrombus in the presence or absence of metalloproteinase inhibition (giving conditions of reduced platelet receptor shedding).

7.2 Thrombus Stability and Embolization

Understanding interactions at the thrombus/surface interface using microfluidic channels coated with vascular wall constituents will enhance our understanding of the thrombus evolution process, incorporating platelet adhesion, activation, aggregation, and thrombus stabilization (Fig. 7-1 A). It also helps advance the biocompatibility of new materials for intravascular devices [1], development of 'synthetic' platelets [2] and improve drug delivery [3]. Microfluidic channel-based assays for thrombus measurements *in vitro* typically only quantitate either surface-driven biophysical processes associated with adhesion, including platelet activation and spreading (Fig. 7-1 B) or the growth, propagation and stability of a thrombus formed on an immobilized prothrombotic surface (Fig. 7-1 C), but not both. The net stability of a thrombus under a parabolic velocity flow profile [4-8], as shown in Fig. 7-1 D, is dependent on a complex set of biophysical parameters. The ability of a thrombus to remain stable can be defined by two key physical interactions, both of which require intact functional platelet receptors, including integrin αIIbβ3 and glycoproteins (GP) Ib-IX-V and GPVI. GPIb-IX-V and GPVI are metalloproteolytically shed from activated platelets [9]. The first is the physical attachment of platelets to a substrate (immobilized agonist), where adhesive platelets spread (Fig. 7-1 B) and aggregate during the initial phase of thrombus formation [10]. The second is the platelet-platelet interactions and thrombus consolidation processes occurring during the accumulation phase, with the net effect represented by changes in thrombus mass (Fig. 7-1 D). Surface-driven effects are defined by the activities of basal adhesive platelets, including platelet spreading and formation of podia at the base of a thrombus on an agonist-rich surface. Both the intra-thrombus stability and the surface-driven platelet activities contribute to the overall stability of a thrombus [10]; that is,

how well thrombi adhere to and build on a substrate-coated surface with minimal changes in mass as it withstands changes to velocity flow gradients.

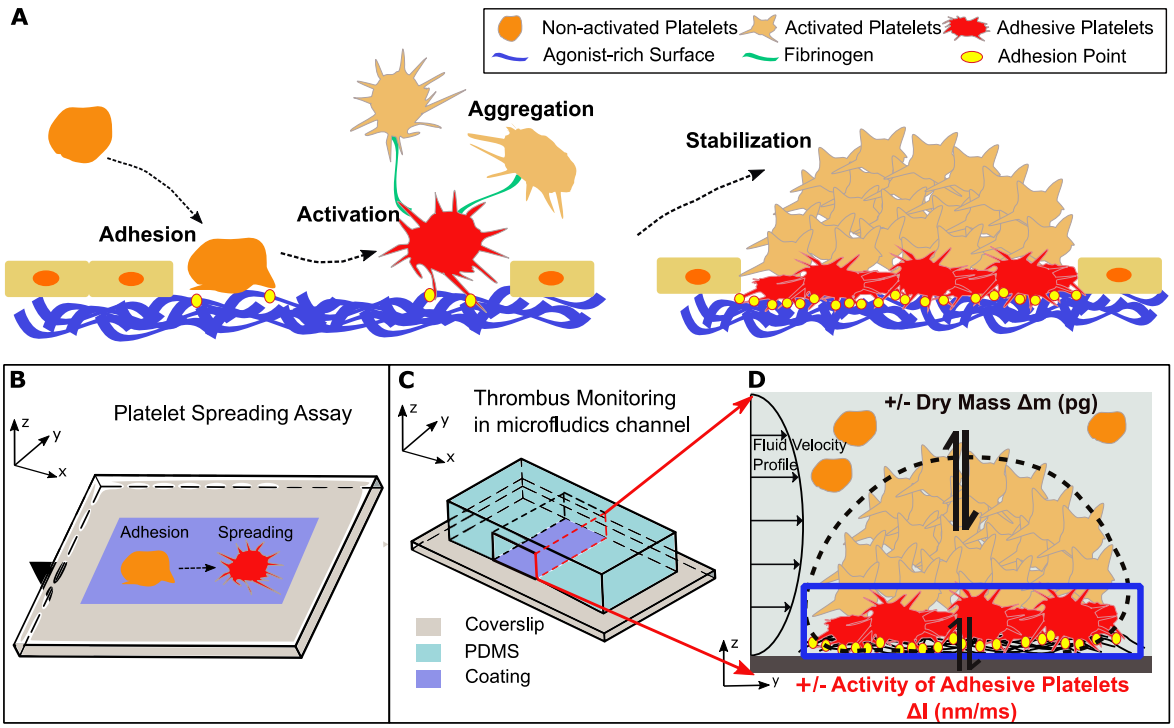

Figure 7-1 Approaches to measuring changes in mass and local platelet activities in single adherent platelets and thrombi. (A) There are four distinct stages of dynamic thrombus formation: platelet adhesion, activation, aggregation, and thrombus stabilization. (B) Cross-section view of a coated microfluidic channel used to visualize surface-driven events during platelet spreading. (C) Cross-section view of a coated microfluidic channel used to visualize surface-driven events during thrombus formation. (D) Inside the coated microfluidic channel, the thrombus formed is comprised of platelets interacting with agonist-coated surfaces (collagen/fibrin). The thrombus is a complex biological system that interacts with the surrounding microenvironment and adapts to changing fluid shear forces. Intra-thrombus stability can be quantified as changes in dry mass (coloured in caramel) and adhesive platelet activity (coloured in red). Here, adhesive platelets are represented as the layer of platelets directly associated with the coated surface.

In clinical settings, rapid *in vitro* diagnostic tests that quantify intra-thrombus dynamics are frequently conducted without fluorescence labelling. Haemostasis tests, using the platelet function analyser [11], optical platelet aggregometry [12], and thromboelastography [13], quantify the time to occlude a channel or form aggregates in suspension or on a surface with

some physical properties. These clinical tools have several limitations, including the requirement of a platelet count of at least 100 x 10^9/L, eliminating platelet function testing, and quantitation of occlusion time of thrombocytopenic patients [14, 15]. Further, these tests do not inform on sub-micrometre scale changes occurring within the thrombus or provide information on platelet adhesion dynamics during thrombus formation. Here, we combine QPM [7, 16, 17], an interferometry-based method, with COSI to study how initial adhesive platelets behave on agonist-coated surfaces, including collagen and von Willebrand Factor (VWF), whilst simultaneously quantifying intra-thrombus mass [18-20]. Synchronized multi-parameter label-free imaging will therefore better inform on how membrane activity of adhesive platelets and overall morphological of thrombus changes. COSI-QPM system represents the first label-free thrombus micro-imaging tool that can simultaneously quantify adhesive platelet activity and intra-thrombus mass (Table 7-1).

7.3 Sample Preparation and Data Processing

7.3.1 Mimic Blood Vessel using Microfluidics

Thrombus formation under flow is assessed using microfabricated straight channels (dimensions: 400 μm width, 100 μm height and 1.2 cm length), made from PDMS (polydimethylsioxane) from Sylgard 184 (Dow Corning) with 10:1 base to curing agent ratio using soft lithography processes (Fig. 7-1 C). The microfluidic channel is coated with 100 μg/mL collagen Reagent HORM (Takeda, Austria) overnight at 4°C or 2 hours at 23°C. Before each experiment, the channel is washed with saline at 300 μL/min for 2 minutes. PRP is then drawn into the channel (opposite input used for agonist coating) with the syringe pump (Harvard Apparatus PHD 2000) in the suction mode for 5 min at a shear rate of 7500 s^{-1} (flow rate: 300 μL/min and shear stress: 75 dyne/cm^2) to induce thrombus formation. Due to

the interference of light scattering by RBCs, the current system relies on PRP to measure thrombus formation and embolization. Removing RBCs from the sample changes the viscosity and reduces the margination of platelets to the surface (usually observed when RBCs are present. Therefore, we have to rely on a higher shear rate for thrombi to form. The reservoir is then switched to saline, and thrombi are exposed to shear rates of 7500 s^{-1} for 5 minutes followed by 12,500 s^{-1} for 2 min to mimic pathophysiological shear rates and induce embolization events. PRP is pre-treated with 250 µM GM6001 >10 min before experiments for metalloproteinase inhibition experiments.

7.3.2 Mass Quantification

Off-axis quantitative phase microscopy (QPM) is well-suited to measure the dry mass of a developing thrombus without labelling [21]. A change in refractive index provides a signature optical phase delay that can be recorded and quantified through interferometry and optical scattering [16]. The optical phase difference is measured between two coherent light paths; the transmitted light path through the sample and another projected directly onto the camera. The recorded interference intensity pattern is then numerically processed to retrieve the phase delay $\phi_t(x, y)$ [16, 22]. For a given refractive index difference (Δn) [23], a phase delay $\phi_t(x, y)$ is imposed onto the transmitted light for a narrowband wavelength light source. This refractive index change of biomolecules approximate change in dry mass and can be determined from changes in phase [19-21, 24].

The mass of a homogenous sample can be directly calculated using volume and density (d*v). The mass of the polystyrene microsphere is calculated with d = 1.05 g/cm^3 [16, 19]. For most of the biological cells, the change in the refractive index corresponds to linear increases in dry biomass (proteins and nucleic acids without water) that falls within a very narrow range of approximately $\alpha = 1.8 \times 10^{-4}$ m^3/kg (= 0.18 $\mu m^3/pg$) that allows one to

estimate the dry mass of thrombi and cells [19, 21]. The equation used to reconstruct the dry mass of thrombi from phase $\phi_t(x,y)$ is shown in Eq. 7.1.

$$m_t(x,y) = \frac{1}{\alpha}\int \frac{\lambda \cdot \phi_t(x,y)}{2\pi} dA \tag{7.1}$$

For a pixel with an actual size of 0.1 μm x 0.1 μm, the dry mass of a 1 rads phase delay calculates as follow:

$$m = \frac{1}{0.18}\left(\frac{pg}{\mu m^3}\right) \times \frac{0.6328\ \mu m \times 1 \times 0.1\mu m \times 0.1\mu m}{2\pi} = 5 \times 10^{-3}\ pg \tag{7.2}$$

Note that the volume of a large population of platelets can vary over an order of magnitude, previously shown using flow cytometry data [23]. For completeness, we analysed several resting platelets using QPM to identify a standard deviation of mass to be up to an order of magnitude, i.e. between 0.5-6 picogram as shown in Fig. 7-2 that is consistent with [23]. Therefore, it is safe to conclude that a large variation of platelet mass is to be expected.

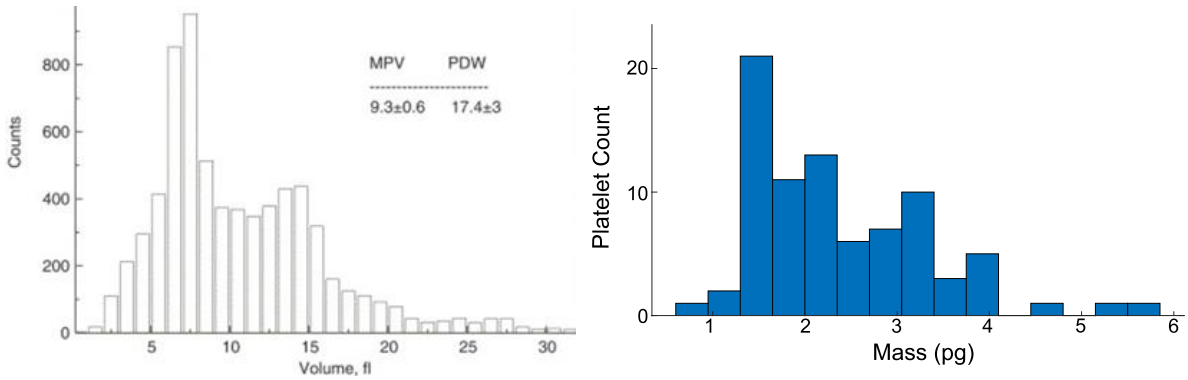

Figure 7-2 Quantification of platelet volume and mass with flow cytometry and COSI. The figure from flow cytometry is reprinted with permission from Kolesnikova *et al.* [23] © 2006 Elsevier

The resolution and upper limit of the reconstructed height or dry mass from the phase delay measurement can be affected by a range of factors, such as pixels size of the camera, fringe density, defocusing of the sample [25] and unwrapping algorithm [26]. Samples with large

size and complex structure create many jumps in the wrapped phase that might be difficult to resolve accurately using the unwrapping program, therefore, limiting the range of dry mass that can be measured. So far, the largest sample we have used to calibrate the system is 6 μm polystyrene beads (6.3×10^{-2} pg in dry mass per pixel). In thrombus experiment, the size of formed thrombi was around 10 -20 μm in height (3.3×10^{-3} - 6.6×10^{-3} pg in dry mass per pixel) and can be resolved and reconstructed without any issues. However, to accurately test the limitation of phase delay that can be reconstructed using the QPM setup, further calibrations can be designed in the future.

Change in dry mass of the thrombus identifies the affinity/recruitment of platelets into aggregate, which is determined by the mass difference before and after the flow of saline (0.9% NaCl) as shown in Eq. 7.3.

$$m_{loss}(x,y) = m_{end}(x,y) - m_1(x,y) \tag{7.3}$$

7.3.3 Activity Quantification of Adhesive Platelet

The method to calculate platelet activity is described in chapter 5. Here we use the standard deviation of the activity to identity the variations in activity in a given time period. Hence, we define this measurement as the change in activity, as shown in Eq. 7.5.

$$I_f = I_{n+1} - I_n \tag{7.4}$$

$$\sigma I(x,y) = \sqrt{\frac{\sum_1^n \left(I_{fn}(x,y) - \bar{I}_f(x,y)\right)^2}{n}} \tag{7.5}$$

7.3.4 Mapping Platelet Mass and Activity

A binary mask is generated by thresholding the 2D backscattering map to filter out the background on the mass and backscattering maps so that only the thrombus region is quantified. For example, high-resolution images of a single thrombus of 60 µm by 80 µm, in Fig. 7-6 with a pixel resolution of 100 nm would generate up to 48,000 data points. We bin a series of pixels (each dot represented in plots – Fig. 7-6 and Appendix F) is intensities of 10 x10 pixels on the filtered mass distribution map and backscattering map, respectively. This means that the final plot in Fig. 7-6 includes over 4000 sampling points that allow us to measure heterogeneity in single thrombi. Each binned pixel is assigned the value of mass change to the y-axis, and the standard derivation of scattering intensity to the x-axis on the scatter plot to generate one scatter. The data points that fall more than three standard deviations from the mean are removed to show the scatter plot distribution. The data points are classified into four different clusters by defining threshold values for mass change and scattering intensity. The threshold value for mass is 0 pg which differentiates gain and loss in mass, while the threshold for scattering intensity defines the low and high level of activity and is calculated from the mean value of the intensity for all the data points.

In order to show the trend in change in mass and activity of a formed thrombus during embolization, the length of whiskers (defined as ± 1.5 x interquartile range) of each boxplot is normalized to the colour-coded plot. Here, the ± 1.5 x interquartile range equals to three standard deviations that covers 99.9^{th} percentiles of the data points on a single thrombus. Because the sample we used here is from human blood and we have limited sample size for the experiment (N = 7), we would like to cover as many as data points when quantifying change in mass/activity. We believe that the 99.9th percentiles can cover sufficient data points to represent the range of variation in mass/activity during quantification. The colour-

coded plot ranges from 0 (blue) to 1 (red), with 0 and 1 representing the minimal and maximum change in mass/activity within the 30 seconds time period during embolization. Below, we show how the values from the colour-coded plot are calculated.

For the boxplot in Fig. 7-6 B (i), showing the change in mass of a formed thrombus without treatment, the upper and lower boundaries of the whiskers of the boxplots read as [0.457, 0.470, 0.461, 0.464, 0.360, 0.319, 0.286, 0.231, 0.250] pg and [-0.433 -0.412, -0.415, -0.414, -0.327, -0.291, -0.275, -0.220, -0.244] pg respectively. The length of whiskers is then calculated as the range in between upper and lower boundaries as [0.890, 0.882, 0.876, 0.879, 0.687, 0.610, 0.561, 0.451, 0.494] pg so the normalized values are calculated as [1, 0.982, 0.968, 0.974, 0.537, 0.362, 0.250, 0, 0.099].

7.4 Mapping Intrathrombus Mass and Activity

7.4.1 Mapping Mass and Activity of Single Platelet

Fig. 7-3 shows representative COSI-QPM imaging frames of two individual platelets within a single imaging field of view, labelled as the region of interest (ROI) 1 and ROI 2 in terms of the reconstructed mass distribution ($m(t)$) and the backscattering intensity map ($I_{back}(t)$) respectively. COSI-QPM can distinguish the difference of mass between the two platelets; the platelet in ROI 1 possesses a mass of 1.4 pg while the platelet in ROI 2 had a mass of 2.6 pg (Fig. 7-3 C), consistent with published mean platelet mass measurements of 1.85 ± 0.2 pg [27].

Platelets in ROI 1 and ROI 2 have distinctively different physical behaviours, displaying finger-like morphologies that are consistent with platelet activation [28] in Fig. 7-3 B (ii) and very distinct intensity hot spots (200-400 nm in size) at 30 frames per second. Membrane protrusions extended and retracted at different timepoints (arrows, t_1, t_3, and t_4

(Fig. 7-3 B (ii)). The discrete scattering hotspots of the platelet in ROI 1 displayed fewer temporal changes reflecting reduced movement along the fibrin-coated surface. In contrast, the larger platelet (ROI 2) displays less membrane protrusion but high intensity in hot spots and spatiotemporal movements. While the scattering intensity signal across each platelet for both ROIs fluctuates over time, the platelet in ROI 2 (green) has a greater signal than the platelet in ROI 1 (Fig. 7-3D) which matches its mass, i.e. a higher mass has a greater magnitude of scattering. The results above confirm that COSI can readily observe changes in dry mass in adherent versus spread (more activated) single platelets.

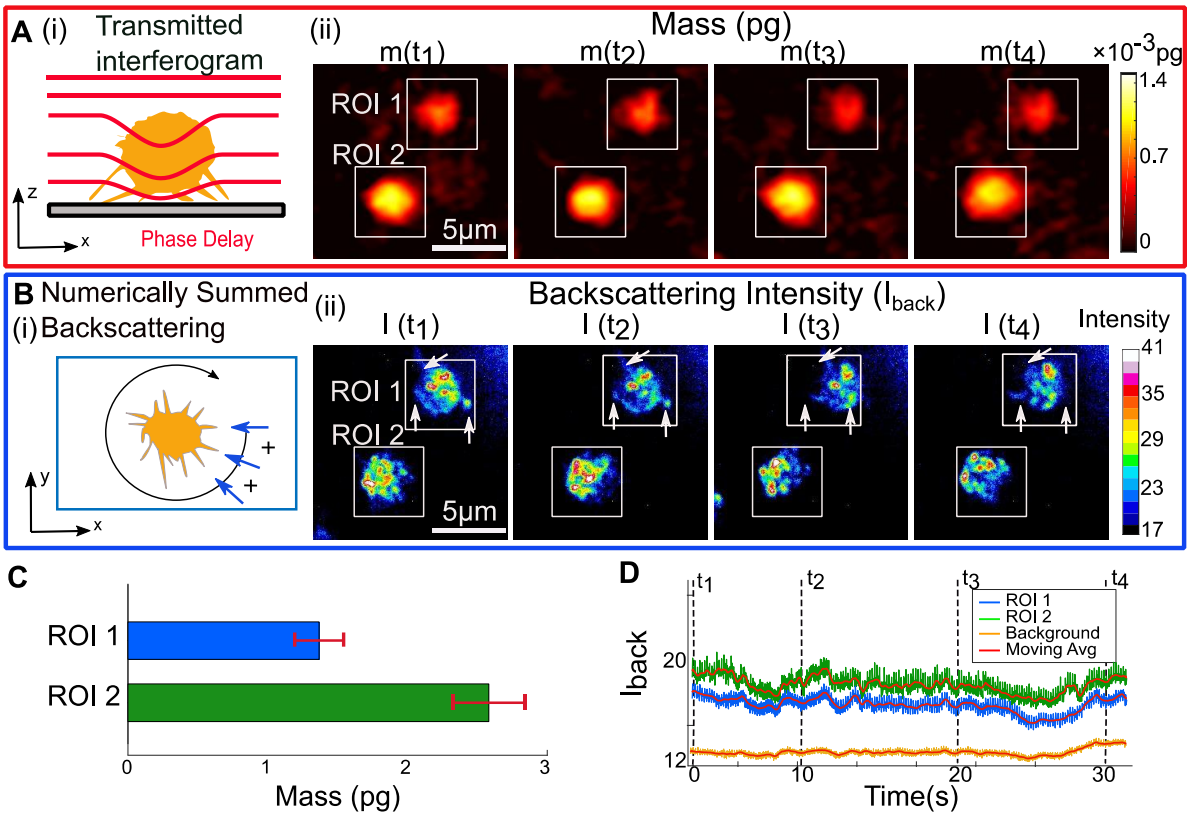

Figure 7-3 (A) (i) Light transmitted through the sample imposes a phase delay due to refractive index differences. This phase delay is retrieved from the interferogram to quantify platelet dry mass. (ii) Mass distribution map of ($\boldsymbol{m(t)}$) of the spreading platelet. (B) (i) The sample is illuminated sequentially from the full azimuthal 2π angle, and the backscattering signal under each azimuthal angle is numerically summed to remove backscattering artifacts. (ii) Backscattering signal ($\boldsymbol{I(t)}$) with fluctuating hotspots (arrow). (C) Total mass of the selected platelets at different times after spreading. Error bars = Standard Deviation (D) Intensity fluctuation of corresponding ROIs.

7.4.2 Adhesive Platelet Activity During Thrombus Formation

Next, we measure spatiotemporal dynamics to an entire developing thrombus (Fig. 7-4) using coated collagen layer. As with the single platelet images in Fig. 7-4 A, the collagen bundles act as a fiducial marker to focus the imaging field of view and site of activation. This ensures that we capture early adhesive platelet events before assimilating into a platelet aggregate. We adjust the incident angle of the illumination to 50° to achieve a backscattering imaging depth of field of just around a single platelet thick (z = 4 μm). The spatial-temporal map (Fig. 7-4 A) captures the surface activity of platelets accumulating into a thrombus at 1800 s-1 shear rate in a microfluidic channel, based on the monotonically increasing scattering intensity from 0 s, 30 s, 60 s, 120 s and 240 s. Using the differential method introduced in chapter 5.2.2 (Fig. 7-4 B), we observe that the magnitude of activity did not increase at all, indicative of a highly stable basal surface during thrombus formation consistent with existing thrombus formation.

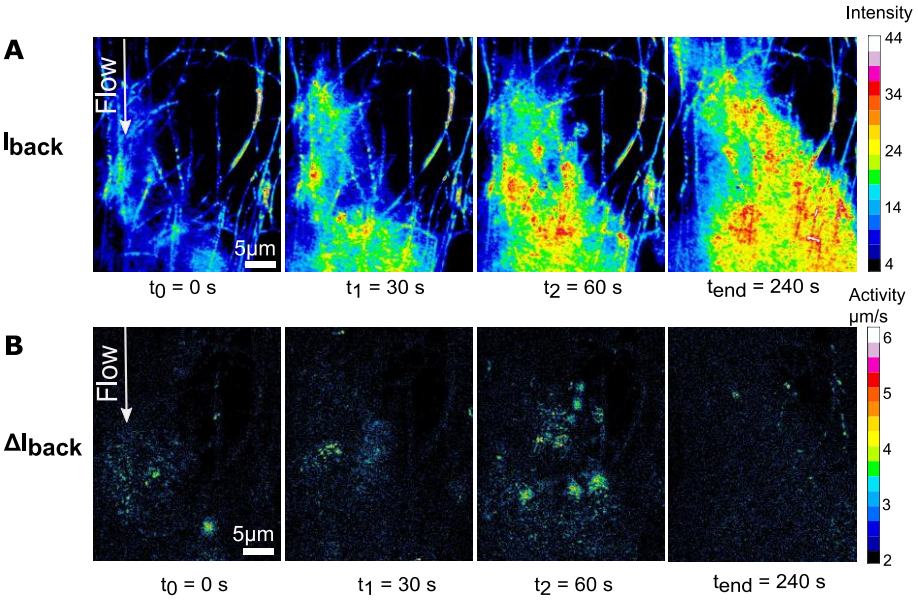

Figure 7-4 Scattering signal and activity of adherent platelets in a developed thrombus. Scattering signal (A) at 0 s, 30 s, 60 s, 120 s, and 240 s illustrate thrombus formation in a time series and the corresponding platelet activities at 10 ms. (B) is the corresponding activity map using the differential method.

7.4.3 Mapping Intrathrombus Mass and Activity during Embolization

To date, label-free platelet imaging [29-31] has not been able to simultaneously quantify adhesive platelet activity and the physical progression of the thrombus (growth and embolization). Even less is known about the overall impact of thrombus mass on thrombus stability [32]. Data in Fig. 7-5 demonstrates how COSI-QPM approaches can extract information on both thrombus stability and membrane fluctuations of adhesive platelet-platelets (Fig. 7-5 A). Fig. 7-5 B-E shows quantification of intra-thrombus mass (pg) and membrane activity level of adhesive platelet during embolization under (patho)physiological fluid shear by continuously flowing saline solution over the formed thrombus for 5 minutes under 7500 s^{-1} to help mimic embolization. Fig. 7-5 B (i) and (ii) depict two reconstructed QPM images of thrombi formed under 7500 s^{-1} shear stress, taken 5 minutes apart, indicating a loss in thrombus mass due to platelet detachment. At the same time, we record membrane fluctuations of activated adherent platelets ~ 30 ms apart, which show a heightened activity map of up to 18 μm/s that are heterogeneously distributed across the whole thrombus during embolization events (Figure 7-5 C). These results demonstrate a highly complex interaction between platelets and the adhesive layer of thrombus during embolization.

Fig. 7-5 D and 7-5 E contain a 2D map of mass change (Δm) and standard deviation of membrane activity signal (ΔI_{back}) at a shear rate of 7500 s^{-1} taken 5 minutes apart, respectively. We observe a highly heterogeneous distribution of gain $+13x10^{-3}$ pg and loss of thrombi mass $-13x10^{-3}$ pg across the 5 minutes of high shear rate exposure from the activity maps. Interestingly, the adherent platelet activity is spread in a concentric pattern with cores of the average activity of 6.6 μm/s surrounded by regions of lower activity of 4.7 μm/s. 2D maps of mass and platelet activity from three individuals are shown in Appendix F.

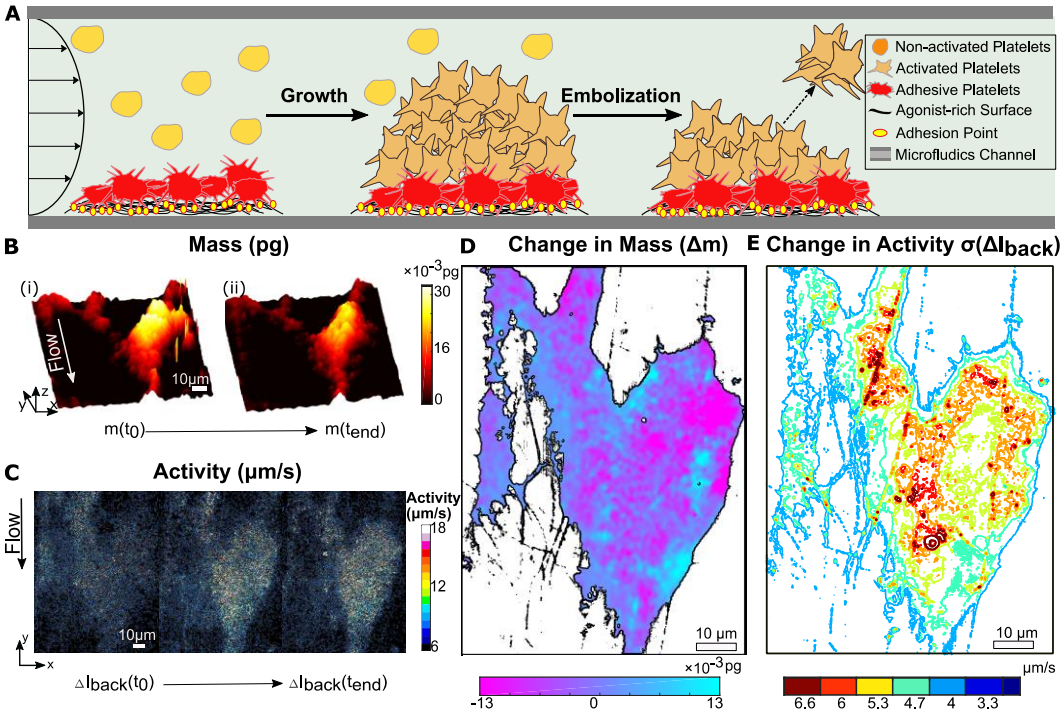

Figure 7-5 Quantifying intra-thrombus stability (changes in mass) and adhesive platelet activity during embolization. (A) Schematic of thrombus stability (growth and embolism). To induce thrombus formation, PRP was perfused over a collagen-coated microfluidic channel for 5 min at a shear rate of 7500 s-1 (flow rate: 300 µL/min, shear stress: 75 dyne/cm2). The reservoir was then switched to saline, and thrombi were exposed to shear rates of 7500 s-1 for 5 minutes followed by 12,500 s-1 for 2 min to mimic pathophysiological shear rates and induce embolization events. (B) QPM images show thrombus mass at (i) start (m(t0)) and (ii) end (m(tend)) of 5 minutes of embolization. (C) Platelet activity map (Δt = 30 ms) of the formed thrombus during embolization. The signal in subtraction plots is multiplied 10 times, enhancing contrast. (D) The change in thrombus mass during embolization is defined as the mass difference between a given time. Example of the 2D plot showing the change in the mass distribution of a thrombus exposed to 5 minutes of 7500 s-1 shear stress. Purple = mass loss, blue = mass gain. The region and border line of the thrombus (black line) is determined by thresholding and tracing using an activity map. (E) Corresponding 2D activity map. The activity map calculates the standard deviation of activity across an imaging session and is plotted using a contour plot where red and blue represent more and less activity, respectively. Scale bar: 10 µm.

7.5 Investigating Role of Platelet Shedding

Next, we evaluate mass variation and adhesive platelet activity at different stages of thrombus embolization. COSI-QPM can produce high-resolution images of thrombi with a pixel resolution of 100 nm. For a thrombus of 60 µm by 80 µm, in Fig. 7-5 D, this would generate up to 48,000 data points without binning. In Fig.7-5, we binned 10 x10 pixels on the filtered mass distribution map and backscattering map, which includes over 4000 sampling points for a thrombus. The changes in thrombus mass (Fig. 7-5 D) and adherent platelet activity (Fig. 7-5 E) are quantified at different time points over a 5-minute experiment and plotted as boxplots to illustrate the distributions of mass and platelet activities (Fig. 7-6 A, full data set at 5 minutes shown in Appendix F). The time series plots indicate that activity gradually increases from 30-120 seconds, whilst the mass exchange remains consistent, with minimal change in activity and mass distribution observed after 120 seconds, suggesting a level of thrombus stabilization has been achieved, most likely via cytoskeletal remodelling.

The whiskers of the box plots defining the upper and lower limits (Fig. 7-6 B) highlight variability in mass exchange and activity in blood samples from healthy donors. Complete data for 7 donors are shown in Appendix F. Upon activation, platelets shed the ligand-binding ectodomain portion of key adheso-signalling receptors that initiate and propagate thrombus formation [9]. We investigate whether the prevention of activation-induced metalloproteolytic cleavage of receptors such as GPIb of the GPIb-IX-V complex [31] and GPVI [32, 33,] which are important for thrombus stability, resulted in changes in changes to surface activities of changes in mass (as measured using COSI-QPM). To evaluate whether a more stable thrombus is formed under conditions where proteolytic receptor shedding is blocked, PRP from seven different donors was pre-treated with 250 µM GM6001 (a broad range metalloproteinase inhibitor) or vehicle control. Mass exchange and surface activity in

time series are compared of thrombi exposed to buffer at 7500 s^{-1} and 12500 s^{-1} shear rates. Fig. 7-6 C shows heat maps representing the respective change in mass and activity (based on normalization of the ± 1.5 interquartile range). Donor variation in mass change and surface activity of thrombi imaged is observed in the vehicle and GM6001-treated samples (Appendix E). Although heterogenous thrombi behaviours (spikes and reductions in mass and platelet activities) are observed between donors at different times, there is a general tendency for thrombus mass not to decline with time following GM6001 treatment (as represented by blue boxes). Five out of seven donors appear to reach a steady state of thrombus mass after around 2 minutes (Fig. 7-6 C (ii)), indicating there is potentially reduced mass exchange and development of a more stable thrombus when blocking receptor proteolysis. When exposing the thrombi of most donors to 12500 s^{-1} shear stress, there is a brief initial increase in mass followed by a reduction in mass before a stable thrombus is achieved (no relative change in mass). This is observed both with and without GM6001 treatment (Fig. 7-6 D (i) and (ii)). Interestingly, a more stable thrombus mass after exposure to 7500 s^{-1} shear stress is associated with increases in platelet activity in six/seven donors (shift from blue to red), with increased activity appearing to be more associated with stable mass with GM6001 treatment (Fig. 7-6 C iii and iv). However, the surface activity at higher shear rates shows more variations between donors both with and without GM6001 treatment (Fig. 7-6 D (iii) and (iv)).

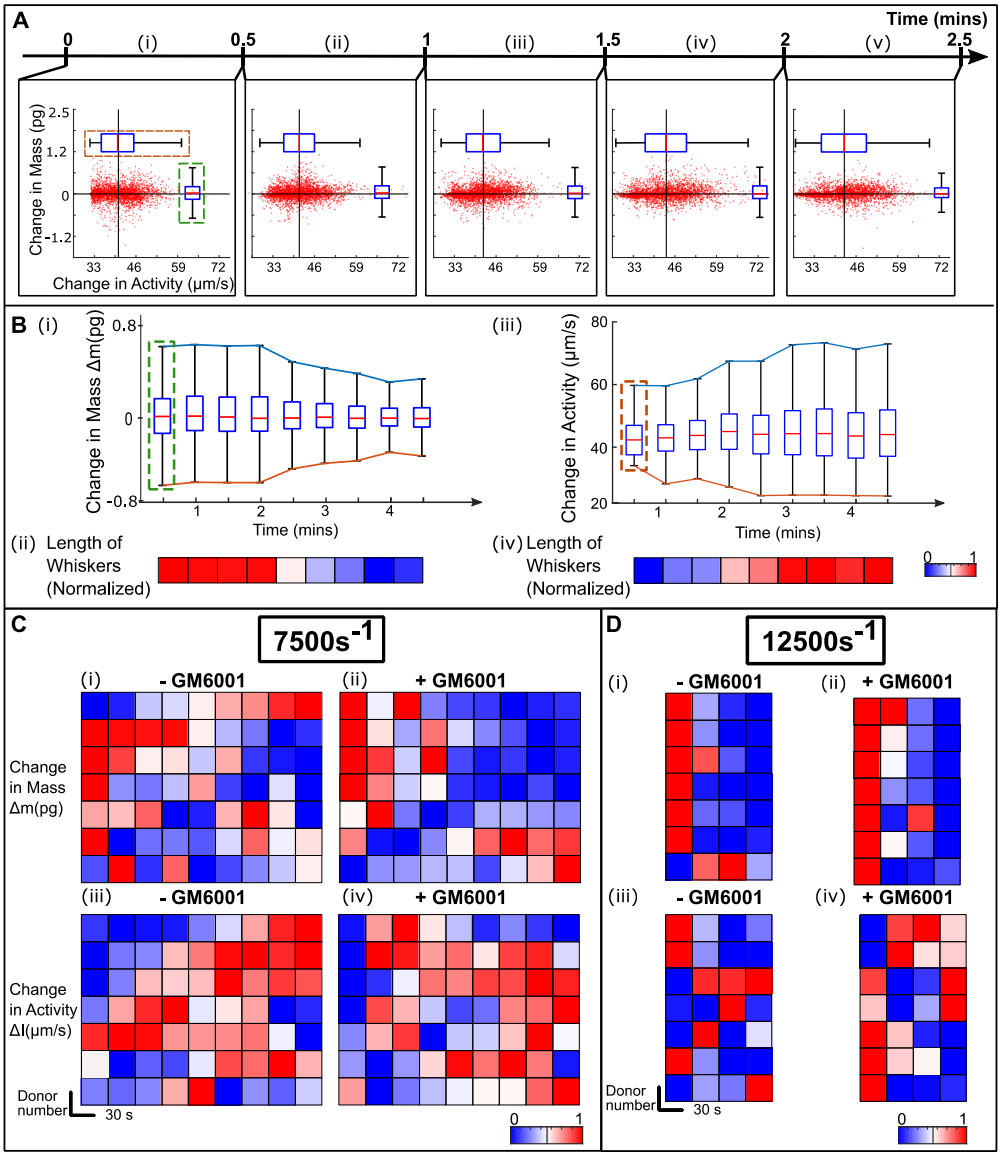

Figure 7-6 Mass and activity changes in thrombi of multiple donors with and without metalloproteinase inhibition (GM6001 250 μM; broad metalloproteinase inhibitor). (A) Scatter plot of thrombus under 7500 s-1 shear rate at 30 s time intervals showing the corresponding changes in mass and activity of individual binned pixels after spatially mapping the 2D activity and mass map of the thrombus with a binning size of 10*10 pixels. The scattered plot is divided into four quadrants distinguishing loss and gain in mass and activity level. Boxplots from each scatter plot are used to represent the overall trends of (B) (i) mass and (iii) platelet activity change over time. The upper and lower limits of the boxplots are drawn to highlight the length of whiskers. The colour-coded plot represents the normalized length of whiskers of each box of change in (ii) mass and (iv) activity. The colour-coded plot of change in mass and surface activity of the developing thrombus under (D) 7500 s-1 and (E) 12500 s-1 shear rates with and without 250 μM GM6001 pre-treatment (donor size = 7). The change in mass and activity is calculated as the normalized value of the length of whiskers (± 1.5 interquartile range) of each boxplot.

7.6 Conclusion

Since COSI-QPM is compatible with coated microfluidic chips, it can provide a new means to decipher the heterogeneous properties within thrombi interacting with different types of substrate-coated surfaces. These types of multiparameter imaging measurements will advance our understanding of how platelets differentially interact with various agonists, for example, to assess relative contributions of GPVI or GPIb-IX-V interactions with collagen, fibrin(ogen), von Willebrand Factor and other matrix proteins. We can evaluate the effects of each interaction on thrombus evolution and stability, which is important for future anti-thrombotic therapeutic development. In addition, we expect combinatory approaches of quantitative label-free microfluidic imaging tools to open up new clinically relevant opportunities to evaluate different platelet subpopulations with the thrombus structure and how they function during thrombus formation under fluid shear force.

Final data in Fig. 7-6 are extracted from high-resolution images of thrombi formation in Fig.7-5 that display a pixel resolution of 100 nm. This means that a single thrombus of 60 µm by 80 µm (Fig. 7-5) can generate up to 48,000 data points. Even with pixel binning (10 x10 pixels) - a single thrombus- can generate up to over 4000 sampling points (shown in Fig. 7-6 as a single dot in scattered plots). High spatial-temporal information density allows us to measure subtle heterogeneity in a single thrombus over different timepoints. In Fig. 5 C and D, we collected data from 7 different donors to investigate the heterogeneity and robustness of our measurement under broad metalloprotease inhibitors. While we appreciate that this is a small sample number, this is a proof-of-concept project, and we aim to develop the automated readout processes in the future. Overall, we argue that the COSI-QPM aims to unify microfluidic platelet and thrombus flow assays for both single platelet and thrombus quantification and is applicable for both microscopy imaging and clinical diagnosis.

COSI-QPM enables real-time longitudinal temporal evaluation of the impact of metalloproteinase inhibition on platelet aggregate formation and stability that has not previously been shown. The correlation of thrombus mass exchange with change in the surface activity of adhesion platelets suggests that a stable intra-thrombus and a heightened adhesive platelet activity are best achieved when platelet metalloproteinases are inhibited. Platelet receptors undergo significant basal surface rearrangement as a platelet adheres and spreads on a substrate, and this is critical for the transmission of activating signals that trigger a host of pro-aggregatory events [33]. Therefore, the COSI-QPM system can easily be expanded to test the effect of new and existing anti-thrombotic agents and specific receptor antagonists on thrombus size and stability. Further COSI-QPM approaches could be expanded in clinical situations to help identify platelet defects in unexplained bleeding patients or diagnose embolism risk.

7.7 Contribution

Dr Samantha J. Montage and I designed the platelet experiments. Dr Samantha J. Montage, Ms Sarah Hicks, Ms Samina Nazir, and Dr Yean Jin Lim did the work related to platelet preparation. I performed all the experiments and interpreted the results.

	Label-free Technique	Functionality Measurements				Incorporates fluid shear stress	Imaging resolution
		Spreading /cytoskeletal changes	Adhesion	Aggregation	Intrathrombus Stability		
Clinical methods	Platelet function analyzer (PFA)	No	No	Yes	No	Yes	N/A
	Light transmission aggregometry (LTA)	No	No	Yes	Yes	No	N/A
	Impedance aggregometry	No	No	Yes	Yes	No	N/A
	Thromboelastography	No	No	Yes	Yes	No	N/A
	iCoagLab	No	No	Yes	Yes	No	Micrometre
Imaging-based methods	Bright field, Phase Contrast, Differential interference contrast	Yes	No	No	No	Yes	Micrometre
	RICM	Yes	Yes	No	No	Yes	Sub-micron
	QPM	No	No	Yes	Yes	Yes	Sub-micron
	ROCS	Yes	Yes	No	No	Yes	Sub-micron
	COSI (QPM + ROCS)	Yes	Yes	Yes	Yes	Yes	Sub-micron

Table 7-1. Comparisons between various techniques that evaluate platelet function and thrombus formation. Functionality attributes listed here are specific to platelets' motion either in suspension or across an agonist-coated surface, i.e. single platelet and thrombus formation. Readouts for imaging-based methods here are based on platelet morphology [34]. Also included are techniques that can incorporate platelet or blood exposure to fluid shear stress.

7.8 References

1. Jaffer, I. H.; Fredenburgh, J. C.; Hirsh, J.; Weitz, J. I., Medical device-induced thrombosis: What causes it and how can we prevent it? *Journal of Thrombosis and Haemostasis* **2015,** *13* (S1), S72-S81.

2. Bertram, J. P.; Williams, C. A.; Robinson, R.; Segal, S. S.; Flynn, N. T.; Lavik, E. B., Intravenous hemostat: Nanotechnology to halt bleeding. *Science Translational Medicine* **2009,** *1* (11).

3. Papa, A. L.; Jiang, A.; Korin, N.; Chen, M. B.; Langan, E. T.; Waterhouse, A.; Nash, E.; Caroff, J.; Graveline, A.; Vernet, A.; Mammoto, A.; Mammoto, T.; Jain, A.; Kamm, R. D.; Gounis, M. J.; Ingber, D. E., Platelet decoys inhibit thrombosis and prevent metastatic tumor formation in preclinical models. *Science Translational Medicine* **2019,** *11* (479).

4. Neeves, K. B.; Onasoga, A. A.; Hansen, R. R.; Lilly, J. J.; Venckunaite, D.; Sumner, M. B.; Irish, A. T.; Brodsky, G.; Manco-Johnson, M. J.; Di Paola, J. A., Sources of variability in platelet accumulation on type 1 fibrillar collagen in microfluidic flow assays. *PLoS ONE* **2013,** *8* (1), e54680.

5. Neeves, K. B.; Maloney, S. F.; Fong, K. P.; Schmaier, A. A.; Kahn, M. L.; Brass, L. F.; Diamond, S. L., Microfluidic focal thrombosis model for measuring murine platelet deposition and stability: PAR4 signaling enhances shear-resistance of platelet aggregates. *J. Thromb. Haemost.* **2008,** *6* (12), 2193-2201.

6. Nesbitt, W. S.; Westein, E.; Tovar-Lopez, F. J.; Tolouei, E.; Mitchell, A.; Fu, J.; Carberry, J.; Fouras, A.; Jackson, S. P., A shear gradient-dependent platelet aggregation mechanism drives thrombus formation. *Nat. Med.* **2009,** *15* (6), 665-673.

7. He, X.; Montague, S. J.; Tao, X.; Gardiner, E. E.; Lee, W. M., Quantifying embolism: Label-free volumetric mapping of thrombus structure and kinesis in a microfluidic system with optical holography. *Adv. Biosyst.* **2018,** *2* (10), 1800089.

8. Li, M.; Ku, D. N.; Forest, C. R., Microfluidic system for simultaneous optical measurement of platelet aggregation at multiple shear rates in whole blood. *Lab Chip* **2012,** *12* (7), 1355-1362.

9. Montague, S. J.; Andrews, R. K.; Gardiner, E. E., Mechanisms of receptor shedding in platelets. *Blood* **2018,** *132* (24), 2535-2545.

10. Rivera, J.; Lozano, M. L.; Navarro-Núñez, L.; Vicente, V., Platelet receptors and signaling in the dynamics of thrombus formation. *Haematologica* **2009,** *94* (5), 700-711.

11. Escolar, G.; Cases, A.; Vinas, M.; Pino, M.; Calls, J.; Cirera, I.; Ordinas, A., Evaluation of acquired platelet dysfunctions in uremic and cirrhotic patients using the platelet function analyzer (PFA-100): influence of hematocrit elevation. *Haematologica* **1999,** *84* (7), 614-619.

12. Hayward, C. P. M.; Pai, M.; Liu, Y.; Moffat, K. A.; Seecharan, J.; Webert, K. E.; Cook, R. J.; Heddle, N. M., Diagnostic utility of light transmission platelet aggregometry: Results from a prospective study of individuals referred for bleeding disorder assessments. *J. Thromb. Haemost.* **2009,** *7* (4), 676-684.

13. Bolliger, D.; Seeberger, M. D.; Tanaka, K. A., Principles and practice of thromboelastography in clinical coagulation management and transfusion practice. *Transfus. Med. Rev.* **2012,** *26* (1), 1-13.

14. Harrison, P., The role of PFA-100® testing in the investigation and management of haemostatic defects in children and adults. *Br. J. Haematol.* **2005,** *130* (1), 3-10.

15. Boknäs, N.; Macwan, A. S.; Södergren, A. L.; Ramström, S., Platelet function testing at low platelet counts: When can you trust your analysis? *Res. Pract. Thromb. Haemost.* **2019,** *3* (2), 285-290.

16. He, X.; Nguyen, C. V.; Pratap, M.; Zheng, Y.; Wang, Y.; Nisbet, D. R.; Williams, R. J.; Rug, M.; Maier, A. G.; Lee, W. M., Automated fourier space region-recognition filtering for off-axis digital holographic microscopy. *Biomed. Opt. Express* **2016,** *7* (8), 3111-3123.

17. Kim, M. K., Principles and techniques of digital holographic microscopy. *SPIE Reviews* **2010,** *1* (1).

18. Lui, M.; Gardiner, E. E.; Arthur, J. F.; Pinar, I.; Lee, W. M.; Ryan, K.; Carberry, J.; Andrews, R. K., Novel stenotic microchannels to study thrombus formation in shear gradients: Influence of shear forces and human platelet-related factors. *Int. J. Mol. Sci.* **2019,** *20* (12), 2967.

19. Zangle, T. A.; Teitell, M. A., Live-cell mass profiling: An emerging approach in quantitative biophysics. *Nat. Med.* **2014,** *11* (12), 1221-1228.

20. Davies, H. G.; Wilkins, M. H. F., Interference microscopy and mass determination. *Nature* **1952,** *169* (4300), 541.

21. Baker-Groberg, S. M.; Phillips, K. G.; McCarty, O. J. T., Quantification of volume, mass, and density of thrombus formation using brightfield and differential interference contrast microscopy. *J. Biomed. Opt.* **2013,** *18* (1).

22. Marquet, P.; Depeursinge, C.; Magistretti, P. J., Exploring neural cell dynamics with digital holographic microscopy. *Annu. Rev. Biomed. Eng.* **2013,** *15*, 407-431.

23. Kolesnikova, I. V.; Potapov, S. V.; Yurkin, M. A.; Hoekstra, A. G.; Maltsev, V. P.; Semyanov, K. A., Determination of volume, shape and refractive index of individual blood platelets. *J. Quant. Spectrosc. Radiat. Transf.* **2006,** *102* (1), 37-45.

24. Young, G.; Hundt, N.; Cole, D.; Fineberg, A.; Andrecka, J.; Tyler, A.; Olerinyova, A.; Ansari, A.; Marklund, E. G.; Collier, M. P.; Chandler, S. A.; Tkachenko, O.; Allen, J.; Crispin, M.; Billington, N.; Takagi, Y.; Sellers, J. R.; Eichmann, C.; Selenko, P.; Frey, L.; Riek, R.; Galpin, M. R.; Struwe, W. B.; Benesch, J. L. P.; Kukura, P., Quantitative mass imaging of single biological macromolecules. *Science* **2018,** *360* (6387), 423-427.

25. Rinehart, M. T.; Park, H. S.; Wax, A., Influence of defocus on quantitative analysis of microscopic objects and individual cells with digital holography. *Biomed Opt Express* **2015,** *6* (6), 2067-2075.

26. Park, S.; Kim, Y.; Moon, I., Automated phase unwrapping in digital holography with deep learning. *Biomed Opt Express* **2021,** *12* (11), 7064-7081.

27. Boos, C. J.; Beevers, G. D.; Lip, G. Y. H., Assessment of platelet activation indices using the ADVIATM 120 amongst 'high-risk' patients with hypertension. *Ann. Med.* **2007,** *39* (1), 72-78.

28. Aslan, J. E.; Itakura, A.; Gertz, J. M.; McCarty, O. J. T., Platelet shape change and spreading. *Methods Mol. Biol.* **2012,** *788*, 91-100.

29. Tomaiuolo, M.; Matzko, C. N.; Poventud-Fuentes, I.; Weisel, J. W.; Brass, L. F.; Stalker, T. J., Interrelationships between structure and function during the hemostatic response to injury. *Proceedings of the National Academy of Sciences of the United States of America* **2019,** *116* (6), 2243-2252.

30. Papa, A. L.; Jiang, A.; Korin, N.; Chen, M. B.; Langan, E. T.; Waterhouse, A.; Nash, E.; Caroff, J.; Graveline, A.; Vernet, A.; Mammoto, A.; Mammoto, T.; Jain, A.; Kamm, R. D.; Gounis, M. J.; Ingber, D. E., Platelet decoys inhibit thrombosis and prevent metastatic tumor formation in preclinical models. *Sci. Transl. Med.* **2019,** *11* (479), eaau5898.

31. Du Plooy, J. N.; Buys, A.; Duim, W.; Pretorius, E., Comparison of platelet ultrastructure and elastic properties in thrombo-embolic ischemic stroke and smoking using atomic force and scanning electron microscopy. *PLoS ONE* **2013,** *8* (7), e69774.

32. Welsh, J. D.; Muthard, R. W.; Stalker, T. J.; Taliaferro, J. P.; Diamond, S. L.; Brass, L. F., A systems approach to hemostasis: 4. How hemostatic thrombi limit the loss of plasma-borne molecules from the microvasculature. *Blood* **2016,** *127* (12), 1598-1605.

33. Poulter, N. S.; Pollitt, A. Y.; Owen, D. M.; Gardiner, E. E.; Andrews, R. K.; Shimizu, H.; Ishikawa, D.; Bihan, D.; Farndale, R. W.; Moroi, M.; Watson, S. P.; Jung, S. M., Clustering of glycoprotein VI (GPVI) dimers upon adhesion to collagen as a mechanism to regulate GPVI signaling in platelets. *J. Thromb. and Haemost.* **2017,** *15* (3), 549-564.

34. Pike, J. A.; Simms, V. A.; Smith, C. W.; Morgan, N. V.; Khan, A. O.; Poulter, N. S.; Styles, I. B.; Thomas, S. G., An adaptable analysis workflow for characterization of platelet spreading and morphology. *Platelets* **2020**, 1-5.

Chapter 8 Conclusion and Future Work

8.1 Conclusion

Understanding and characterizing platelet function through morphological, biochemical, and mechanical responses have great potential in interpreting platelet dysfunction, leading to serious health prognosis. However, functional imaging of platelets during thrombus formation under flow shear is a grand challenge due to its small physical size (~2 -3 μm), rapid activation at milliseconds, sensitivity to shear forces, and unsuitability for genetic manipulation in human samples. The limitations in acquisition speed and genetic manipulation restrict the application of super-resolution fluorescence microscopy in assessing haemostasis and platelet function.

This thesis proposed a label-free imaging method (COSI) based on light scattering and interferometry to study single platelet activation and thrombus stability. Unlike fluorescence-based approaches that use fluorophore as imaging probes, scattering light microscopy uses the refractive index as a stable biomarker and collects the scattered light for high-contrast imaging. The COSI system demonstrated that we could capture single platelet adhesion and migration dynamics during thrombus formation under flow shear at high spatial-temporal resolution. Moreover, we developed two different variants of the COSI system: COSI-F that collaborates fluorescence detection, and COSI-QPM that cooperates quantitative phase imaging. The COSI-F system shows high-contrast imaging of platelet migration on coated agonists, providing rich quantifications in axial displacements of rear and leading edge of a migrating platelet and morphological features. In the last part of this thesis, we demonstrated the thrombus stability assay that quantified adhesive platelet activity (at μm/s) and dry mass (at pg accuracy) of the thrombus simultaneously with the effect of a

metalloproteinase inhibitor. Overall, this thesis focuses on developing label-free scattering techniques for the quantitative study of platelets and blood thrombus under flow.

The following sections discuss the limitations and future work adopted to improve the COSI system and experimental ideas on platelet function analysis.

8.2 Investigating Role of Integrin/Receptors in Cell Protrusions

Chapter 6 used COSI-F to study platelet migration on fibrin(ogen) coated surfaces. In this study, we labelled the fibrin(ogen) and monitored platelet migration based on fluorescence intake. We also tracked the axial fluctuation of a migrating platelet and spotted a difference in axial displacement pattern between the rear and leading edge. However, the reason behind the high axial fluctuation of the leading edge remains questioned. Nicolai *et al.* [1] have demonstrated that the leading edge has a much higher concentration of Arp 2/3 complex (using a fixed sample) related to actin polymerization. This highly concentrated Arp 2/3 could lead to a more rapid change in actin polymerization and possibly lead to a large axial fluctuation. Future studies that focus on real-time detection of integrins or proteins variations during adhesion and migration would be valuable when interpreting the morphology of the membrane protrusions.

We also observed an interesting effect during the platelet adhesion and spreading process, where a filopodium would be folded to form the edge of a lamellipodium (Fig. 6-6). This change of filopodia structure could relate to actin filament organization during cytoskeleton rearrangement, but the mechanism remains unclear. The 3D structure of the membrane protrusions has been studied to verify the role of integrin αIIbβ3 and ion cations in actin organization and polarity using the cryoelectron tomography (cryo-ET) [2] as shown in Fig. 8-1. The study reveals the high density of membrane receptors is concentrated at the

plasma membrane (inlet images in Fig. 8-1 C) with the presence of αIIbβ3. However, the limitation of the study is the lack of dynamic information during filopodia formation because live-cell imaging can not be conducted using electron microscopy. Therefore, COSI-F can be used to study the mechanisms of actin organization and how integrin and membrane receptors contribute to actin polymerization. With real-time detection of the biochemical signalling and high contrast morphological study focusing on the membrane protrusions, COSI-F could bring new insight into the cytoskeleton rearrangement during platelet adhesion and activation.

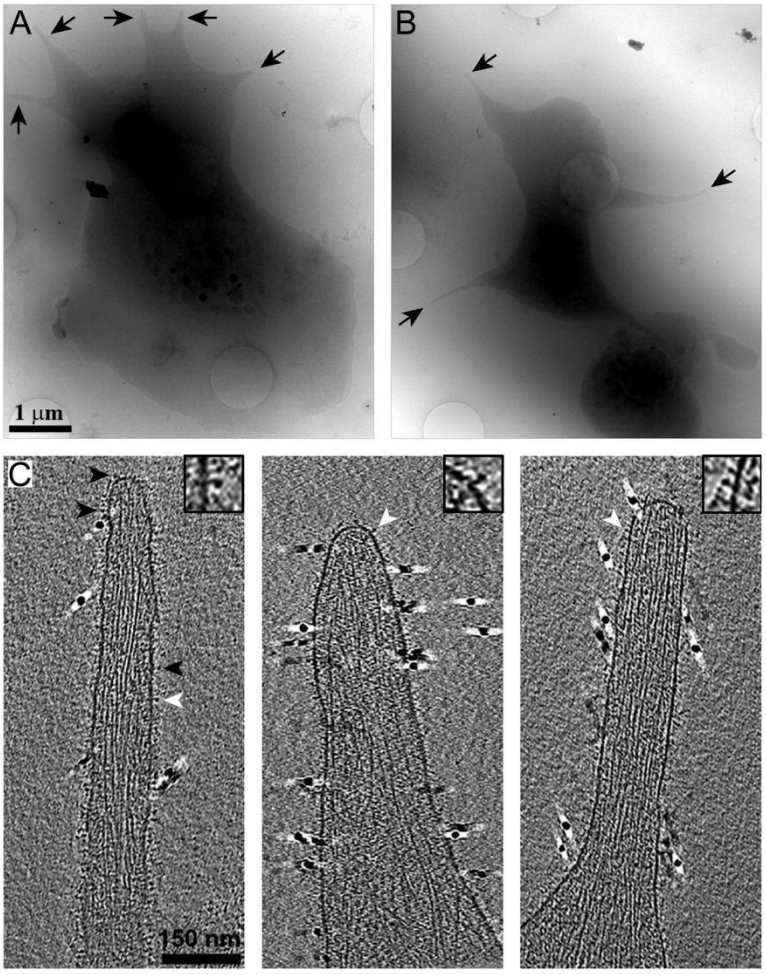

Figure 8-1 Visualizing platelet pseudopodia using cryo-ET. (A-B) images of platelets spreading on fibrinogen-functionalized SiO2- coated gold girds with dark arrows indicating the pseudopodia. (C) Cryotomograms slices of the pseudopodia in 10 nm thickness. The insets show the magnified membrane receptors (white arrowheads). This figure is reprinted with permission from Sorrentino *et al.* [2] © 2021 National Academy of Sciences.

8.3 Enhancing Axial Resolution of COSI-F

In chapter 6.3, we calibrated the axial displacement of the thin lamellipodia using polystyrene nanoparticles by swapping the sample (fixed particles on a coverslip) across the focus of the objective. From the calibration curve, we observed transitions from positive to negative contrast, indicating the effect of the Gouy phase at different axial positions. We chose this method to replicate the lamellipodia as a thin-firm model because platelet lamellipodia do not have a complex internal morphology (actin and lipid bilayer). However, to achieve a more accurate axial displacement from the interference signal, re-calibrating axial intensity profile using a non-coverslip adhesion probe is needed [3].

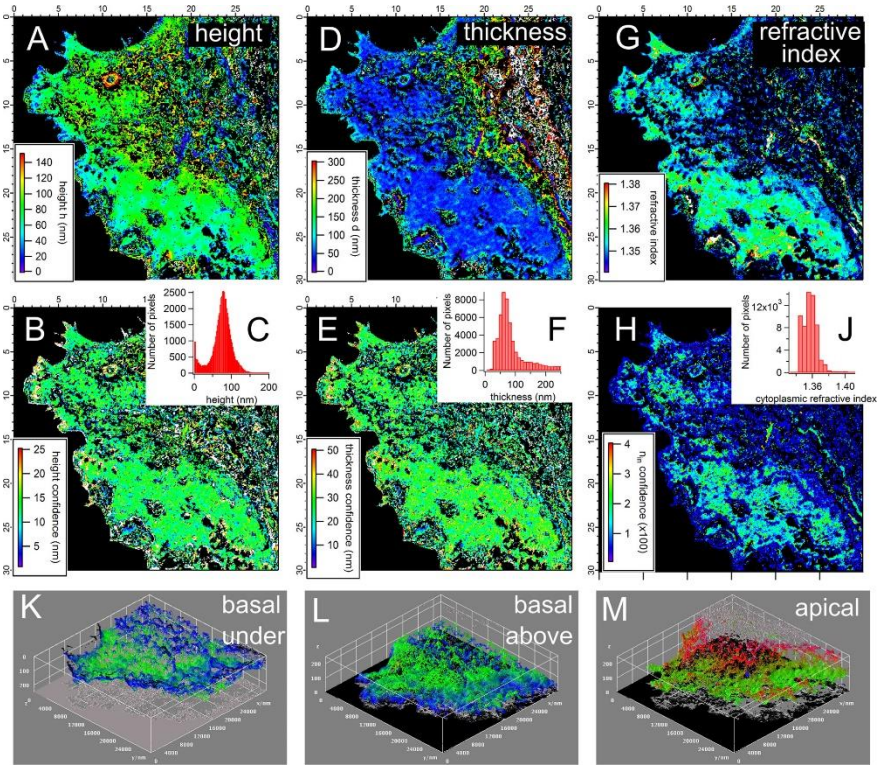

Figure 8-2 Calculated (A) height (distance to the coverslip), (D) thickness, and (G) refractive of the lamellipodia based on the reconstruction algorithm from 3D-RICN. The confidence intervals for these calculations are shown in (B), (E), and (H), respectively. The 3D representation of the basal membrane and apical membrane can be seen in (K-M). This figure is reprinted with permission from Dejardin [4] *et al.* © 2018 American Chemical Society.

Another method that extracts axial position, thickness, and refractive index is based on the numerical simulations of the interference signal (3D-RICN [4]). 3D reflection interference contrast nanoscopy (3D-RICN) calculates the axial positions and thickness of the sample by modelling the reflected light at different interference (glass -medium - lipid - cytoplasm). A complete reconstruction requires multi-wavelength RICM images at different (at least three) illumination numerical apertures (INA). And the reconstruction is restricted to the lamellipodia region only due to the complexity of the structure. Fig. 8-2 illustrates the example of reconstructing height (distance to the coverslip), thickness, and refractive index using 3D-RICN and the confidence intervals.

The interference detection in the COSI system shares the same imaging concept as RICM, and the circular scanning pattern modifies illumination angle that could replicate the images taken at different INAs. Therefore, we argue that the 3D-RICN method could be applied to the COSI system to interpret axial displacement by cooperating multi-wavelength illumination and modifying the reconstruction algorithm.

8.4 Improving *In-silico* Modelling using Imaging Data

Computational models of platelet-platelet interaction and dynamics of thrombus formation can provide insights into the clinically relevant prediction of functional responses when platelet dysfunction is presented. Particle-based models treat each individual platelet as one particle and model the forces generated by membrane receptors or integrins (adhesion and repulsion) to mimic platelet-platelet interaction. As the model is single platelet based, it preserves the heterogeneous behaviour of platelet activation, cytosolic calcium, and α-granule secretion within a forming thrombus. Additionally, modelling thrombus formation permits the study of the mechanistic relationship of fluid transport and platelet activation and allows a

predictive step toward the structural properties of thrombus under fluid shear and especially on stability (Fig. 8-3A).

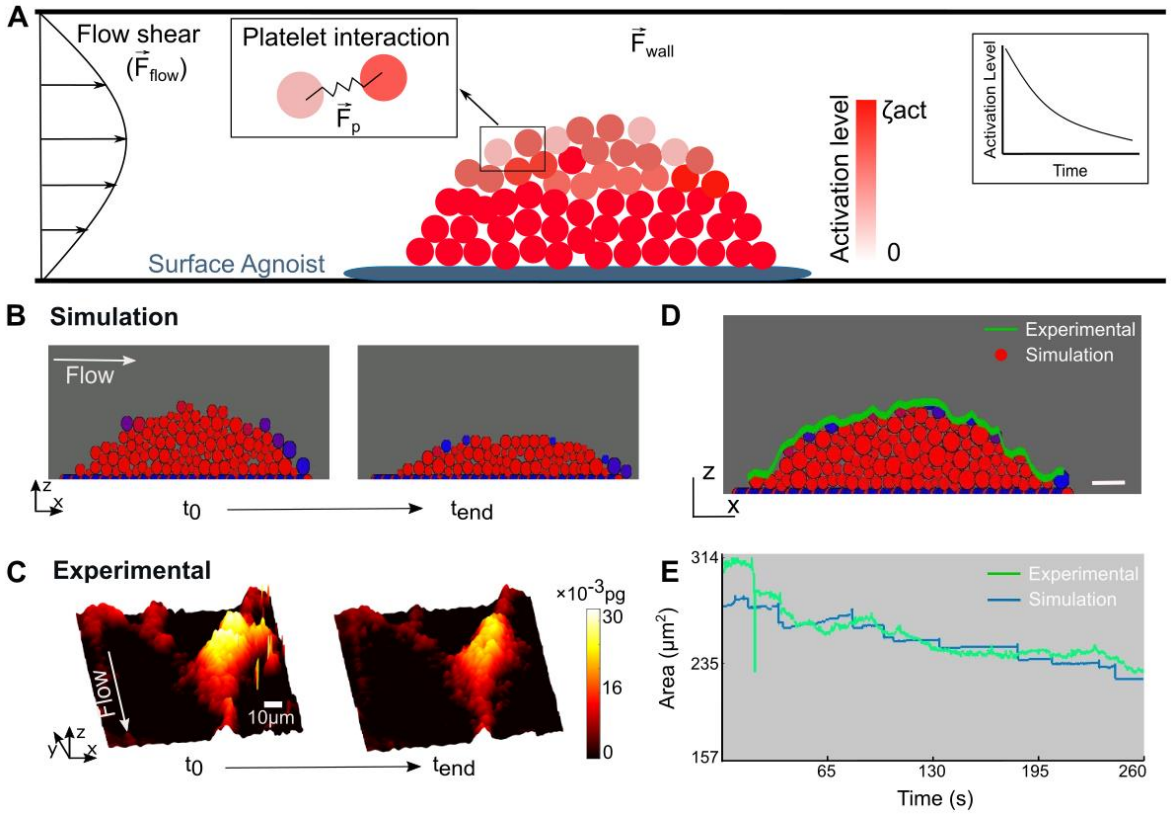

Figure 8-3 (A) Particle-based modelling shows the platelet-platelet interaction determined by fluid shear, surface agonist, vessel geometry, platelet activation, membrane receptors, and integrin. Example of (B) one model built based on (C) experimental conditions. The simulation profile of the thrombus during the embolization test is tuned based on the experimental results and matched (D-E).

However, effective and reliable particle modelling requires repeated experimental datasets to fine-tune the model and decide when platelets interact to accumulate and detach. The accumulation and detachment of platelets during thrombus formation can be tracked with quantitative imaging approaches [5] (chapter 7) by monitoring the whole thrombus's volume or mass, which could serve as the baseline for fine-tuning the thrombus models. Here, we demonstrated the initial results of the thrombus modelling (Fig. 8-3 B) during the embolization test based on the experimental data (Fig. 8-3 C). By fine-tuning the activation level of the platelets in a forming thrombus, we could match the predicted thrombus

embolization with the experimental results (Fig. 8-3 D-E). Future work measuring the platelet activation level and integrin expression using fluorescence imaging techniques could further improve the model and prediction of thrombus stability.

8.5 Investigating Collagen Alignment in Thrombus Formation

Adhesion ligands play a critical role in triggering platelet activation and adhesion, and different agonists could bind to specific receptors and integrins, leading to completely different platelet morphological [6, 7]. In our thrombus formation and embolization experiments, the surface is coated with collagen fibre randomly distributed in the microfluidic channel. However, the alignment and density of collagen fibre might impact the initial platelet adhesion and thrombus formation. The collagen fibre aligned with the flow direction could increase the chance of platelet migration along with the collagen fibre, resulting in a higher chance of binding due to the extra exposed bind sites.

To test the effect of collagen alignment on thrombus formation, we first investigate the methods and metrics that could quantify collagen coating. In Fig. 8-4, we show the image of a collagen coating microfluidics channel, captured using the second-harmonic signal by two-photon microscopy. We also used three different metrics for collagen alignment: fibre length, straightness, and fibre angle. Future works to investigate the surface coating of microfluidics channels are needed to study the effects of collagen alignment.

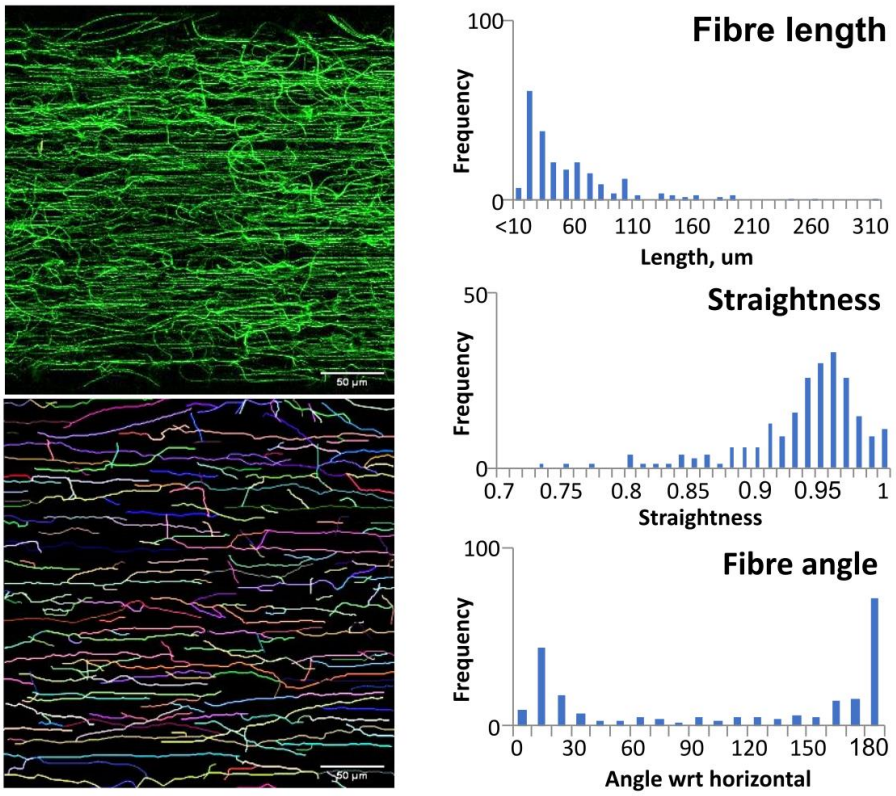

Figure 8-4 Quantification of collagen alignment. The second-harmonic signal of collagen fibres are captured using two-photon microscopy, and the binary image with extracted collagen fibres is generated using Cellprofiler. The fibre length, straightness, and fibre angle quantifications are demonstrated as collagen alignment metrics.

8.6 Improving the Control System for COSI-F

The COSI-F system combines three different imaging modalities with two detection cameras, which could be confusing for users to distinguish signals from each modality. Therefore, developing a user-friendly interface is critical, allowing users to access the system easily. Fig. 8-5 shows a proposed block diagram of the control system, listing the key input parameters (from the user) and the three imaging channels. In this case, the galvanometer needs to be scanned at two different voltages (interference V2 and scattering V1 detection shown in blue and red, respectively). The camera trigger must be synchronized with the switching between interference and scattering detection. The frame rate (K) of the capture

determines the period of one sinusoidal signal, and the exposure (Ts) determines the duty cycle of the trigger output.

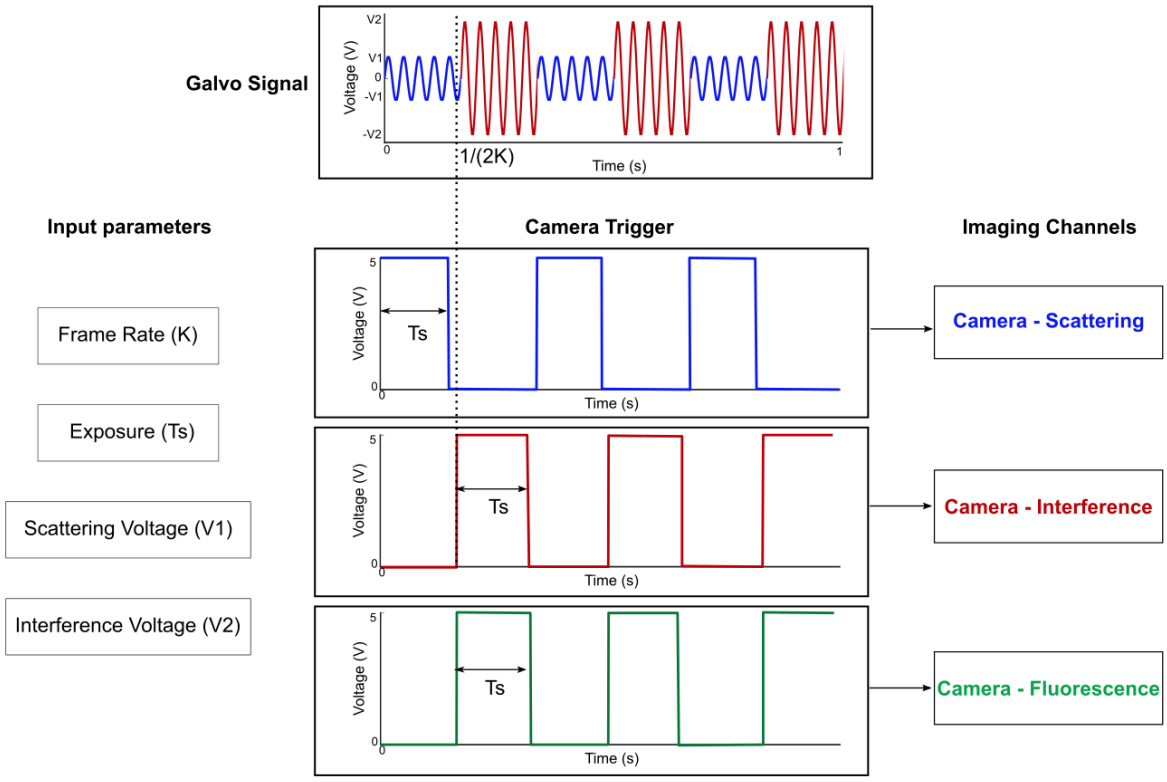

Figure 8-5 Blocking diagram showing the proposed control system and the user interface.

Contribution

Mr Efim Bershadsky did the thrombus simulation shown in Fig.8-3. Mr Jasper Li did the collagen measurement in Fig. 8-4.

8.7 References

1. Nicolai, L.; Schiefelbein, K.; Lipsky, S.; Leunig, A.; Hoffknecht, M.; Pekayvaz, K.; Raude, B.; Marx, C.; Ehrlich, A.; Pircher, J.; Zhang, Z.; Saleh, I.; Marel, A. K.; Löf, A.; Petzold, T.; Lorenz, M.; Stark, K.; Pick, R.; Rosenberger, G.; Weckbach, L.; Uhl, B.; Xia, S.; Reichel, C. A.; Walzog, B.; Schulz, C.; Zheden, V.; Bender, M.; Li, R.; Massberg, S.; Gaertner, F., Vascular surveillance by haptotactic blood platelets in inflammation and infection. *Nature Communications* **2020,** *11* (1).

2. Sorrentino, S.; Conesa, J. J.; Cuervo, A.; Melero, R.; Martins, B.; Fernandez-Gimenez, E.; De Isidro-Gomez, F. P.; De la Morena, J.; Studt, J. D.; Sorzano, C. O. S.; Eibauer, M.; Carazo, J. M.; Medalia, O., Structural analysis of receptors and actin polarity in platelet protrusions. *Proceedings of the National Academy of Sciences of the United States of America* **2021,** *118* (37).

3. Mahmoodabadi, R. G.; Taylor, R. W.; Kaller, M.; Spindler, S.; Mazaheri, M.; Kasaian, K.; Sandoghdar, V., Point spread function in interferometric scattering microscopy (iSCAT). Part I: aberrations in defocusing and axial localization. *Optics Express* **2020,** *28* (18), 25969-25988.

4. Dejardin, M. J.; Hemmerle, A.; Sadoun, A.; Hamon, Y.; Puech, P. H.; Sengupta, K.; Limozin, L., Lamellipod Reconstruction by Three-Dimensional Reflection Interference Contrast Nanoscopy (3D-RICN). *Nano Letters* **2018,** *18* (10), 6544-6550.

5. He, X.; Montague, S. J.; Tao, X.; Gardiner, E. E.; Lee, W. M., Quantifying Embolism: Label-Free Volumetric Mapping of Thrombus Structure and Kinesis in a Microfluidic System with Optical Holography. *Advanced Biosystems* **2018,** *2* (10).

6. Nguyen, T. H.; Palankar, R.; Bui, V. C.; Medvedev, N.; Greinacher, A.; Delcea, M., Rupture Forces among Human Blood Platelets at different Degrees of Activation. *Scientific Reports* **2016,** *6*.

7. Ruggeri, Z. M.; Mendolicchio, G. L., Adhesion mechanisms in platelet function. *Circulation Research* **2007,** *100* (12), 1673-1685.

Appendix A Mie Theory

Mie theory considers a sphere with radius r embedded in an absorbing medium, the origin of a cartesian coordinate is selected to be at the centre of the sphere, with the positive z-axis representing the direction of propagation of a linearly polarized incident wave. The incident electric vector is assumed to be polarized in the direction of the x-axis. Considering the cases where the medium is optically linear so that the superposition principle is valid, the electromagnetic field can be expressed in vector spherical harmonics [1] based on the amplitude of the incident wave at the origin E_0 in Eq. A.1.

$$E = E_0 \sum_n (a_n M_n + b_n N_n) \qquad (A.1)$$

Following the vector spherical harmonics, the incident, internal and scattered field can be expressed with Legendre polynomials and Bessel functions in Eq. A.2 – A.4.

$$E_i = E_0 \sum_{n=1}^{\infty} i^n \frac{2n+1}{n(n+1)} \left(M_{oln}^{(1)} - i N_{eln}^{(1)} \right) \qquad (A.2)$$

$$E_1 = \sum_{n=1}^{\infty} E_n (c_n M_{oln}^{(1)} - i d_n N_{eln}^{(1)}) \qquad (A.3)$$

$$E_s = \sum_{n=1}^{\infty} E_n (i a_n N_{eln}^{(3)} - b_n M_{oln}^{(3)}) \qquad (A.4)$$

$$with\ E_n = \frac{i^n E_0 (2n+1)}{n(n+1)}$$

The expansion coefficients are written as a_n, b_n, c_n and d_n, where n is the expansion index going from n = 1 to n = ∞, that is determined by resolving the equation system with the

boundary condition that the tangential component of the electromagnetic field be continuous across the spherical surface of the sphere.

$$a_n = \frac{m\psi_n(mx)\psi_n'(x) - \psi_n(x)\psi_n'(mx)}{m\psi_n(mx)\xi_n'(x) - \xi_n(x)\psi_n'(mx)} \quad (A.5)$$

$$b_n = \frac{\psi_n(mx)\psi_n'(x) - m\psi_n(x)\psi_n'(mx)}{\psi_n(mx)\xi_n'(x) - m\xi_n(x)\psi_n'(mx)} \quad (A.6)$$

$$c_n = \frac{-im}{\psi_n(mx)\xi_n'(x) - m\xi_n(x)\psi_n'(mx)} \quad (A.7)$$

$$d_n = \frac{-im}{m\psi_n(mx)\xi_n'(x) - \xi_n(x)\psi_n'(mx)} \quad (A.8)$$

where ψ and ξ are the Riccati-Bessel function defined as:

$$\psi_n(\rho) = \rho j_n(\rho) \quad (A.9)$$

$$\chi_n(\rho) = \rho y_n(\rho) \quad (A.10)$$

$$\xi_n(\rho) = \rho h_n^{(2)}(\rho) \quad (A.11)$$

The vector spherical harmonics in the expansion of internal field and scattered field in Eq. A.12 to A.15 is given as:

$$M_{oln} = cos\phi\pi_n(cos\theta)z_n(\rho)\hat{e}_\theta - sin\phi\tau_n(cos\theta)z_n(\rho)\hat{e}_\phi \quad (A.12)$$

$$M_{eln} = -sin\phi\pi_n(cos\theta)z_n(\rho)\hat{e}_\theta - cos\phi\tau_n(cos\theta)z_n(\rho)\hat{e}_\phi \quad (A.13)$$

$$N_{oln} = sin\phi n(n+1)sin\theta\pi_n(cos\theta)\frac{z_n(\rho)}{\rho}\hat{e}_r + sin\phi\tau_n(cos\theta)\frac{[\rho z_n(\rho)]'}{\rho}\hat{e}_\theta$$

$$+ cos\phi\pi_n(cos\theta)\frac{[\rho z_n(\rho)]'}{\rho}\hat{e}_\phi \quad (A.14)$$

$$N_{eln} = cos\phi n(n+1) sin\theta \pi_n(cos\theta) \frac{z_n(\rho)}{\rho} \hat{e}_r + cos\phi \tau_n(cos\theta) \frac{[\rho z_n(\rho)]'}{\rho} \hat{e}_\theta$$

$$- sin\phi \pi_n(cos\theta) \frac{[\rho z_n(\rho)]'}{\rho} \hat{e}_\phi \qquad (A.15)$$

where π_n and τ_n are the angle-dependent functions (Eq. A.16 and A.17), and z_n denotes the spherical Bessel function.

$$\pi_n = \frac{2n-1}{n-1} \mu \pi_{n-1} - \frac{n}{n-1} \pi_{n-2} \qquad (A.16)$$

$$\tau_n = n\mu\pi_n - (n+1)\pi_{n-1} \qquad (A.17)$$

$$with\ \mu = cos\theta, \pi_0 = 0\ and\ \pi_1 = 1$$

T-matrix (translation matrix) is also called null field method or extended boundary condition method (EBCM) that was originally formulated by waterman in 1965 [2]. The translation matrix correlates the relationship between scattering coefficients of the single scatterer related to its entire structure. In the case of multiple particles within the homogenous structure, the incident field for each particle is the summation of the original incident field and the total scattered field from all other particles (Eq. A.18). Similarly, the overall incident field coefficient considers the original incident field coefficient and the scattered field coefficient from all other particles (Eq. A.19)**.** T- matrix describes the near field and far field information on how the object interacts with any illumination. It only depends on the particle properties, e.g. composition, size, geometry, and orientation. The T-matrix of a sphere is known analytically as the Mie coefficients, as shown in Eq. A.20. The calculated initial field coefficient and T – matrix, scattered field coefficient, and field intensity can be derived using the spherical vector wave function (Eq. A.22).

$$E_{inc}^{i}(r) = E_{inc}(r) + \sum_{i' \neq i} E_{scat}^{i'}(r) \qquad (A.18)$$

$$a_n^i = a_{inc,n}^i + \sum_{i' \neq i} \sum_{n'} W_{nn'}^{ii'} b_{n'}^{i'} \qquad (A.19)$$

$$T_{nn'}^{i} = Q_{\tau l}^{i} \delta_{\tau\tau'} \delta_{mm'} \delta_{ll'} \qquad (A.20)$$

$$\sum_{i',n'} M_{nn'}^{ii'} b_{n'}^{i'} = \sum_{n'} T_{nn'}^{i}\, a_{inc,n'}^{i} \qquad (A.21)$$

$$E_{scat} = \sum_{i' \neq i} E_{scat}^{i'}(r) = \sum_{i' \neq i} b_i * \psi_{\tau lm}^{(v)}(r) \qquad (A.22)$$

References

1. Bohren, C. F., *Absorption and scattering of light by small particles*. John Wiley & Sons: 2008; p 82-129.

2. Waterman, P. C., Matrix Formulation of Electromagnetic Scattering. *Proceedings of the IEEE* **1965,** *53* (8), 805-812.

Appendix B Quantitative Phase Microscopy

Quantitative imaging refers to methods that extract the quantifiable features from images to assess the functionality of object [1]. In cell biology, quantifying these features include volume, mass, thickness, and density plays an essential role in understanding cell migration and morphogenesis dynamics. Fluorescence imaging provides quantifications based on the intensity of emitted light from the sample, which is highly dependent on the quality of labelling and suspectable to photobleaching in long-time imaging. Label-free imaging methods use phase information encoded in the transmitted light as the marker to retrieve phase shift and optical thickness, permitting fast and reliable quantifications of morphology changes in three-dimensional.

Techniques that exploit phase in light microscopy are originated from the 1930s, when Fritz Zernike invented optical phase microscopy [2], aiming to improve imaging contrast of biological samples. The phase contrast microscopy uses a phase plate to shift the phase of the scattered light from the sample by -90 degrees, which results in destructive interference of the scattered light and the illumination [3]. This shift in phase converts phase difference to intensity contrast (amplitude difference) and allows details of the specimen to appear relatively dark against the bright background. Several implementations of phase microscopy have been developed includes differential interference contrast (DIC) [4] and Hoffman modulation contrast [5] to maximize imaging contrast in brightfield microscopy for biological samples. Still, all of them can only be used for viewing purposes and qualitative analysis [6]. In this section, I shall review the imaging techniques that could extract phase information from the interference pattern based on numerical approach and explain the process of phase

retrieve, followed by describing quantifications of sample properties such as volume and mass using phase.

The ability to use phase to extract quantitative information for the sample can be traced back to the 1940s, where Gabor proposed a holography method to record both intensity and phases in one photograph [7]. The term holography was created from two Greek words, “holos” and “grafe”, which means “entire” and “writing”, emphasizing that the entire information of the light field is being written. In Gabor’s original method, the object was placed after the focus of a coherent source, and a photographic plate was positioned at the far-field to record the interference between the light diffracted by the object and the collinear background. Around 20 years later, in the early 1960s, with the development of the laser, this method was applied in optical microscopy and supported the application of quantitative imaging.

Quantitative phase-contrast microscopy or quantitative phase imaging (QPM) is a group of imaging techniques that use interferometry to reconstruct the optical thickness profile of transparent samples within sub-wavelength accuracy [8]. The optical thickness relates to the sample's physical thickness and refractive index. Therefore, it can be used as a stable and accurate biomarker to reveal three-dimensional morphology for investigating the structure and dynamics of biological samples and tissues [8]. Digital holographic microscopy (DHM) is one type of QPM that utilizes holography in light microscopy [9].

Principle

In (DHM), the interference pattern is created by combing two arms of light from the same light source at the camera plane: an object arm passing through the sample (E_o) and a plain reference (E_r) that only passes through a series of optics. Two arms of light interfere

and form distinctive intensity fringes resulting from constructive and destructive interference. The phase shift (ϕ) due to change in the sample's refractive index in the object arm is encoded onto intensity variations along the fringes (Fig. B-1B). The amplitude and phase information can be accessed by calculating the complex optical fields numerically. As the phase information is encoded in the intensity of fringes, the fringe visibility plays an essential role in retrieved phase quality. Fringe contrast can be optimized both optically and computationally. The former requires matching the intensity and optical path difference between the object and reference arm, while the latter adopts machine learning algorithms to enhance fringe visibility [10].

There are two types of configurations of DHM based on how the reference and object arm are combined: in-line [11] and off-axis [12] holography. In the in-line interferometric configuration, the angle between the reference and object arm is set to zero. In contrast, the reference and object arms are projected with an angle θ in the off-axis configuration (Fig. B-1A). Here we use $E_r(\vec{r},t)$ and $E_o(\vec{r},t)$ represent complex light field of reference wave and the object wave, k_r and k_o indicate the wavenumber of the reference and object field, which have different values due to the different projection angle between the reference and object arm [13] (Eq. B.1 and B.2).

$$E_r(\vec{r},t) = E_r \times \exp\left(j\left(-\omega t + \left(\overrightarrow{k_r}\cdot\vec{r}\right)\right)\right) \tag{B.1}$$

$$E_o(\vec{r},t) = E_0 \times \exp\left(j(-\omega t + (\overrightarrow{k_o}\cdot\vec{r} + \varphi))\right) \tag{B.2}$$

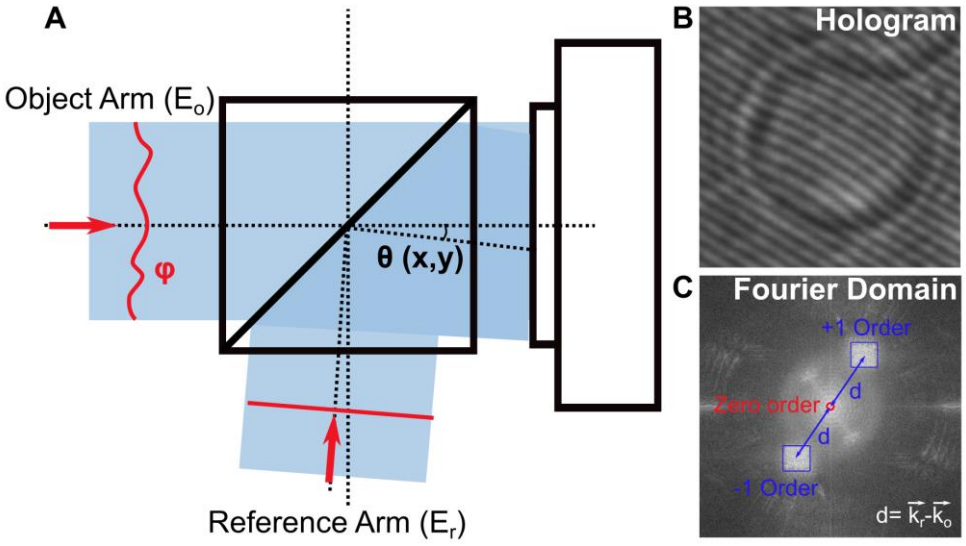

Figure B-1 principle of the off-axis hologram. (A) The object and reference arms are projected with an angle θ to the CCD, creating off-axis holography. (B) The hologram is generated by off-axis holography. (C) Fourier domain of the hologram.

The interference of these two beams can then be added together, and the expression could be determined as follows:

$$I_H = |E_r(\vec{r},t) + E_o(\vec{r},t)|^2 = E_r^2 + E_o^2 + E_r E_o \times \exp\left(j\left(\varphi + \left(\overrightarrow{k_o} - \overrightarrow{k_r}\right)\cdot\vec{r}\right)\right)$$

$$+O_0R_0 \times \exp\left(-j\left(\varphi - \left(\overrightarrow{k_r} - \overrightarrow{k_o}\right)\cdot\vec{r}\right)\right) \quad \text{(B.3)}$$

As indicated in the equation, the zero-order $O_0^2 + R_0^2$ is located in the origin point (centre point) of the spatial frequency domain, representing the zero-order. The two components containing the phase information from the sample $\exp\left(j\left(\varphi + \left(\overrightarrow{k_o} - \overrightarrow{k_r}\right)\cdot\vec{r}\right)\right)$ and $\exp\left(j\left(-\varphi + \left(\overrightarrow{k_r} - \overrightarrow{k_o}\right)\cdot\vec{r}\right)\right)$ are in symmetrical locations (+1/-1 order), resulting from the difference in wavenumber between reference and objective arm as shown in Fig. 2-1C. The phase term φ could be simply extracted by filtering out the +1 or -1 order in the frequency domain. However, in in-line holography configuration, as ko = kr, the twin-image in +1/-1 order will overlap with the zero-order, requiring a more complex numerical method

or multiple interferograms [11] to reconstruct the phase information. In the next section, I shall briefly explain extracting phase information by utilizing the +1/-1 order in the frequency domain.

Reconstruction process

The computational method for extracting phase information from the hologram is shown in Fig. B-2. The process transfers the hologram showing disturbed interference fringes with the posed phase delay to its frequency domain using Fast Fourier transformation (FFT). After that, a binary mask is generated to spatially filter out the first-order component in the frequency domain. The filtered component is manually placed at the centre of the field of view. The inverse Fast Fourier Transform (iFFT) was then performed that transferred the image back to the time domain showing as a complex field, with absolute value and angle of the complex matrix representing intensity and phase information, respectively. As the phase information is folded or wrapped within 0 to 2π, a 2D unwrapping process was then applied to obtain the final unwrapped phase map. In the final step, the curvature of the wavefront resulting from the reference and object beam passing through different optical elements is removed to obtain the corrected phase retrieved from the hologram. The retrieve phase information enables the reconstruction of quantitative measurement of the biological sample, including quantifications like volume, mass, and centre of mass. In the next section, I shall discuss converting phase information to quantifiable measurement.

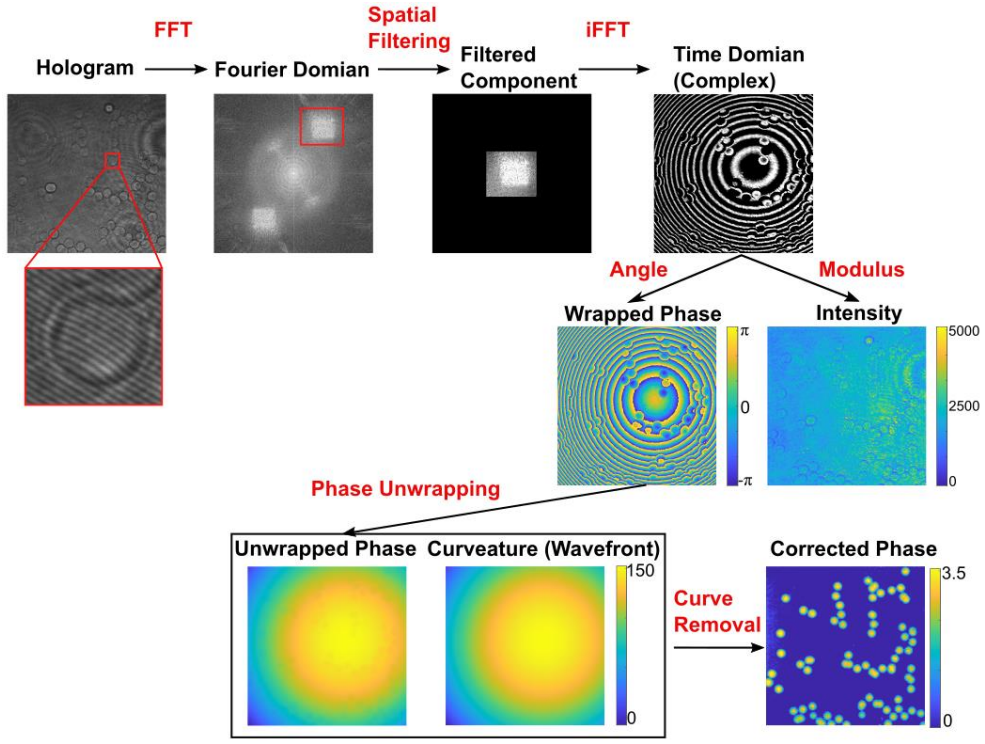

Figure B-2 Computation process of reconstructing phase information from the hologram.

Phase information for quantitative measurements

Monitoring biological cells using quantitative phase imaging has been demonstrated in various applications [14, 15]. The work by Dunn in 1989 has shown long-time imaging of chick heart fibroblast and illustrated the spread area is related to the dry mass of the cell [16]. The calculation of the dry mass of the sample is based on the optical phase delay introduced by a change in the refractive index. For most of the biological cells, the change in the refractive index corresponds to a linear increase in dry biomass (proteins and nucleic acids without water) that falls within a very narrow range of approximately $\alpha = 1.8 \times 10^{-4}$ m^3/kg (= 0.18 $\mu m^3/pg$) that allows one to estimate the dry mass of cells [17, 18]. Based on the translating factor, the dry mass of the biological sample can be calculated using the phase shift $\phi(x, y)$ from the sample as shown in Eq. B.4. In additional, the mass of a synthetic sample can be directly calculated using volume and density (d*v), e.g. the mass of the polystyrene microsphere can be calculated using d = 1.05 g/cm^2 [13, 18].

$$m_t(x,y) = \frac{1}{\alpha}\int \frac{\lambda \cdot \phi_t(x,y)}{2\pi} dA \quad \text{(B.4)}$$

The thickness (t) of the sample can also be calculated based on refractive index (n) and optical path length (OPL=n×t) [19]. As the phase shift is directly related to the optical path difference between passing through the sample and the medium, the heightmap can be converted from phase shift as shown in Eq. B.5, where Δn represents the difference in refractive index between the cell and aqueous solution. The total volume of the sample can be calculated using Eq. B.6, with S_p representing the pixel size of the imaging system.

$$h(x,y) = \frac{\phi(x,y)\lambda_0}{2\pi\Delta n} \quad (B.5)$$

$$V = \sum_{x,y} s_p \times h(x,y) \quad (B.6)$$

Quantitative phase imaging extracts the phase component of the light pass through the sample using interferometry, enabling the reconstruction of thickness, volume, and dry mass of biological samples. As fluorescence utilizes intensity to quantify volume and thickness, QPM only relies on the difference in refractive index, which can be treated as a stable biomarker than fluorophore. With off-axis holography, only one hologram is required to calculate these quantifiable features, which promote high-speed imaging and quantitative measurements of the dynamic process in cell migration and development.

Auto-focusing and evaluation matrix

One of the advantages of using phase imaging is that the image can be digitally refocused as quantitative information of the optical phase can be influenced by the focal plane of the measurement. Digital refocusing is achieved using a computational method based on Fresnel – Kirchhoff integral that describes the propagation of a wave field. Figure

B-3 illustrates the process of refocusing, in which the intensity and wavefront-corrected phase are combined to receive the complex amplitude before converting it to the frequency domain using FFT. After that, we calculated a defocusing matrix with a set propagation distance and then projected the matrix onto the complex field of the object. The iFFT is then performed on the propagated field, in which the phase information can be extracted from the angle information of the complex field with a phase unwrapping algorithm.

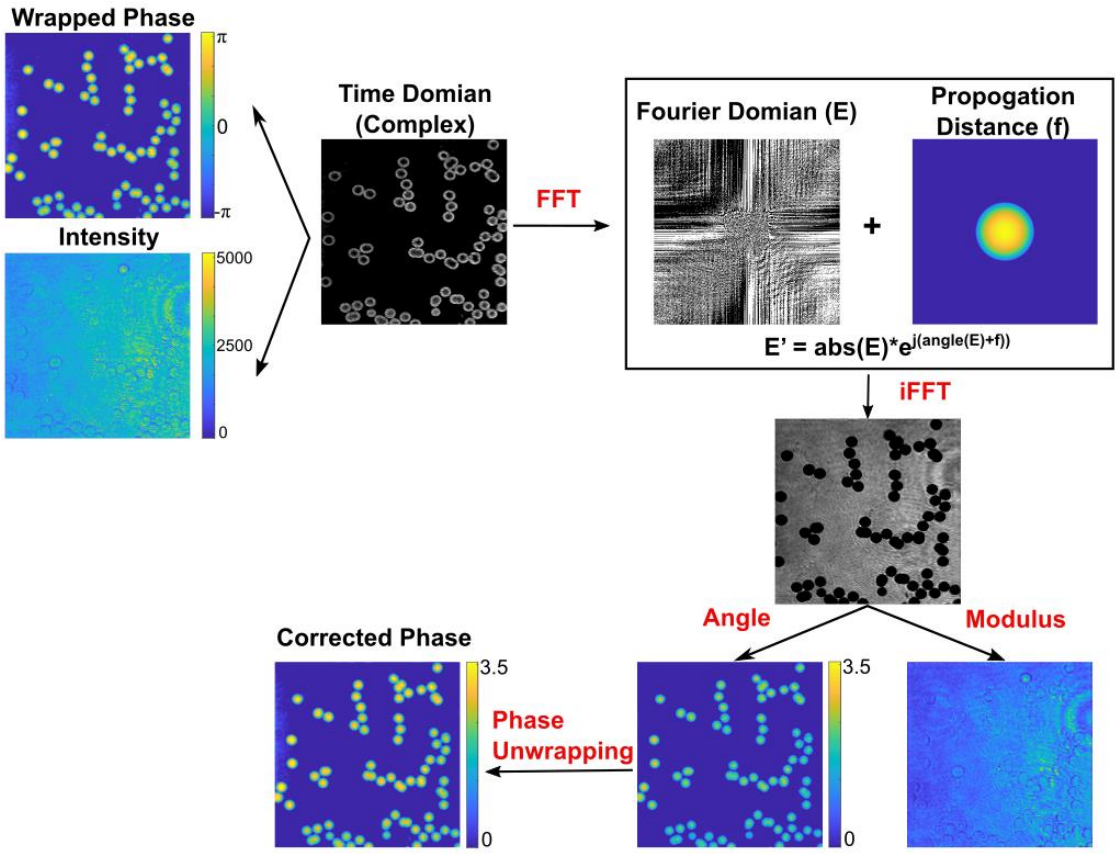

Figure B-3 Computation process of digital refocus

To determine the optimized focus position, a few benchmarks have been applied to check the reconstructed intensity imaging [20], including methods to evaluate the imaging contrast and edge detection method. Quantifying the variance (VAR) of grey value distribution [21-23] is the most well-known method for comparing imaging contrast, as shown in

Eq. B.7, where g(x,y) represents the intensity of individual pixel and Nx and Ny indicates the dimension of the image.

$$VAR = \frac{1}{N_x N_y} \sum_{x,y} [g(x,y) - \bar{g}]^2 \qquad (B.7)$$

Algorithms using edge detection, including gradient calculation [22, 24] and Laplace [21, 22] filtering are also demonstrated in Eq. B.8 and B.9.

$$GRA = \iint \sqrt{\left(\frac{\delta g(x,y)}{\delta x}\right)^2 + \left(\frac{\delta g(x,y)}{\delta y}\right)^2}$$

$$= \sum_{x=1}^{N_{x-1}} \sum_{y=1}^{N_{y-1}} \sqrt{\big(g(x,y) - g(x-1,y)\big)^2 + \big(g(x,y) - g(x,y-1)\big)^2} \qquad (B.8)$$

$$LAP = \iint \big(\Delta g(x,y)\big)^2 dxdy$$

$$\approx \sum_{x=1}^{N_{x-1}} \sum_{y=1}^{N_{y-1}} [g(x+1,y) + g(x-1,y) + g(x,y+1) + g(x,y-1)$$

$$- 4g(x,y)]^2 \qquad (B.9)$$

The digital refocusing of a 5.4 μm silica microsphere (index = 1.45) along with three benchmarks are shown in Fig. B-4. The reconstructed phase images at three different planes are selected where (i), (ii), and (iii) in Fig. B-4 are imaging planes before the focus, in focus, and after focus, respectively. The effectiveness of the three benchmarks is also compared in Fig. B-4, where they also have a minimized value around a similar propagation distance.

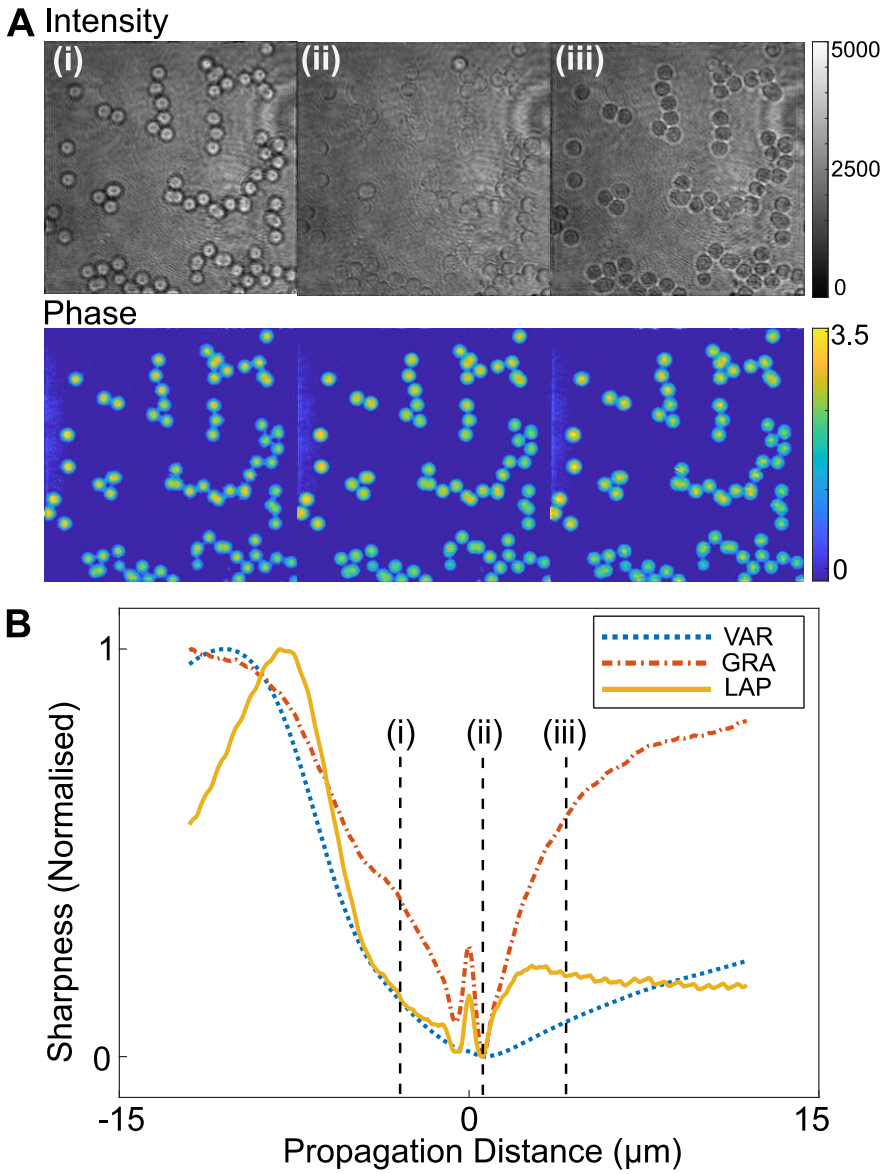

Figure B-4 The refocused (A) intensity and (B) phase images of 5.4 μm silica microsphere at three selected focusing planes. (C) Quantification of image sharpness using three algorithms.

Matlab code for autofocusing and sharpness calculation

```
inten = double(inten);
phase = double(phase);

laserWavelength = 632.8*(10^-9);

[imx,imy]=size(phase);
pixr=0.1e-6;
kx0=linspace(-pi/pixr,pi/pixr,imy);
ky0=linspace(-pi/pixr,pi/pixr,imx);
kx=repmat(kx0,imx,1);
```

```
ky=repmat(ky0.',1,imy);
k0=2*pi/laserWavelength;
kk=k0^2-kx.^2-ky.^2;
kk(kk<0) = 0;
start=-100e-6;
dist=1e-6;
time=200;
im=1;

writerObj = VideoWriter('C:\Users\anuaolab\Desktop\3.tif_output_folder\inten3.avi');
writerObj.FrameRate = 30;
open(writerObj);
figure1 = figure;
axes1 =axes('Parent',figure1,'YDir','reverse','Layer','top','DataAspectRatio',[1 1 1], 'CLim',[-4
10]);

for ii=1:time
   distance=dist*(ii-1);
   [ phase_out,intensity_out,shiftf,reald,slope,sharpness_VAR,sharpness_GRA,...
        sharpness_LAP] = digitalfocus_unwrap(phase,inten,kk,start,distance);
   if im==1
      hold on
      imagesc(intensity_out);
      caxis([0 800])
      axis tight;

      colormap(gray)
      colorbar
      title(['propagation distance =',num2str(reald),'m'])
      pause(0.05)
      hold off
      frame = getframe(gcf);
        writeVideo(writerObj, frame);
   end
   sharp_var(ii)=sharpness_VAR;
   sharp_gra(ii)=sharpness_GRA;
   sharp_lap(ii)=sharpness_LAP;

   disp(ii)
end
  close(writerObj);

sharpness_VAR_norm = (sharp_var - min(min(sharp_var)))/(max(max(sharp_var))-
min(min(sharp_var)));
sharpness_GRA_norm = (sharp_gra - min(min(sharp_gra)))/(max(max(sharp_gra))-
min(min(sharp_gra)));
sharpness_LAP_norm = (sharp_lap - min(min(sharp_lap)))/(max(max(sharp_lap))-
min(min(sharp_lap)));
xx=(start:dist:reald)/1e-6;
figure
```

```
plot(xx,sharpness_VAR_norm,xx,sharpness_GRA_norm,xx,sharpness_LAP_norm)
ylim([-0.1 1.1])
legend('VAR','GRA','LAP')
title('intensity analysis')

[M,I] = min(sharpness_VAR_norm(:));
[M2,I2] = min(sharpness_GRA_norm(:));
[M3,I3] = min(sharpness_LAP_norm(:));

function [ phase_out,intensity_out,shiftf,reald,slope, sharpness_VAR,sharpness_GRA,sharpness_LAP]
= digitalfocus_unwrap(phase,intensity,kk,start,dist)
object_o=intensity.*exp(1j*phase);
obj_f_o = fftshift(fft2(object_o));

reald=start+dist;
shiftf=-sqrt(kk)*(reald);

ccdImfft0=abs(obj_f_o).*exp(1i*((angle(obj_f_o))+shiftf));
centeredImage_s = ifft2(fftshift(ccdImfft0));

intensity_out=(abs(centeredImage_s)).^2;

f=angle(centeredImage_s);
xx = size(phase,1);
yy = size(phase,2);
unwrapper = LeastSquares_Unwrapper(xx,yy);
phase_unwrap = unwrapper.unwrap(f);
phaseIms = gather(phase_unwrap);

[slope,yy,xx] = cruveremoval( phaseIms);
phase_out= phaseIms-slope;

abs_o=imfilter(intensity_out , fspecial('gaussian',[1*3+1 1*3+1],1));
sharpness_VAR=std2(abs_o)^2;
sharpness_GRA = 0;

for xn = 2:yy
   for yn = 2:xx
      GRA = sqrt((abs_o(xn,yn)-abs_o(xn-1,yn))^2+(abs_o(xn,yn)-abs_o(xn,yn-1))^2);
      sharpness_GRA = sharpness_GRA + GRA;
   end
end

sharpness_LAP = 0;
for xn = 2:yy-1
   for yn = 2:xx-1
      LAP = (abs_o(xn+1,yn)+abs_o(xn-1,yn)+abs_o(xn,yn+1)+abs_o(xn,yn-1)-...
         4*abs_o(xn,yn))^2;
      sharpness_LAP = sharpness_LAP + LAP;
   end
end

end
```

References

1. Rosenkrantz, A. B.; Mendiratta-Lala, M.; Bartholmai, B. J.; Ganeshan, D.; Abramson, R. G.; Burton, K. R.; Yu, J. P. J.; Scalzetti, E. M.; Yankeelov, T. E.; Subramaniam, R. M.; Lenchik, L., Clinical Utility of Quantitative Imaging. *Academic Radiology* **2015,** *22* (1), 33-49.

2. Zernike, F., How I discovered phase contrast. *Science* **1955,** *121* (3141), 345-349.

3. Mann, C. J.; Yu, L.; Lo, C. M.; Kim, M. K., High-resolution quantitative phase-contrast microscopy by digital holography. *Optics Express* **2005,** *13* (22), 8693-8698.

4. Allen, R. D.; Allen, N. S.; Travis, J. L., Video - enhanced contrast, differential interference contrast (AVEC - DIC) microscopy: A new method capable of analyzing microtubule - related motility in the reticulopodial network of allogromia laticollaris. *Cell Motility* **1981,** *1* (3), 291-302.

5. Hoffman, R., The modulation contrast microscope: principles and performance. *Journal of Microscopy* **1977,** *110* (3), 205-222.

6. Curl, C. L.; Harris, T.; Harris, P. J.; Allman, B. E.; Bellair, C. J.; Stewart, A. G.; Delbridge, L. M. D., Quantitative phase microscopy: A new tool for measurement of cell culture growth and confluency in situ. *Pflugers Archiv European Journal of Physiology* **2004,** *448* (4), 462-468.

7. Gabor, D., A new microscopic principle. *Nature* **1948,** *161* (4098), 777-778.

8. Park, Y. K.; Depeursinge, C.; Popescu, G., Quantitative phase imaging in biomedicine. *Nature Photonics* **2018,** *12* (10), 578-589.

9. Cuche, E.; Bevilacqua, F.; Depeursinge, C., Digital holography for quantitative phase-contrast imaging. *Optics Letters* **1999,** *24* (5), 291-293.

10. Zhang, Z.; Zheng, Y.; Tienan, X. U.; Upadhya, A.; Lim, Y. J. I. N.; Mathews, A.; Lexing, X. I. E.; Lee, W. M., Holo-UNet: hologram-to-hologram neural network restoration for high fidelity low light quantitative phase imaging of live cells. *Biomedical Optics Express* **2020,** *11* (10), 5478-5487.

11. Garcia-Sucerquia, J.; Xu, W.; Jericho, S. K.; Klages, P.; Jericho, M. H.; Kreuzer, H. J., Digital in-line holographic microscopy. *Applied Optics* **2006,** *45* (5), 836-850.

12. Marquet, P.; Rappaz, B.; Magistretti, P. J.; Cuche, E.; Emery, Y.; Colomb, T.; Depeursinge, C., Digital holographic microscopy: A noninvasive contrast imaging technique allowing quantitative visualization of living cells with subwavelength axial accuracy. *Optics Letters* **2005,** *30* (5), 468-470.

13. He, X.; Nguyen, C. V.; Pratap, M.; Zheng, Y.; Wang, Y.; Nisbet, D. R.; Williams, R. J.; Rug, M.; Maier, A. G.; Lee, W. M., Automated fourier space region-recognition filtering for off-axis digital holographic microscopy. *Biomed. Opt. Express* **2016,** *7* (8), 3111-3123.

14. Rappaz, B.; Marquet, P.; Cuche, E.; Emery, Y.; Depeursinge, C.; Magistretti, P. J., Measurement of the integral refractive index and dynamic cell morphometry of living cells with digital holographic microscopy. *Optics Express* **2005,** *13* (23), 9361-9373.

15. Dubois, F.; Yourassowsky, C.; Monnom, O.; Legros, J. C.; Debeir, O.; Van Ham, P.; Kiss, R.; Decaestecker, C., Digital holographic microscopy for the three-dimensional dynamic analysis of in vitro cancer cell migration. *Journal of Biomedical Optics* **2006,** *11* (5).

16. Dunn, G. A.; Zicha, D., Dynamics of fibroblast spreading. *Journal of Cell Science* **1995,** *108* (3), 1239-1249.

17. Baker-Groberg, S. M.; Phillips, K. G.; McCarty, O. J. T., Quantification of volume, mass, and density of thrombus formation using brightfield and differential interference contrast microscopy. *J. Biomed. Opt.* **2013,** *18* (1).

18. Zangle, T. A.; Teitell, M. A., Live-cell mass profiling: An emerging approach in quantitative biophysics. *Nat. Med.* **2014,** *11* (12), 1221-1228.

19. Kim, M. K., Principles and techniques of digital holographic microscopy. *SPIE Reviews* **2010,** *1* (1).

20. Langehanenberg, P.; Kemper, B.; Dirksen, D.; Von Bally, G., Autofocusing in digital holographic phase contrast microscopy on pure phase objects for live cell imaging. *Applied Optics* **2008,** *47* (19), D176-D182.

21. Sun, Y.; Duthaler, S.; Nelson, B. J., Autofocusing in computer microscopy: Selecting the optimal focus algorithm. **2004,** *65* (3), 139-149.

22. Groen, F. C. A.; Young, I. T.; Ligthart, G., A comparison of different focus functions for use in autofocus algorithms. *Cytometry* **1985,** *6* (2), 81-91.

23. Özgen, M. T.; Tuncer, T. E., Object reconstruction from in-line Fresnel holograms without explicit depth focusing. *Optical Engineering* **2004,** *43* (6), 1300-1310.

24. Thelen, A.; Bongartz, J.; Giel, D.; Frey, S.; Hering, P., Iterative focus detection in hologram tomography. *Journal of the Optical Society of America A: Optics and Image Science, and Vision* **2005,** *22* (6), 1176-1180.

Appendix C Calibration of COSI system

Imaging depth

The imaging depth of field of scattering light was tailored by changing the oblique illumination angle. To visualize different depths, we show the backscattering signal of 3 μm polystyrene spheres and a formed thrombus at various depths in Fig. C-1. We can observe the reduction in scattering signal and out of focused light as the imaging depth becomes thinner.

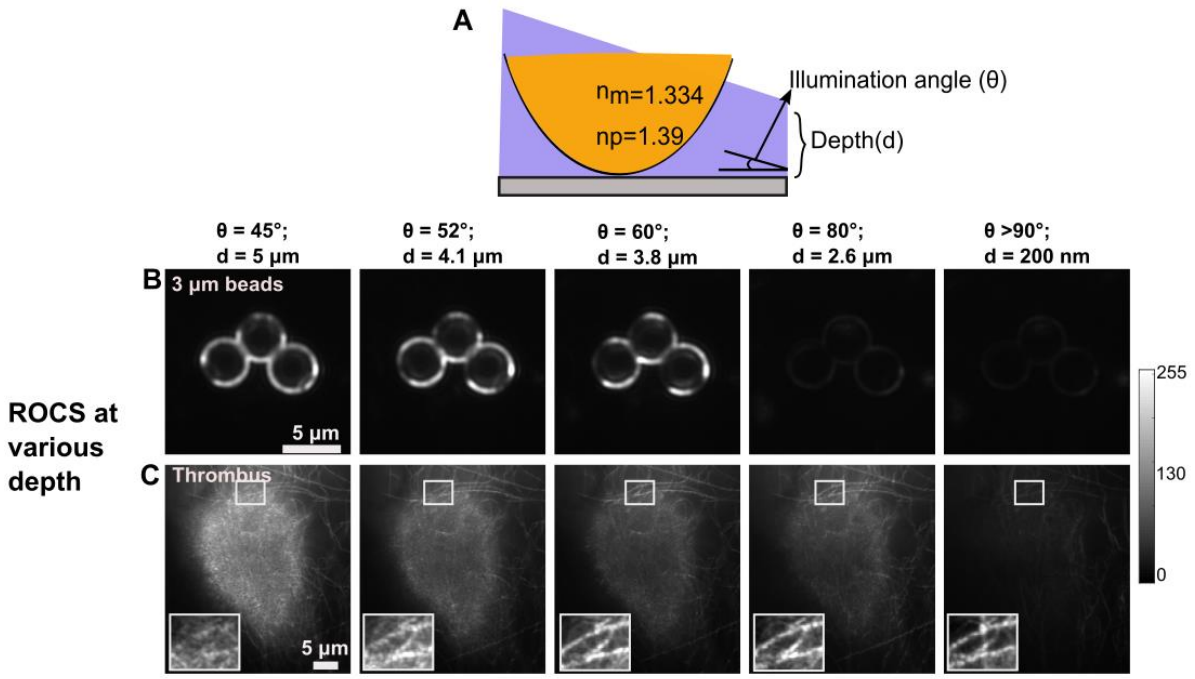

Figure C-1 Backscattering intensity of a single platelet and thrombus at different illumination angles. (A) Illustration of the general relationship of the oblique and illumination angle (θ) and imaging depth (d). The backscattering intensity signal of (B) 3 μm polystyrene microspheres (refractive index = 1.59) and (C) a formed thrombus at 5 different oblique angles corresponding to 5 μm, 4.1 μm, 3.8 μm, 2.6 μm and 200 nm axial slice thicknesses. Inlet images show the magnified image of collagen fibre structure.

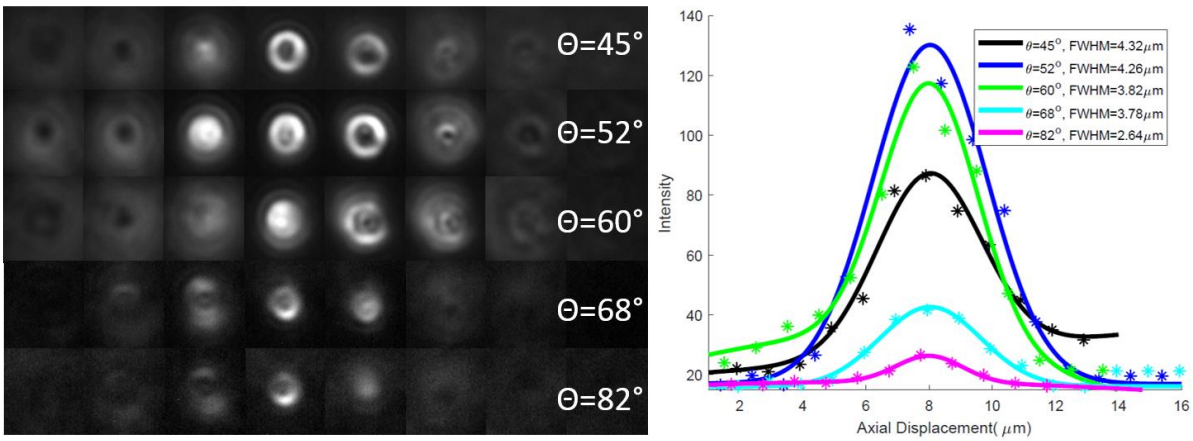

Figure C-2 Measured imaging depths of the scattering signal under various illumination angles using a 1 μm bead (curves were fitted with a Gaussian function, achieving an R-squared value of 0.95).

The imaging depth was then calibrated by moving a single layer of 1 μm microspheres along the axial direction at 1 μm increments. Scattering images were collected and plotted in Fig. C-2, showing the normalized mean intensity distribution and the images for each illumination angle. The imaging depth is estimated by evaluating the full-width half maximum of the fitted Gaussian curve (goodness of fit ~ 0.95) as shown in Eq. C.1.

$$y = \sum_{i=1}^{2} a_i e^{\left[-\left(\frac{x-b_i}{c_i}\right)^2\right]} \qquad C.1$$

Backscattering Intensity and Refractive Index

Additionally, COSI quantitates the refractive index difference of the microspheres and medium through the magnitude of backscattered intensity. Fig. C-3 shows the COSI scattering signal with a mixture of microspheres with average refractive index differences ranging from 0.035 to 0.25. The measured scattering signal (signal to noise ratio – (SNR)) was plotted against the refractive index difference. The calibration between refractive index difference and scattering signal is done using microspheres made with polystyrene (3 μm diameter and refractive index 1.59) and silica (5.2 μm diameter and refractive index 1.51)

embedded in sucrose solutions. The refractive index of the sucrose solution varies from 1.334 to 1.45 (HI 96802 Hanna Instruments), creating differences in Δn. To ensure consistency, the incident angle of the beam to the objective is altered to ensure the sample is illuminated under same the oblique angle (50^{o}). To quantify the signal-to-noise ratio, we define the scattering intensity as signal and the imaging background as noise in our system. Based on the SNR measurement of microspheres in different mediums, we calculated the SNR of scattering signal from a single platelet membrane ranging from 1.19 – 1.33. Using the silica bead calibration plot (Fig. C-3), we obtained an estimated refractive index of 1.40 that agrees with the measurement of $n_{platelet} \approx 1.399$ [1] with the assumption that $n_{pbs} \approx 1.335$ [2].

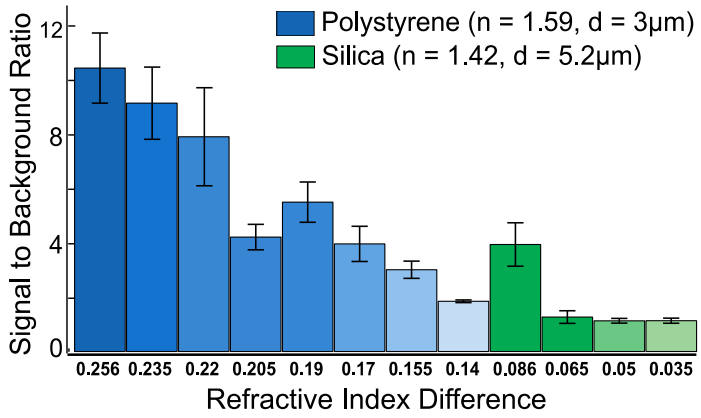

Figure C-3 Averaged scattering intensity signal to background ratio (SBR) of ten different polystyrene and silica beads of refractive index difference n_2=1.59, d = 3 μm and n_2=1.42, d = 5.2 μm respectively.

Stability of the COSI system

To calibrate the stability of the SNR measurement through the COSI system, we quantified the SNR variations from continuous backscattering signals of different samples under different flow conditions, as shown in Fig. C-4. Fixed silica microsphere (5.2 μm diameter, refractive index 1.42) with no flow and coated collagen fibre in microfluidics chamber are shown in Fig. C-4 A-B and C-D, respectively. We plotted SNR over imaging

time across three field views for both samples, and we did not observe any significant changes in SNR throughout the imaging period, as shown in Fig. C-4 B and D.

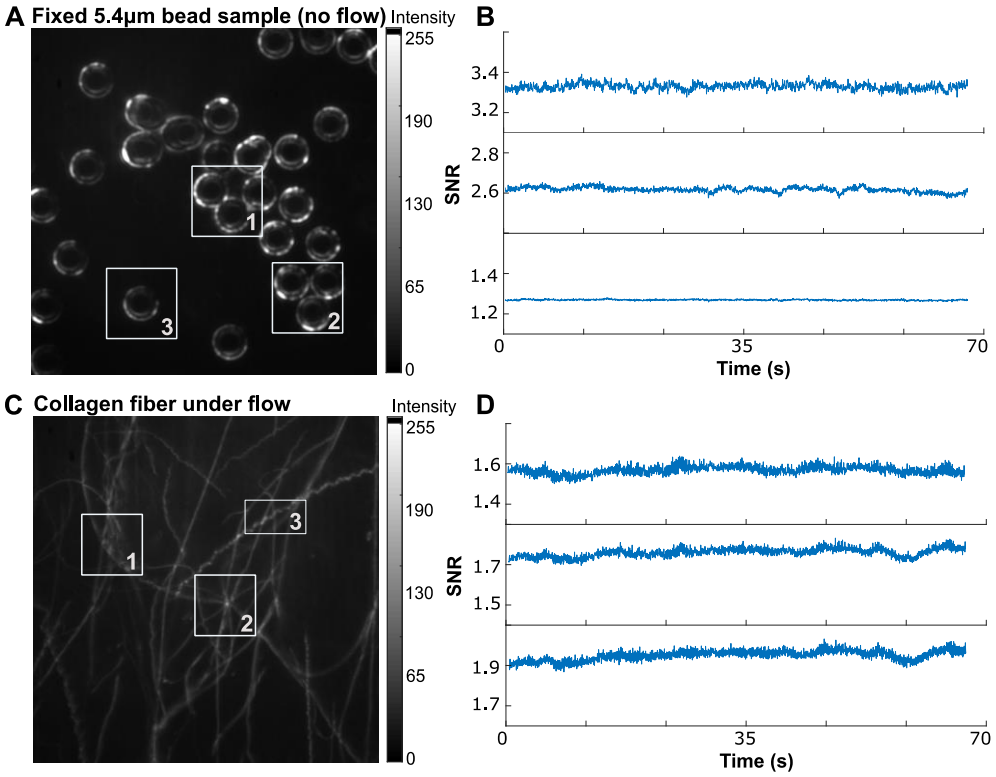

Figure C-4. Monitoring signal to noise ratio (SNR) over time. (A) Backscattering signal collected from COSI of fixed beads sample (5.2 μm) on a coverslip with no flow (static conditions) for 90 seconds. (B) Time series plots of signal to noise ratio (SNR) for three selected regions (1), (2), (3). in the microsphere are plotted over 70 seconds. All regions within the imaging field of view show a high level of stability. (C) Scattering signal from collagen fibre adhered onto the surface of glass slide of microfluidics chamber under flow for 70 seconds. (D) Time series plot of SNR from three regions of interest labelled 1-3 in (C) of adherent collagen fibre are plotted over time.

Quantification of Signal to Noise Ratio (SNR)

The foundation of interferometric scattering signal (I_{det}) lies in three components: the back-reflection intensity (reference field, $I_r = |\overline{E_r}|^2$), pure scattering field ($I_s = |\overline{E_s}|^2$) known as sample field in ROCS [18], and the superposition of reference and scattering ($2E_rE_s\cos\phi$, wherein $\phi = \phi_r - \phi_s$ are the relative phase difference between sample and reference) that refers to interferometric scattering [25, 29] (Eq. 6.1).

$$I_{det} \propto |\overline{E_r} + \overline{E_s}|^2 = I_r + I_s + 2E_rE_scos\phi \quad (6.1)$$

For nanoscale imaging, scattered intensity (E_s) is significantly lower than the reference intensity (E_r). The superpositioning of the reference and sample amplitude E_rE_s would be imbalanced and so results in poor interference visibility. To access interferometric scattering, it is crucial to ensure that the superposition intensity $2E_rE_scos\phi$ is not being masked by the dominant reference field ($I_r = |\overline{E_r}|^2$). We first measure the background intensity at different illumination angles in Fig. 6-1. By slightly shifting the beam from on-axis (0°) to 5.7° (Fig. 6-1 B-C), the reflected intensity drops drastically, to about only 10% of the on-axis background, indicating the oblique beam could optimize the background intensity to extract the interference component. The intensity of the reflected beam can be further optimised by adjusting the illumination angle from 5.7° to 35°, before being blocked by the diaphragm at 55° for darkfield detection.

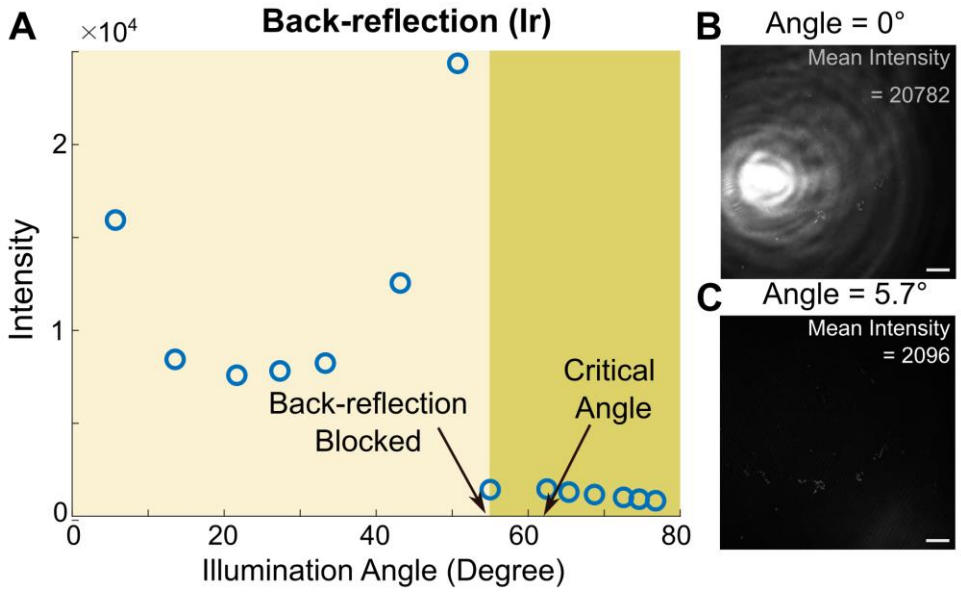

Figure C-5 Measurement of back-reflection intensity from the coverslip. (A) Plotting of back-reflection intensity at various illumination angles (5° to 76°). The intensity is measured by capturing the reflected light of an empty coverslip covered with water (refractive index = 1.33) at fixed exposure of 30 ms. Example of back-reflection signal and calculated mean intensity with (B) on-axis illumination (θ = 0°) and (C) oblique illumination (θ = 5.7°), measured at the exposure of 5 ms. Scale bar = 10 μm

To quantify the SNR of the gold/polystyrene particle, different particles were firstly diluted to desire concentration using distilled water and dried on a NO.1 coverslip. Before the imaging session, a drop of distilled water (100 μL) is added to cover the dried nanoparticles. To calculate the SNR of the nanoparticles at a specific illumination angle, a minimum of 50 regions containing a single particle are cropped from the original image captured by the camera. The peak value and averaged background are used for computing SNR using Eq. 6.2, and the outliner was removed beyond ± 1.5×std.

$$SNR = \frac{abs(I_s - I_{bkg})}{I_{bkg}} \tag{6.2}$$

References

1. Kolesnikova, I. V.; Potapov, S. V.; Yurkin, M. A.; Hoekstra, A. G.; Maltsev, V. P.; Semyanov, K. A., Determination of volume, shape and refractive index of individual blood platelets. *J. Quant. Spectrosc. Radiat. Transf.* **2006,** *102* (1), 37-45.

2. Hoang, V. T.; Stępniewski, G.; Czarnecka, K. H.; Kasztelanic, R.; Long, V. C.; Xuan, K. D.; Shao, L.; Śmietana, M.; Buczyński, R., Optical properties of buffers and cell culture media for optofluidic and sensing applications. *Appl. Sci. (Basel)* **2019,** *9* (6), 1145.

Appendix D MATLAB Code for Hardware Control

Generate continuous radical scan

```
function ScanButtonPushed (app, event)

    % initiate DAQ card for galvanometer and camera control
    app.dq = daq("ni");
    % enables analogue output
    addoutput(app.dq, "Dev4", "ao0", "Voltage");
    addoutput(app.dq, "Dev4", "ao1", "Voltage");
    % set condition for continuously scanning
    stopa = 1;
    % set output galvanometer voltage (vout)
    vout = 0.5*app.polar_angle;
    % generate 1 scanning pattern, sampling is number of scans per scan circle
    a = vout*sin(linspace(0, 2*pi,app.sampling+1))';
    b = vout*cos(linspace(0, 2*pi,app.sampling+1))';

    % set scanning rate
    app.dq.Rate = app.sampling*100*2;

    % generate repeating scanning pattern (>1s)
    c=repmat([b(1:end-1,:),a(1:end-1,:)],800,1);

    % set framerate of the camera
    app.ctr.Frequency = app.frame_rate_cosi;

    % set delay and duty cycle of camera trigger (determines exposure)
    app.ctr.InitialDelay = 0;
    app.ctr.DutyCycle = 0.6;
```

```
        % start scanning
        start(app.dq,"RepeatOutput")
        write(app.dq,c)

        % check if the stop button is pressed. If yes, stop scanning
        while stopa == 1
           drawnow
           if app.stop_scanning == true
              stop(app.dq)
              app.stop_scanning = false;
              stopa=0;
           end
        end
end
```

Generate a single scan

```
        write(app.dq,[vout*cosd(app.az_angle) vout*sind(app.az_angle)]);
```

Camera control

```
% initiate camera settings
obj.model = 'pco_edge';
obj.vid = videoinput(obj.pco_edge_cam,0,'CameraLink');

obj.vid.FramesPerTrigger = Inf;
obj.vid.ReturnedColorspace = 'grayscale';
obj.vid.LoggingMode = 'disk';
triggerconfig(obj.vid, 'immediate');

obj.src = getselectedsource(obj.vid);
obj.src.B1BinningHorizontal = '01';
obj.src.B2BinningVertical = '01';
obj.src.D1DelayTime_unit = 'us';
```

```
obj.src.E1ExposureTime_unit = 'us';
obj.src.E2ExposureTime = exposure;
obj.src.PCPixelclock_Hz = '95333333';
obj.src.TMTimestampMode = 'No Stamp';

diskLogger = VideoWriter('default.avi', 'Grayscale AVI');
obj.vid.DiskLogger = diskLogger;
% recording
classdef recorder < handle
    properties
        diskLogger
    end
    methods
        function obj = recorder()
        end
        function start(obj, camera, filepath)
            obj.diskLogger = VideoWriter(filepath, 'Grayscale AVI');
            if strcmp(camera.model, 'blackfly_s')
                obj.diskLogger.FrameRate = camera.src.AcquisitionFrameRate;
            end
            camera.vid.DiskLogger = obj.diskLogger;
            start(camera.vid);
        end
        function stop(~, camera)
            stop(camera.vid);
        end
        function [frame] = snap(~, camera)
            frame = getsnapshot(camera.vid);
        end
    end
end
```

Appendix E Sample Preparation

Washed platelets for spreading assay (Chapter 5)

Washed platelet is used in single platelet spreading assay. Venous whole blood was collected in anticoagulants, 3.2% trisodium citrate (for platelet-rich-plasma (PRP) experiments) or acid-citrate-dextrose (ACD; 97 mM trisodium citrate, 111 mM glucose, 78 mM citric acid). To obtain PRP, whole blood was centrifuged at 110 *g* for 20 minutes at room temperature, no brake. ACD-treated PRP was centrifuged at 1271 g for 15 minutes at room temperature with high brake to obtain washed platelets. The platelet-poor plasma (PPP) was removed, and the platelet pellet was resuspended in 123 mM NaCl containing 13 mM trisodium citrate and 33.3 mM glucose, pH 7.0, and then centrifuged at 1271 *g* for a further 15 minutes. After repeating this washing step three times, the platelet pellet was resuspended in Tyrode's buffer (5.5 mM glucose, 137 mM NaCl, 12 mM $NaHCO_3$, 1.8 mM $CaCl_2$, 0.49 mM $MgCl_2.6H_2O$, 2.7 mM KCl, 0.36 mM $NaH_2PO_4.H_2O$, pH 7.4) to reach a platelet count of 2×10^7 platelets/mL.

Glass coverslips (#1.5 thickness) were coated overnight at 4°C with 100 μg/mL collagen Reagent HORM (Takeda, Austria) or 5 μg/mL collagen-related peptide (CRP) or fibrin (100 μg/mL human fibrinogen for 30 min, then 1 U/mL thrombin for 15 min, followed by heparin 50 U/mL for 15 min). The coated coverslips were rinsed with phosphate-buffered saline (PBS) then blocked for 30 min with 5 mg/mL heat-inactivated bovine serum albumin in PBS, to minimize non-specific binding. Coverslips were rinsed before adding 50 μL of platelets (~2×10^7 platelets/mL), and morphology was monitored using COSI at indicated times. For platelets spreading assay with actin polymerization inhibitor, 50 μL of platelets (~1×10^8 platelets/mL) were added to the coverslips. The coverslips were then washed with PBS

after 1 minute of loading so that only adherent platelets were allowed to spread. PBS, 1% DMSO or 10 μM Cytochalasin D was then added to the spreading platelet at indicated times.

Washed platelets for migration study (Chapter 6)

The protocol of isolation human platelet is adapted [1]. Venous whole blood was collected in acid-citrate-dextrose (ACD; 11.9 mM trisodium citrate, 10.9 mM citric acid, 15.54 mM glucose). To obtain washed platelets, whole blood was firstly diluted 1:1 with modified Tyrode's buffer (137 mM NaCl, 2.8 mM KCl, 12 mM NaHCO3, 5.5 mM glucose, 10mM HEPES, pH = 6.5) and centrifuged at 70 g for 30 min at room temperature with the brakes switched off. The supernatant containing the platelet-rich plasma (PRP) was further washed by diluting PRP (1:3) with PGI2 (0.1 μg/ml, Cayman Chemical) in modified Tyrode's buffer (pH = 6.5). The washed platelet count was measured using the CELL-DYN Emerald 22 blood analyser (Abbott Laboratory, Illinois, USA). After obtaining the count, the washed platelets were centrifuged at 1250 g for 10 min at room temperature. The pellet was then re-suspended in modified Tyrode's buffer (pH = 7.4) to reach a platelet count of 5×10^8 cells/mL.

Fixation and Staining of Fibroblast Cells

L929 murine fibroblast cell lines are maintained in Dulbecco's modified Eagle's medium (DMEM) containing 10% Fetal Bovine Serum (FBS) in a humidified 10% CO_2 atmosphere 37 °C. Before each experiment, cells are re-plated onto a custom-built PDMS imaging chamber and grow for an additional 1−2 days until they reach final confluency of ~70%. Cells are fixed with 4% paraformaldehyde (PFA, Thermo Scientific) in PBS for 15 minutes, followed by three PBS washes, and then permeabilized with 0.1% Triton X-100 for 15 minutes. Fixed cells are washed with PBS three times and then incubated with Alexa Fluor

488 conjugated Phalloidin (Actin Green 488 ReadyProbes, Invitrogen) for 30 minutes, followed by three PBS washes before imaging.

References

1. Gaertner, F.; Ahmad, Z.; Rosenberger, G.; Fan, S.; Nicolai, L.; Busch, B.; Yavuz, G.; Luckner, M.; Ishikawa-Ankerhold, H.; Hennel, R.; Benechet, A.; Lorenz, M.; Chandraratne, S.; Schubert, I.; Helmer, S.; Striednig, B.; Stark, K.; Janko, M.; Böttcher, R. T.; Verschoor, A.; Leon, C.; Gachet, C.; Gudermann, T.; Mederos y Schnitzler, M.; Pincus, Z.; Iannacone, M.; Haas, R.; Wanner, G.; Lauber, K.; Sixt, M.; Massberg, S., Migrating Platelets Are Mechano-scavengers that Collect and Bundle Bacteria. *Cell* **2017,** *171* (6), 1368-1382.e23.

Appendix F Supplementary Data for Thrombus Stability Experiment

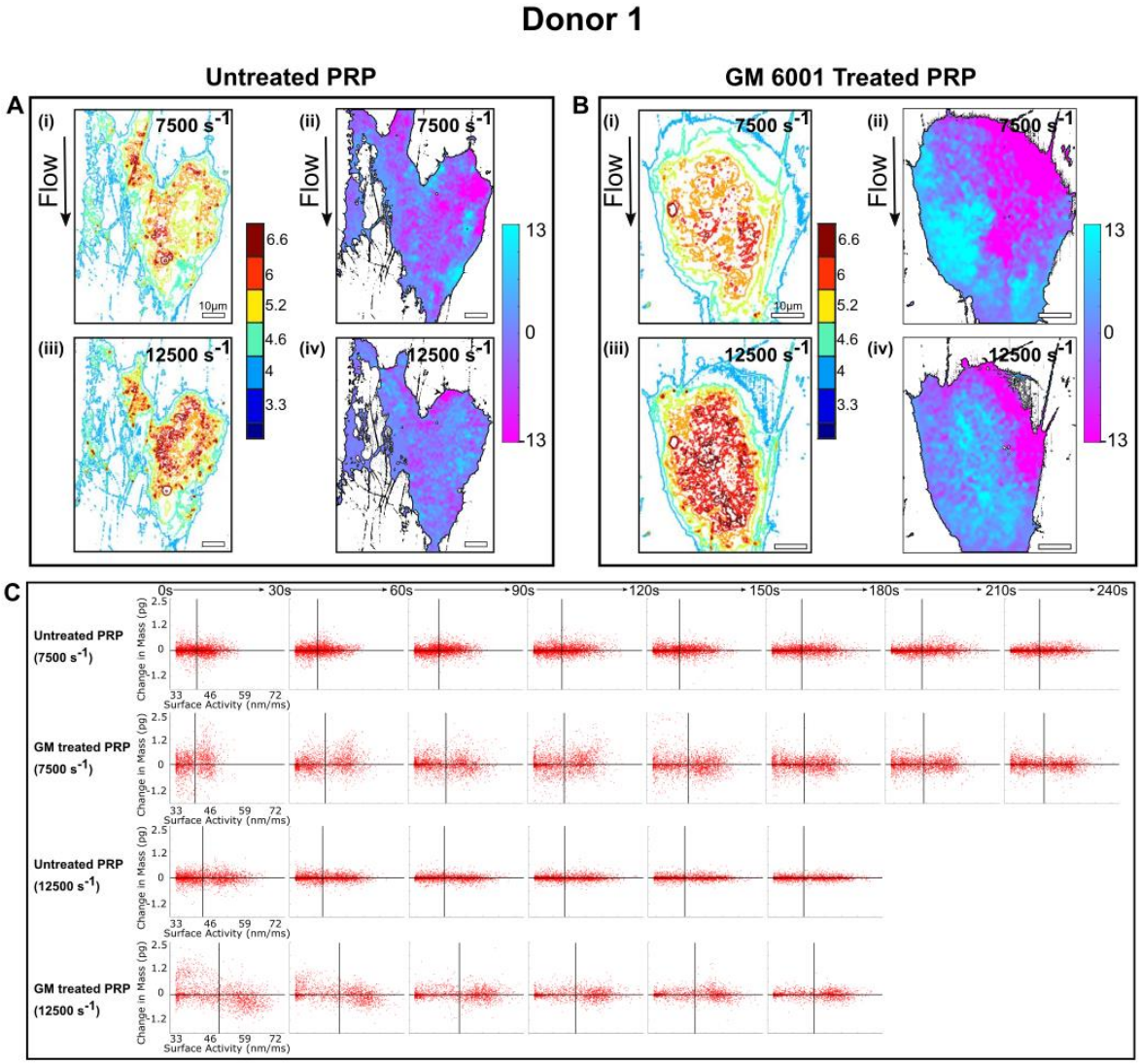

Figure F-0-1 (A-B) 2D mass and activity maps of thrombi during stability tests with and without metalloproteinase inhibition. (C) Mass and activity differences between donors and with and without GM6001 treatment

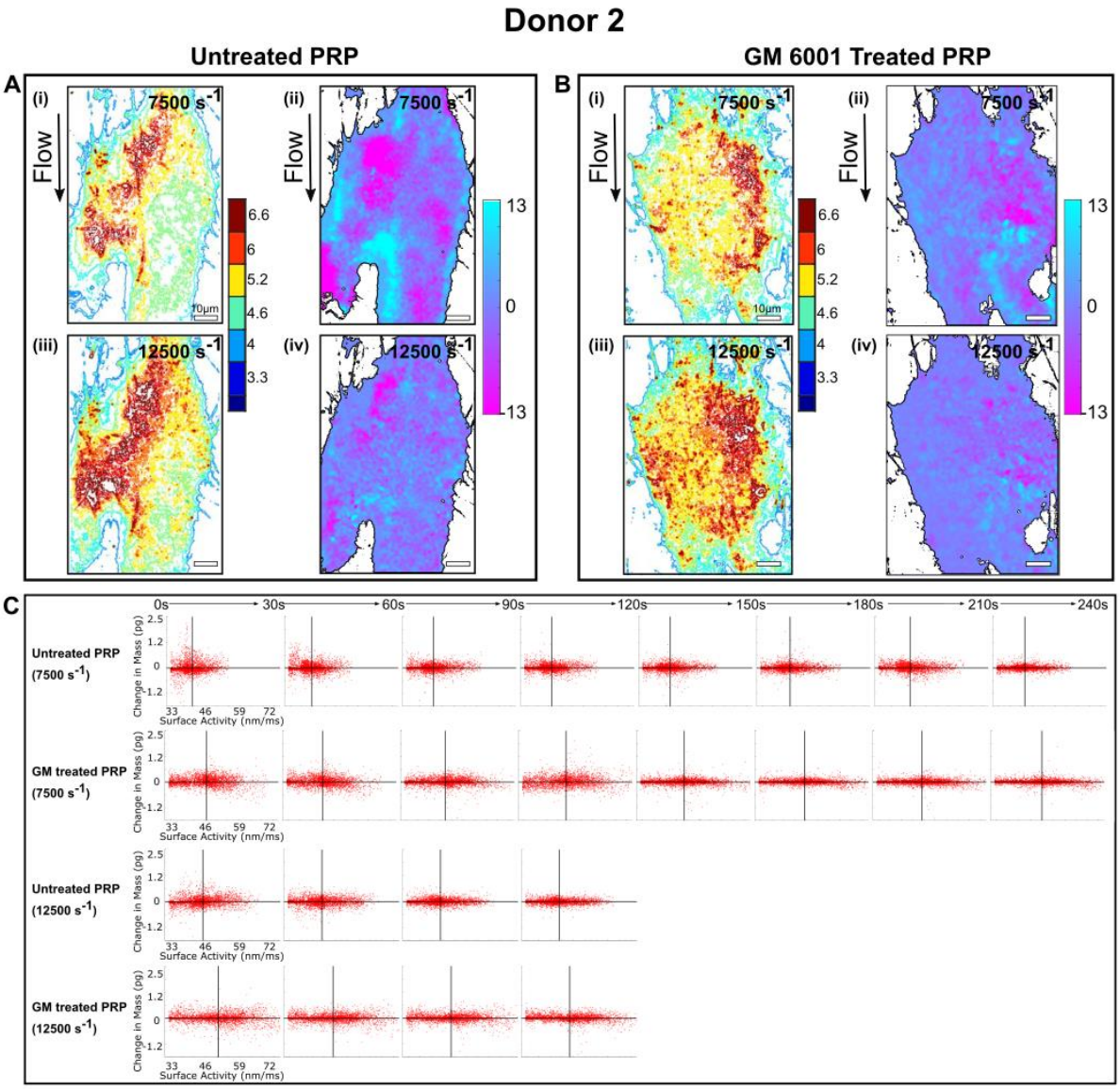

Figure F-2 (A-B) 2D mass and activity maps of thrombi during stability tests with and without metalloproteinase inhibition. (C) Mass and activity differences between donors and with and without GM6001 treatment

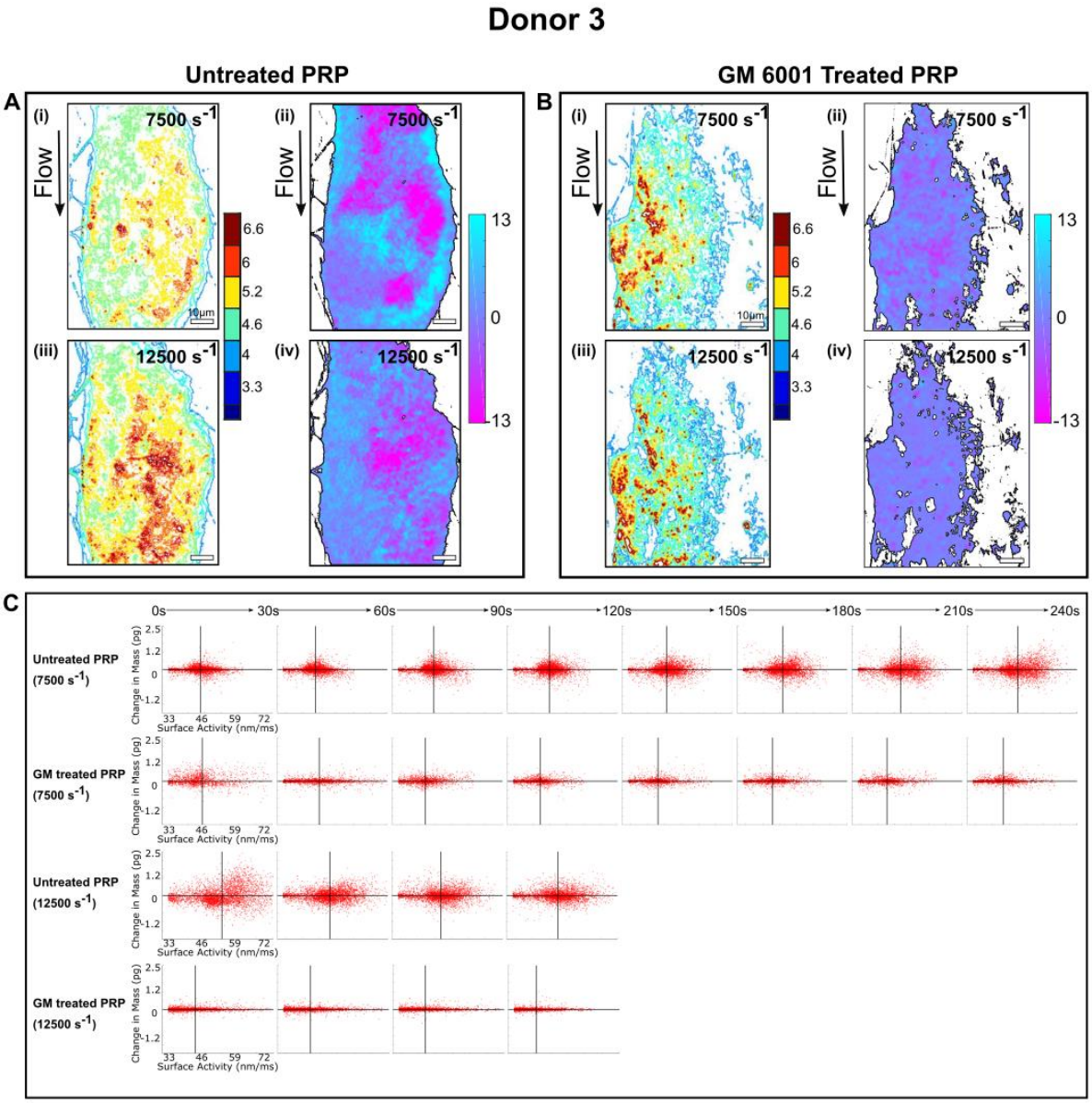

Figure F-3 (A-B) 2D mass and activity maps of thrombi during stability tests with and without metalloproteinase inhibition. (C) Mass and activity differences between donors and with and without GM6001 treatment

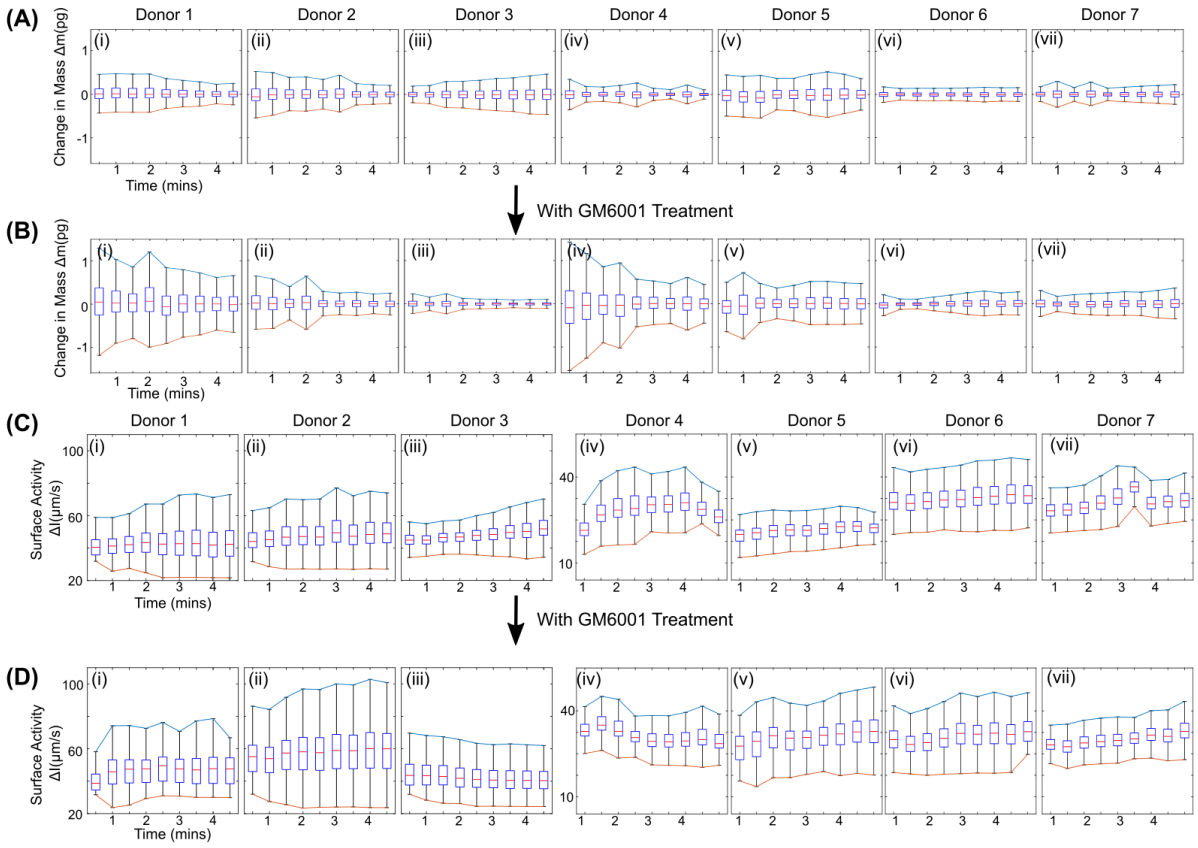

Figure F-4 Box plots showing changes in thrombus mass and platelet activity during embolization (for Fig. 5.). (A-B) Box plots showing changes in thrombus mass overtime during embolization at 7500 s-1 shear rate of seven donors without (A) and with (B) GM6001 pre-treatment. (C-D)Surface platelet activity over time during embolization at 7500 s-1 without (C) and with (D) GM6001 pre-treatment. Natural donor variation is observed with and without GM6001 treatment.